# DESIGN OF COMPOSITE STRUCTURES FOR BLAST MITIGATION

A Dissertation
Presented to
The Academic Faculty

by

Siddharth Avachat

In Partial Fulfillment
of the Requirements for the Degree
Doctor of Philosophy in the
School of Mechanical Engineering

Georgia Institute of Technology
December, 2015

**DESIGN OF COMPOSITE STRUCTURES FOR BLAST MITIGATION**

Approved by:


Dr. Min Zhou, Advisor
G.W.W. School of Mechanical Engineering
*Georgia Institute of Technology*

Dr. Julian J. Rimoli
School of Aerospace Engineering
*Georgia Institute of Technology*

Dr. Kyriaki Kalaitzidou
G.W.W. School of Mechanical Engineering
*Georgia Institute of Technology*

Dr. Shuman Xia
G.W.W. School of Mechanical Engineering
*Georgia Institute of Technology*

Dr. George A. Kardomateas
School of Aerospace Engineering
*Georgia Institute of Technology*


Date Approved: October 5, 2015

*Dedicated to my family*

# PREFACE

The research work reported in this dissertation was performed at the Georgia Institute of Technology. The research was sponsored by the Office of Naval Research through grant numbers N00014-09-1-0808 and N00014-09-1-0618 under the auspices of Dr. Yapa D. S. Rajapakse. Calculations were carried out using computational resources provided by the Department of Defense High Performance Computing Modernization Program (DoD HPCMP) and Georgia Tech Partnership for an Advanced Computing Environment (PACE).

The purpose of this dissertation is to present, in a comprehensive manner, the research carried out to assess and enhance the blast resistance of marine structures. The research topics discussed here involve experimental and computational techniques, and optimization and scaling. This thesis is divided into 11 chapters and includes an exhaustive literature review, information pertaining to materials selection and manufacturing techniques, analysis of the dynamic response of composite structures subjected to underwater impulsive loads in different environmental conditions, and design guidelines for the development of blast resistant marine structures.

Siddharth Avachat

Atlanta, GA, USA

Fall, 2015

## ACKNOWLEDGEMENTS

I owe a debt of gratitude to my advisor, Dr. Min Zhou, for his unfailing support and encouragement, and for an educational experience which encompassed academic research, independent thinking, decision making, and technical communication. I thank the members of my committee Drs. Kyriaki Kalaitzidou, George Kardomateas, Julian J. Rimoli and Shuman Xia for their comments and suggestions. I would like to thank Dr. Ashish K. Lele of the National Chemical Laboratory, India for an opportunity to work in the Complex Fluids and Polymer Engineering lab, and Dr. Mukund Y. Gokhale and Dr. Giridhar M. Joshi of the University of Pune, India for their advice and support. I am grateful for generous financial support from the United States Department of Defense, Office of Naval Research (ONR), and for guidance from Dr. Yapa D. S. Rajapakse.

I would also like to express heartfelt gratitude for the graciousness of the American scientific establishment in enabling me to pursue my research interests.

I am thankful to my fellow graduate students for their support and memorable discussions over endless cups of coffee. I would like to thank my lab members Ananda Barua, Yifan Gao, Barett Hardin, Seokpum Kim, Christopher Lammi, Christopher Miller, and Yan Li. I would also like to thank fellow graduate students Peter Marshall, Michael Kirka, William Musinki, Patxi Fernandez-Zelaia, Shreevant Tiwari, Andrea Marcon, Anirban Patra, Jeffery Lloyd, Hannes Daepp, Martin Cacan, and Brett Ellis for their friendship over the last few years and I wish all of them the best in their future endeavors.

Last, but not the least, I am eternally indebted to my family for their emphasis on the value of education and a strong work ethic, and their unconditional love and support.

## TABLE OF CONTENTS

## LIST OF TABLES

Page

## LIST OF FIGURES

Page

## SUMMARY

Structural design of ships and submersibles is a complex undertaking, because the deformations experienced by naval vessels are a result of the combined effects of multiple loads acting simultaneously. The analysis of the blast response of marine composite structures is further complicated by material heterogeneities, geometric nonlinearities and multi-axial loading conditions which cause unpredictable failure. Effective design of marine composite structures requires an intimate understanding of dynamic deformation and failure and a capability to predict and control their performance. The complexity of technical issues necessitates detailed experiments that account for realistic service environments and a complementary computational framework that allows a wide range of scenarios to be explored. The input from such parametric technical approaches can be utilized to address the need for better designed, more durable, blast resistant and lightweight marine vessels.

The proposed research aims to address this need and provide quantitative guidance for structural design of navy ships. To this end, a novel test environment is constructed to specifically provide controlled underwater impulsive loading and measure time- and space-resolved deformation and failure in composite structures. These measurements allow the characterization of failure modes and collapse behavior of composite structures in ways that have not been possible until now. Concurrent finite-element simulations are carried out to accurately track the different damage modes and evaluate the energy dissipation and impulse resistance characteristics of different materials and structures. This combined experimental and numerical approach enables exhaustive exploration of design scenarios involving simultaneous variations in loading

conditions, material properties and geometric attributes to develop quantitative loading-structure-performance relationships. The proposed research is expected to yield data and criteria for the design of blast resistant composite structures and vessels for next generation naval applications.

# 1. INTRODUCTION

Marine vessels are designed to operate in hostile environments consisting of corrosive sea-water, hot and cold temperature extremes, transient dynamic loads like hull-slamming and complex multi-axial hydrostatic loads. Additionally, naval structures are required to withstand weapons impacts and blast loads resulting from surface and underwater explosions. Recent assessments of marine structures have demonstrated that composite materials and sandwich structures can provide high strength-to-weight ratios and good blast mitigation. In particular, sandwich composites can provide superior blast mitigation due to their high strength-to-weight ratios and high shear and bending resistances. Through the combination of a thick, low-density core and thinner, stiff facesheets, sandwich structures achieve higher shear and bending stiffness to weight ratios than homogeneous plates of equivalent mass made exclusively of either the core or the facesheet material. The primary factors that influence the structural response of sandwich structures are (1) facesheet stiffness, (2) core thickness, (3) core density, and (4) interfacial strength. Other issues of relevance are the loading intensities, angles of incident impulse, service conditions and environments.

The deformation and failure of composite structures subjected to underwater impulsive loads from explosions are complicated due to competing damage mechanisms, failure modes, interfacial effects and material heterogeneities. The material properties of the different components significantly affect the blast resistance of the structures. In addition, loading conditions (intensity, boundary conditions, and environments) influence the failure modes in rather unpredictable and complex ways. Despite recent advances in

understanding the dynamic response of composite materials, several issues pertaining to underwater blast response of composites remain unresolved. Among these, an important open research topic is the lack of design relations that quantify the performance of a structure as a function of constituent materials, structural attributes and loading environments. To obtain such quantitative relations, detailed experiments and numerical approaches that account for these different features of marine composites are required. Diagnostics that provide in-situ, time-resolved response measurements are also needed and until recently, such experiments and numerical approaches remained unavailable.

The primary impediment to the failure analysis of composite structures under blast loads is the lack of detailed, repeatable experiments and quantitative measurements and diagnostics. In recent years, a number of experimental facilities have been constructed with the aim to analyze the deformation response of marine structures under realistic loading conditions. However, such facilities involve closed experimental setups with only the distal face visible to observers [1]. In a number of cases, none of the regions of the structure are observable and failure analysis must be carried after the event has taken place [2, 3]. Since structural collapse and failure is predicated on deformation that occurs near the impulse face in early stages of dynamic response, there is a need for developing an experimental facility that can capture spatial and temporal evolution of dynamic deformation and provide real-time experimental data that can be correlated with numerical approaches. A complementary computational framework is needed to provide further insight into the deformation response of structures and enable the simulation of complex conditions that may be difficult to achieve experimentally. Such a framework must account for internal damage in foam cores and composite laminas as well as

interfacial damage due to delamination and core-face debonding. Finally there is a need for developing quantitative relations that take into consideration the loading conditions, structural attributes and blast response of structures using parametric approaches and dimensional analysis. Such an integrated approach to structural design of composite structures for blast mitigation has been missing.

The proposed research is focused on the dynamic response of composite materials and structures to underwater impulsive loading. This research work encompasses blast/shock loading; rupture and penetration; fluid structure interaction (FSI) effects; dynamic constitutive relations and strain-rate effects; damage-modeling; and proposing concepts for damage mitigation. The research work consists of three parts: (1) experimental methodology; (2) computational framework; and (3) quantitative structural design guidelines. First, a novel experimental technique is developed allowing the generation of high-intensity underwater impulsive loads in a controlled environment based on a projectile impact mechanism. Secondly, fully detailed finite-element simulations are carried out, explicitly accounting fluid-structure interaction (FSI) effects and different deformation mechanisms and failure modes in constituent materials. Finally, results from parametric studies based on this combined experimental and numerical approach are presented in the form of design-maps to establish loading-structure-performance relationships and enable scaling and materials-selection for the design of marine structures with enhanced blast-mitigation.

Chapter 1 provides the objectives of current research in addition to a detailed overview of this dissertation. Chapter 2 includes an exhaustive literature review of previous and current work in the field of air-blast and water-blast loaded structures. The

literature review is divided into four distinct sections: (1) underwater explosions; (2) dynamic response of metal and composite plates; (3) dynamic response of sandwich structures; and (4) scaling and structural design approaches used previously. Literature on both experimental and computational research is reported.

Chapter 3 outlines the materials used in this research and associated manufacturing techniques. Details about fiber reinforcements, matrix materials, prepreg curing techniques and sandwich structure construction are provided here. This chapter also gives a detailed overview of the different constitutive and damage models corresponding to each material, including composites, structural foams, adhesives, metals and the Coupled Eulerian-Lagrangian approach. This includes the Hashin model for composites, Johnson-Cook model for steel and aluminum, Mie-Grüneisen equation-of-state for water, and Deshpande-Fleck model for compressible foams.

Chapter 4 covers the design and development of an experimental setup to generate underwater impulsive loads in a controlled and repeatable manner without using explosives. The different diagnostics envisioned and developed for the Underwater Shock Loading Simulator (USLS) are explained including laser-interferometry, high-speed digital imaging, and pressure and force transducers. An elastic solution is derived for the USLS from first principles to show that theoretical and experimental observations are in agreement. Finite element studies are carried out to study the effects of gas reservoir pressure, valve pressure, projectile velocities and piston thickness on impulsive load generation in the USLS.

Chapter 5 deals with the structural design methodology used in this research to invent quantitative metrics and develop loading-structure-performance maps

encompassing a range of material properties, structural attributes, specimen geometries, loading intensities and boundary conditions.

Chapter 6 consists of research carried to evaluate the blast resistance of monolithic composite laminates. The composite laminates consist of carbon-fiber and glass-fiber reinforced epoxy with a range of layups such as biaxial, quasi-isotropic, and unidirectional. The computational approach is validated by comparing with experimental results. The deformation response and blast resistance of each laminate is evaluated using the out-of-plane displacement, transmitted impulse and accumulated damage under similar loading conditions and incident impulse magnitudes with a peak pressure of ~196 MPa. Finally, the effects of load obliquity on structural response are evaluated by tilting the test specimen at different angles and subjecting it to a constant impulse.

Chapter 7 contains an overview of the dynamic compressive response of structural polymeric foams subjected to a range of incident impulses. The study focuses on the overall deformation, strain recovery and impulse transmission which are quantified as functions of structural attributes such as core density, front and backface masses and incident impulsive load intensity. Measurements obtained using high-speed digital imaging and pressure and force sensors allow the computational models to be calibrated and verified. Quantitative loading-structure-performance maps are developed between the response variables and structural and load attributes. The results reveal that core density has the most pronounced influence on core compressive strain and impulse transmission. Specifically, for severe impulse intensities, a 100% increase in core density leads to a 200% decrease in compressive strain and a 500% increase in normalized transmitted impulse. On the other hand, structures with low density cores are susceptible to collapse

at high impulse intensities. Additionally, the compressive strains and transmitted impulses increase monotonically as the mass of the frontface increases, but are unaffected by backface mass.

Chapter 8 concerns the load-carrying capacity of simply-supported glass-fiber/vinylester structural PVC foam composite structures under water-based impulsive loads. The analysis focuses on the role of core density and the effect of varying structural attributes and environmental conditions on deformation and failure mechanisms in monolithic as well as sandwich composites. For the analysis carried out, the material properties of the sandwich cores are varied while the total mass is kept constant. The structures are subjected to impulsive loads of different intensities using a novel new projectile-impact-based facility called the Underwater Shock Loading Simulator (USLS). In-situ high-speed digital imaging and postmortem analysis are used to study the deformation and failure of individual components, focusing on the effects of loading intensities, failure modes and material heterogeneity. Depending on the loading rate, shear cracking and/or collapse are the primary failure modes of the polymeric foam cores. Core density and height also significantly influence the response and failure modes. On a per unit weight basis, structures with low density cores consistently outperform structures with high density cores because the former undergo smaller deflections, acquire lower velocities and transmit a smaller fraction of incident impulses. Scaling relations in the form of deflection and impulse transmitted as functions of core density and load intensity are obtained to provide guidance for structural design.

Chapter 9 consists of experiments and computations carried out to analyze the load-carrying capacity of simply-supported carbon-fiber/epoxy structural PVC foam composite structures under water-based impulsive loads. Three types of structures are tested: (1) sandwich structures with similar areal masses but different thicknesses; (2) sandwich structures with similar thicknesses and different areal masses; and (3) sandwich structures with graded cores consisting of three section with different core densities stacked with respect to the impulsive loading direction. Three structural foam densities are considered: 60, 100 and 250 $kg \cdot m^{-3}$.The facesheets and PVC foam cores are bonded using 3M AF-163 structural adhesives. The analysis focuses on the role of core density and the effect of varying structural attributes and environmental conditions on deformation and failure mechanisms in monolithic as well as sandwich composites. In-situ high-speed digital imaging and postmortem analysis are used to study the deformation and failure of individual components, focusing on the effects of loading intensities, failure modes and material heterogeneity. Scaling relations in the form of deflection and impulse transmitted as functions of core density and load intensity are obtained to provide guidance for structural design.

Chapter 10 covers a set of simulations to examine the effect of the ratio between facesheet thickness and core thickness on the dynamic response of composite sandwich structures. To this end, the core thickness and core density are kept constant and the thickness of the facesheets is varied. The dynamic behavior of composite structures is quantified using fiber and matrix damage, facesheet deflections and energy dissipation. The results are analyzed in both normalized and non-normalized forms to gain insight into underlying trends that can be explored in the design of materials and structures.

Chapter 11 deals with experiments and computational analysis of hybrid metal/composite plates subjected to water-based impulsive loads. The analysis focuses on the effect of varying material properties on load-carrying capacity, deflection, impulse transmission, energy dissipation and damage. The three structural designs studied are unmodified monolithic aluminum plates, unmodified monolithic composite plates and hybrid metal/composite laminates. The plates are circumferentially clamped and subjected to transverse, out-of-plane impulses of varying intensities. The experiments are supported by fully dynamic numerical simulations using a Coupled Eulerian-Lagrangian (CEL) framework which accounts for fluid-structure interactions and damage and failure in the constituent materials. Results show that load intensity determines the deformation and failure modes. The monolithic composite plates exhibit large-scale in-ply cracking, delamination and shear rupture near the clamped edges, while the aluminum plates undergo plastic deformation and petalling. The hybrid metal/composite structures show superior blast-resistance than both types of monolithic plates in terms of failure loads and energy dissipation, with the stacking sequence of the composite and metal layers significantly influencing the behavior.

Chapter 12 provides a summary of research work and the conclusions in each chapter and a discussion on future work.

# 2. LITERATURE REVIEW

## 2.1 Underwater explosions and fluid structure interaction (FSI)

R.H. Cole, in his book Underwater Explosions [4], gives a detailed account of the shock waves generated during an explosions and the effect of these waves on structures. Explosive materials are inherently unstable compounds which undergo chemical reactions to form stable products. Explosive reactions are triggered by imparting sufficient energy to the compound. Heated fuses or frictional heat from impact by a firing pin are most commonly used to initiate these reactions. Once initiated, the original material is rapidly converted into a gas at very high temperatures and pressures. This process is called "detonation" and it creates a shock front which advances at the speed of several thousand meters per second. This shock front is termed "detonation wave" and chemical transformation resulting from detonation occurs simultaneously with the progression of this wave. When this wave reaches the boundary of the explosive material and surrounding medium, the pressure is transmitted through the boundary at a finite pressure and velocity. In the case of underwater explosions, the surrounding medium is water which can be regarded as a homogeneous fluid incapable of sustaining shear stresses. A shock wave travelling through water has two distinct physical characteristics - shock-wave velocity and local particle velocity. At the pressures considered here, the speed of sound wave in water is independent of peak pressure and is ~1440 m/s. The speed of sound waves in water changes at extreme pressures and temperatures; that phenomenon is not discussed here.

Trinitrotoluene (TNT) is commonly used to generate, characterize and study underwater explosions. TNT has a specific energy of 4500 kJ/kg and the specific energy released by other explosive compounds is often expressed in the form of equivalent mass of TNT for the purpose of calibration. Upon detonation, TNT forms nitrogen, water, carbon-monoxide and solid carbon, and generates a large amount of pressure - on the order of 14000 MPa [5]. This pressure compresses the surrounding medium and radiates a high-pressure disturbance which decays exponentially in a phenomenon called "explosive decay." The velocities commonly observed for TNT are several times the limiting value of ~1440 m/s in water. The maximum pressure in this wave falls off rapidly with distance and approaches steady state behavior at large distances. The temporal profile of the wave broadens gradually as the wave radiates outward. This behavior of the blast wave is illustrated in Figure 1. With respect to the scaling behavior of underwater blasts (when considering larger quantities of explosives), the "principle of similarity" holds.

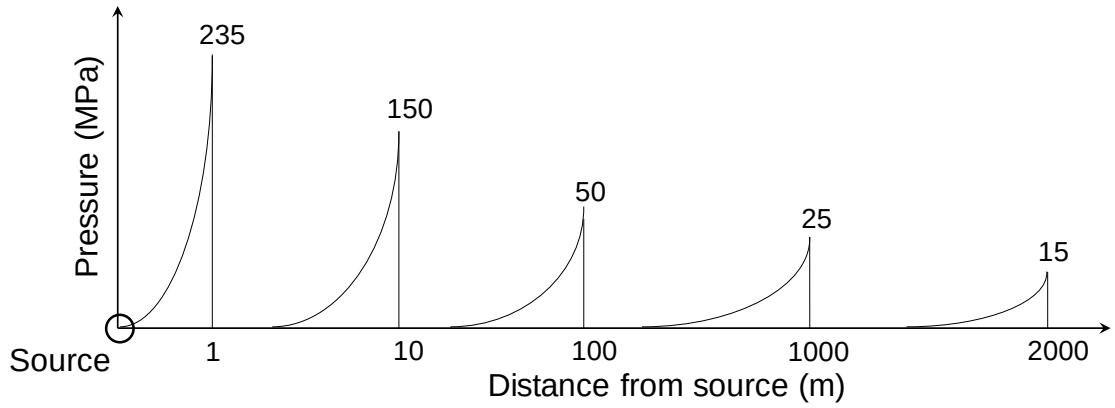


Figure 1 Spatial evolution of blast pulse for a TNT explosion. Figure not to scale. [4]

As the gas expands, it forms a bubble by displacing the water surrounding it. After reaching a maximum radius, the bubble contracts. The cyclical expansion and contraction of this gas-bubble is called "bubble oscillation." Bubble oscillations generate secondary pressure waves with ~10% initial blast overpressure and the peak pressure reduces with increasing number of oscillations. The gas-bubble simultaneously travels to the surface and once it reaches the surface, creates the characteristic plumes observed after an underwater explosion (shown in Figure 2). Of the total energy generated during a detonation event, ~40% is available for damage creation in marine structures while the rest is expended on bubble oscillations. Figure 2 shows the oscillations experienced by a gas-bubble as it expands and contracts and a schematic of the pressure generated due to oscillations. Unlike the exponentially decaying pressure profile after detonation, pressure generated by bubble oscillations causes a gradual rise in pressure followed by a decrease in pressure on the order of milliseconds. The peak pressure generated by each successive oscillation is 20% less than the previous one. Since the initial shock wave creates a high-magnitude impulse, subsequent pressure pulses due to bubble oscillations can be

neglected - except in one special case. If the gas-bubble rises underneath the ship hull, it can create complex loads on the structure. The rising gas bubble creates large pressures and pushes the ship hull outwards. When the bubble collapses, it pulls the hull inwards towards the center of the bubble. Consequently, this complex loading condition can create significant damage - sometimes exceeding the damage caused by the initial shock wave. If the frequency of the bubble oscillations matches the natural frequency of the ship structures, it can lead to large bending moments and cause whipping damage.

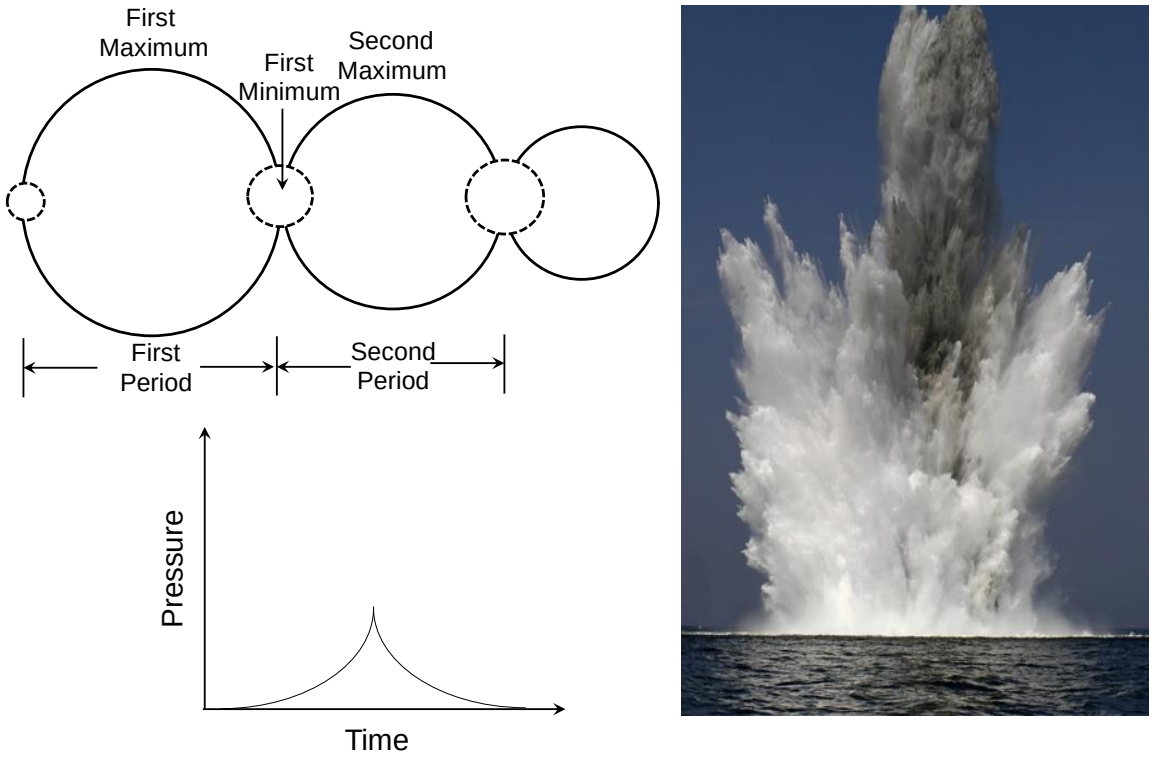


Figure 2 Bubble oscillations and pressure profile generated due to oscillations [4] and a "plume" created when an underwater explosion bubble reaches the water surface. Figure not to scale.

Close to the shore, detonation can create three types of waves - (1) direct wave from the explosion, which travels at the highest speed and reaches the ship earlier than the rest of the waves; (2) a surface wave, created when the pressure pulse reaches the

water-surface and (3) bottom-reflected wave, created when the initial pressure pulse reaches the ocean-floor and is reflected back. The types of waves that are caused by an underwater explosion are illustrated in Figure 3. In the research work presented in this thesis, the primary focus is on direct waves - waves that emanate from the explosion source and impinge a marine structure. The other types of waves are not considered here.

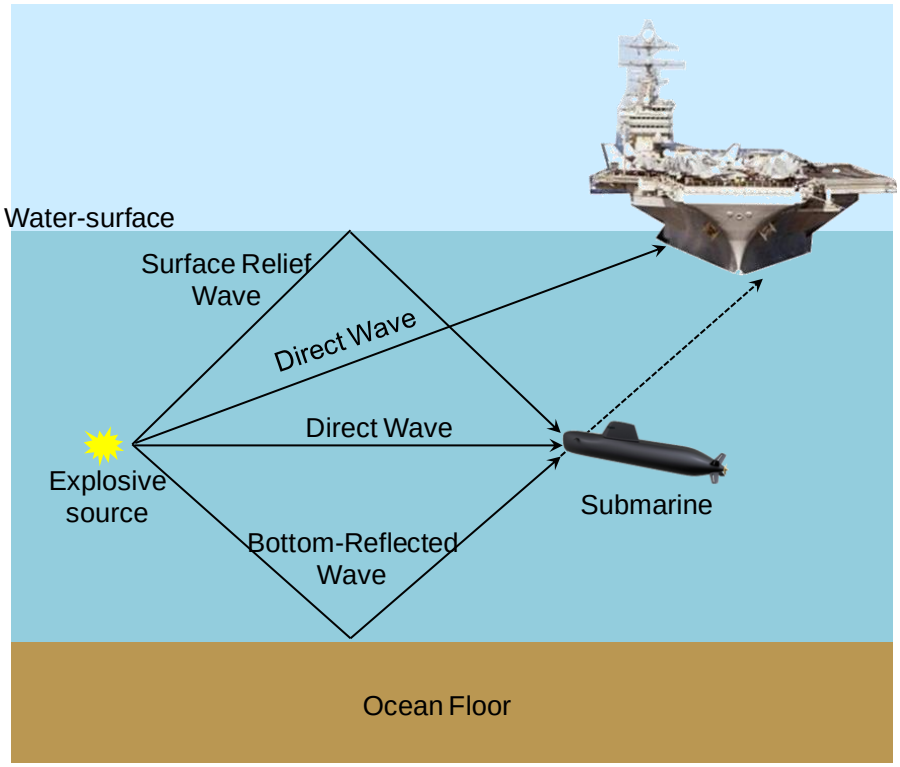


Figure 3 Types of waves generated by an underwater explosion [6]. Figure not to scale.

Proximity to an underwater explosion plays an important role in the dynamic behavior of a marine structure. If an underwater explosion occurs close to the ship hull, the resulting pressure wave will rupture the hull and cause significant damage to surrounding equipment. On the other hand, if the explosion occurs far from the ship, the blast wave will have a planar front and the pressure loading will be non-uniform. In this case, each section of the marine structure will respond differently to an incident pressure

pulse. The defining characteristics of a pressure pulse are the peak-pressure and pressure-time history. The peak pressure resulting from and underwater blast, $p_0$, is given by

$$p_0 = K_1 \left( \frac{M^{1/3}}{R} \right)^{\alpha_1}, \tag{1}$$

where $K_1$ and $\alpha_1$ are material constants (with values $K_1 = 5 \times 10^7$ and $\alpha_1 = 1.15$ for TNT), $M$ is the mass of TNT used and $R$ is the distance from explosive source [4, 5]. The blast decay constant, $\theta$, for the pressure pulse created due to an underwater explosion is given by

$$\theta = M^{1/3} K_2 \left( \frac{M^{1/3}}{R} \right)^{\alpha_2}, \tag{2}$$

where $K_2$ and $\alpha_2$ are material constants (with values $K_1 = 92 \times 10^6$ and $\alpha_2 = -0.22$ for TNT) source [5]. The decay constant defines the decay time for the peak-pressure.

G.I. Taylor proposed the earliest solution to a fluid-structure interaction problem based on a planar wave impinging upon a free-standing, rigid plate [6, 7]. According to Taylor's analysis of one-dimensional impulsive waves impinging on a light, rigid, free standing plate, the pressure in the fluid at a distance from the explosive source follows the relation

$$p(t) = p_0 \exp\left( -\frac{t}{t_0} \right), \tag{3}$$

where $p_0$ is the peak pressure, $t$ is time and $t_0$ is the pulse time on the order of milliseconds. The area under the pressure-time curve is the impulse carried by the wave and is given by

$$I_0 = \int_0^t p(t)\,dt. \tag{4}$$

For a free standing plate of areal mass $m$, the impulse transferred to the plate is

$$\frac{I_T}{I_0} = \psi^{\left(\frac{\psi}{1-\psi}\right)} \text{ where } \psi = \frac{\rho_w c_w t_0}{m}, \tag{5}$$

where $\psi$ is the fluid-structure interaction (FSI) parameter, $\rho_w$ is the density of water and $c_w$ is the speed of sound in water. For the upper limit i.e. an infinitely heavy plate subjected to an intense shock, the entire incident impulse is transferred to the plate such that $I = \int p(t)\,dt = 2p_0 t_0$. The FSI parameter $(\psi)$ is an important aspect of Taylor's analysis because it helps delineate the effects of a pressure pulse applied instantaneously versus the effects of a pressure pulse decaying over a certain time period. It has been shown that this FSI effect can be exploited to improve the blast mitigation capability of structures subjected to transient loads [8, 9]. Taylor's one-dimensional analysis can be used to estimate the impulse imparted to the facesheet of a sandwich structure subjected to an underwater blast, provided the core strength is relatively low and the pulse time is sufficiently short (less than 1 millisecond). The impulse transmitted to a sandwich plate will lie between the lower limit of a light, free-standing plate and an immovable rigid body. With respect to sandwich structure design, an incoming wave will transfer a very small impulse to a light plate supported by a core with very low strength. Conversely, if the core is strong and resists deformation, then a larger impulse is transferred to the structure than that predicted by Taylor's analysis. Taylor's analysis has been extended to sandwich plates by homogenizing the core into a low-density, low-strength continuum and providing additional terms to account for the deformation in a sandwich structure.

Xue and Hutchinson [10] provided a correction for eqn. (5) to account for a "pushback" effect when the frontface of areal mass resists motion by virtue of being supported by a core with compressive yield strength $\sigma_Y^c$ such that

$$\frac{I_T}{I_0} = \psi^{\left(\frac{\psi}{1-\psi}\right)} + 0.63\frac{\sigma_Y^c}{p_0}\left(1-\psi^{\left(\frac{\psi}{1-\psi}\right)}\right) \text{ where } \psi = \frac{\rho_w c_w t_0}{m_f}, \tag{6}$$

and $m_f$ is the mass per unit area of the frontface. Taylor's $I_T/I_0$ relation is independent of impulsive load intensity while Xue and Hutchinson's $I_T/I_0$ relation is dependent on peak pressure of the incident impulse as well as the yield strength of the core, leading to a loss in generality. It is yet to be ascertained if such simplified approaches can sufficiently capture the response of sandwich plates in rather complex cases consisting of different core densities, facesheet thicknesses, high intensity impulsive loads and water-backed conditions.

Since the mechanical impedance of water is much higher than air, underwater blasts travel large distances before attenuating sufficiently to be harmless. When underwater blast waves interact with marine structures, they can cause significant plastic dissipation and fracture. For large unsupported ship sections, damage is in the form of bending and tensile necking. For supported ship sections, damage is in the form of shear rupture and tearing. Figure 4 shows the damage in US navy ship the USS Tripoli due to an underwater mine. The oblique view shows the hull sheared off at supports. The front view shows significant petalling with characteristic tearing damage. Figure 5 shows the damage in USS Cole due to a combination of impact and blast wave loading while Figure 6 shows the cracked hull of the USS Princeton. An underwater blast resulted in shock

wave loading from beneath the ship. The gas-bubble formed due to this explosion rose underneath the ship and resulted in bending of the hull.

Front view Oblique view

Figure 4 Hull damage in USS Tripoli. Photographs from US Navy archives.

Figure 5 Hull damage in USS Cole. Photographs from US Navy archives.

Figure 6 Cracked hull of USS Princeton. Photographs from US Navy archives.

## 2.2 Dynamic response of monolithic structures

Early research in the dynamic response of marine structures was motivated by the need to improve the blast resistance of steel naval vessels and design better weapons during World War II. Initial work focused on dynamic plasticity in clamped circular thin-plates. Early experimental investigations were carried out by Taylor [11] who measured the center-displacement and deformed volume of an impulsively loaded thin diaphragm. Travis and Johnson [12] studied explosive forming of metallic plates while Johnson, Poynton et al. [13] developed diagnostics to measure the displacement and velocity of plates using pin-contacts. Williams [14] reported the first instance of high-speed dynamic imaging of blast-loaded plates. Finnie [15] carried out a parametric study by varying the charge mass and stand-off distance and its effect on thin plates. Bednarski [16] filmed high-speed deformation in membranes at ~6000 frames per second. Symonds and Jones

[17] studied the bending behavior of thin plates while Bodner and Symonds [18] reported dynamic plasticity in clamped plates and extended this research to viscoelastic structures [19]. Taylor [11], Richardson and Kirkwood [20] and Hudson [21] carried out theoretical studies of the dynamic response of thin plates. They proposed solutions based on bending and plastic deformation. Frederick [22] and Griffith and Vanzant [23] theorized dynamic load carrying capacities for thin plates that were significantly greater than corresponding static load carrying capacities. These studies showed that shear-strain increased with the rate-of-loading. For high-rate loads, circumferential strains were negligible. Hopkins and Prager [24] proposed an exact solution based on a thin plate subjected to transverse loads for a non-hardening plastic material and Tresca flow rule. Wang and Hopkins [25] and Florence [26] proposed a similar solution for a circular clamped plate – showing that circumferentially supported plates simplified the problem significantly. Hopkins [27] proposed a more general theory for plates subjected to non-uniform transverse loads while Shapiro [28] studied a thin plate supported at the center and loaded at the circumference. Other studies carried out during this period focused on variations in material models, materials and loading configurations. Detailed reviews of experimental and theoretical work are provided by Jones [29] and Nurick [30, 31].

Prior research on the dynamic behavior of composites has focused on low-velocity, contact-based loads such as drop weight and projectile impact [32-37]. Results showed that key damage mechanisms include matrix cracking, fiber breakage and interlaminar delamination. The primary driving forces for the damage processes are transverse shear stresses [38-40]. Interlaminar delamination is the most detrimental to stiffness and strength and, therefore, is a major concern because delamination is not

visible on the surface. Chang and coworkers [41-43] have studied the damage behavior of composite laminates under low velocity impact loading, concluding that in-ply matrix cracking precedes delamination growth and shear and bending crack initiation. The damage behavior of composite laminates is significantly influenced by matrix material, composite layup and geometric aspects such as size, thickness and loading area [44-46]. Minnaar and Zhou [47] used a novel interferometric experimental setup to show that interlaminar crack speeds in carbon-fiber/epoxy laminates are significantly higher under shear loading, and that crack speeds are strongly influenced by loading rate in mode II. There is a dearth of systematic studies pertaining to the response of composite laminates to impulsive loads such as those observed in air and water blasts. There are numerous reasons for this, such as a lack of advanced diagnostics, inability to obtain clean measurements, difficulties associated with creating repeatable and consistent loading conditions and complications arising from material and structural heterogeneities.

## 2.3 Dynamic response of sandwich structures

Sandwich structures first found application in the defense industry due to high strength-to-weight ratios, exceptional bending-resistance, durability and low life-cycle costs. In recent years, sandwich structures with strong facesheets and lightweight cores have become central structural components of blast resistant naval vessels. By virtue of the combination of a thick core and thin facesheets, sandwich structures achieve higher shear-stiffness-to-weight ratios and bending-stiffness-to-weight ratios than equivalent homogeneous plates made exclusively of the core material or the facesheet material. Additionally, sandwich cores can be designed to fulfill specific functionalities. The

primary factors that influence the structural response of a sandwich structure are (1) facesheet thickness, (2) core thickness and (3) core density. Zenkert [48] provided a review of the mechanics of sandwich structures, expanding on the previous work of Plantema [49] and Allen [50]. A major advantage of sandwich structures is the ability to use a variety of materials and core geometries – called topologies. In composite sandwich structures, faces are often composed of stiff carbon-fiber or glass-fiber sheets and the cores are manufactured from polymeric foams. Prior research on the dynamic behavior of sandwich composites has involved low velocity contact-based loads such as drop weight and projectile impact [32, 33, 51-55]. It is found that the overall deflection experienced by sandwich plates is significantly lower than monolithic plates of equivalent mass [10, 56-63]. Additionally, the forces and impulses transmitted by sandwich structures are also smaller than those by monolithic structures [56, 59, 60]. These studies show that fluid-structure interaction needs to be considered to accurately characterize impulsive loads. Sandwich structures subjected to exponentially decaying pressure histories outperform those subjected to instantaneous loads. Sandwich structures handily out-perform monolithic plates when deformation is dominated by bending. In the stretching regime, monolithic plates, due to their susceptibility to necking, show higher plastic dissipation than sandwich plates. Results show that core design greatly influences dynamic response of sandwich structures. Stiff cores perform poorly while light cores exhibit higher blast mitigation. A combination of buckling and stretching in the core provides the highest blast mitigation. For computational studies, continuum cores cannot accurately capture the various damage modes associated with prismatic sandwich structures. Rupture and core buckling can only be evaluated using detailed finite element simulations with

explicitly modeled cores. Figure 7 shows experimental results for sandwich plates subjected to air-shocks.

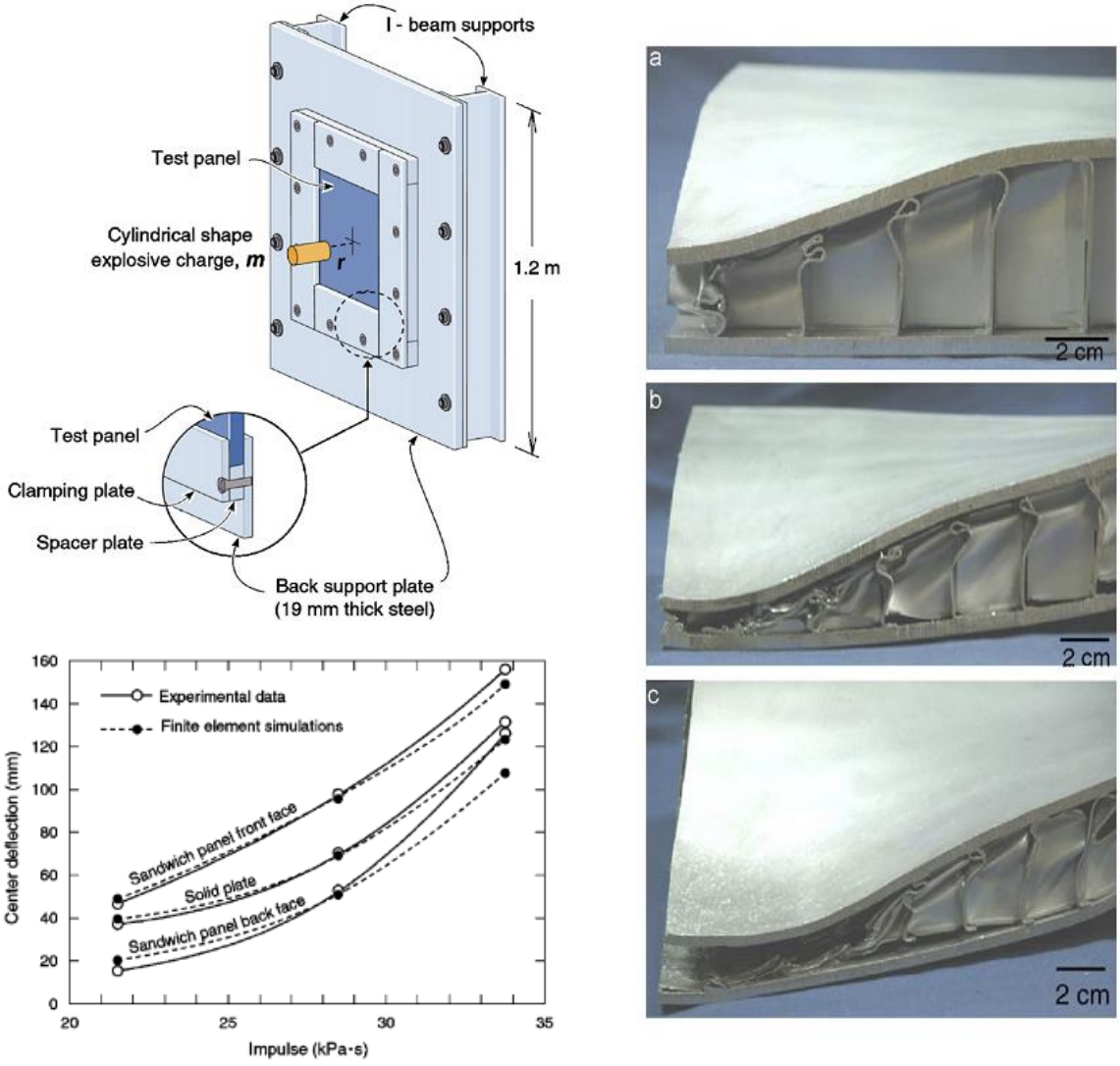


Figure 7 Dynamic response of sandwich plates with square honeycombs subjected to air-shocks [64]. Deflections are plotted as functions of impulse.

Experiments and computations focusing on different core topologies, specimen sizes, loading configurations and optimization have been carried out. Fleck and co-workers [2, 58, 62, 63, 65-71] have carried out analytical studies and numerical simulations of sandwich structures subjected to dynamic loads. Concurrent numerical

simulations and optimization studies have been carried out by Hutchinson and co-workers [10, 59, 60, 72-76]. Constitutive models have been developed to convert the sandwich core consisting of complicated geometry into a continuum in order to simplify computations [77, 78]. Shukla and co-workers [79-83] examined the dynamic response of woven E-glass composite facesheets and stitched core sandwich structures to air-based shock loading and concluded that stitched cores exhibit superior mechanical performance. They observed an increase in blast resistance when sandwich structure cores were multi-layered with increasing relative core densities. In addition to the fact that sandwich structures are greatly superior to monolithic plates for blast mitigation, these studies show that fluid-structure interaction effects need to be considered to accurately characterize impulsive loads. The presence of this complicated FSI effect can be exploited to enhance blast mitigation and improve survivability.

Taylor's analysis of fluid-structure interaction indicates that the impulse transferred to a structure can be minimized by reducing the mass of the structure. Sandwich structures offer this potential for two reasons: (i) higher bending stiffness using a lighter panel; (ii) careful choice of core density and facesheet mass distribution to exploit the FSI effect. Cellular materials, particularly foams, have been recognized as excellent shock and energy absorbers due to their long, flat stress-strain response due to stress-saturated compressive straining. Early experiments involving impulsive loading of structures consisted of impacting sandwich structures with metal foams [63, 84-88]. This strategy allowed for loading a "patch" over a range smaller than the support span with the foam projectile creating a load similar to fluid-based impulsive loading. Although such foam-projectile impact experiments can generate shock loads of a similar nature to blasts,

they cannot accurately capture the effect of fluid-structure interaction, cavitation and blast loading. Consequently, in recent years there have been significant efforts to develop experimental facilities capable of generating controlled water-based impulsive loads. Espinosa and co-workers used gas-gun based impact loading to generate underwater pressure impulses in a conical chamber [1, 89-93]. Wadley and co-workers [2, 64, 94, 95] developed an experimental facility called the "Dynocrusher" in which explosive sheets were used to generate planar pressure impulses in a water-tank. Diagnostics were primarily force-measurements and post-mortem visual characterizations. Researchers from US Navy have developed an underwater blast loading facility for use in controlled blast loading [96]. Common failure modes that have been identified include core indentation and cracking, core shear, facesheet buckling and delamination, core-facesheet debonding and perforation. The majority previous research in underwater blast mitigation has focused on metallic sandwich structures under planar impulsive loads. There is a need for further research in a number of areas, especially with regard to composite sandwich structures under realistic loading conditions, intensities and environments.

## 2.4 Hybrid metal composite structures

Early studies pertaining to the response of metallic plates subjected to transverse impulsive loads was carried out by Hudson [97] and Wang and Hopkins [98] who developed theoretical models for dynamic plasticity under blast loads. Experiments and simulations involving impulsively-loaded steel plates have revealed a range of deformation mechanisms and failure modes primarily dependent on load intensity [99, 100]. At low values of incident impulse, the plates experience bending and stretching

without rupture, exhibiting a primarily Mode I deformation response. At intermediate values of incident impulse, plate stretching occurs, followed by tensile necking and Mode II rupture near the supports. Theoretical studies by Lee and Wierzbicki [101, 102] have revealed discing and petalling deformation modes that resemble Mode II failure. Experimental studies involving explosive impulsive loads carried out by Balden and Nurick [103] have revealed shear rupture mode of failure (Mode III). Kazemahvazi et al. [67] analyzed the underwater blast response of axisymmetrically clamped copper plates and confirmed the dependence of failure modes on impulse intensity, concluding that failure modes are highly sensitive to peak pressure but relatively insensitive to blast decay time.

In recent years, composite materials have been employed in naval construction and the off-shore industry. As a consequence, understanding the response of composite structures to high intensity underwater impulsive loads has gained importance. Many investigations have been carried out on the dynamic deformation and failure of layered materials. Most of the studies on sandwich composites have focused on low velocity contact-based loads due to drop weight and projectile impact [32, 33, 51-55]. Results show that key damage mechanisms include matrix cracking, fiber breakage and interlaminar delamination. The primary driving forces for the damage processes are transverse shear stresses [38-40]. Interlaminar delamination is the most detrimental to stiffness and strength and, therefore, is a major concern because delamination is not visible on the surface. Chang and co-workers [41-43] have studied the damage behavior of composite laminates under low velocity impact loading, concluding that in-ply matrix cracking precedes delamination growth and shear and bending crack initiation. The

damage behavior of composite laminates is significantly influenced by matrix material, composite layup and geometric aspects such as size, thickness and loading area [44-46]. Minnaar and Zhou [47] used a novel interferometric experimental setup to show that interlaminar crack speeds are significantly higher under shear loading, and that crack speeds are strongly influenced by loading rate in mode II. However, only limited study has been reported on the dynamic response of composites to water-based impulsive loads. Analyses have primarily focused on sandwich structures because such structures offer considerably high shear and bending stiffness to weight ratios than homogeneous plates of equivalent mass. Experiments and computations focusing on different core topologies and specimen sizes have been carried out by Espinosa and co-workers [1, 93, 104] and McShane et al. [105] using underwater pressure impulses generated by gas gun impact and by Dharmasena et al. [64] using planar pressure impulses generated by explosive sheets. Battley and co-workers developed a high-speed servo-hydraulic testing system and concluded that slamming impacts on a deformable sandwich panels result in different peak and residual pressures to those from a rigid panels [106, 107]. Shukla and co-workers [79-83] examined the dynamic response of sandwich structures consisting of woven E-glass composite facesheets and stitched core to air-based shock loading and concluded that stitched cores exhibit superior mechanical performance. A combined experimental and computational analysis of the response to underwater blast by Avachat and Zhou [108] has revealed that sandwich structures significantly outperform monolithic structures at all impulsive levels and environmental conditions including air-backed and water-backed structures. Additionally, a balance of core stiffness and softness provides

optimal blast resistance by allowing load spreading and energy dissipation while mitigating the effects of localized core compressive failure and rupture.

Although polymer matrix composites are finding increasing applications in marine applications due to their high strength-to-weight ratios and fatigue and corrosion resistance, these materials may have lower impact resistance and higher cost of manufacturing in comparison to metallic structures. In recent years, hybrid material systems combining composites and metals have been developed in order to symbiotically provide superior stiffness, strength and impact resistance in comparison to either monolithic composite or metallic structures. Fiber-Metal Laminate (FML) concepts such as GLARE (Glass Laminate Aluminum Reinforced Epoxy), CARALL (Carbon fibre Reinforced Aluminum Laminate) and ARALL (Aramid fiber Reinforced Aluminum Laminate) are finding applications in aircraft due to their superior blast and impact resistance [109]. Seyed Yaghoubi and Liaw [110-112] performed an experimental and computational analysis of the ballistic response of GLARE FMLs and showed that cross-ply composites dissipate more energy than unidirectional composites. Fatt et al. [113] showed that energy dissipation was primarily governed by out-of-plane bending in ballistic impact of clamped GLARE panels. High-velocity impact experiments performed by Abdullah and Cantwell [114] demonstrated that energy dissipation is highly dependent on stretching during flexure in metallic layers which perform independently of composite layers. Fan et al. [115] performed low-velocity impact testing of GLARE FMLs which show enhancement in penetration resistance with increasing composite layer thickness. Langdon et al. [116, 117] analyzed the response of FMLs to blast loading, revealing a number of failure modes in the form of perforation of aluminum and composite layers,

debonding between aluminum layers and shear failure in composite plates. Finite element simulations on impulsively loaded FMLs highlight the need for accurate modelling of the blast loading and accounting for constitutive behavior of each constituent of the hybrid structures [118-121].

Despite recent interest in the mechanical response of hybrid metal-composite structures, especially their behavior under blast loading, there are a number of unresolved issues. Specifically, only limited studies have been reported on the behavior of both monolithic and hybrid plates subjected to water-based impulsive loading [92, 93, 105]. Since there are significant differences in air-blasts and water-blasts, understanding the response of hybrid structures under water-based impulsive loading is of critical importance in the design of marine structures. Independently assessing the performance of composite and metallic plates subjected to high-intensity underwater impulsive loads is essential for accurately delineating the response of each component. Additionally, the role of stacking sequence and the relative positioning of composite and metallic layers in the hybrid structure has not been analyzed. Finally, the deformation and failure of hybrid plates subjected to underwater impulsive loads are complicated due to fluid-structure interaction (FSI) effects, competing damage mechanisms, complex failure modes, interfacial effects and material heterogeneity and, therefore, require a physically-based multiphysics computational framework in order for each of the aspects to be accounted for.

## 2.5 Scaling and structural design approaches

Since the emergence of research involving blasts and impulsive loads, researchers have expressed the need for scaling methodologies that allow experimental results to be applicable to full-scale marine structures. Dimensionless analysis provides a method to enable scaling between geometrically similar plates of different sizes subjected to impulsive loading. One of the earliest studies on underwater blast response was carried out by G. I. Taylor [6, 11] who used dimensional analysis to develop quantitative relations between the explosive source, peak pressure, decay time and transmitted impulse. Based on purely dimensional considerations, Taylor derived scaling laws relating pressure at the blast front with distance from the explosion and elapsed time. Other dimensionless variables developed by Taylor include an FSI parameter $\psi = \rho_w c_w t_0 / m,$ the ratio of transmitted impulse to incident impulse $I_T / I_0,$ and out-of-plane deflection $\delta / r,$ where $\delta$ is displacement and $r$ is the radius of the plate. Johnson [122] and Jones [123] independently proposed dimensionless numbers in which the impact velocity and material properties were taken into consideration to assess the regime of the behavior of monolithic metal plates in projectile impact situations. The dimensional analysis approach has been extended to sandwich plates by Fleck and coworkers [66] and Hutchinson and coworkers [10] by introducing a number of parameters that take into account the material properties of the sandwich core such as core density, yield strength and extent of core compression. Steeves and Fleck [32, 124] developed failure mode maps based on a quasi-static three-point bending experiment and correlated localized failure in the core with applied load and core density. Overall, rather

limited research has been reported relating to the quantitative structural design of composite laminates and sandwich structures for quasi-static loads as well as blast or impact mitigation. For the specific case of underwater impulsive loading, there is a lack of systematic, parametric studies relating loading conditions to structural attributes and mechanical responses.

# 3. MATERIALS, MANUFACTURING AND COMPUTATIONAL MODELING

## 3.1 Introduction

Manufacturing of composite structures is at the heart of structural design of marine composites. For all the experiments reported here, the test specimens were manufactured in-house. The materials used for constructing test specimens include glass-fiber reinforced epoxy, carbon-fiber reinforced epoxy, structural polymeric foams, 1100 aluminum and epoxy resin for joining. This chapter deals with the different materials, manufacturing techniques and computational approaches implemented in this research.

## 3.2 Composite materials

Fiber-matrix composites are composed of two distinct phases: (1) reinforcements like glass-fibers or carbon-fibers and (2) matrix materials like epoxy, polyester, etc. These materials can be molded into complex shapes due to their flexibility. The strength and stiffness of the finished composite is determined by the volume fraction and directionality of fibers with respect to external loads. The matrix is primarily used as a medium to hold fibers and can be varied depending on the final application of the material. The method of fabrication depends on the curing temperature, curing time and volatilization of the resin. For high-corrosion resistance and a smooth water-proof finish, epoxy is recommended. Two types of composite materials are used in this analysis: glass-fiber reinforced epoxy and carbon-fiber reinforced epoxy.

### 3.2.1 Glass-fiber reinforced epoxy

The glass-fiber reinforced prepregs have the designation "XF0920/346-AA-675 E-Glass 300 GSM 36% RW 24-inch Wide". **XF0920** is the resin designation, **346-AA-675** is the identification number of Owens Corning 346 Type 30 roving, **300 GSM** denotes the 300 grams per square meter areal mass of the aforementioned glass fiber, **675** denotes the length of the roving in yards per pound, and **36% RW** stands for resin weight in each lamina.

### 3.2.2 Carbon-fiber reinforced epoxy

The carbon-fiber reinforced prepregs have the designation "VTM 264/792/HTR40-300gsm 36% RW 24-inch Wide". **VTM 264** is a variable temperature, vacuum processable epoxy resin developed by Cytec, **HTR40** is the identification number of Toho Tenax continuous fiber reinforcement, **300 GSM** denotes 300 grams per square meter areal mass of the aforementioned fiber reinforcement, and **36% RW** stands for resin weight in each lamina.

The composite laminates are manufactured by curing the prepregs under pressure in a high temperature oven 100 °C. The thickness of each cured lamina is calculated using

$$\text{Cured Ply Thickness} = \frac{\text{Fiber Areal Weight}}{\text{Fiber density} \times \text{Fiber Volume} \times 10}, \tag{7}$$

and is ~0.23 mm per layer.

### 3.2.3 Computational modeling of composite laminates

The laminates are assumed to perfectly elastic prior to onset of damage. Damage is said to occur when there is a degradation in material stiffness due to various deformation mechanisms. Based on the energy required for initiation, matrix damage occurs first, followed by combined fiber-matrix damage, termed "fiber-pullout" and finally fiber fracture. Damage occurring in the facesheets is accounted for by energy-based damage evolution [125] and [126].

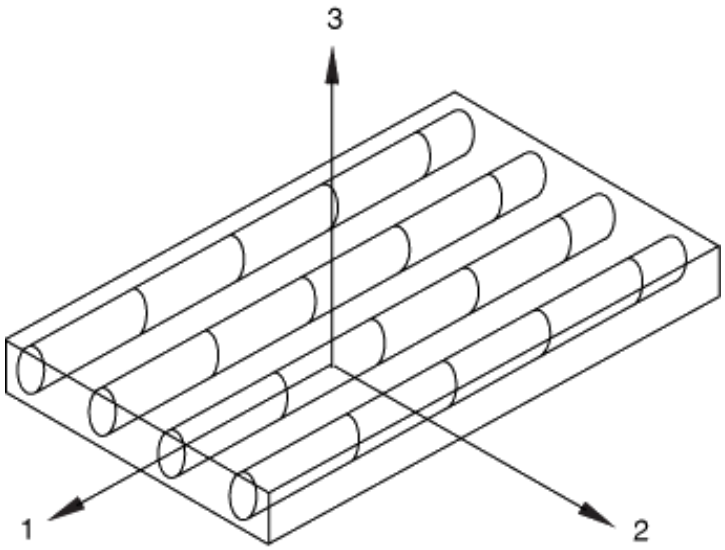


Figure 8 A transversely isotropic solid with fibers oriented in longitudinal direction (11).

Both these models assume a transversely isotropic solid shown in Figure 8, such that

$$\frac{E_{11}}{E_{22}} >> 1, \quad \frac{T_{11}}{T_{22}} >> 1, \quad \frac{C_{11}}{C_{22}} >> 1, \tag{8}$$

where $E, T$ and $C$ are tensile-modulus, tensile-strength and compressive-strength and the subscript "11" denotes longitudinal direction while the subscript "22" denotes

transverse direction. The in-plane/longitudinal shear strengths are $S_{12} = S_{31}$ while the out-of-plane/transverse shear strength is $S_{23}$. The elastic response of transversely isotropic material is given by

$$\begin{pmatrix} \varepsilon_{11} \\ \varepsilon_{22} \\ \gamma_{12} \end{pmatrix} = \begin{pmatrix} \frac{1}{E_{11}} & \frac{\nu_{21}}{E_{11}} & 0 \\ -\frac{\nu_{12}}{E_{22}} & \frac{1}{E_{22}} & 0 \\ 0 & 0 & \frac{1}{S_{12}} \end{pmatrix} \begin{pmatrix} \sigma_{11} \\ \sigma_{22} \\ \tau_{12} \end{pmatrix}, \tag{9}$$

where $\varepsilon_{11}$ and $\varepsilon_{22}$ are the strains and $E_{11}$ and $E_{22}$ are the moduli in directions 1 and 2 respectively. $\gamma_{12}$ is the shear strain and $S_{12}$ is the shear modulus, $\nu_{12}$ and $\nu_{21}$ are Poisson's ratios. The composite material is considered to be linear-elastic prior to damage initiation.

The following damage initiation mechanisms are considered for a transversely isotropic laminate:

matrix tension, $F_m^T$, given by

$$F_m^T = \left( \frac{\sigma_{11}}{T_{11}} \right)^2 + \left( \frac{\tau_{12}}{S_{12}} \right)^2; \tag{10}$$

matrix compression $F_m^C$,

$$F_m^C = \left( \frac{\sigma_{22}}{2S_{23}} \right)^2 + \left( \frac{\tau_{12}}{S_{12}} \right)^2 + \left[ \left( \frac{C_{22}}{2S_{23}} \right)^2 - 1 \right] \frac{\sigma_{22}}{C_{22}}; \tag{11}$$

fiber tension $F_f^T$,

$$F_f^T = \left( \frac{\sigma_{11}}{T_{11}} \right)^2 + \left( \frac{\tau_{12}}{S_{12}} \right)^2 ; \tag{12}$$

and fiber compression $F_f^C$ ,

$$F_f^C = \left( \frac{\sigma_{11}}{C_{11}} \right), \tag{13}$$

where $\sigma_{11}, \sigma_{22}$ and $\tau_{12}$ are components of effective stress tensor $\sigma$ and are used to evaluate damage initiation. The parameters used in these calculations can be found in [55] and [127]. In finite element simulations, a material-point has an initial, undamaged value of 1 and as the material-point experiences damage, this value decreases. The lowest value, before the material-point is removed from the simulation, is 0. The material properties of glass-fiber reinforced epoxy and carbon-fiber reinforced epoxy are provided in Table 1 and Table 2 [128, 129] respectively.

Table 1 Material properties for unidirectional glass-fiber/epoxy laminates.

| **Parameter** | **Symbol** | **Unit** | **Value** |
|---|---|---|---|
| Density | $\rho$ | $kg \cdot m^{-3}$ | 1850 |
| Tensile modulus | $E_{11}$ | MPa | 39000 |
| Transverse modulus | $E_{22}$ | MPa | 9000 |
| Shear modulus | $G_{12}, G_{13}$ | MPa | 3500 |
| Longitudinal tensile strength | $T_{11}$ | MPa | 1200 |
| Longitudinal Compressive Strength | $C_{11}$ | MPa | 900 |
| Transverse tensile strength | $T_{22}$ | MPa | 45 |
| Transverse compressive strength | $C_{22}$ | MPa | 128 |
| Longitudinal shear strength | $S_{12}, S_{21}$ | MPa | 51 |
| Transverse shear strength | $S_{23}$ | MPa | 51 |

Table 2 Material properties for unidirectional carbon-fiber/epoxy laminates.

| **Parameter** | **Symbol** | **Unit** | **Value** |
|---|---|---|---|
| Density | $\rho$ | $kg \cdot m^{-3}$ | 1580 |
| Longitudinal tensile modulus | $E_{11}$ | MPa | 138000 |
| Transverse tensile modulus | $E_{22}$ | MPa | 10000 |
| Shear modulus | $G_{12}, G_{13}$ | MPa | 5240 |
| Longitudinal tensile strength | $T_{11}$ | MPa | 2280 |
| Longitudinal compressive strength | $C_{11}$ | MPa | 1440 |
| Transverse tensile strength | $T_{22}$ | MPa | 57 |
| Transverse compressive strength | $C_{22}$ | MPa | 228 |
| Longitudinal shear strength | $S_{12}, S_{21}$ | MPa | 71 |
| Transverse Shear strength | $S_{23}$ | MPa | 71 |

Table 3 Material properties for epoxy [130].

| **Parameter** | **Symbol** | **Unit** | **Value** |
|---|---|---|---|
| Normal stiffness | $K_n$ | MPa | 2000 |
| Shear stiffness | $K_s, K_t$ | MPa | 2000 |
| Critical normal traction | $t_{\mathrm{n}}^0$ | MPa | 50 |
| Critical shear traction | $t_{\mathrm{s}}^0, t_{\mathrm{t}}^0$ | MPa | 50 |
| Critical normal fracture energy | $G_n^C$ | N/mm | 4.0 |
| Critical shear fracture energy | $G_s^C, G_t^C$ | N/mm | 4.0 |

### 3.2.4 Cohesive finite element framework to track delamination

In the finite element simulations, each unidirectional lamina is simulated explicitly to accurately represent the behavior of the entire carbon-fiber/epoxy laminate and capture damage and deformation. The epoxy layers between two laminas, also called "resin rich layers", are modeled using cohesive elements to capture interfacial fracture and delamination. Due to the inherently heterogeneous nature of fiber-reinforced composites, interfacial separation plays a very important role in deformation. Interfacial separation of directionally stacked layers in the composite is called delamination. Delamination requires very little energy and is the dominant damage mode in composite materials subjected to impact or impulsive loads. It occurs primarily due to matrix failure and reinforcing fibers are relatively intact. Similarly, core-facesheet separation is an important damage mode that occurs due to interfacial separation and fracture. If the bond between facesheet and core is weak, interfacial separation occurs. If the bond between the facesheet and the core is strong, tensile fracture in the foam leads to separation. Some commonly used metrics to evaluate the damage resistance of composites to impact loads are impact energy, displacement, delamination-area and extent of rupture.

The cohesive finite element method (CFEM) has been extensively used to study a wide variety of issues related to delamination and fracture such as tensile decohesion (Needleman [131]), quasi-static crack growth (Tvergaard and Hutchinson[132]), ductile fracture (Tvergaard and Needleman [133, 134]), dynamic fracture (Xu and Needleman [135]), dynamic fragmentation (Camacho and Ortiz [136], Espinosa et al. [137]), delamination in composites (Camanho et al. [138], Minnaar and Zhou [139]) and microstructural fracture (Zhai and Zhou [140]). Here, cohesive elements are specified at

the interfaces between individual laminas in the composite structure as well as the interfaces between the aluminum and composite sections in the hybrid plates. The cohesive elements allow damage initiation and development in the interlaminar regions to be captured.

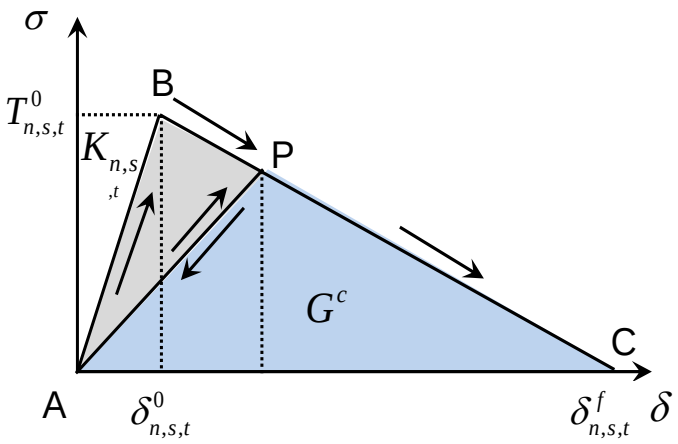


Figure 9 Bi-linear law for cohesive traction-separation behavior.

A bilinear traction-separation law shown in Figure 9 is adopted to describe the behavior of the cohesive elements [138]. The linear-elastic part of the traction-separation law relates the traction vector **t** to the element stiffness **K** and the separation **u** resulting from the traction vector **t**. This relationship is given by

$$\mathbf{t} = \mathbf{K}\mathbf{u}. \tag{14}$$

The above equation can be expressed in matrix form to indicate coupling between the normal and shear components of the traction-separation relationship, i.e.,

$$\begin{pmatrix} t_n \\ t_s \\ t_t \end{pmatrix} = \begin{bmatrix} K_{nn} & K_{ns} & K_{nt} \\ K_{ns} & K_{ss} & K_{st} \\ K_{nt} & K_{st} & K_{tt} \end{bmatrix} \begin{pmatrix} u_n \\ u_s \\ u_t \end{pmatrix}. \tag{15}$$

Full coupling between normal and shear components in the traction-separation response is represented by the off-diagonal terms. For the purposes of this work, an uncoupled relation is chosen, i.e.,

$$\begin{pmatrix} t_n \\ t_s \\ t_t \end{pmatrix} = \begin{bmatrix} K_{nn} & 0 & 0 \\ 0 & K_{ss} & 0 \\ 0 & 0 & K_{tt} \end{bmatrix} \begin{pmatrix} u_n \\ u_s \\ u_t \end{pmatrix}. \tag{16}$$

Although the linear-elastic part of the response has no coupling between shear and normal components, damage initiation and evolution have a mixed-mode form. Damage initiation follows the quadratic interaction relationship shown in Equation (17), where $t_{\mathrm{n}}$ is the normal stress in a cohesive element, $t_{\mathrm{s}}$ is the shear stress, and $t_{\mathrm{n}}^0$ and $t_{\mathrm{s}}^0$ are the critical values of $t_n$ and $t_s$, respectively, which represent the respective cohesive strengths. In this paper, $t_{\mathrm{s}}^0$ and $t_{\mathrm{t}}^0$ are assumed to have the same value. Because it is not physically meaningful for compressive tractions to contribute to damage initiation, only non-negative (tensile) normal tractions are considered in the damage initiation rule. This is indicated by the presence of the Macaulay brackets around $t_n$. Specifically, damage is initiated when

$$\left( \frac{\langle t_n \rangle}{t_n^0} \right)^2 + \left( \frac{t_s}{t_s^0} \right)^2 + \left( \frac{t_t}{t_t^0} \right)^2 = 1. \tag{17}$$

A schematic representation of the bilinear traction-separation law is shown in Figure 10. Loading initially proceeds from point A to B, at which point softening occurs with increasing separation until failure. Once damage is initiated in a cohesive element, the interface follows the mixed-mode fracture criterion of Benzeggagh and Kenane given

in Equation (18) [141]. In this relationship, $G_n, G_s$ and $G_t$ are the work performed by tractions $t_n, t_s$ and $t_t$ respectively. $G_n^C, G_s^C$ and $G_t^C$ are the critical fracture energies in the normal and shear directions, respectively. These quantities are used to determine the degree of damage in a cohesive surface pair. For convenience, the critical fracture energies in the two shear directions are treated as equal (i.e., $G_s^C = G_t^C$). The criterion is written as

$$G_n^C + \left(G_s^C - G_n^C\right)\left(\frac{G_s + G_t}{G_n + G_s + G_t}\right) = G^C . \tag{18}$$

The parameters for all cohesive relations used are obtained from the work performed by Lapczyk and Hurtado [130] and are presented in Table 3. The traction-separation stiffness for cohesive elements along interfaces between the laminas is $10^3$ times the stiffness of the corresponding bulk elements. This choice has two benefits. First, artificial softening of the model is avoided. Second, the work of separation associated with the linear-elastic portion of the cohesive behavior is minimized, ensuring that the bulk of the work is in the fracture energy, providing adequate softening in the cohesive response. Although the method of constituent preparation can have a significant influence on the resulting composite fracture toughness [142], only a single set of interface properties are considered in this paper.

After failure of cohesive elements, contact between element faces is considered in the model using the a contact algorithm similar to that developed by Camacho and Ortiz [136]. The algorithm identifies free surfaces and fractured surfaces as potential contact surfaces in each time step of the simulation. Nodal coordinates at the end of every time

step are used to define master and slave surfaces for the next time step. Nodal displacements are then calculated at the beginning of every time step. The corresponding nodal coordinates are used to check whether nodes of one internally defined surface have penetrated another internally defined surface. If penetration is predicted, then penalty forces of sufficient magnitude are applied to the surfaces in the direction of their normal such that there is contact between them but no interpenetration.

## 3.3 Structural polymeric foams

### 3.3.1 Divinycell HP Poly-Vinyl Chloride foams

The materials analyzed are structural Poly-Vinyl Chloride (PVC) foams manufactured by DIAB Inc. [143] under the trade name Divinycell HP. These foams are used because their high residual strengths and dimensional stability make them ideal for vacuum bagging and vacuum assisted resin-transfer molding (VARTM). The high strength-to-weight ratio of sandwich structures manufactured using these foams lead to higher vehicle speeds, greater payload capacities, and reduced power demand, all of which result in better operating economy. Additionally, these structural foams possess high chemical resistance, low water absorbency and good thermal insulation and make ideal core materials in sandwich constructions for marine applications. Here, PVC foams with densities of 60, 100, 130, 200 and 250 $kg \cdot m^{-3}$ are studied. The height of the specimen ($T_c$) is 50 mm and the diameter ($D$) is 75 mm. The total thickness of the specimen is $T = T_c + T_f + T_b$ where $T_c$, $T_f$ and $T_b$ are the core, frontface and backface thicknesses, respectively. The compressive stress-strain responses for the core materials,

as obtained by George et al. [144], are shown in Figure 10. Material parameters for the PVC foams are provided by the manufacturer and listed in Table 4. The stress-strain relations are linear initially and subsequently show yielding and stress saturation before core densification which leads to a rise in stress. This unique characteristic of the compressive deformation makes the foams especially useful for applications requiring compression and energy absorbency. To compare the effects of different core densities, a normalized density in the form of

$$\bar{\rho} = \frac{\rho_{core}}{\rho_{face}} \tag{19}$$

is used, where $\rho_{core}$ is the density of the foam and $\rho_{face}$ is the density of the facesheet material (aluminum). Foam cores of five different densities are subjected to impulsive loads of four different impulse magnitudes, yielding 20 experimental cases. Finite element simulations are carried out in conjunction with the experiments to ensure that the range of constitutive behaviors captures the essential deformation modes of interest for foam cores expected of sandwich applications. The PVC foams and composite laminates were joined using epoxy adhesives by curing at 100°F under 60 psi pressure in an autoclave.

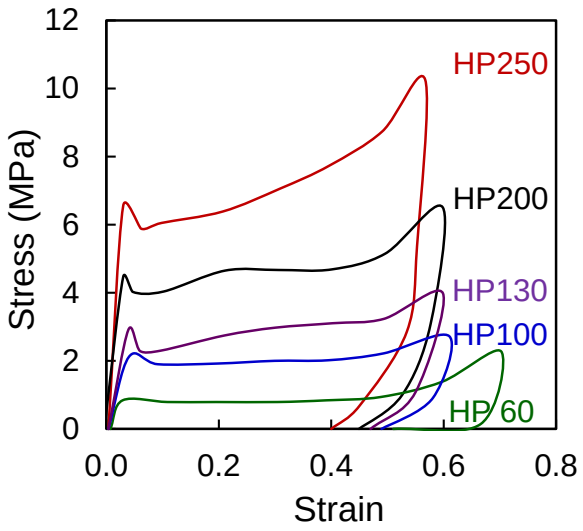


Figure 10 Stress-strain curves for the DIAB Divinycell HP foam cores studied [144].

Table 4 Properties of DIAB Divinycell HP core materials.

| **Parameter** | **Unit** | **HP60** | **HP100** | **HP130** | **HP200** | **HP250** |
|---|---|---|---|---|---|---|
| Density | $kg \cdot m^{-3}$ | 65 | 100 | 130 | 200 | 250 |
| Tensile Modulus | MPa | 20 | 100 | 175 | 250 | 320 |
| Tensile Strength | MPa | 1.8 | 3.5 | 4.8 | 7.1 | 9.2 |
| Compressive Modulus | MPa | 74 | 135 | 145 | 310 | 400 |
| Compressive Strength | MPa | 0.95 | 2.0 | 3.0 | 5.4 | 7.2 |
| Shear Modulus | MPa | 20 | 33 | 50 | 73 | 97 |
| Shear Strength | MPa | 0.85 | 1.6 | 1.9 | 3.2 | 3.9 |

### 3.3.2 Sandwich structure manufacturing

The composite laminate facesheets are manufactured using the technique explained in *3.2 Composite materials*. The composite facesheets and cellular core are bonded using 3M adhesives and the system is cured under pressure at 100 °C. The adhesives used are AF-163 and AF3109.

### 3.3.3 Constitutive and damage models for PVC foams

The high strain rate behavior of cellular foams has been investigated using Split Hopkinson Pressure Bar apparatuses [53, 54, 145-147]. The experiments show that PVC foams exhibit mild strain-rate sensitivity in the rate range of $\dot{\varepsilon} = 10^{-2}$ to $10^{3}\ \mathrm{s}^{-1}$ and negligible strain rate sensitivity in the rate range of $\dot{\varepsilon} = 10^{-4}$ to $10^{-2}\ \mathrm{s}^{-1}$. The primary mechanism for energy absorption in foam cores is local wall collapse and stress-saturated volumetric compression. Compressive stress-strain responses for these cores are shown in Figure 10 and are obtained from the work of George et al. [144]. Constitutive models for foams often rely on homogenized continuum descriptions of the cellular materials [77, 148]. The PVC foam core used in the experiments is DIAB Divinycell HP [143] with densities of 60, 100, 130, 200 and 250 $\mathrm{kg \cdot m^{-3}}$. The Deshpande and Fleck crushable foam plasticity model [149] is used to describe the constitutive behavior of the PVC foams. In this model, the yield surface for volumetric hardening is defined as

$$F = \sqrt{q^2 + \alpha^2 \left( p - p_0 \right)^2} - B = 0, \tag{20}$$

where $p$ is the pressure, $q$ is the von Mises stress, $\alpha = B/A$ is the shape factor of the yield ellipse that defines the relative magnitude of the axes. $B$ is the size of the $q-$axis

of the yield ellipse and $A$ is the size of the $p-$axis of the yield ellipse. The shape factor is specified by

$$\alpha = \frac{3k}{\sqrt{(3k_t + k)(3-k)}}, \text{ where } k = \frac{\sigma_c^0}{p_c^0} \text{ and } k_t = \frac{p_t}{p_c^0} \ , \tag{21}$$

where $\sigma_c^0$ is the initial yield stress in uniaxial compression, $p_c^0$ is the initial yield stress in hydrostatic compression and $p_t$ is the yield strength in hydrostatic tension. Material parameters for the PVC foams are provided by the manufacturer and listed in Table 4. Experiments performed show that fracture and fragmentation are significant damage mechanisms in composite sandwich structures subjected to underwater impulsive loads. A phenomenological damage criterion proposed by Hooputra et al. [150] is implemented to predict the onset of rupture due to strain localization and to capture the subsequent fragmentation of the core material. The damage model assumes that the equivalent plastic strain at the onset of damage ($\bar{\varepsilon}_D^{pl}$) is a function of stress triaxiality and equivalent plastic strain rate, i.e.

$$\bar{\varepsilon}_D^{pl} = \bar{\varepsilon}_D^{pl}\left(\eta, \dot{\bar{\varepsilon}}^{pl}\right), \tag{22}$$

where $\eta = -p/q$ is the stress triaxiality, $-p$ is the hydrostatic stress, $q$ is the von Mises equivalent stress and $\dot{\bar{\varepsilon}}^{pl}$ is the equivalent plastic strain rate. The criterion for damage initiation is met when

$$\omega_D = \int \frac{d\bar{\varepsilon}^{pl}}{\bar{\varepsilon}_D^{pl}\left(\gamma, \dot{\bar{\varepsilon}}^{pl}\right)} = 1, \tag{23}$$

where $\omega_D$ is a state variable that increases monotonically with plastic deformation. At each increment during the analysis, the incremental increase in $\omega_D$ is computed as

$$\Delta\omega_D = \frac{\Delta\bar{\varepsilon}^{pl}}{\bar{\varepsilon}_D^{pl}\left(\eta, \dot{\bar{\varepsilon}}^{pl}\right)} \geq 0. \tag{24}$$

The evolution of damage is based on fracture energy per unit area dissipated during the damage process. The data for fracture toughness is obtained from experiments carried out by Poapongsakorn and Carlsson [151].

## 3.4 Structural aluminum alloy

### 3.4.1 Constitutive and damage models for aluminum

The metal plates studied here are made of 1100 aluminum alloy. It is highly resistant to seawater and industrial chemicals and has a relatively high yield strength, high strain hardening and high ductility. The Johnson-Cook model [152] which accounts for strain-hardening, thermal softening, and strain rate dependence is used to describe the material's response. Specifically,

$$\bar{\sigma}\left(\bar{\varepsilon}^{pl}, \dot{\varepsilon}^{pl}, \theta\right) = \left[A + B\left(\bar{\varepsilon}^{pl}\right)^n\right]\left[1 + C\ln\left(\frac{\dot{\varepsilon}^{pl}}{\dot{\varepsilon}_0}\right)\right]\left[1 - \left(\hat{\theta}\right)^m\right], \tag{25}$$

where $\bar{\sigma}$ is the Mises equivalent stress, $\bar{\varepsilon}^{pl}$ is the equivalent plastic strain, $\dot{\varepsilon}^{pl}$ is the equivalent plastic strain rate, and $A, B, C, m$ and $n$ are material parameters measured at or below the transition temperature, $\theta_{transition}$ , $\dot{\varepsilon}_0$ is a reference strain rate, and $\hat{\theta}$ is the non-dimensional temperature defined as

$$\hat{\theta} \equiv \begin{cases} 0, & \text{for} \quad \theta < \theta_{transition}; \\ \left(\theta - \theta_{transition}\right)/\left(\theta_{melt} - \theta_{transition}\right), & \text{for} \quad \theta_{transition} \le \theta \le \theta_{melt}; \text{ and} \\ 1, & \text{for} \quad \theta > \theta_{melt}. \end{cases} \tag{26}$$

In the above expressions, $\theta$ is the current temperature, $\theta_{melt}$ is the melting temperature and $\theta_{transition}$ is the transition temperature below which the yield stress is independent of the temperature. When the temperature exceeds the melting temperature, the material behaves like a fluid and has no shear resistance. The use of the Johnson–Cook constitutive model partly reflects the nature of the deformations analyzed and partly reflects the fact that extensive experimental data is available and has been used to calibrate this model for the conditions analyzed. Indeed, there are more "sophisticated" models than the Johnson–Cook model. These models use different parameters or internal stare variables to deal with issues such as complicated loading paths, varying stress triaxiality, and deformation mechanisms. However, the key aspects of the loading conditions analyzed in this paper are dynamic, rate-dependent, monotonic (no unloading considered), and approximately proportional. Under such conditions, the constitutive response of the steels considered here can be well-characterized as dependent on strain, strain rate and temperature. Models using relations between stress and these quantities are effectively similar or equivalent, as long as enough parameters exist to allow a good fit to experimental data. Another way to look at it is that, for the conditions stated above, many more sophisticated models using, say, certain internal state variables (ISVs) essentially simplify to relations involving stress, strain, strain rate and temperature as independent variables.

The failure model is based on the value of equivalent plastic strain. The damage parameter, $\omega$, is defined as

$$\omega = \sum \left( \frac{\Delta \bar{\varepsilon}^{pl}}{\bar{\varepsilon}_f^{pl}} \right), \tag{27}$$

where $\Delta \bar{\varepsilon}^{pl}$ is an increment of the equivalent plastic strain, $\bar{\varepsilon}_f^{pl}$ is the strain at failure, and the summation is performed over all increments up to the hitherto state in the analysis. The strain at failure is assumed to be dependent strain rate and temperature such that

$$\bar{\varepsilon}_f^{pl} = \left[ D_1 + D_2 \exp\left( -D_3 \frac{p}{\bar{\sigma}} \right) \right] \left[ 1 + D_4 \ln\left( \frac{\dot{\bar{\varepsilon}}^{pl}}{\dot{\varepsilon}_0} \right) \right] \left[ 1 + D_5 \hat{\theta} \right], \tag{28}$$

where $D_1$, $D_2$, $D_3$, $D_4$, and $D_5$ are experimentally determined damage parameters, $p = -\sigma_{ii}/3$ is the hydrostatic pressure. The values the parameters are obtained from Johnson and Cook [152], Raftenberg [37] and Corbett [153], and are shown in Table 5.

Table 5 Parameters for the Johnson-Cook model for aluminum [152, 153].

| **Parameter** | **Symbol** | **Unit** | **Value** |
|---|---|---|---|
| Density | $\rho$ | $kg \cdot m^{-3}$ | 2700 |
| Young's modulus | $E$ | GPa | 70 |
| Poisson's ratio | $\upsilon$ | - | 0.33 |
| Johnson-Cook constant | $A$ | MPa | 324 |
| Johnson-Cook constant | $B$ | MPa | 113 |
| Johnson-Cook constant | $C$ | - | 0.002 |
| Johnson-Cook constant | $m$ | - | 1.34 |
| Johnson-Cook constant | $n$ | - | 0.42 |
| Melting temperature | $\theta_{melt}$ | $^{o}C$ | 1200 |
| Reference temperature | $\theta$ | $^{o}C$ | 25 |
| Johnson-Cook constant | $D_1$ | - | -0.77 |
| Johnson-Cook constant | $D_2$ | - | 1.45 |
| Johnson-Cook constant | $D_3$ | - | 0.47 |
| Johnson-Cook constant | $D_4$ | - | 0.00 |
| Johnson-Cook constant | $D_5$ | - | 1.60 |

## 3.5 Modeling of fluid-structure interaction

The model consists of a Lagrangian domain for the solids and an Eulerian domain for the water. In the Lagrangian domain, nodes are fixed within the material and nodal displacements track the material deformation. Since each Lagrangian element is always 100% within a single material, the material boundary coincides with element boundaries. In contrast, Eulerian the domain consists of nodes that are fixed in space and the material flows through the elements that do not experience deformation. Eulerian elements may also be partially or completely void, allowing material to flow into empty space, capturing cavitation, a crucial aspect of fluid flow. Materials tracked by Eulerian elements can interact with Lagrangian elements through Eulerian-Lagrangian contact algorithms to allow fully coupled multi-physics simulations like fluid-structure interactions. This Coupled Eulerian-Lagrangian (CEL) framework allows the severe deformation in water and the FSI to be captured. In addition to simulating the blast wave propagation in the USLS, the Eulerian formulation also captures the exponentially decaying pressure waves and resulting cavitation at the fluid-structure interface. The interaction between the water and structure is effected by tying the nodes in the water to the corresponding nodes of the structure, thereby ensuring continuity of displacements when contact occurs. Figure 11 shows the Coupled Eulerian Lagrangian (CEL) computational framework with different components and the respective computational constitutive models in each case.

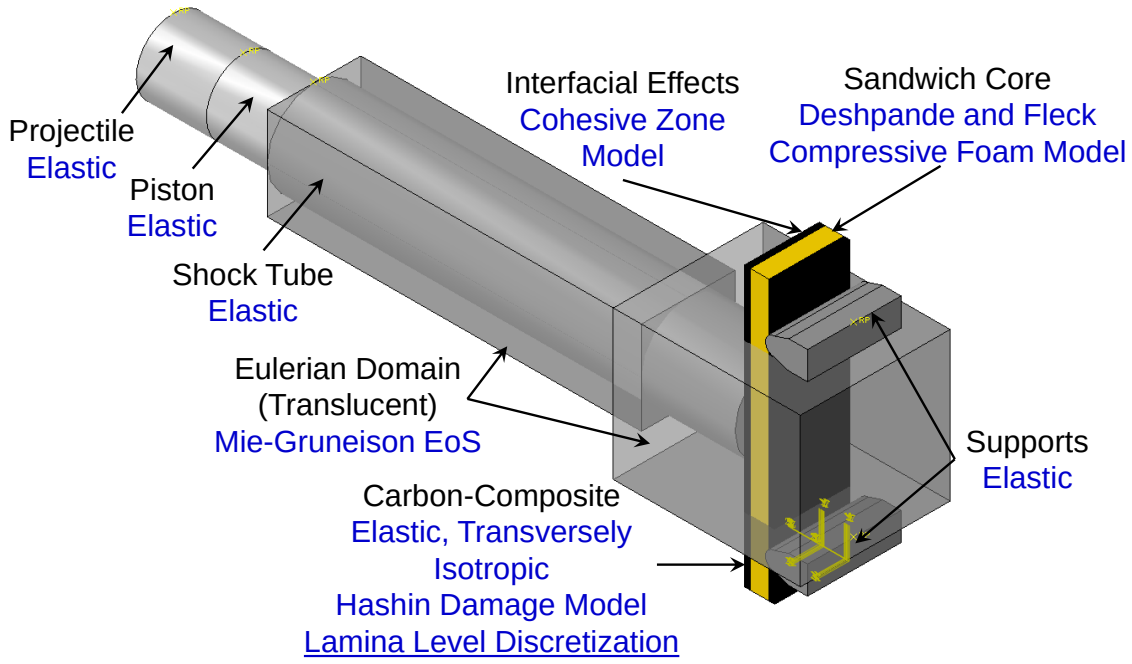


Figure 11 Coupled Eulerian Lagrangian multiphysics computational model.

The response of water in the Eulerian domain is described by the Mie-Grüneisen equation of state

$$p = \frac{\rho_0 c_0^{\,2}\eta}{(1-s\,\eta)^2}\left(1-\frac{\Gamma_0\eta}{2}\right)+\Gamma_0\rho_0 E_m\,, \tag{29}$$

where $p$ is pressure, $c_0$ is the speed of sound, $\rho_0$ is initial density, $E_m$ is internal energy per unit mass, $\Gamma_0$ is Grüneisen's Gamma at a reference state, $s = dU_s/dU_p$ is the Hugoniot slope coefficient, $U_s$ is the shock wave velocity, and $U_p$ is particle velocity which is related to $U_s$ through a linear Hugoniot relation

$$U_S = c_0 + sU_p. \tag{30}$$

The parameters for the Mie-Grüneisen equation of state are listed in Table 6. The space enclosed by the shock-tube is prescribed the properties of water while the space that is outside the shock-tube is kept as a "void", allowing water to flow into it as a result of high-pressure wave impinging on the target. This has the effect of instantaneously relieving the pressure in the water-chamber in a manner consistent with experimental observations. In the case of specimen rupture, the CL framework allows water to flow out of the breached portion.

Table 6 Parameters for the Mie-Gruneisen equation of state for water.

| **Parameter** | **Symbol** | **Unit** | **Value** |
|---|---|---|---|
| Density of water | $\rho$ | $kg/m^3$ | 1000 |
| Speed of sound in water | $c$ | m/s | 1482 |
| Gruneisen's Gamma | $\Gamma_0$ | - | 0.1 |

## 3.6 Mesh dependence in damage modeling

A coupled Eulerian-Lagrangian framework is used to capture the impulse generation and transfer in the USLS. The experimentally measured and calculated pressure pulses show good agreement in terms of peak pressures and decay times. The calculated profiles show slightly faster wave attenuation than the measured profiles. The coupled Eulerian-Lagrangian framework and the Mie-Gruneisen equation of state allow most essential features of the loading pulses in the experiments to be captured.

In the current computational approach, the mesh size selection must ensure satisfactory strain resolution, realistic energy dissipation and must qualitatively reflect the experimentally observed deformation modes. The computations should also reflect the

damage creation under varying incident impulsive load intensities for a combination of materials. As discussed in section 4, the rupture criteria for the Johnson-Cook damage model, Hashin damage model and cohesive traction-separation are all based on critical values of strain, displacement and separation respectively. Failure is predicted when the damage operator in the respective case reaches unity. Once this rupture criterion is satisfied, the properties of failed elements are modified so that only compressive stresses are supported and tensile and shear stresses are eliminated. However, the predictions of damage and structural response based on failure criteria are inherently mesh-size dependent as shown by Needleman and Tvergaard [134] and Gullerud et al. [154]. When the stress-strain diagram exhibits a negative slope, the strain-softening damage tends to localize in a zone that is governed by element size. Since the damage dissipation per unit volume is finite, the vanishing damage zone causes the structure to fail at zero energy dissipation. The mesh size and failure strain together dictate the amount of localized deformation prior to failure, energy dissipation through damage and overall structural response.

To counteract this spurious mesh dependence associated with material softening, a characteristic element length $L_E$ is introduced in ABAQUS. For 3-D elements, $L_E$ is the cube-root of element volume. Following damage initiation, an equivalent displacement $\delta$ is introduced such that $\delta = L_E \cdot \varepsilon$ and evolves according to $\dot{\bar{\delta}} = L_E \cdot \dot{\bar{\varepsilon}}$ until it reaches a critical value. Although the implementation of a characteristic length serves to counteract the effect of mesh density, mesh sensitivity is still a significant factor in cases where extreme strain localization is expected prior to failure. An alternative

solution to mitigate the effects of mesh sensitivity is a nonlocal approach which defines a characteristic length $L_M$ as a material property. In accordance with the non-local approach proposed by Pijaudier-Cabot and Bazant [155] and Comi [156], the local strain is replaced by a weighted average strain over a representative volume determined by $L_M$. Non-local modeling of a complicated, heterogeneous structure comprising of metals, composites and adhesives is beyond the scope of the current study. However, a mesh size determination study is carried out in this analysis to approximate a non-local approach and provide a sound basis of computational modeling of structural response.

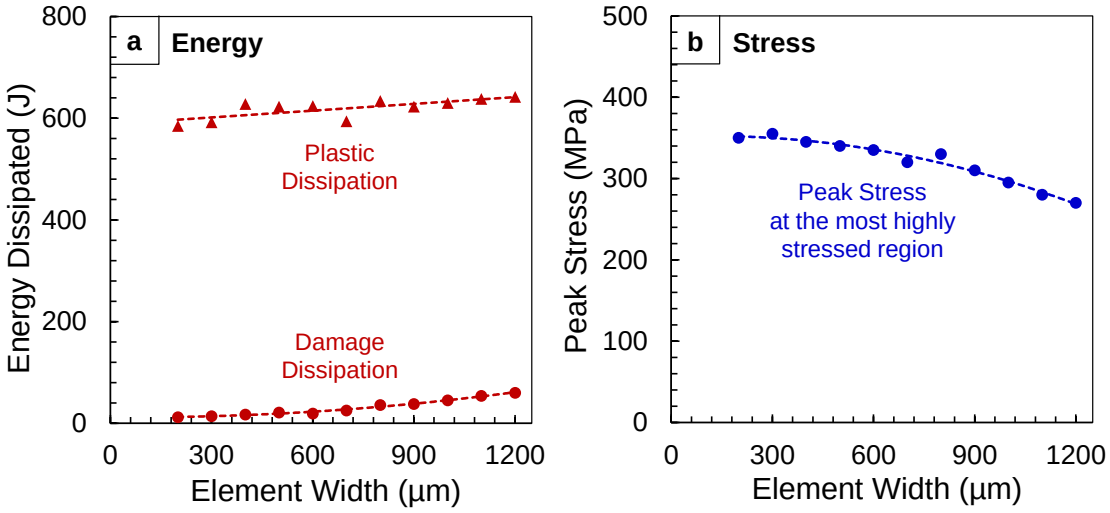


Figure 12 (a) Energy dissipated through inelastic deformation; and (b) peak stress at supports as a function of element size.

The mesh width, $w$, is varied over a range of $w =$ 100 μm to 1200 μm and the incident load is fixed at $\bar{I} = 0.20$ to evaluate mesh sensitivity. Figure 12(a) and (b) shows the energy dissipated through inelastic deformation and peak stress prior to failure as functions of mesh size respectively. When the numerical results are plotted, it is revealed that inelastic dissipation scales monotonically with $w$ and in the limit where $w \to 0$, the

energy dissipation vanishes. Thus, although mesh refinement is essential for adequate strain resolution, excessive mesh refinement has the adverse effect of yielding anomalously low energy dissipation. As shown in Figure 12(b), the numerical solution reaches convergence for a mesh width of $w = 500$ μm. Consequently, the mesh width selected for this calculation is $w = 500$ μm, which is sufficient for numerical convergence but still provides a reasonable approximation of energy dissipated in the process. The selection of a certain mesh size in conjunction with the implementation of a characteristic length equal to the cube root of the element volume provides an approximately non-local basis for damage initiation and evolution. The strain (and damage) calculated over each element in this approach resembles an average strain over a representative volume, converting the strain into a material parameter in a manner similar to that proposed by Pijaudier-Cabot and Bazant [155] and Comi [156]. Although the selection of this mesh size is rather arbitrary, it is further bolstered by the fact that the numerical model captures the damage modes observed in high-speed photographs of impulsively loaded clamped plates, as shown in the following section.

## 3.7 Concluding remarks

Overall, six different materials are used in this research: water, glass-fiber reinforced epoxy, carbon-fiber reinforced epoxy, structural PVC foams, 1100 aluminum and epoxy. Each of these materials is simulated independently in the multiphysics computational framework.

# 4. EXPERIMENTAL METHODS

## 4.1 Conceptualization of a blast simulator

Early experiments involving impulsive loading of structures consisted of impacting sandwich structures with metal foams and enclosed water-chamber setups both of which provided limited visual access. With considerable improvements in optics and lasers, there is a need for an experimental facility that can combine impulsive loading with state-of-the-art diagnostics. The major objectives of the USLS are as follows:

1. Develop an experimental facility to generate a range of controlled underwater impulsive loads by non-explosive means.
2. Develop diagnostics to measure temporal and spatial evolution and failure of composite structures under a variety of impulsive loading conditions.
3. To test marine structures with water on one-side (loading side) and water on both sides (loading-side as well as back-side).
4. To test marine structures with different boundary conditions mimicking the various sections in a ship structure.

## 4.2 Design and development

The USLS has been developed as part of a research effort to study the dynamic response of composite structures to underwater blast loading. Since it is intended to be used in a laboratory with state-of-the-art diagnostics, explosives are avoided. However, it is necessary to generate predictable and controlled high-intensity underwater impulsive

loads for testing marine structures. A gas-gun based impact loading is used to create underwater pressure impulses. A projectile is accelerated down the length of a gas-gun barrel. This projectile then impacts a flyer plate fitted in a sealed water- chamber. The stress-wave generated inside the flyer plate is transmitted through the flyer-water interface into the water-chamber. By varying the projectile velocity and mass, pressure waves of varying magnitudes can be generated in the water-chamber. The stress-wave in steel passes into the water with reduced amplitude. The pressure wave generated in the water-chamber travels down the length of the chamber (~700 mm) and impinges on the target - this time with increased amplitude. Figure 13 shows a schematic of the USLS. Before fabrication, an analytical and numerical study was carried out to determine the peak-pressures, projectile-velocities, dimensions and materials for each component.

## 4.3 Analytical solution to gas-gun based impulsive loading

An analytical solution can be divided into two distinct but connected problems: (1) the projectile-flyer impact and (2) stress-wave transmission/reflection at an interface. Figure 14 shows a schematic of projectile-flyer impact with the flyer in contact with water. When the projectile impacts the flyer plate, it generates a stress-wave in the flyer plate. For the purpose of this analysis, projectile and flyer-plate are considered to be perfectly elastic.

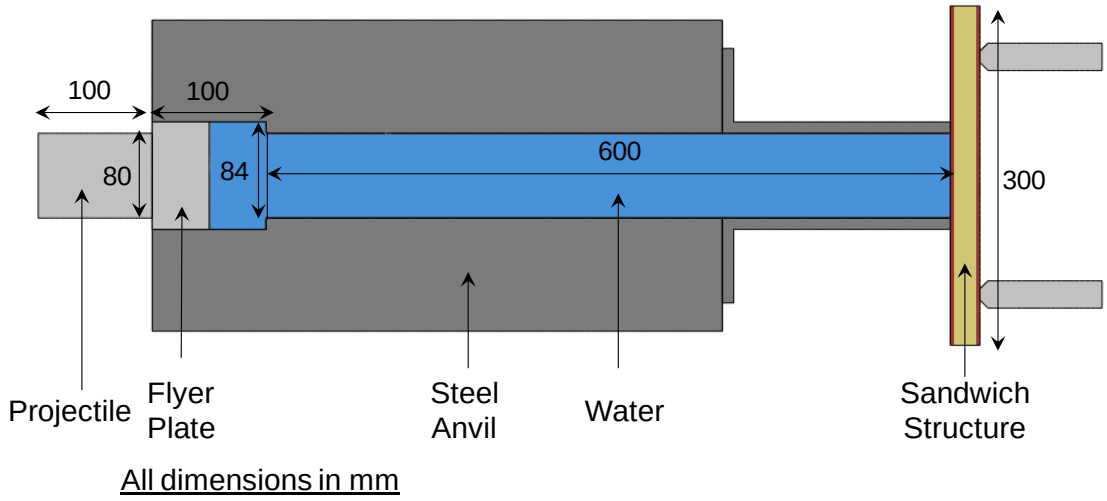


Figure 13 Schematic of Underwater Shock Loading Simulator (USLS). A high-velocity projectile strikes the flyer-plate and creates a stress-wave which travels through the flyer-plate and into the water, generating an impulse identical to one produced by an underwater explosion.

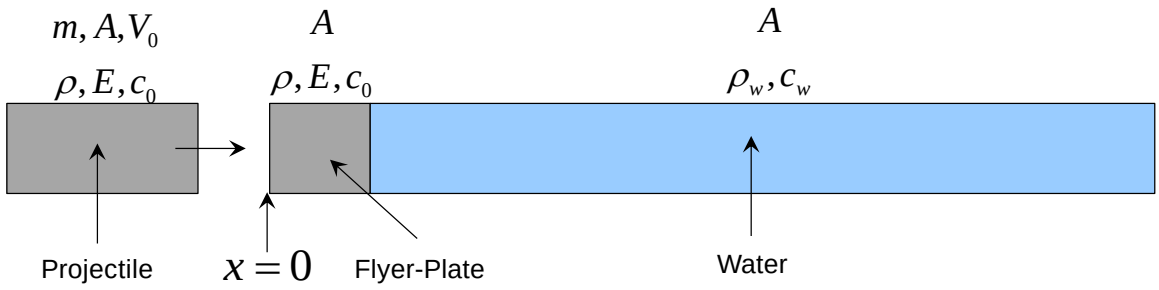


Figure 14 Schematic of the plate-impact and transmission-reflection problem at 2 interfaces - (1) projectile-flyer plate and (2) flyer-plate-water.

For the projectile, the velocity is $V_0$, mass is $m$, the speed of sound in the projectile is $c_0$, the elastic modulus is $E_0$ and the cross-sectional area is $A_0$. The equation of motion is given by

$$E_p \frac{\partial^2 u}{\partial^2 x} = \rho_p \frac{\partial^2 u}{\partial^2 t}$$
$$\text{or} \tag{31}$$
$$\frac{\partial^2 u}{\partial^2 x} = \frac{1}{c_p^2} \frac{\partial^2 u}{\partial^2 t}, c_p = \sqrt{\frac{E}{\rho}},$$

where $u$ is the displacement, $x$ is the position and $t$ is the time. Using the general solution for the wave-equation is given by [157] and [158] and modifying it for the USLS (for the projectile and flyer-plate) leads to

$$u(x,t) = \boldsymbol{I}(c_0 t - x), \tag{32}$$

where "$\boldsymbol{I}$" denotes the incident wave. From Newton's law and conservation of momentum

$$mV_0 - \int_0^t F(t)\,dt = mV_{\boldsymbol{I}}(t). \tag{33}$$

The initial conditions are as follows: (1) the projectile has a velocity $V_0$; (2) the interface between the projectile and flyer-plate is traction-free; (3) there exists stress and velocity continuity across the interface and (4) projectile and flyer-plate can both be considered elastic in the time it takes for the stress-wave to travel into the water-chamber. Using the wave-solution, the velocity at the interface is given by

$$V_I(t) = \frac{d}{dt}\left[\boldsymbol{I}(c_0 t - x)\right] = c_0 \boldsymbol{I}'(c_0 t), \tag{34}$$

and the force at the interface is

$$F(t) = -EA\frac{d}{dx}\left[\boldsymbol{I}(c_0 t - x)\right] = -EA\boldsymbol{I}'(c_0 t). \tag{35}$$

After substituting equations, we get

$$-EA\int_0^t \boldsymbol{I}'(c_0 t)\,dt = m\left[c_0 \boldsymbol{I}'(c_0 t) - V_0\right]. \tag{36}$$

substituting 44

$$\boldsymbol{I}'(c_0 t) + \frac{EA}{mc_0{}^2}\boldsymbol{I}(c_0 t) = \frac{EA}{mc_0{}^2}\boldsymbol{I}(0)\frac{V_0}{c_0}. \tag{37}$$

The first order differential can be solved by

$$\boldsymbol{I}(c_0 t) = D\ \exp\left(-\frac{EA}{mc_0}t\right) + \boldsymbol{I}(0) + \frac{mc_0}{EA}V_0, \tag{38}$$

where $D$ depends on initial condition such that $\boldsymbol{I}(0) = 0$. Substituting this in gives

$$D = \frac{mc_0 V_0}{EA}. \tag{39}$$

Substituting back into  leads to

$$u(0,t) = u(c_0 t) = \frac{mc_0 V_0}{EA}\left[1 - \exp\left(-\frac{EA}{mc_0}t\right)\right]. \tag{40}$$

The general solutions for displacement, velocity, strain and force are

$$u(x,t)=\frac{mc_0V_0}{EA}\left[H\langle c_0t-x\rangle\right]\left[1-\exp\left(-(c_0t-x)\frac{EA}{mc_0{}^2}\right)\right],$$

$$v(x,t)=\frac{d}{dt}u(x,t)=V_0\left[H\langle c_0t-x\rangle\right]\left[\exp\left(-(c_0t-x)\frac{EA}{mc_0{}^2}\right)\right],$$

$$\varepsilon(x,t)=\frac{d}{dx}u(x,t)=-\frac{V_0}{c_0}\left[H\langle c_0t-x\rangle\right]\left[\exp\left(-(c_0t-x)\frac{EA}{mc_0{}^2}\right)\right], \tag{41}$$

$$F(x,t)=\frac{d}{dt}EAu(x,t)=\frac{EAV_0}{c_0}\left[H\langle c_0t-x\rangle\right]\left[\exp\left(-(c_0t-x)\frac{EA}{mc_0{}^2}\right)\right].$$

At the interface where the projectile and flyer-plate make contact, since $x=0$, the generalized relations can be given by

$$u(0,t)=\frac{mc_0}{EA}V_0\left[1-\exp\left(-\frac{EA}{mc_0}t\right)\right],$$

$$v(0,t)=\frac{d}{dt}u(x,t)=V_0\left[\exp\left(-\frac{EA}{mc_0}t\right)\right],$$

$$\varepsilon(0,t)=\frac{d}{dx}u(x,t)=-\frac{1}{c_0}V_0\left[\exp\left(-\frac{EA}{mc_0}t\right)\right], \tag{42}$$

$$F(0,t)=\frac{d}{dt}EAu(x,t)=\frac{EA}{c_0}V_0\left[\exp\left(-\frac{EA}{mc_0}t\right)\right].$$

The stress at $x=0$ is given by

$$\sigma(0,t)=\frac{1}{A}F(0,t)=\frac{E}{c_0}V_0\left[\exp\left(-\frac{EA}{mc_0}t\right)\right]. \tag{43}$$

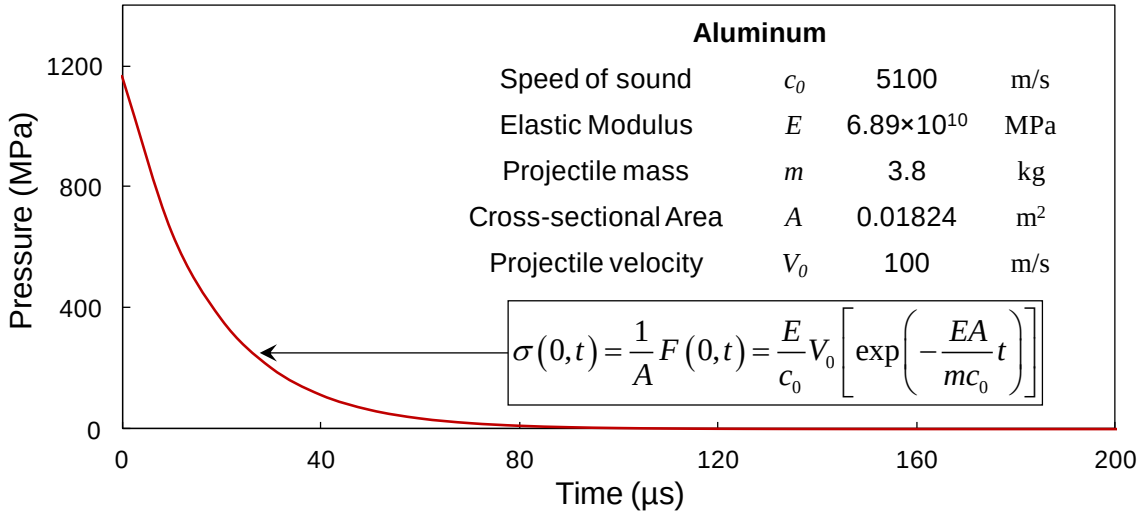


Figure 15 Profile of stress-wave generated in the flyer-plate after projectile impact at $x=0$.

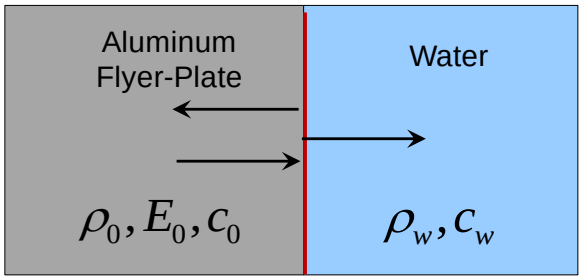


Figure 16 Reflection and transmission of a stress-wave at the aluminum-water interface. Aluminum transmits ~16 % of the impulse into water, a larger fraction than steel which transmits ~6%.

The theoretical stress-wave profile is shown in Figure 15.The stress-wave generated at the projectile-flyer interface travels through the flyer-plate and reaches the flyer-water interface in ~10 μs. Figure 16 shows a magnified view of the flyer-water interface. The displacement fields of particles, assuming an exponential harmonic wave solution, can be given by

$$u_{\boldsymbol{I}} = \boldsymbol{I}\left(x - c_0 t\right) = \boldsymbol{M}_{\boldsymbol{I}} \sin\left(k_0 x - \omega t\right),$$

$$u_{\boldsymbol{R}} = \boldsymbol{R}\left(x + c_0 t\right) = -\boldsymbol{M}_{\boldsymbol{R}} \sin\left[-\left(k_0 x + \omega t\right)\right], \tag{44}$$

$$u_{\boldsymbol{T}} = \boldsymbol{T}\left(x - c_w t\right) = \boldsymbol{M}_{\boldsymbol{T}} \sin\left(k_w x - \omega t\right),$$

where "$\boldsymbol{I}$","$\boldsymbol{R}$" and "$\boldsymbol{T}$" denotes the incident, reflected and transmitted waves and $\boldsymbol{M}$ is the wave amplitude. $k$ is the wavenumber and is given by

$$k = \frac{\omega}{v} \tag{45}$$

Displacement continuity at the interface leads to

$$v\left(x,t\right) = \frac{d}{dt} u\left(x,t\right) \equiv v_{\boldsymbol{I}} + v_{\boldsymbol{R}} = v_{\boldsymbol{T}}. \tag{46}$$

Force continuity at the flyer-water interface gives

$$\sigma\left(x,t\right) = E \frac{d}{dx} u\left(x,t\right) \equiv \sigma_{\boldsymbol{I}} + \sigma_{\boldsymbol{R}} = \sigma_{\boldsymbol{T}}. \tag{47}$$

The displacement fields in reflected wave are given by

$$\boldsymbol{M}_{\boldsymbol{R}} = \frac{\rho_w c_w - \rho_0 c_0}{\rho_0 c_0 + \rho_w c_w} \boldsymbol{M}_{\boldsymbol{I}}, \tag{48}$$

and in the transmitted wave by

$$\boldsymbol{M}_{\boldsymbol{T}} = \frac{2\rho_0 c_0}{\rho_0 c_0 + \rho_w c_w} \boldsymbol{M}_{\boldsymbol{I}}. \tag{49}$$

The stress fields in reflected wave are given by

$$\sigma_R = \frac{\rho_w c_w - \rho_0 c_0}{\rho_0 c_0 + \rho_w c_w}\sigma_I, \tag{50}$$

and in the transmitted wave by

$$\sigma_T = \frac{2\rho_w c_w}{\rho_0 c_0 + \rho_w c_w}\sigma_I. \tag{51}$$

Theoretical stress-profile in the flyer-plate and pressure in the water-chamber are plotted in Figure 17. While a steel flyer-plate would transmit 6% of the incident pressure into the water-chamber, an aluminum flyer-plate will transmit 16% of the incident pressure into the water-chamber.

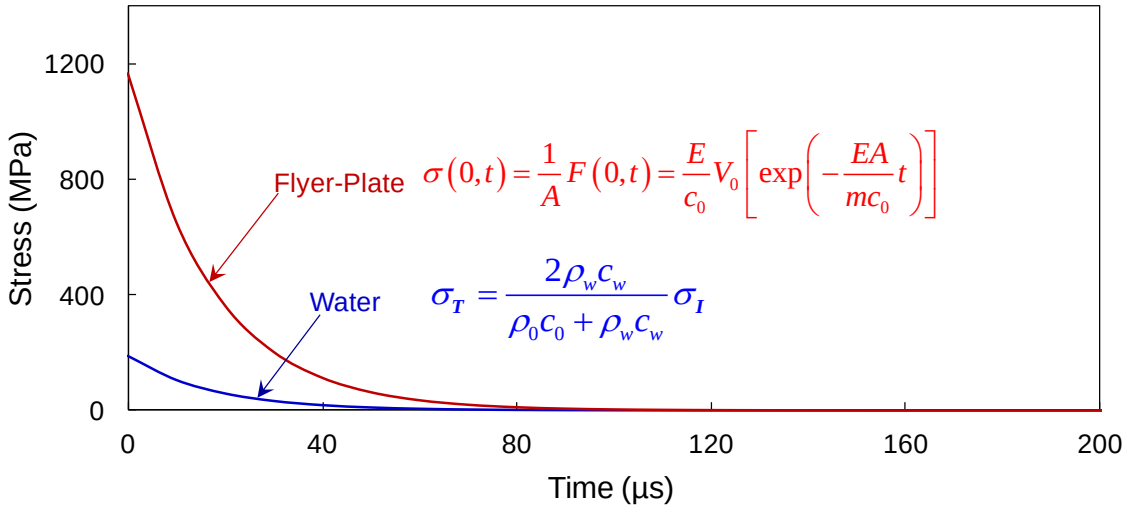


Figure 17 Theoretical stress-profile in the flyer-plate and pressure-profile in the water-chamber for a projectile velocity of 100m/s.

Based on theoretical calculations, it was determined that projectile velocities ranging from 25 m/s up to 200 m/s would be sufficient to generate impulsive loads of varying intensities. The gas-reservoir capacity was finalized at 5 MPa which gives a maximum projectile velocity in excess of 500 m/s to give a maximum peak pressure

exceeding 500 MPa and different decay times. These load intensities mimic different amounts and stand-off distances of the explosive source.

## 4.4 Computational modeling of USLS

A computational model was developed to design the sealing mechanism of the water-chamber and ensure that the stresses generated in the flyer-plate and the walls of the chamber are within acceptable limits. Figure 18 shows the finite element mesh for a two-dimensional computational model of the USLS. The mesh is refined near the flyer-plate and target. The water-chamber is fixed at the edges and the target is clamped. The projectile is prescribed an initial velocity and non-penetrating, frictionless contact is prescribed at all interfaces.

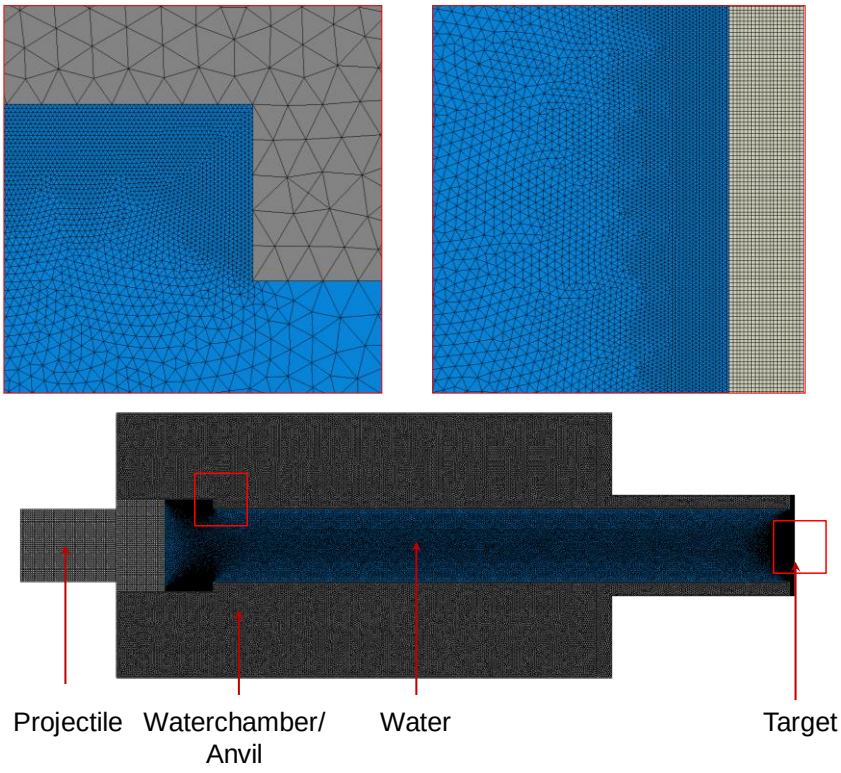


Figure 18 Side-view of finite element mesh for the USLS. The target is fully clamped.

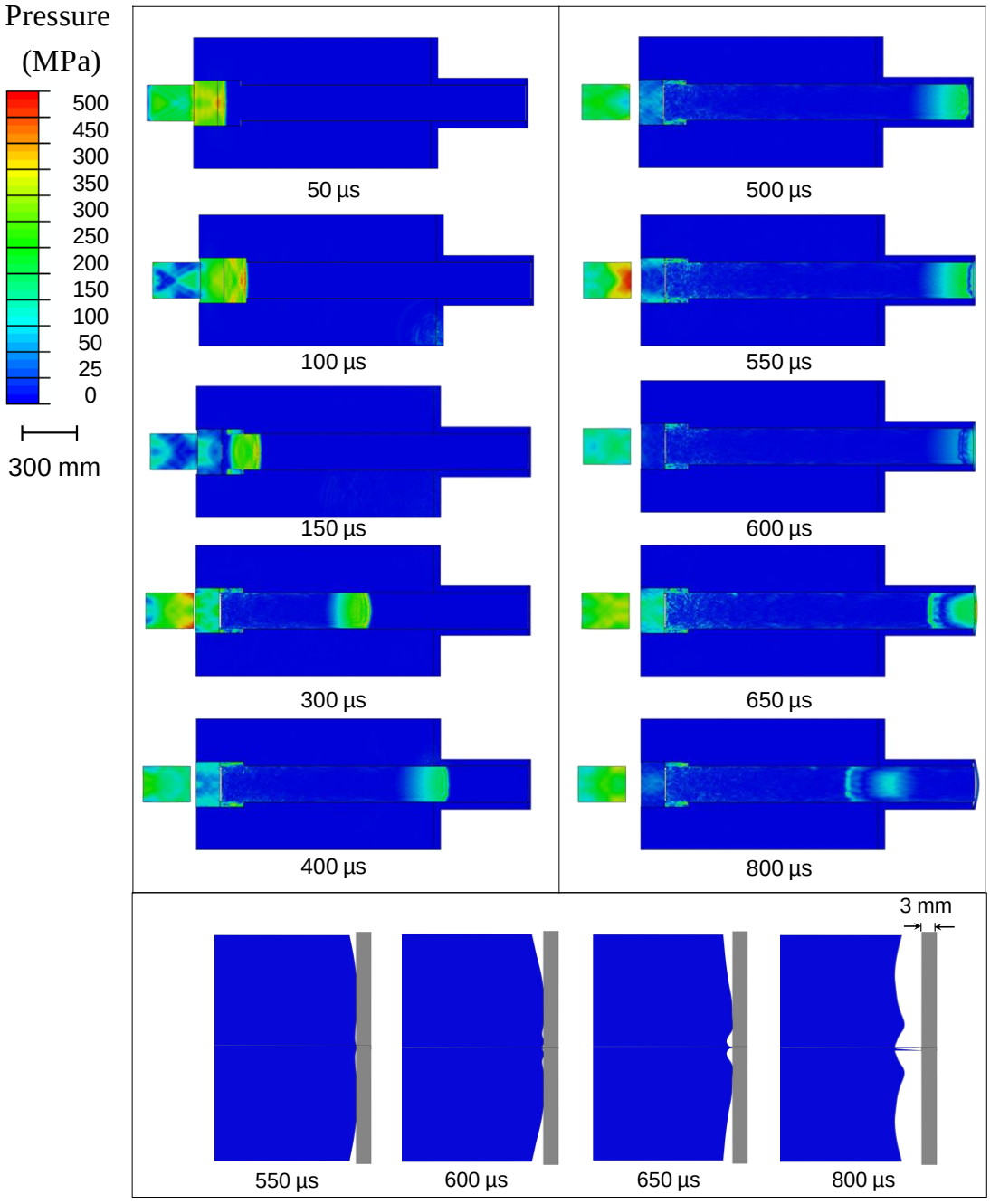


Figure 19 Contour plots of pressure for an impulsive wave generated in the water-chamber due to projectile impact. Cavitation at the water-structure interface is shown. Projectile velocity is 100 m/s.

The projectile impacts the flyer-plate and generates a stress-wave inside the flyer-plate which then passes into the water. This pressure wave is illustrated in Figure 19. The water-chamber is designed such that the flyer-plate will have the least possible displacement and the pressure-wave will be in the form of a shock pulse. The central cylindrical cavity is tapped from behind and has a larger diameter. The flyer-plate that closes the water-cavity on this side also has a larger diameter than the projectile. When the pressure wave is generated in the water-chamber, it is reflected immediately from the edges of this back-tapped portion.

## 4.5 Underwater Shock Loading Simulator (USLS)

The USLS was designed after ascertaining the peak pressures and velocities needed to generate underwater impulsive loads identical to those during an underwater explosion. The central cavity was designed such that the pressure-wave would be in the form of a pulse. The design enables the generation of planar loads which are easier to analyze and uniform through the cross-section. Peak pressure and pressure-histories are measured using ballistic pressure-transducers from PCB Inc. with a maximum pressure of 550 MPa, rise time of 2 μs and sampling frequency of 400 kHz. The peak pressures generated in the experiment and simulations are in good agreement. Both experimental and computational peak pressures are slightly lesser than the theoretical peak pressure. Pressure histories for all three cases are shown in Figure 20.

The gas-gun, water-chamber and support-structure were fabricated by Applied Physics Inc. in Dayton, OH. The gas-reservoir maximum pressure is 5 MPa and a quick-acting ball-valve between the reservoir and projectile. The gun-barrel has an inner

diameter of 75 mm and a total length of 3 m. When the valve is engaged, the gas escapes the reservoir and accelerates a projectile down the length of the barrel. The projectile exits the gun-barrel and impacts upon the flyer-plate. This flyer-plate is sealed using rubber o-rings and is in contact with water. The stress-wave generated in the flyer-plate is transmitted into the water-chamber in the form of an exponentially decaying pressure-pulse. This planar pressure-pulse impinges on the target.

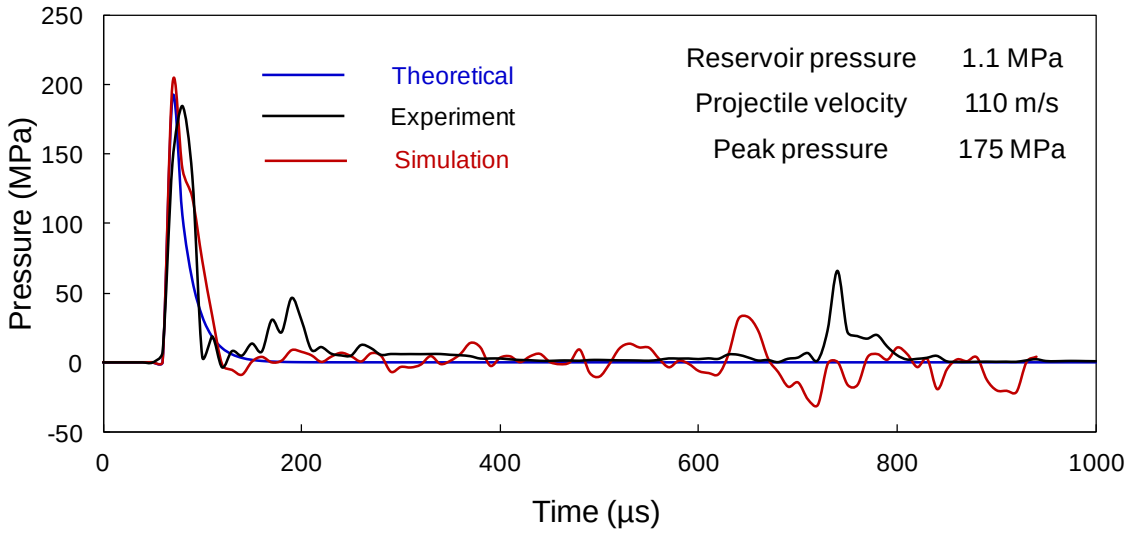


Figure 20 Comparison of theoretical, computational and experimental pressures in the water-chamber. Peak pressures and decay times show good agreement.

Figure 21 shows the photograph of the USLS with different components. Diagnostics for the USLS consist of a high-speed camera - Imacon 200D capable of capturing 200 million frames per second and a resolution of 1368 × 1368. The enclosure is fitted with transparent PMMA sheets to enable in-situ high-speed digital imaging of sandwich structures subjected to impulsive loads. Boundary conditions play an important role in dynamic behavior of marine structures [2]. The USLS enables the testing of three

types of boundary condition- free-standing, simply-supported and clamped with each boundary condition simulating different components of a naval structure.

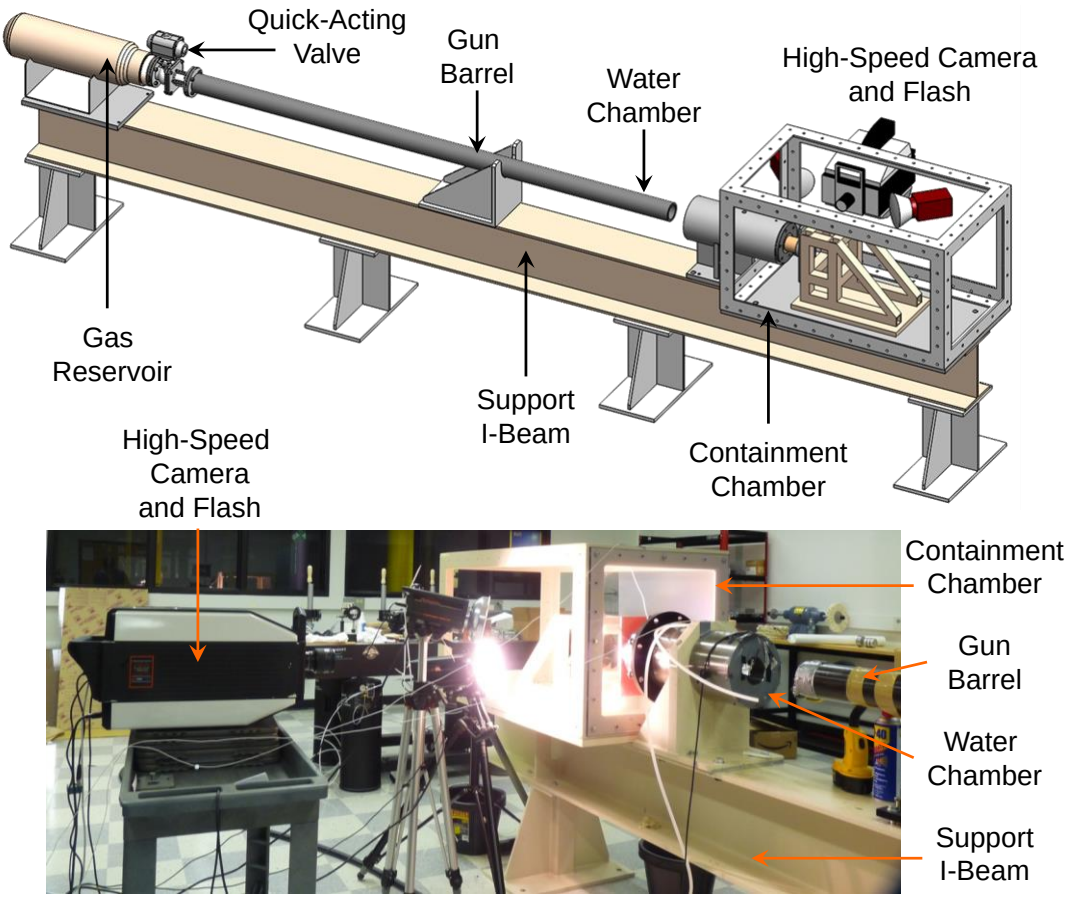


Figure 21 A schematic illustration of the Underwater Shock Loading Simulator (USLS) and a photograph of the facility. Pictured are the gas reservoir, gun barrel, water chamber and the Imacon 200D high-speed camera and light sources.

## 4.6 Concluding remarks

An underwater impulsive loading facility, the Underwater Shock Loading Simulator (USLS) has been designed and fabricated. The facility makes use of a gas-gun based projectile-impact mechanism to generate controlled, planar underwater impulsive loads which impinge on the target structure. A highly modular support system allows in-

situ high-speed digital imaging of the dynamic deformations in marine structures. An Imacon 200D high-speed camera is used to take photographs and dynamic pressure-transducers are used to measure the impulse intensity. The facility can be modified to test oblique and curved structures.

# 5. STRUCTURAL DESIGN METHODOLOGY

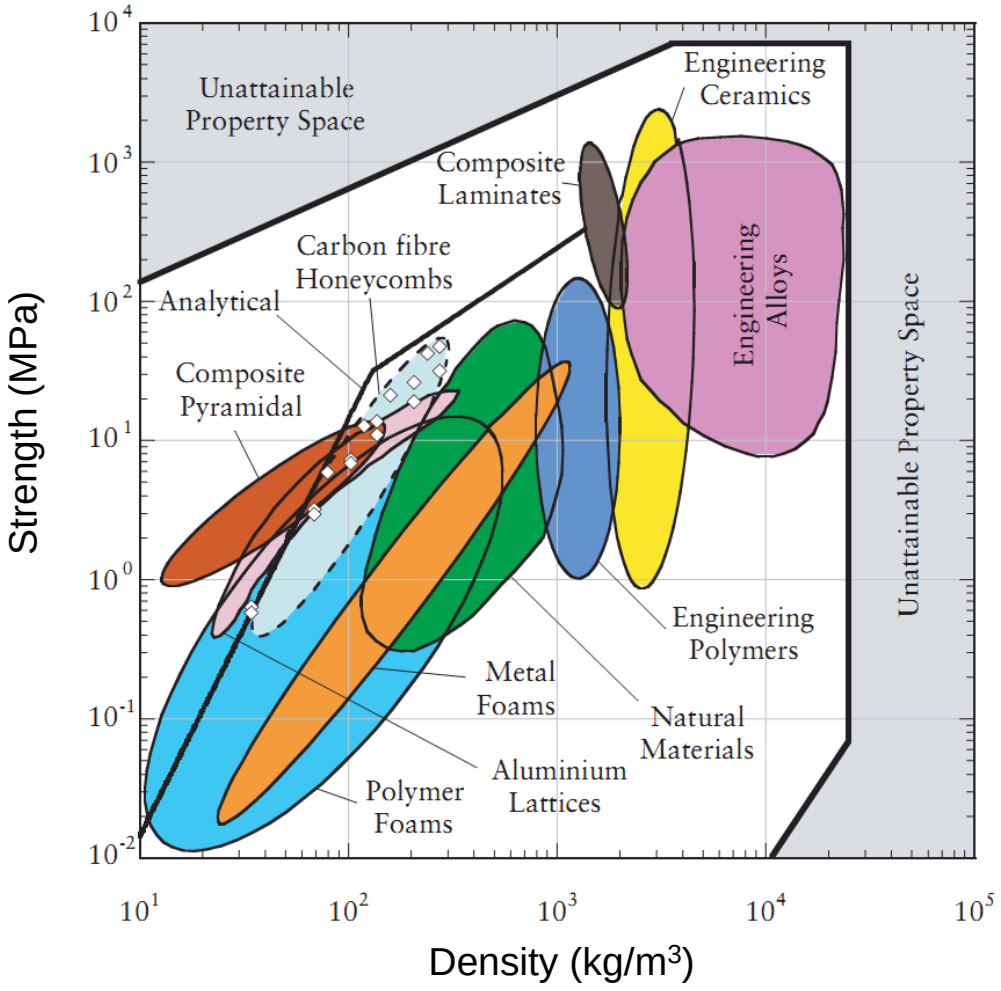


Figure 22 Ashby Map for lightweight structures showing the relationship between density and strength for a range of materials [159].

The design analysis proposed in this research is inspired by the approach promulgated by Ashby and co-authors [159]. Structural design involves selecting materials and designing structures that match the performance profile required by a particular application. A performance profile defines the characteristics required by a structure to excel in its application and defines material indices that capture stated design

objectives: minimizing weight, deflection, impulse transmission, cost or maximizing energy absorption, efficiency, bending strength and so on. It is identified by examining the function of the component, the objectives that the designer wishes to fulfill and constraints that the component must meet to perform adequately. Some commonly used indices in more conventional material and structural design research consist of specific stiffness $E/\rho$ , specific strength $\sigma_Y/\rho$ and many others. These material indices guide the optimal selection of material for component level design. It should be noted that previous design approaches are based on uniaxial compressive loading which is a well-established and quantified loading case. Conversely, in the current scenario consisting of a multitude of loading conditions, structures and materials, the indices must account for a greater number of constraints and variables. Rather simple indices used in previous approaches will be insufficient in this particular case. The design requirements and metrics are specified in Table 7 and are as follows:

Table 7 Design requirements for naval structures.

| | |
|---|---|
| **Function** | Sustain impulsive loads in hulls and internal components of marine vessels |
| **Objective** | High bending stiffness, energy absorption and impulse resistance; Low deflection for minimum achievable mass and thickness |
| **Constraints** | Must have length $L$, width $B$<br>Must conform to specified material properties and limits<br>Must not fail in regular service conditions (non-blast, non-impact loads)<br>Must undergo predictable failure under dynamic loads |
| **Free variables** | Total thickness, Total mass<br>Incident impulsive load intensity, Incident impulse loading angle<br>Interface strength |

The design of a structural element is specified by three main aspects: functional requirements, structural constraints and constituent material properties. The performance $P$ is described functionally as:

$$\begin{aligned} P &= f\left[\begin{pmatrix}\text{Load Bearing}\\ \text{Requirements, } L\end{pmatrix};\begin{pmatrix}\text{Structural}\\ \text{Attributes, } S\end{pmatrix};\begin{pmatrix}\text{Material}\\ \text{Properties, } M\end{pmatrix}\right] \\ &= f(L,S,M) \text{ or} \\ &= f_1(L)\, f_2(S)\, f_3(M). \end{aligned} \tag{52}$$

The indices in this scenario are $f_1(L)$, $f_2(S)$ and $f_3(M)$, and the optimum subset of loads, structural attributes and material parameters that maximize or minimize the appropriate performance can be identified. In the proposed research, non-dimensional variables will be developed for quantitative evaluation of the dynamic response of composite panels as functions of loading and structural attributes and scalability. These variables are listed in Table 8. Non-dimensionalized parameters are varied independently of each other and the performance of the structure in each case is quantified using these metrics. Based on the experiments and numerical simulations proposed here, loading-structure-performance relations will be developed. These relations are in the form of a power-law such that $P = \left[\lambda \cdot L^{(m)} \cdot \psi^{(n)}\right]$, where $P$ is the acceptable performance attribute, $L$ and $\psi$ are loading and design metrics and $\lambda, m$ and $n$ are power-law constants for that particular case. These relations can be used to inform structural design with the understanding that they should only be used for the specified material, structural parameter ranges and loading conditions. The design process will be carried out systematically and will involve exhaustive parametric studies to encompass as wide a

range of performance as possible. Figure 23 shows the flowchart of the design process and is explained in the following sections.

Table 8 Loading-structure-performance metrics used in the proposed research.

| **Loading Metrics** $(L)$ | | |
|---|---|---|
| Normalized Incident Impulse | Loading Angle | Environments |
| $\bar{I} = \frac{I_0}{\rho_w c_w \sqrt{A}}$ where $I_0 = \int_0^t p(t)\,dt.$ | $\theta^o$ | Air-backed<br>Water-backed |
| **Material and Structural Metrics** $(S,M)$ | | |
| Normalized Density $(\bar{\rho})$ | Thickness Ratios $(\bar{T})$ | Weight Index $(\psi)$ |
| $\frac{\rho_{core}}{\rho_{PVC}}, \frac{\rho_{core}}{\rho_{face}}$ | $\frac{T_C}{T_T}, \frac{T_F}{T_T}, \frac{T_B}{T_T}$ & $\frac{T}{L}$ | $\psi = 2\left(\frac{T}{L}\right) + \left(\frac{\rho_{core}}{\rho_{face}}\right)\left(\frac{T_C}{L}\right)$ |
| **Performance Metrics** $(P)$ | | |
| Deflection/Core Compression | Normalized Transmitted Impulse | Accumulated Damage |
| $\bar{U} = \frac{\Delta}{L}$ or $\varepsilon = \frac{L - L_0}{L_0}$ | $\bar{I}_B = \frac{I_B}{I_0}$ where $I_B = \frac{\int F \cdot dt}{A}$ | $\bar{N} = \frac{N_C}{N_T}$ |

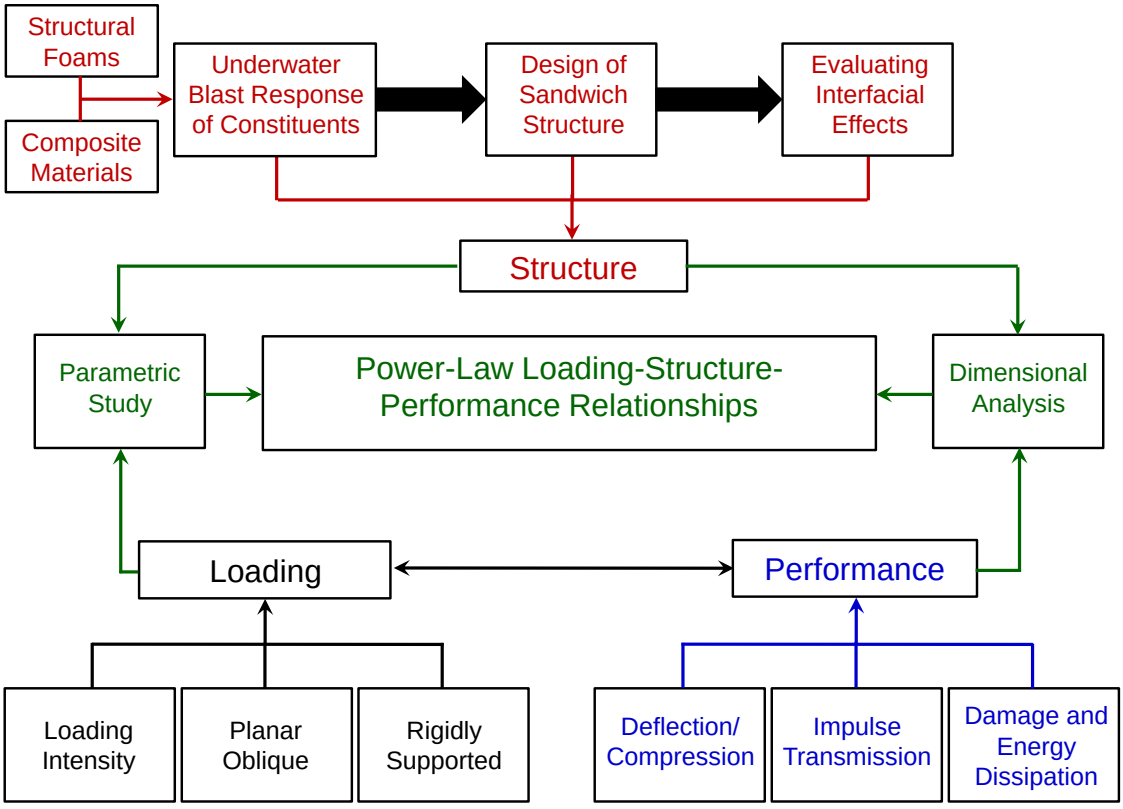


Figure 23 Flowchart of the structural design process to obtain loading-structure-performance maps.

## 5.1 Underwater blast response of constituents

One of the key differences between sandwich structures and other marine structures is the fact that sandwich structures have three very different components that must be evaluated independently and then combined to create the most optimal structure. These three components are facesheets, cores and core-facesheet interfaces and their synergism is key to enhanced blast mitigation. Since underwater explosions create very complex and multi-axial loads, simply evaluating the sandwich structure constituents under conventional tension or compression loads is not sufficient. In the proposed research, all the constituents of the sandwich structure are evaluated based on their response to underwater impulsive loads. Monolithic carbon-fiber reinforced polymer composites with different fiber orientations will be subjected to a range of impulsive loads. Unidirectional, bi-axial and quasi-isotropic orientations will be considered. Since anisotropy in composites is often considered a liability for marine applications because it causes unpredictable failure and hampers repair, this approach aims to quantify the role of orientation on structural response and ascertain the optimal orientation with respect to loading conditions and supports. A simply-supported configuration is employed because it closely resembles the internal stiffeners and substructure of a navy ship. Additionally, structural polymeric foams are tested independently by subjecting them to a range of incident impulsive loads to evaluate the compressive response and impulse transmission characteristics under water blasts. Loading-structure-performance relations are developed for both monolithic laminates and polymeric foams, correlating incident impulsive load intensity with deformation and blast mitigation.

## 5.2 Sandwich structure design

Based on the performance of composite laminates and PVC foams, the optimal composite layup and the two optimal polymeric foam cores will be selected for sandwich structure design. Initially a simple epoxy-resin core-face bond will be used at the core-facesheet interface for bonding. Fixed-weight sandwich structures are those that have similar total masses but different core densities. Since the monolithic structure is 6 mm thick and the sandwich structure faces are 3 mm thick, the only differences are due to changes in core characteristics. Fixed-geometry sandwich structures are those that have the similar dimensions but different total masses. This will allow the evaluation of the most geometrically efficient structure. Graded-core sandwich structures are constructed with the core consisting of multiple sections made of polymeric foams with different densities. Finally, the front and back face thicknesses are varied to optimize the mass distribution of the sandwich structure. This will enable the exploitation of FSI effect while at the same time ensuring that structural rigidity is not compromised. A number of studies have shown that the core-face interface characteristics greatly influence the response of the sandwich structure. To quantify the effect of changes in interface strength, adhesives with a range of strength and compliance developed by 3M have been used. These adhesives will be applied in the most optimal sandwich structures resulting from previous analyses and will help evaluate the role interface strength and identify the most optimal interface strength and compliance.

## 5.3 Role of loading conditions

As discussed previously, the USLS is capable of generating impulsive loads with a range of peak-pressures (10 – 250 MPa) and decay times by varying the projectile mass, projectile velocity and piston thickness. Due to the inherent unpredictability associated with blast loads, it is essential that a range of loads be considered. The primary loading condition for initial structural design is an air-backed, planar simply-supported beam configuration. A navy ship is a complex structure, consisting of geometric and structural nonlinearities based on the location of the structural section. In such cases, the angle of obliqueness of the incident load can be a critical factor in determining structural response. The modular design of the USLS allows a range of incident impulse loading angles from $90^o$ to $45^o$ to be used in experimental analyses. An analysis of structural performance in water-backed conditions is important for the design of critical parts of ship structures like turbine blades, hull and keel. Water-backed conditions also prevail in underwater pipelines and ducts. Moreover, a number of sections in the hull of a marine vessel are backed by movable equipment and machinery which creates conditions similar to water-backed loading conditions. To evaluate the role of the loading environments on sandwich core response, a rigidly-supported configuration has been developed resembling the conditions in a water-backed situation.

# 6. RESPONSE OF MONOLITHIC COMPOSITE PLATES

## 6.1 Introduction

Marine vessels operate in severe environmental conditions involving temperature extremes, dynamic loads and corrosive sea water. In addition to operational loads, the structures are also required to withstand hydrodynamic impulsive loads due to surface and sub-surface blasts and weapons impact. The deformation response of plates under water-based impulsive loads is of great importance in the design of blast-resistant marine structures for naval applications. Fluid structure interaction (FSI) effects play an important role in determining the dynamic response and can be exploited to improve the blast mitigation capability of the structures.

In recent years, composite materials have been employed in naval construction and the off-shore industry. As a consequence, understanding the response of composite structures to high intensity underwater impulsive loads has gained importance. Investigations have been carried out on the dynamic deformation and failure of layered materials. Previous analyses of dynamic deformation in sandwich composites have focused on low velocity contact-based loads due to drop weight and projectile impact [32, 33, 51-55]. Results show that key damage mechanisms include matrix cracking, fiber breakage and interlaminar delamination. The primary driving forces for the damage processes are transverse shear stresses [38-40]. Interlaminar delamination is the most detrimental to stiffness and strength and, therefore, is a major concern because delamination is not visible on the surface. Chang and co-workers [41-43] have studied the

damage behavior of composite laminates under low velocity impact loading, concluding that in-ply matrix cracking precedes delamination growth and shear and bending crack initiation. The damage behavior of composite laminates is significantly influenced by matrix material, composite layup and geometric aspects such as size, thickness and loading area [44-46]. Minnaar and Zhou [47] used a novel interferometric experimental setup to show that interlaminar crack speeds are significantly higher under shear loading, and that crack speeds are strongly influenced by loading rate in mode II. However, only limited study has been reported on the dynamic response of composites to water-based impulsive loads. Analyses have primarily focused on sandwich structures because such structures offer considerably high shear and bending stiffness to weight ratios than homogeneous plates of equivalent mass. Experiments and computations focusing on different core topologies and specimen sizes have been carried out by Espinosa and co-workers [1, 93, 104] and McShane et al. [105] using underwater pressure impulses generated by gas gun impact and by Dharmasena et al. [64] using planar pressure impulses generated by explosive sheets. Battley and co-workers developed a high-speed servo-hydraulic testing system and concluded that slamming impacts on a deformable sandwich panels result in different peak and residual pressures to those from a rigid panels [106, 107]. Shukla and co-workers [79-83] examined the dynamic response of sandwich structures consisting of woven E-glass composite facesheets and stitched core to air-based shock loading and concluded that stitched cores exhibit superior mechanical performance. A combined experimental and computational analysis of the response to underwater blast by Avachat and Zhou [108] has revealed that sandwich structures significantly outperform monolithic structures at all impulsive levels and environmental

conditions including air-backed and water-backed structures. Additionally, a balance of core stiffness and softness provides optimal blast resistance by allowing load spreading and energy dissipation while mitigating the effects of localized core compressive failure and rupture.

Despite recent interest in the mechanical response of composite structures, especially their behavior under blast loading, there are a number of unresolved issues. Comparative analyses of the blast resistance and dynamic performance of different reinforcements (glass-fiber, carbon-fiber), different matrix materials (epoxy, polyester, etc.), and varying boundary conditions (planar, oblique, cylindrical) are lacking. It is well known that glass-fiber and carbon-fiber reinforced composites exhibit dramatically different dynamic response in terms of out-of-plane deflection, impulse absorption and transmission and overall accumulated damage through interlaminar and intralaminar cracking due to differences in stiffness, strength and flexural/bending resistance. Additionally, the deformation and failure of blast loaded composites plates subjected to underwater impulsive loads are complicated due to fluid-structure interaction (FSI) effects, competing damage mechanisms, complex failure modes, interfacial effects and material heterogeneity and, therefore, require a physically-based multiphysics computational framework in order for each of the aspects to be accounted for. Since there are significant differences in projectile impact loads and water-blasts, understanding the response of composite laminates under water-based impulsive loading is of critical importance in the design of marine structures.

The objective of the present study is to characterize the damage response of thick composite laminates with different reinforcements and anisotropy under blat loading. The

focus of this analysis is on understanding the deformation and failure mechanisms, and quantifying the damage in composite structures as a function of structural attributes, material properties, loading conditions and loading rates. The loading of interest is high intensity water-based impulsive loads. Planar impulses resembling those resulting from underwater explosions are generated using the Underwater Shock Loading Simulator (USLS), a novel experimental setup developed recently. The USLS consists of a projectile-impact-based impulsive loading system, a water chamber, a target holder, and a safety enclosure. The target holder allows clamped and simply-supported boundary conditions. The experiments are designed to quantify the resistance of each structural configuration to underwater impulsive loads. The response and failure mechanisms studied include overall deflection, compressive kinking and buckling, inter-play delamination and debonding, in-ply cracking, shear cracking and rupture. Of particular interest is the influence of fiber orientation and stiffness on deformation and failure.

This is a combined experimental and computational study. Coupled Eulerian Lagrangian finite element simulations are carried out, accounting for the experimental conditions and material properties which are measured independently. The simulations also account for the fluid-structure interaction (FSI) effect at the water-composite interface. Failure mechanisms considered include shear cracking and fragmentation, tensile cracking, compressive kinking, and interfacial debonding. The simulations focus on damage initiation and evolution in the early stage of deformation (~1500 μs) since the load-carrying capacity is most critically reflected then. This combined experimental and numerical approach enables the identification of factors that play important roles in

determining the dynamic response of the materials. The analysis uses metrics such as deflection, transmitted impulse and accumulated damage to quantify blast resistance.

## 6.2 Technical approach

### 6.2.1 Composites manufacturing

The research described in this chapter pertains to the deformation response of monolithic composite laminates constructed from carbon-fiber/epoxy and glass-fiber/epoxy . These composite structures are manufactured by curing prepregs in an autoclave. The technical approach to manufacturing composite materials is provided in *3.2 Composite materials*. The composite laminates are manufactured by curing the prepregs under pressure in a high temperature oven at 100 °C. The thickness of each cured lamina is calculated using

$$\text{Cured Ply Thickness} = \frac{\text{Fiber Areal Weight}}{\text{Fiber density} \times \text{Fiber Volume} \times 10}, \tag{53}$$

giving a cured ply thickness of ~0.23 mm per layer or lamina. Each composite laminate is constructed by stacking unidirectional prepregs in the required orientations to create a dense, thick laminate with a total thickness of 6.35 mm. The layups studied in this analysis are bi-axial (0/90), quasi-isotropic (0/-45/45/90), unidirectional with fibers perpendicular to supports (90) and unidirectional with fibers parallel to supports (0). Figure 24 shows the simply-supported planar impulsive loading configuration and the different layups used in laminate construction.

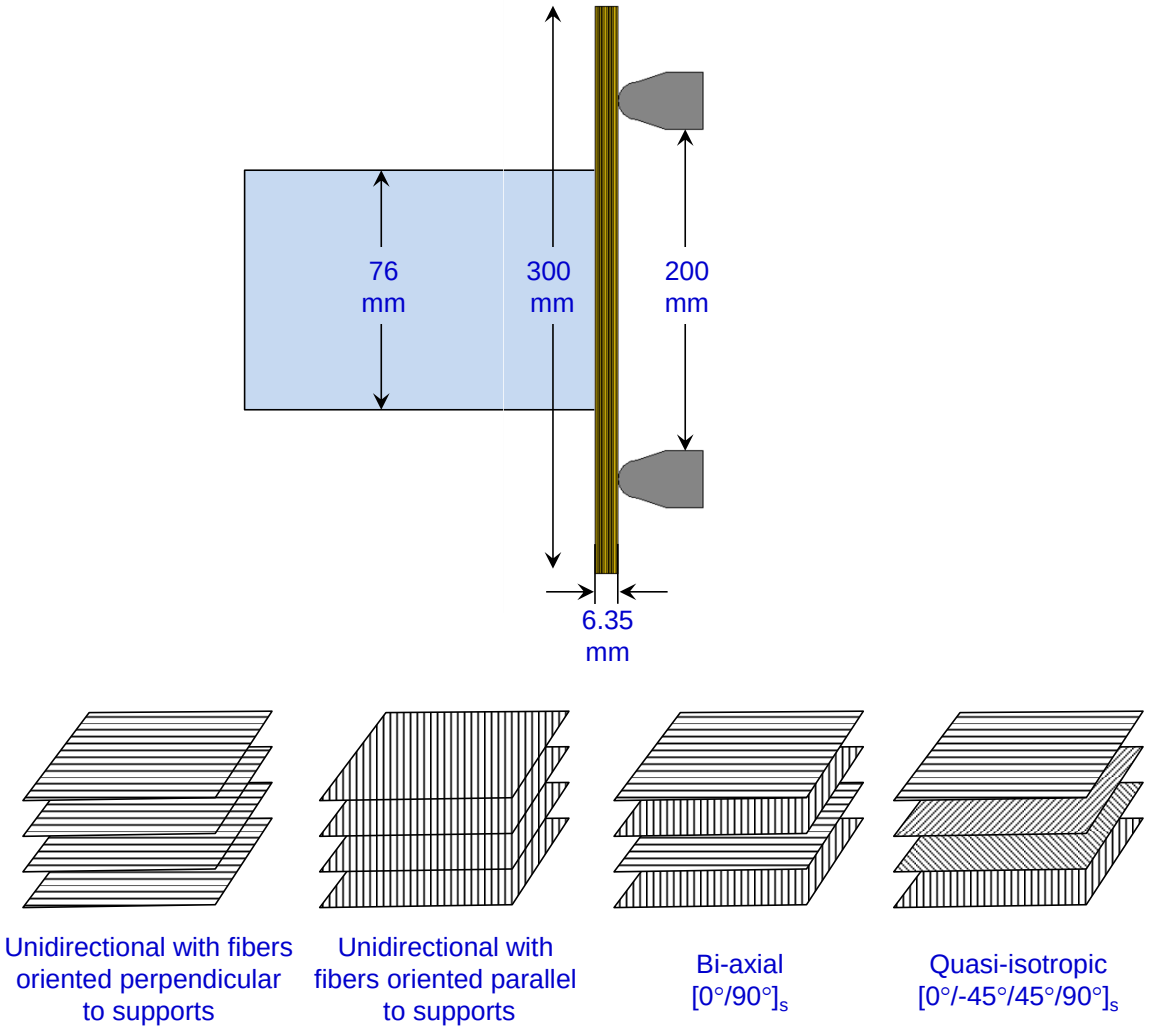


Figure 24 Schematic showing the simply-supported loading $r$ configuration with planar incident impulsive load and different composite layups implemented in the construction of the test specimens.

### 6.2.2 Underwater impulsive loading

Gas gun impact has been successfully used to generate impulsive loading through water [92, 93, 160-162]. To obtain controlled loading and simulate different water-structure contact conditions, the Underwater Shock Loading Simulator (USLS) in Figure 25 is designed to provide a variety of loading configurations with quantitative diagnostics [160-162]. Important features of this facility include the ability to generate water-based

impulsive loading of a wide range of intensity, the ability to simulate the loading of submerged structures, and integrated high-speed photographic and laser interferometric diagnostics. The impulsive load that impinges on the target induces deformation in the specimen at strain rates up to $10^4$ $s^{-1}$. Projectile impact velocities in the range of 15-150 $ms^{-1}$ are used to delineate the effect of loading rate on the deformation and failure behavior of the structures analyzed. This velocity range corresponds to peak pressures between 15 and 200 MPa, which are comparable to pressures observed in underwater explosions [6, 163-165].

According to Taylor's analysis of one dimensional blast waves [7] impinging on a light, rigid, free standing plate, the pressure in the fluid at a distance  from an explosive source follows the relation

$$p(t) = p_0 \exp\left(-\frac{t}{t_0}\right), \tag{54}$$

where $p_0$ is the peak pressure, $t$ is time and $t_0$ is the pulse time on the order of milliseconds. The area under the pressure-time curve is the impulse carried by the wave and is given by

$$I_0 = \int_0^t p(t)\,dt = p_0 t_0. \tag{55}$$

For a free standing plate of areal mass $m$, the impulse transferred to the plate is

$$\frac{I_T}{I_0} = \psi^{\left(\frac{\psi}{1-\psi}\right)}, \tag{56}$$

where $\psi$ is the fluid-structure interaction (FSI) parameter given by

$$\psi = \frac{\rho_w c_w t_0}{m}, \tag{57}$$

and $\rho_w$ is the density of water and  is the speed of sound in water. This FSI parameter is an important aspect of Taylor's analysis because it helps to delineate the effects of a pressure pulse applied instantaneously versus the effects of a pressure pulse decaying over a certain time period.

It has been shown that this FSI effect can be exploited to improve the blast mitigation capability of structures subjected to transient loads [8, 9]. For the current analysis, a non-dimensionalized incident impulse $\bar{I}$ in the form of

$$\bar{I} = \frac{I_0}{\rho_w c_w \sqrt{A}} \tag{58}$$

is used, where $A$ is the area under loading. The experiments and numerical modeling for different $\bar{I}$ values simulate the effects of different standoff distances from an explosive source. Swisdak [7, 166, 167] showed that for an underwater explosion using a Tri Nitro Toluene (TNT) explosive source, there exists a power-law relation between the mass $M$ of the explosive and peak pressure $p_0$ (in MPa) such that

$$p_0 = 52.4\left(\frac{M^{1/3}}{r}\right)^{1.13}, \tag{59}$$

where $r$ is the standoff distance in meters. In the experiments reported here, pressures ranging from 10 MPa to 300 MPa can be generated using different projectile velocities. The rise time of the pressure pulses is on the order of 25 μs and the decay time is on the order of 800 μs. The impulsive load considered in this set of calculations has a peak

pressure of 196 MPa which approximately corresponds to 100 kg of TNT detonating at a distance of 1.7 meters. Although the peak pressures are similar for experiments and simulations, the decay times are slightly different. The normalized impulse magnitude is $\bar{I} = 0.20$ for experiments and $\bar{I} = 0.16$ for simulations.

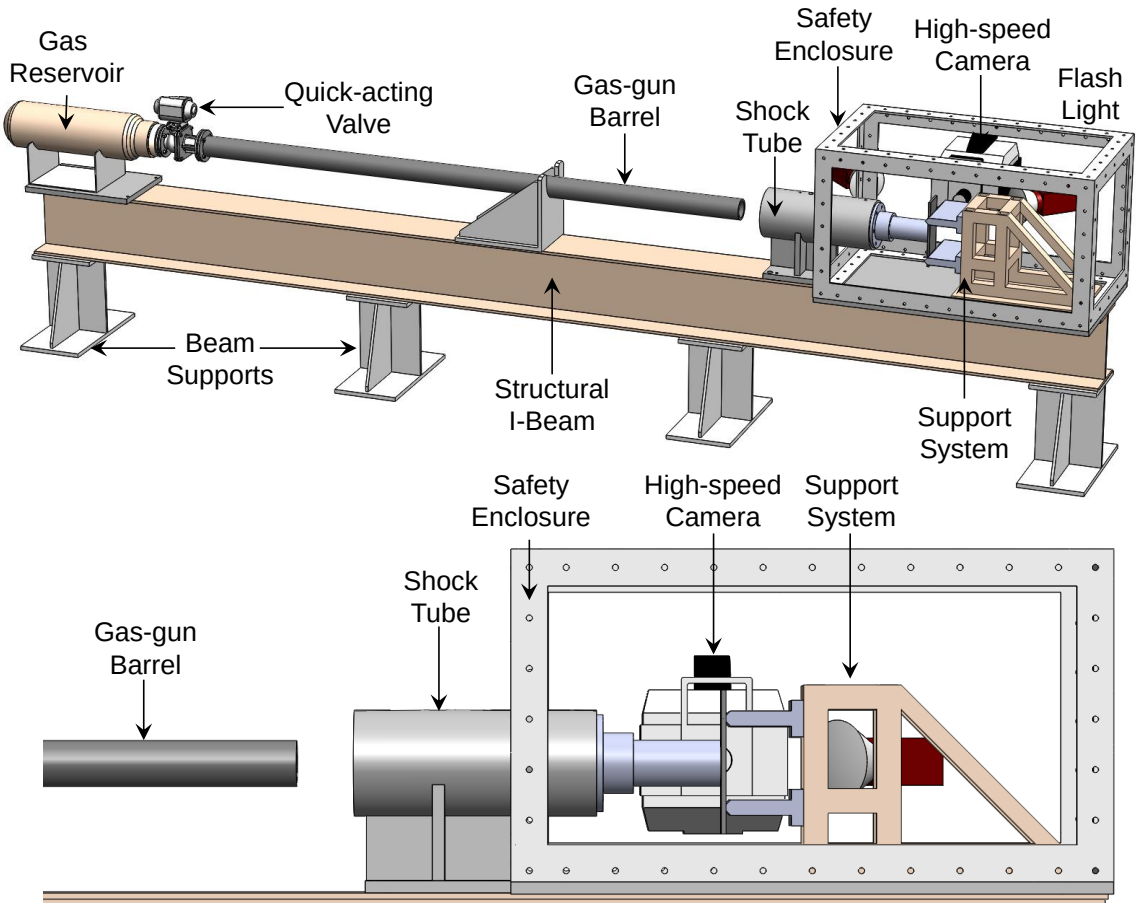


Figure 25 Schematic illustration of the Underwater Shock Loading Simulator (USLS) for testing simply-supported thick laminates. Pictured are the gas reservoir, gun barrel, water chamber, modular support system, specimen and the Imacon 200D high-speed camera.

### 6.2.3 Computational framework

The model consists of a Lagrangian domain for the solids and an Eulerian domain for the water. In the Lagrangian domain, nodes are fixed within the material and nodal displacements track the material deformation. Since each Lagrangian element is always

100% within a single material, the material boundary coincides with element boundaries. In contrast, Eulerian the domain consists of nodes that are fixed in space and the material flows through the elements that do not experience deformation. Eulerian elements may also be partially or completely void, allowing material to flow into empty space, capturing cavitation, a crucial aspect of fluid flow. Materials tracked by Eulerian elements can interact with Lagrangian elements through Eulerian-Lagrangian contact algorithms to allow fully coupled multi-physics simulations like fluid-structure interactions. This Coupled Eulerian-Lagrangian (CEL) framework allows the severe deformation in water and the FSI to be captured. In addition to simulating the blast wave propagation in the USLS, the Eulerian formulation also captures the exponentially decaying pressure waves and resulting cavitation at the fluid-structure interface. The interaction between the water and structure is effected by tying the nodes in the water to the corresponding nodes of the structure, thereby ensuring continuity of displacements when contact occurs. The CEL framework is described in detail in section *3.5 Modeling of fluid-structure interaction*.

In finite element simulations, the laminate is constructed by stacking unidirectional laminas in various orientation. The deformation in individual laminas in the laminate is considered to be elastic prior to the onset of damage. Damage and dissipation in individual layers, also called “intra-laminar damage” or “in-ply damage”, is captured using the Hashin damage model described in section *3.2.3 Computational modeling of composite laminates*. The interlaminar cracking and delamination, also called “inter-laminar damage” or “inter-ply damage”, is accounted for through the user of cohesive finite elements which exhibit a traction-separation response based on critical

values surface traction or surface separation as described in section *3.2.4 Cohesive finite element framework to track delamination*. Figure 26 shows a schematic of the Coupled Eulerian Lagrangian computational framework showing different element types and constitutive models used in the finite element simulations.

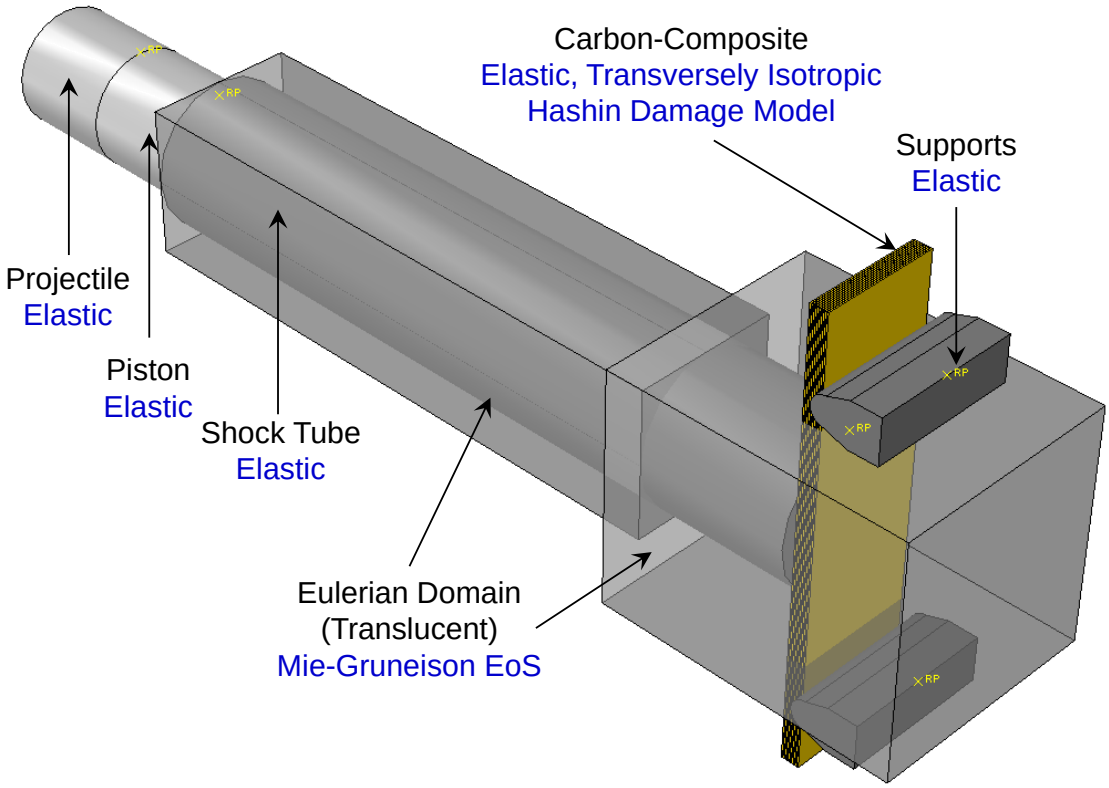


Figure 26 Schematic of the Coupled Eulerian Lagrangian computational framework showing different element types and constitutive models used in the finite element simulations.

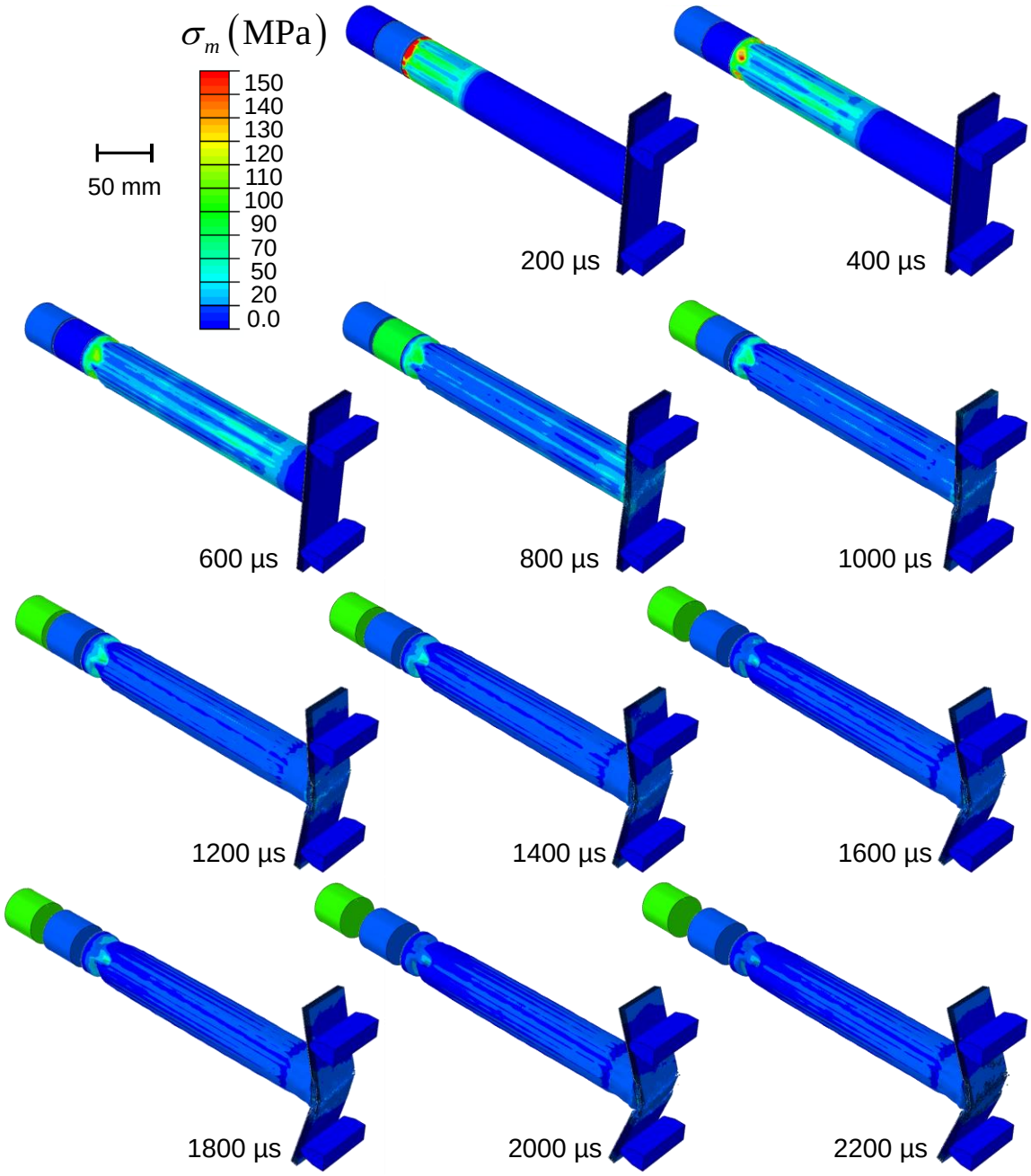


Figure 27 Finite-element simulation of the Coupled Eulerian Lagrangian framework for the Underwater Shock Loading Simulator (USLS) showing the distributions of pressure at different times for an impulsive wave generated in the water chamber when a projectile travelling at a velocity of 110 $ms^{-1}$ strikes the piston plate.

Figure 27 shows the Coupled Eulerian Lagrangian (CEL) finite element model of the USLS with a pressure pulse traveling through the water chamber and impinging upon a simply-supported test specimen. The experimentally measured and calculated pressure pulses show good agreement in terms of peak pressures and decay times, as shown in Figure 28. The experimentally measured profiles show slightly faster wave attenuation than the calculated profiles. Clearly, the coupled Eulerian-Lagrangian framework and the Mie-Gruneisen equation of state allow most essential features of the loading pulses in the experiments to be captured.

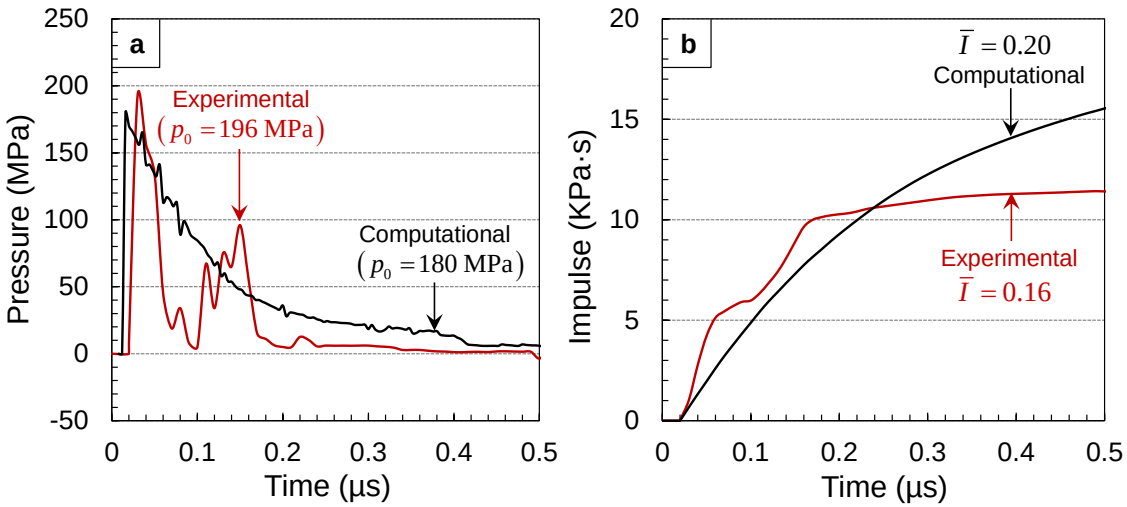


Figure 28 Experimentally measured and numerically calculated pressure and impulse histories in the water chamber for a gas reservoir base pressure of 350 psi and a projectile velocity of ~110 $ms^{-1}$.

Figure 28 shows the comparison of experimentally measured and numerically calculated pressure histories and impulse magnitudes corresponding to a reservoir base pressure of 250 psi and a projectile velocity of ~110 $ms^{-1}$. The rise time of the pressure pulses is on the order of 25 μs and the decay time is on the order of 1500 μs. The

impulsive load considered in this particular analysis has a peak pressure of 198 MPa which approximately corresponds to 100 kg of TNT detonating at a distance of 1.4 meters from the side of a ship. The incident impulse magnitude is $I = \int_0^t p(t)dt = 12$ kPa·s and the normalized impulse magnitude calculated using eqn. (67) is $\bar{I} \approx 0.20$.

In this computational framework, each lamina in the laminate is modeled explicitly. A laminate is discretized into two distinct phases: (1) fiber-reinforced phase in the in-ply or intralaminar regions which are simulated using 3-D brick elements; and (2) resin-rich phase in the inter-ply or interlaminar regions which are simulated using cohesive finite elements of finite thickness. One of the major advantages of this computational framework is the ability to capture damage based on fiber orientations of each lamina. The in-ply damage contours for quasi-isotropic carbon-fiber/epoxy laminate are shown in Figure 29. The plies closest to the impulsive loading face exhibit a combination of shear failure near the loading circumference and compressive failure at the midplane. The plies that are the middle region are relatively undamaged while those that are farthest from the impulsive loading face experience high tensile stresses due to bending and exhibit damage near the midplane. It is also evident that the damage contours are highly dependent on the fiber orientation in each lamina, thereby the computational model to capture the effects of different composite layups and stacking sequences. The inter-ply damage contours the resin rich layers of a quasi-isotropic carbon-fiber/epoxy laminate are shown in Figure 30. The interplay damage contours exhibit significant shear cracking at the impulsive loading side and relatively negligible

cracking on the far side. The interlaminar damage is governed by the orientation of the fiber-reinforced plies in contact with the resin layer.

The mesh width, $w$, is varied over a range of $w =$ 100 μm to 1200 μm and the incident load is fixed at $\bar{I} = 0.20$ to evaluate mesh sensitivity. Figure 31(a) and (b) shows the energy dissipated through inelastic deformation and peak stress prior to failure as functions of mesh size respectively. When the numerical results are plotted, it is revealed that inelastic dissipation scales monotonically with $w$ and in the limit where $w \to 0$, the energy dissipation vanishes. Thus, although mesh refinement is essential for adequate strain resolution, excessive mesh refinement has the adverse effect of yielding anomalously low energy dissipation. As shown in Figure 31(b), the numerical solution reaches convergence for a mesh width of $w =$ 500 μm. Consequently, the mesh width selected for this calculation is $w =$ 500 μm, which is sufficient for numerical convergence (in both, bulk and cohesive elements) but still provides a reasonable approximation of energy dissipated in the process. These element sizes are in accordance with element size recommendations from Tomar et al. [62] for cohesive elements.

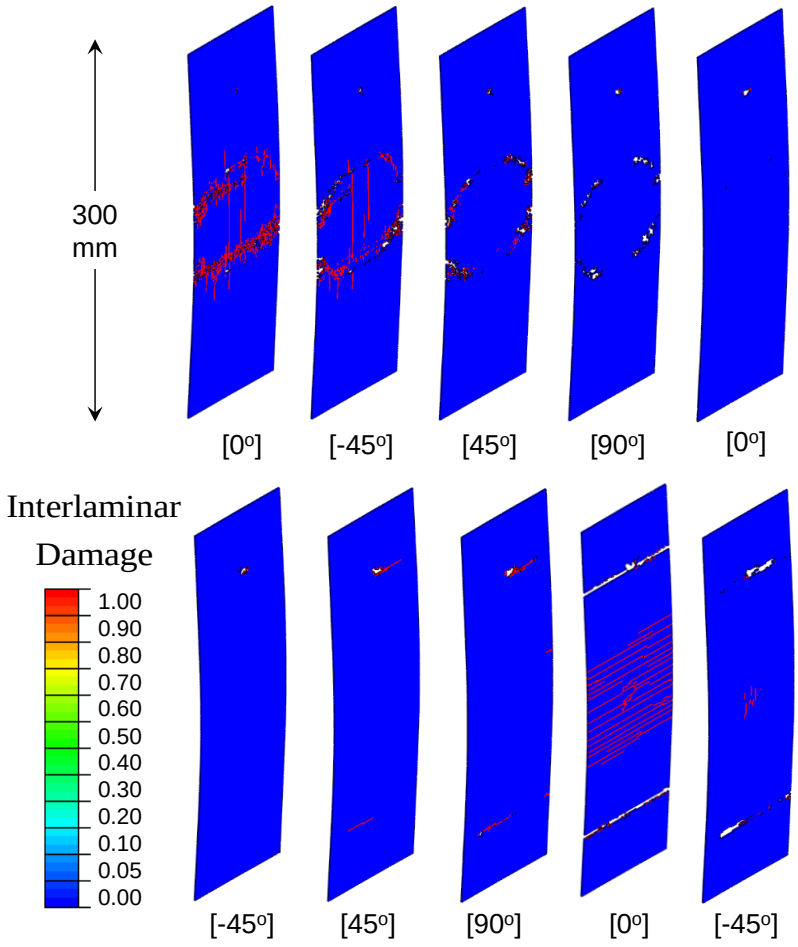


Figure 29 Distributions of in-ply (intralaminar) damage in different layers of a 6.35 mm thick quasi-isotropic carbon-fiber/epoxy composite plate subjected to $\bar{I} = 0.20$. Damage is assessed using the Hashin damage model described in section *3.2 Composite materials.*

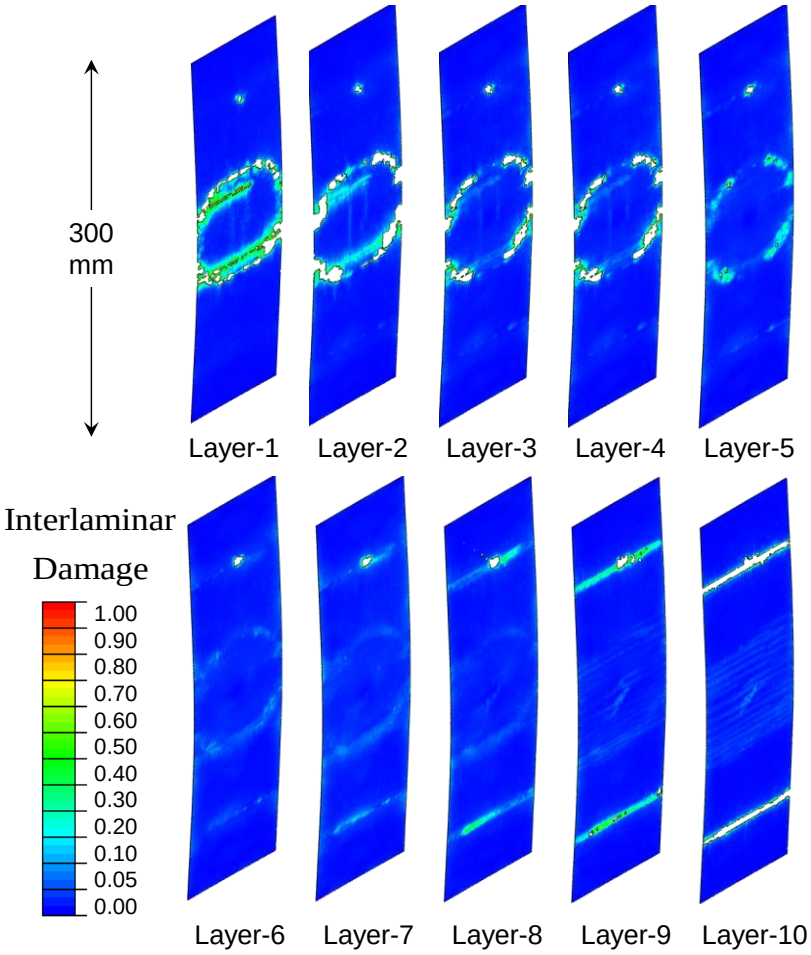


Figure 30 Distributions of inter-ply (interlaminar) damage in different layers of a 6.35 mm thick quasi-isotropic carbon-fiber/epoxy composite plate subjected to $\bar{I} = 0.20$. Damage is assessed using the cohesive finite element framework described in section *3.2 Composite materials.*

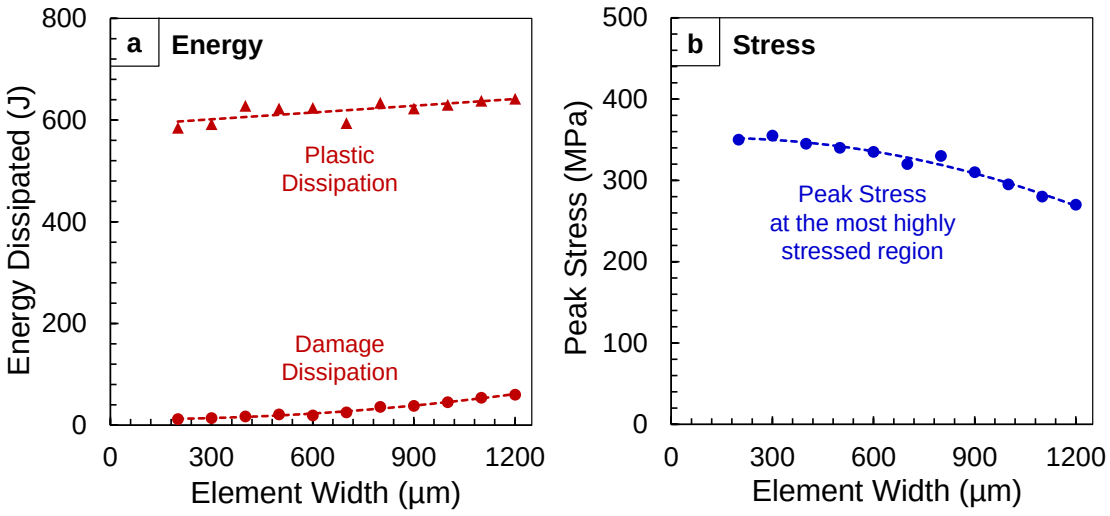


Figure 31 (a) Energy dissipated through inelastic deformation; and (b) peak stress at supports as a function of element size.

## 6.3 Results and discussion

The deformation in a dynamically loaded composite laminate can be divided into two regimes: (1) flexural wave propagation towards the supports and (2) structural deflection. The flexural wave travels towards the supports in a very short time (~50 µs). Although the resolution of the camera is sufficient to capture this phenomenon, we are more interested in structural response in the form of damage and out-of-plane deflection, which take place over a longer time span. Consequently, the temporal resolution of the camera is selected to capture the behavior over a duration of 2 milliseconds. The experiments and simulations are considered together in order to develop a detailed analysis and intimate understanding of structural failure in blast loaded monolithic composite plates. Both quantitative and qualitative approaches are used to evaluate blast response.

In order to accurately compare the performance of composite structures under blast loading, we need to consider laminates of equal areal mass subjected to similar incident impulses. Since quasi-isotropic laminates are most widely used in commercial applications, we identified the incident failure impulse for a 6.35 mm thick quasi-isotropic laminate. A number of experiments were carried out to determine that the quasi-isotropic laminate fails under an impulsive load with a peak pressure of ~196 MPa. It was found that a gas reservoir base pressure of 350 psi generated an underwater pressure wave with a peak pressure of ~196 MPa with a variation of up to 20 MPa.

As discussed previously, the loading configuration consists of a simply supported composite beam which undergoes bending deformation. The magnitude and rate of bending is determined by the incident impulse. Figure 32 shows a sequence of high-speed photographs showing the deformation in a monolithic carbon-fiber/epoxy composite laminate with a quasi-isotropic layup subjected to $\bar{I} = 0.08.$ In this case, the composite laminate undergoes bending deformation, but the impulsive load is insufficient to cause failure. Since there is no failure, the water in the shock tube does not breach the laminate and instead, escapes the chamber by flowing sideways with respect to the composite, in the direction of high-speed camera. Note the lack of any water in the space directly behind the composite as shown at $t = 400\,\mu s$. Figure 33 shows the sequence of high-speed photographs of deformation in a monolithic carbon-fiber/epoxy composite laminate with a biaxial layup subjected to $\bar{I} = 0.16.$ A comparison of deformation at two different impulse magnitudes shows that at $\bar{I} = 0.16,$ the pressurized water breaches the composite laminate and flows through the back side of the bending plate, clearly

signifying rupture and catastrophic failure. In summary, tracking the behavior of the water column in touch with the specimen using high-speed digital imaging can provide an insight into the structural response, failure modes and collapse of each composite laminate.

### 6.3.1. Deformation in carbon-fiber/epoxy laminates

Figure 33 shows a sequence of high-speed photographs and Figure 34 shows corresponding damage contours from computations of a biaxial carbon-fiber/epoxy laminate subjected to underwater impulsive loads of similar magnitudes. Initially, a flexural wave travels towards the supports in a very short time (~50 μs) and bending initiates at $t = 200\,\mu s$. Immediately after the onset of bending, the first signs of cracking appear at $t = 400\,\mu s$, as signified by a piece of the partially ruptured biaxial laminate in the encircled region in Figure 33. As the biaxial laminate continues to experience out-of-plane deflection, the water in the shock tube breaches the plate at $t = 1000\,\mu s$ and exits the backface leading to collapse and catastrophic failure.

Figure 35 shows a sequence of high-speed photographs of a quasi-isotropic carbon-fiber/epoxy laminate subjected to $\bar{I} = 0.16$. Figure 36 shows the in-ply damage contours, and Figure 37 shows the inter-ply damage contours for a quasi-isotropic carbon-fiber/epoxy laminate subjected to $\bar{I} = 0.20$. After the onset of bending deformation at $t = 200\,\mu s$, the quasi-isotropic plate undergoes delamination near the midplane at $t = 400\,\mu s$. The interlaminar cracks propagate towards the supports and cause further delamination near the edge at $t = 600\,\mu s$. Since a simply-supported loading configuration causes maximum stresses near the midplane, a “hinge” or localized

deformation develops in the laminate due to a combination of compressive and tensile stresses through the thickness. This observation is supported by the computational results shown in Figure 36 and Figure 37. It should be noted that although there is widespread delamination and in-ply damage, water flowing out of the shock tube does not breach the plate, instead flowing out of the sides as observed in Figure 32. Results indicate that the computational model accurately captures

As discussed previously, the quasi-isotropic layup exhibits large scale delamination but does not experience failure. Results indicate that delamination is relatively uniform throughout the structure, as seen in Figure 37. In order to determine whether delamination can be localized to smaller region by modifying the laminate layup, laminates are constructed such that all laminas have fibers oriented parallel to the supports. Figure 38 shows a sequence of high-speed photographs and Figure 39 shows corresponding damage contours from computations of a carbon-fiber/epoxy laminate with fibers oriented in a direction parallel to the supports subjected to underwater impulsive loads of similar magnitudes. After the onset of bending delamination at $t = 200\,\mu s$, the plate experiences delamination at $t = 400\,\mu s$. After delamination initiation, the delaminated sections of the laminate experience severe bending stresses leading to in-ply rupture at $t = 1000\,\mu s$, followed by perforation of the plate near the midplane and catastrophic failure at $t = 1200\,\mu s$. The computational framework accounts for the effects of fiber orientation and captures the flow of water through the structure post-failure. Since the fibers are oriented parallel to the supports, a relatively smaller fraction of the incident impulse is transmitted to the supports leading significantly higher deflection and localized in-ply damage and fracture in close proximity to the impulsive

wave loading area. Delamination is observed over a smaller area than the quasi-isotropic laminate, primarily near the loading region.

Figure 40 shows a sequence of high-speed photographs and Figure 41 shows corresponding damage contours from the finite element simulations of a carbon-fiber/epoxy laminate with fibers oriented in a direction perpendicular to the supports subjected to underwater impulsive loads of similar magnitudes. In this case, the plate is extremely stiff in the vertical direction and resists bending much more than the other layups. However, the lack of bending causes high shear stresses in the laminate. Since the laminate lacks stability in the horizontal direction, the high transverse shear stresses cause "splitting" in the composite structure leading to failure at $t = 400\,\mu s$. A comparison of the finite element simulations of the quasi-isotropic laminate with respect to the uniaxially oriented laminates reveals that the quasi-isotropic layup provides superior blat resistance by minimizing shear stresses in any particular region and distributing the incident impulsive load in a uniformly to avoid localized rupture.

Carbon-fiber/epoxy laminates exhibit exceptionally high stiffness and bending resistance due to the high elastic modulus of carbon fibers. Investigation of the underwater blast resistance of such laminates indicates that the composite plates are quite stable and blast resistant prior to damage initiation. However, after damage initiates, the laminates experience a dramatic loss in stiffness and undergo catastrophic failure and collapse. Additionally, carbon-fiber/epoxy laminates significantly more expensive in comparison to glass-fiber/epoxy laminates. With respect to the materials studied here and reported in this analysis, the carbon-fiber/epoxy laminates have a unit cost that is more than twice as much as that of glass-fiber/epoxy laminates. Since marine structures often

require large quantities of composite materials, cost considerations can play a major role in materials selection. To evaluate the differences in structural response of carbon-fiber and glass-fiber/epoxy laminates, a set of experiments and simulations is carried consisting of glass-fiber/epoxy laminates with different fiber layups subjected to incident impulses similar to those for the carbon-fiber/epoxy laminates. For brevity, high-speed photographs of all layups and computational results for only the quasi-isotropic layup are reported. The high-speed photographs are followed by a quantitative analysis of the blast response of both carbon-fiber and glass-fiber/epoxy laminates.

### 6.3.2. Deformation in glass-fiber/epoxy laminates

Figure 42 shows a sequence of high-speed photographs of a biaxially oriented glass-fiber/epoxy laminate subjected to $\bar{I} = 0.16.$ After the onset of bending at $t = 200\ \mu s,$ an in-ply crack initiates at the backface and propagates towards the frontface at $t = 600\ \mu s.$ This propagating crack deflects into two interlaminar cracks at $t = 800\ \mu s.$ The composite laminate loses stiffness and undergoes catastrophic failure at $t = 1200\ \mu s.$

Figure 43 shows a sequence of high-speed photographs of a quasi-isotropic glass-fiber/epoxy laminate subjected to $\bar{I} = 0.16.$ Figure 44 shows the in-ply damage contours, and Figure 45 shows the inter-ply damage contours for a quasi-isotropic glass-fiber/epoxy laminate subjected to $\bar{I} = 0.20.$ The deformation in the composite plate is initially arrested as indicated by the smaller jump in displacement between $t = 400\ \mu s$ and $t = 600\ \mu s$ in comparison to the change in displacement between $t = 200\ \mu s$ and $t = 400\ \mu s.$ However, at $t = 800\ \mu s,$ the deforming laminate experiences cracking at the backface and a 45° crack travels from the backface to the frontface. Comparing the

computational results for the carbon-fiber laminate and glass-fiber laminate shows that the glass-fiber composite plate experiences significantly greater out-of-plane deflection for similar applied impulse. Since the tensile stresses created in a bending plate are strongly dependent on out-of-plane deflection, the glass-fiber laminate primarily undergoes damage and cracking at the midsection. Additionally, interlaminar damage, fracture, and separation are restricted to the region close to the center of the plate.

Figure 46 and shows a sequence of high-speed photographs of impulsively loaded glass-fiber/epoxy laminates with fibers oriented in a direction parallel to the supports. Initially, the composite plate undergoes bending which results in the formation of "hinges" in the plate due to localized deformation, as shown in the figure at $t = 800\,\mu s$. The localized deformation results in cracking, followed by complete collapse of the plate. Figure 46 and shows a sequence of high-speed photographs of impulsively loaded glass-fiber/epoxy laminates with fibers oriented in a direction perpendicular to the supports. The laminate undergoes bending, followed by crack initiation at the backface and propagation. The failure in the plate is primarily in the form of splitting due to a lack of stability in the transverse direction.

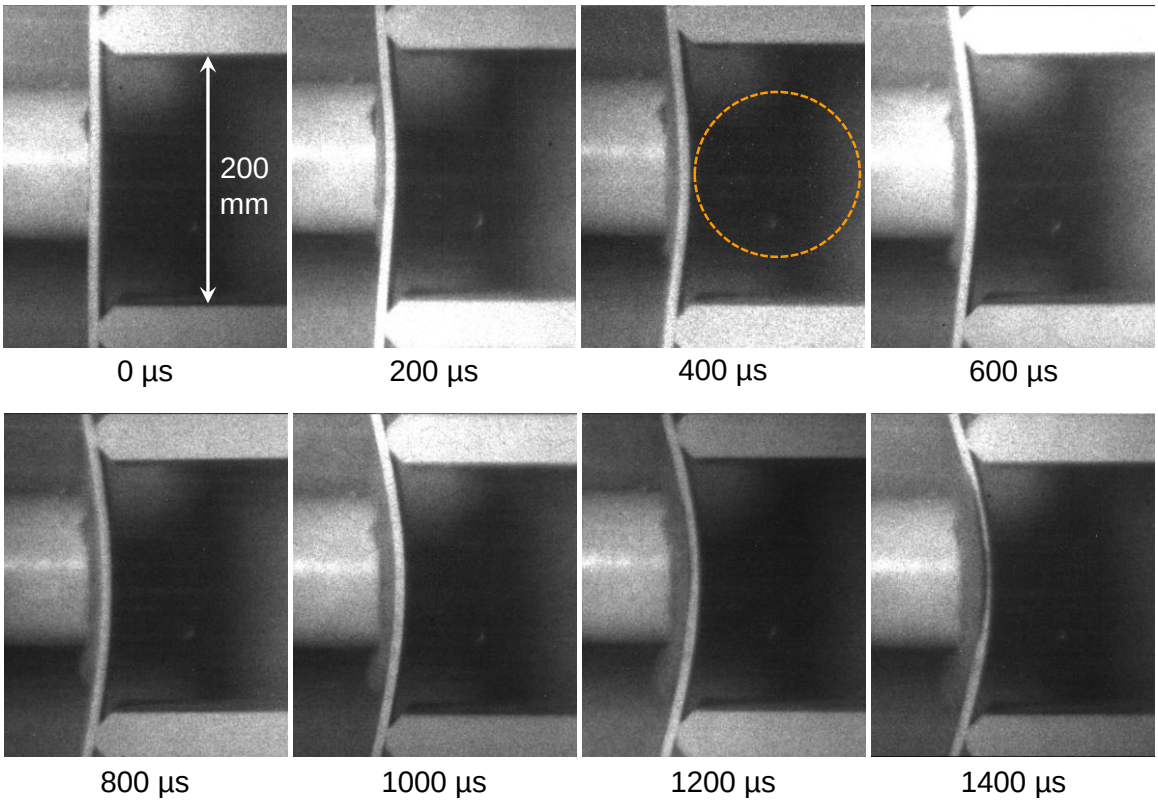


Figure 32 Sequence of high-speed photographs showing the deformation in a monolithic carbon-fiber/epoxy composite plate with a quasi-isotropic layup subjected to $\bar{I} = 0.08$.

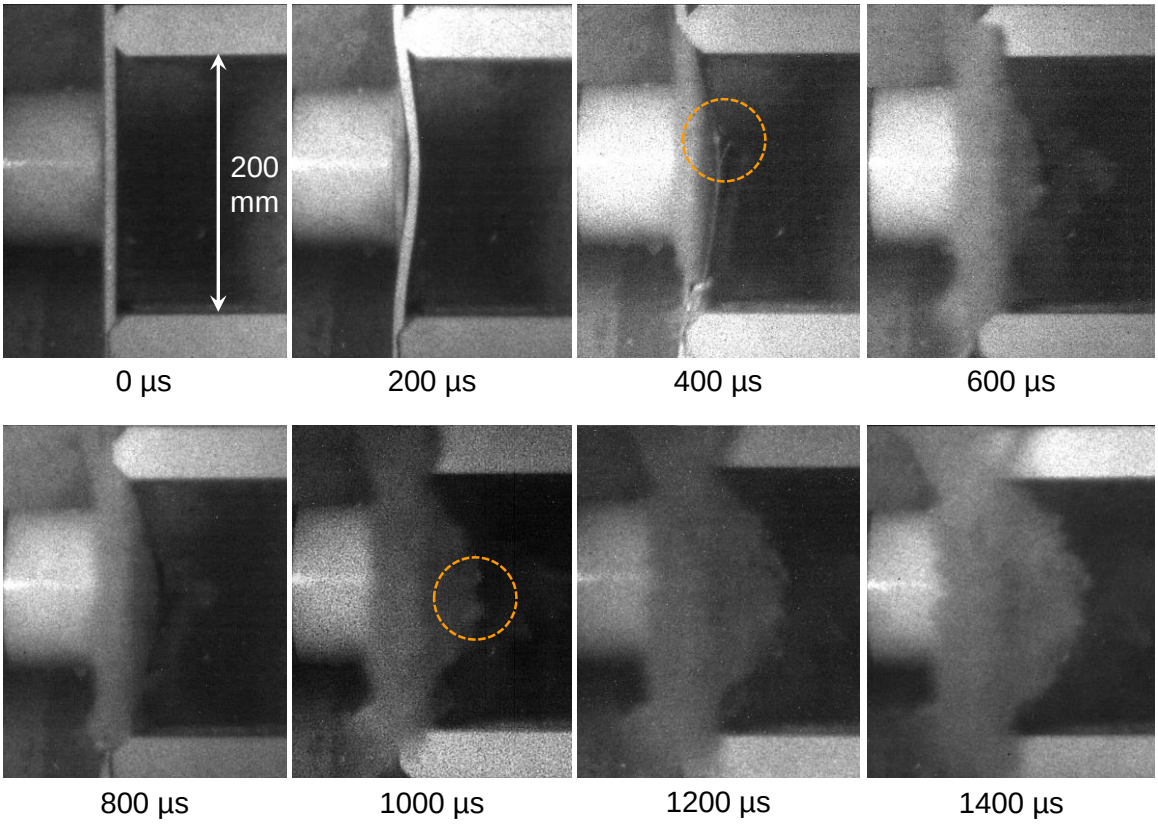


Figure 33 Sequence of high-speed photographs showing the deformation in a monolithic carbon-fiber/epoxy composite laminate with a biaxial layup subjected to $\bar{I} = 0.16$.

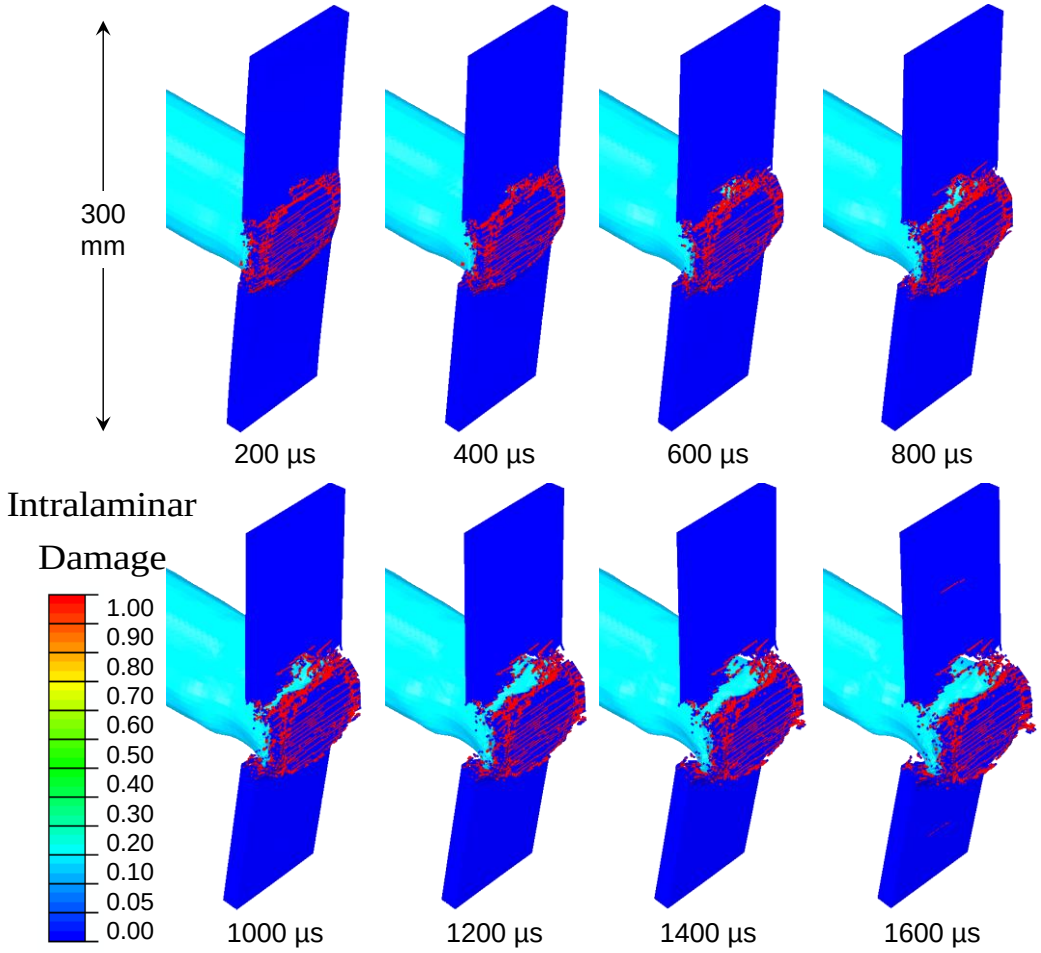


Figure 34 Distributions of damage in a biaxial carbon-fiber/epoxy composite laminate subjected to $\bar{I} = 0.20$.

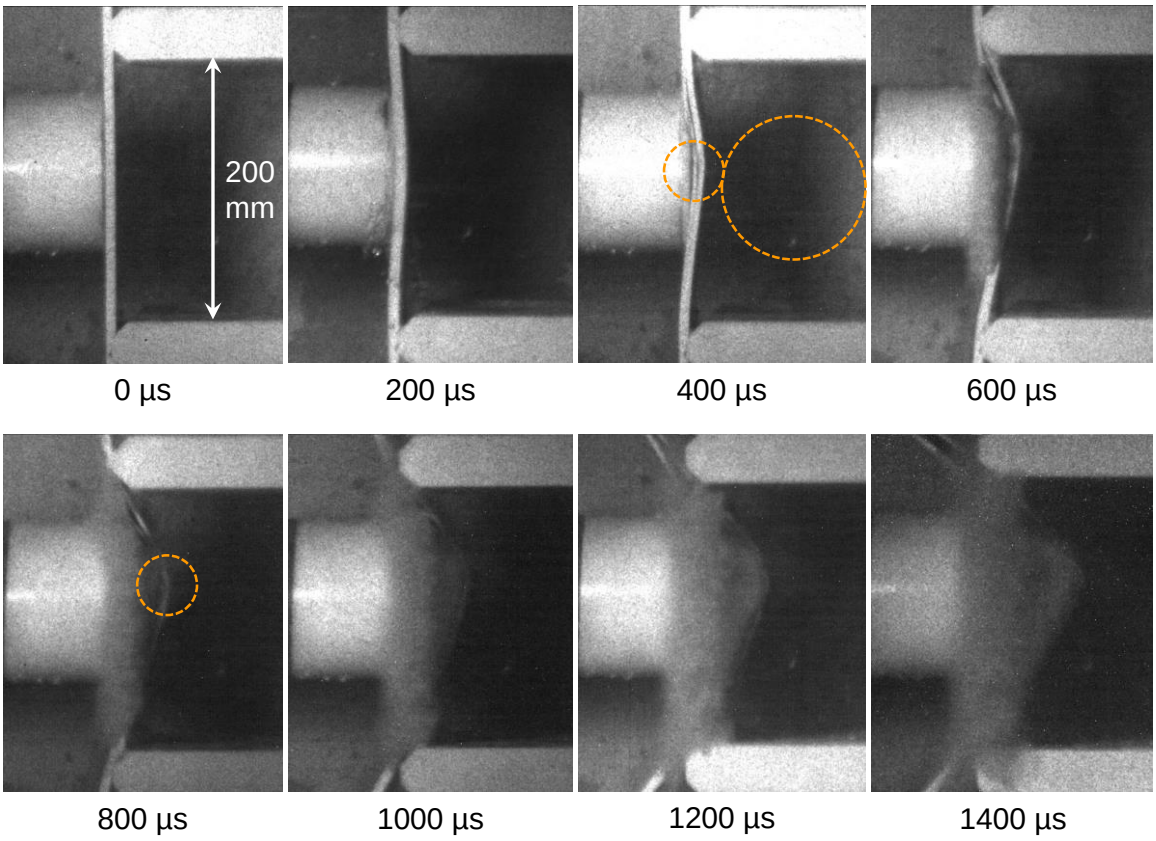


Figure 35 Sequence of high-speed photographs showing the deformation in a monolithic carbon-fiber/epoxy composite plate with a quasi-isotropic layup subjected to $\bar{I} = 0.16$.

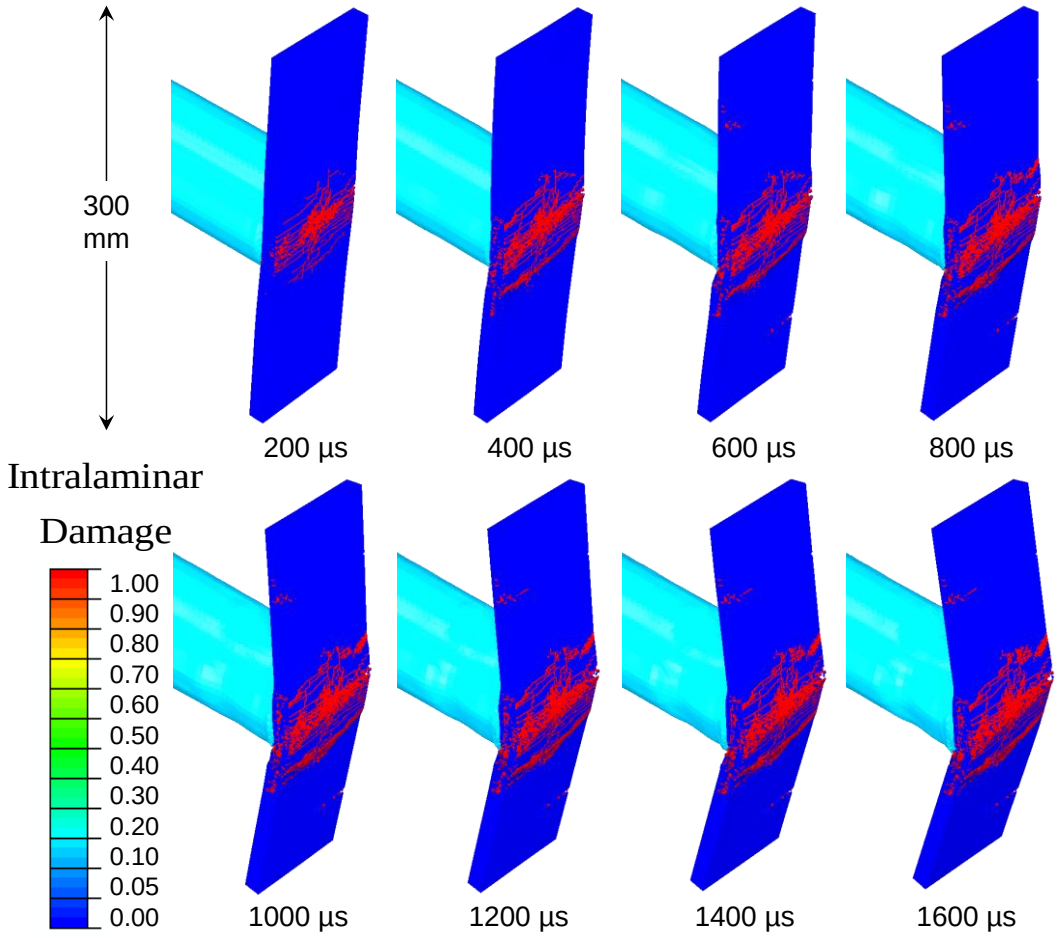


Figure 36 Distributions of in-ply damage in quasi-isotropic carbon-fiber/epoxy composite laminate subjected to $\bar{I} = 0.20$.

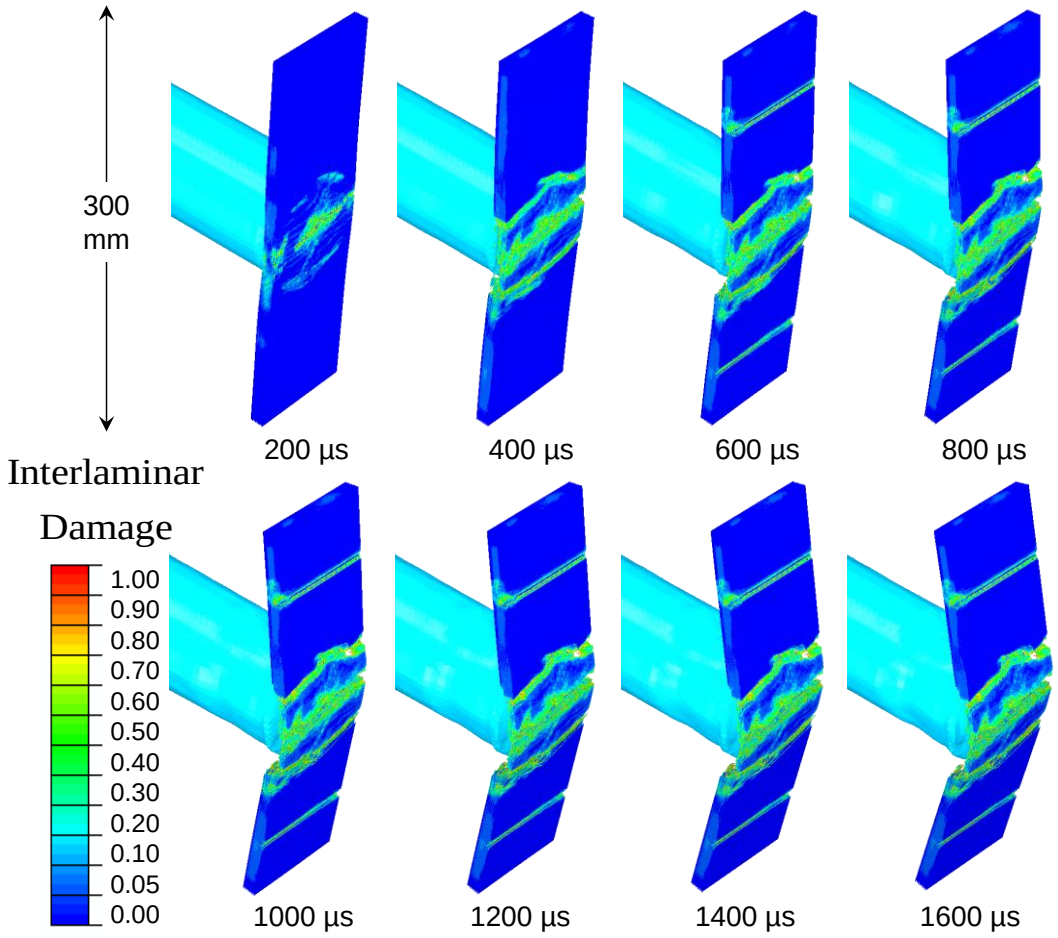


Figure 37 Distributions of inter-ply damage in a quasi-isotropic carbon-fiber/epoxy composite laminate subjected to $\bar{I} = 0.20$.

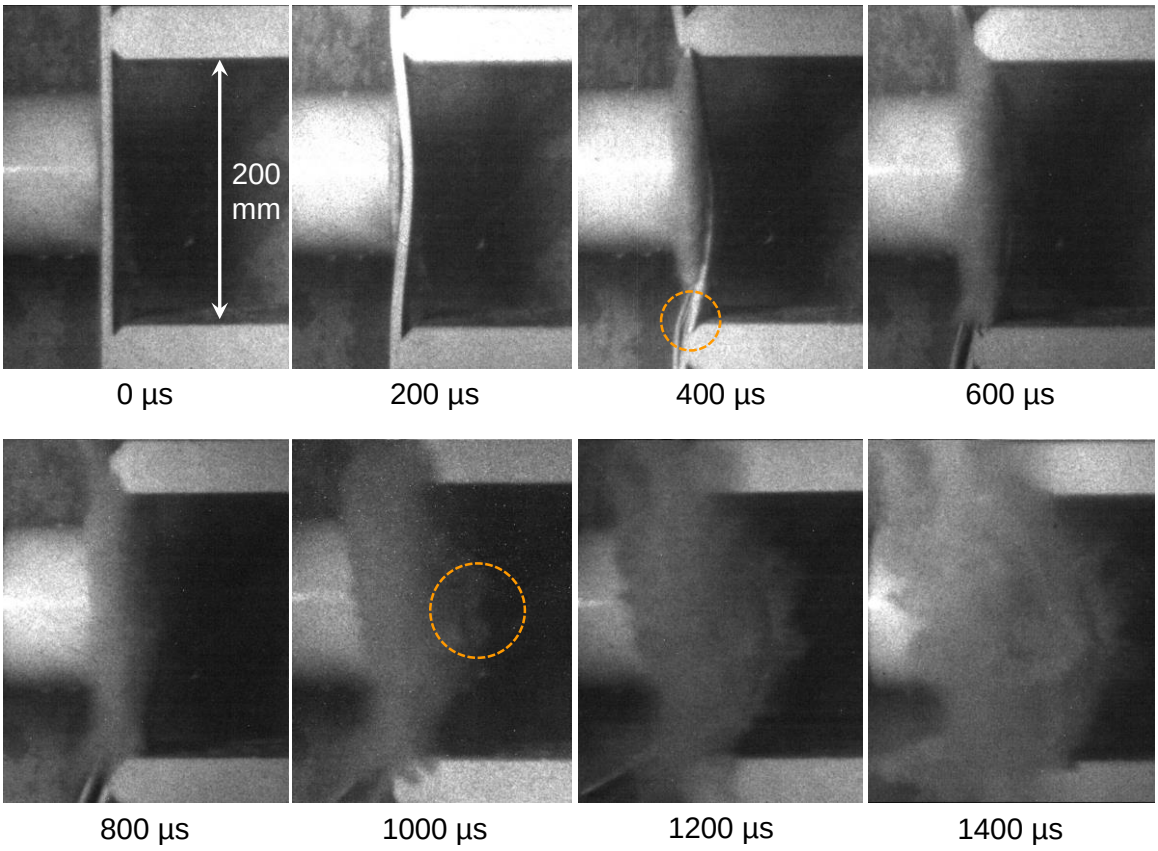


Figure 38 Sequence of high-speed photographs showing the deformation in a monolithic carbon-fiber/epoxy composite laminate with fibers oriented parallel to the supports subjected to $\bar{I} = 0.16$.

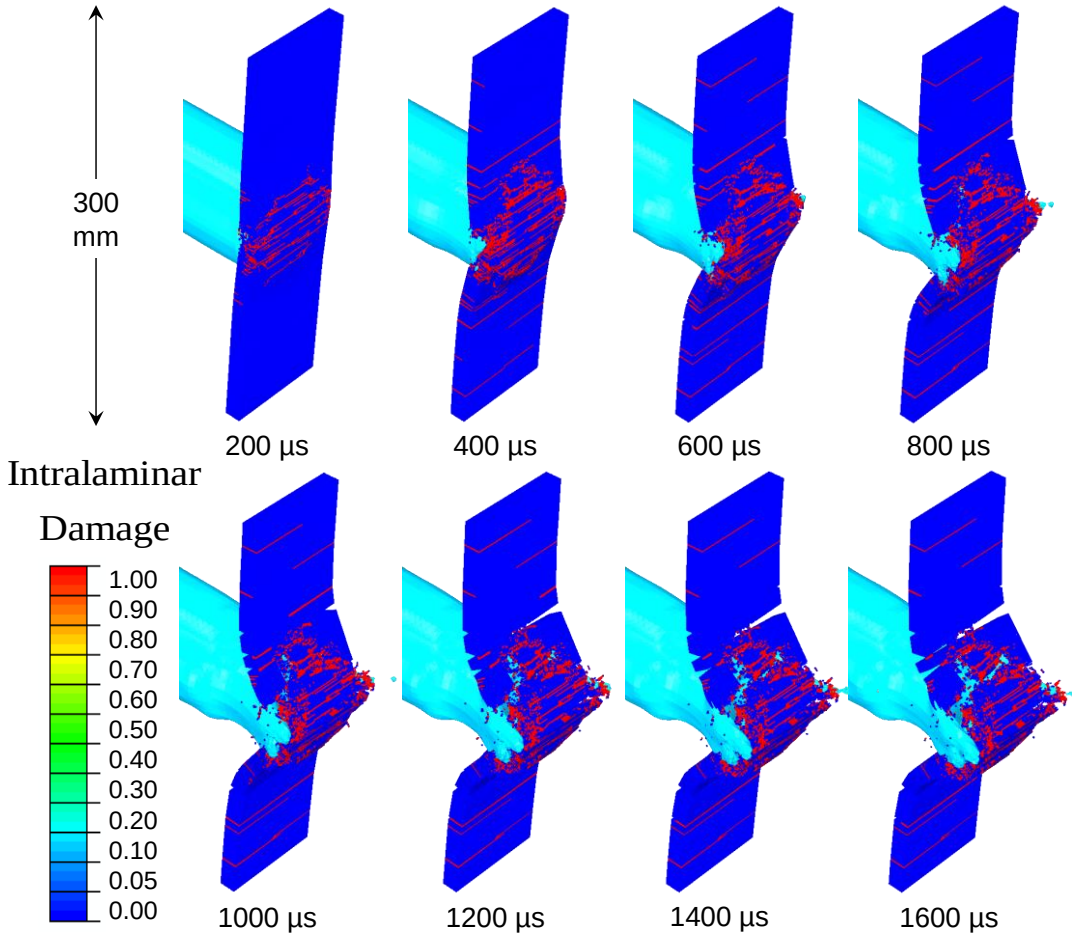


Figure 39 Distributions of in-ply damage in a carbon-fiber/epoxy composite laminate with fibers oriented parallel to the supports subjected to $\bar{I} = 0.20$.

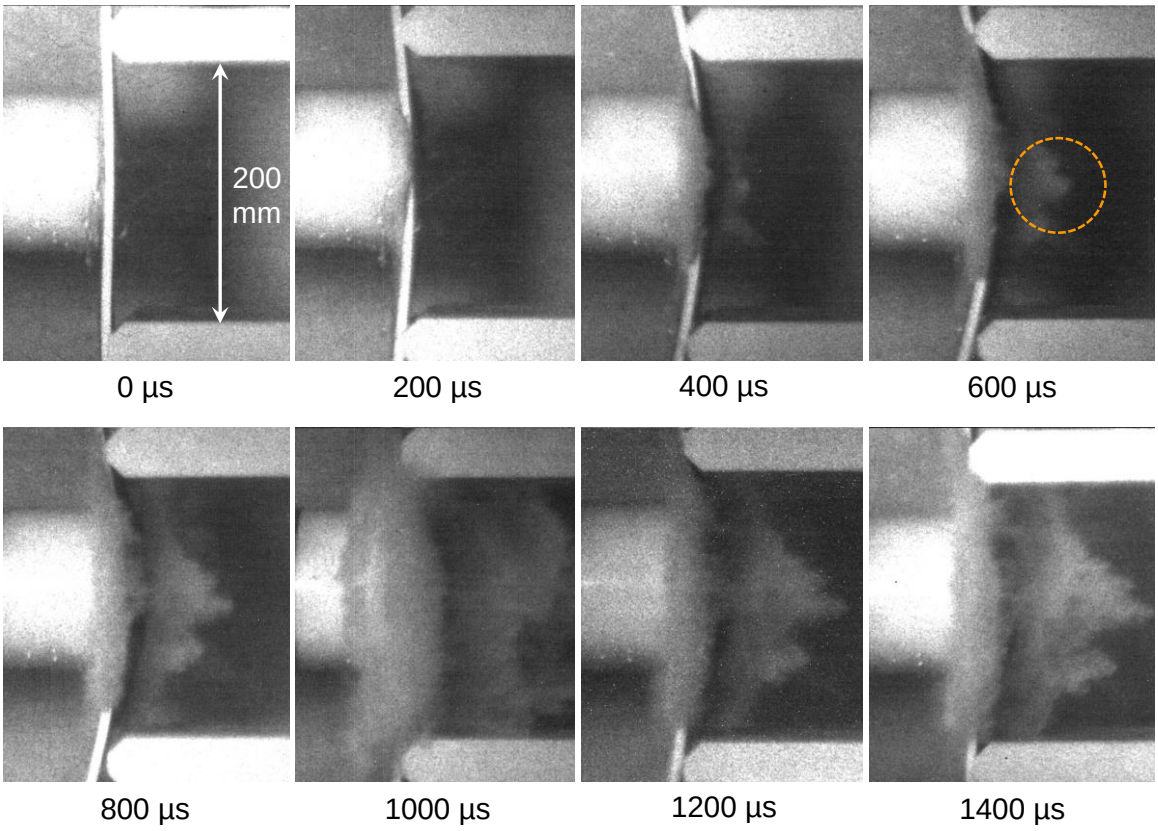


Figure 40 Sequence of high-speed photographs showing the deformation in a monolithic carbon-fiber/epoxy composite laminate with fibers oriented perpendicular to the supports subjected to $\bar{I} = 0.16$.

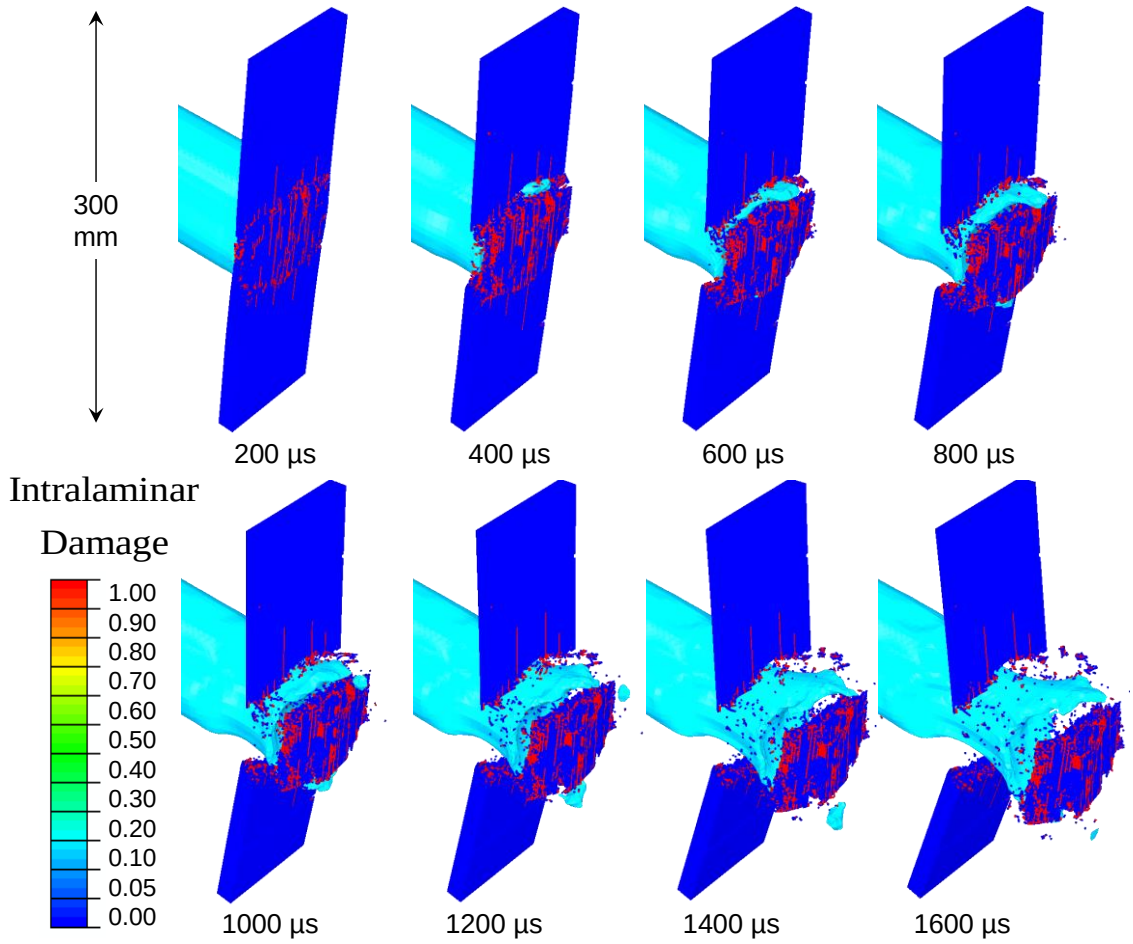


Figure 41 Distributions of in-ply damage in a carbon-fiber/epoxy composite laminate with fibers oriented perpendicular to the supports subjected to $\bar{I} = 0.20$.

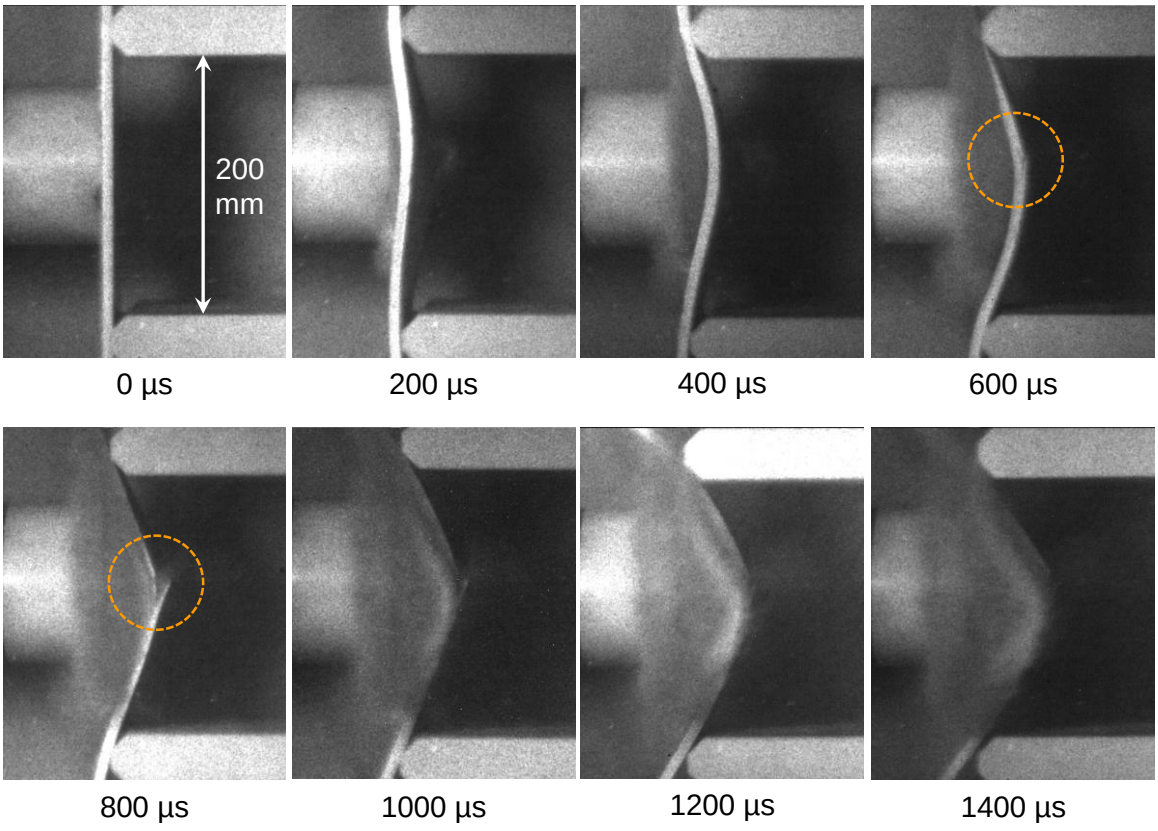


Figure 42 Sequence of high-speed photographs showing the deformation in a monolithic glass-fiber/epoxy composite laminate with a biaxial layup subjected to $\bar{I} = 0.16$.

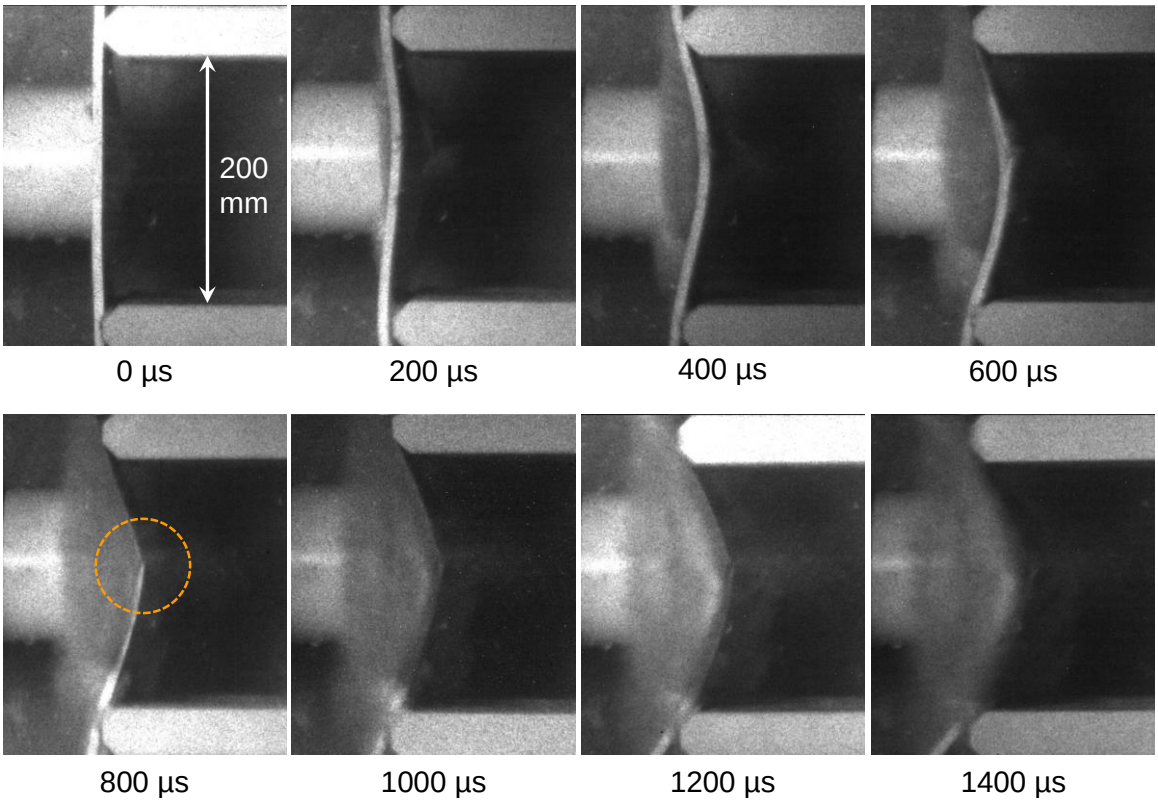


Figure 43 Sequence of high-speed photographs showing the deformation in a monolithic glass-fiber/epoxy composite laminate with a quasi-isotropic layup subjected to $\bar{I} = 0.16$.

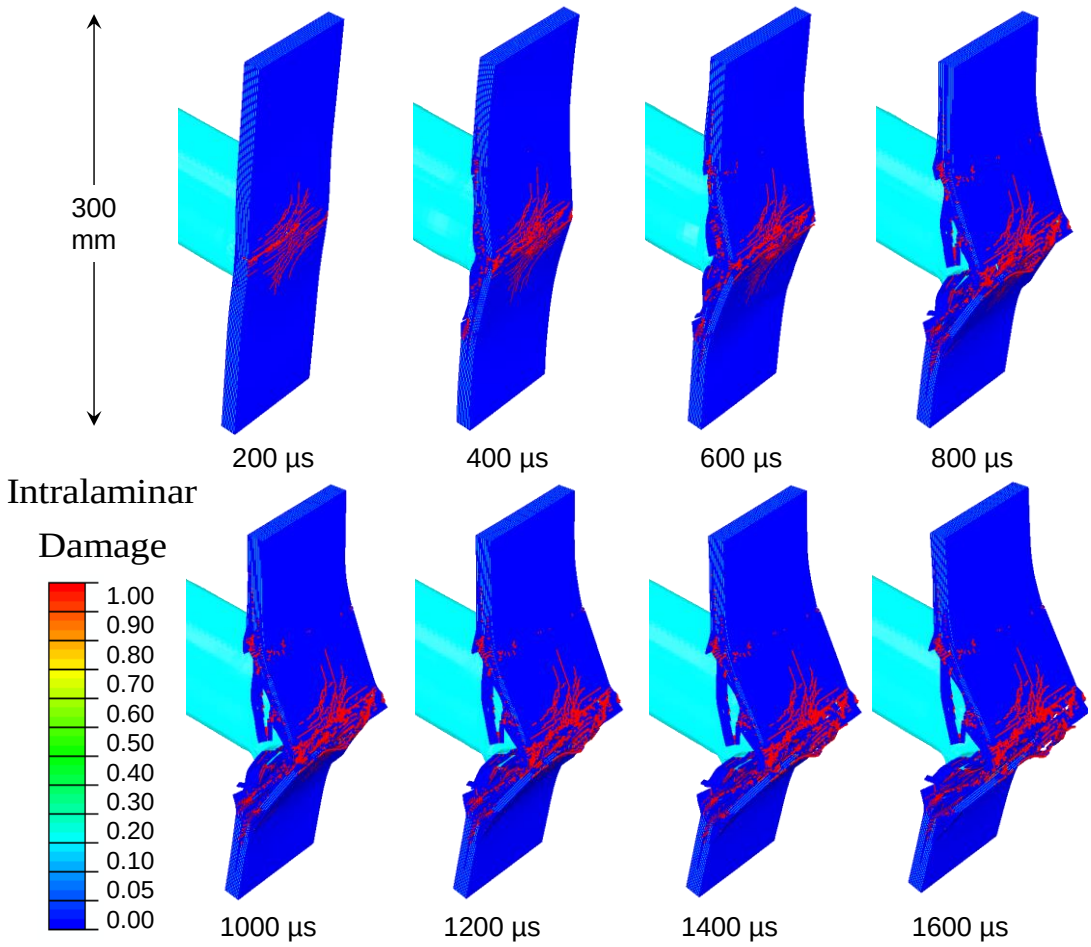


Figure 44 Distributions of in-ply damage in a quasi-isotropic glass-fiber/epoxy composite laminate subjected to $\bar{I} = 0.20$.

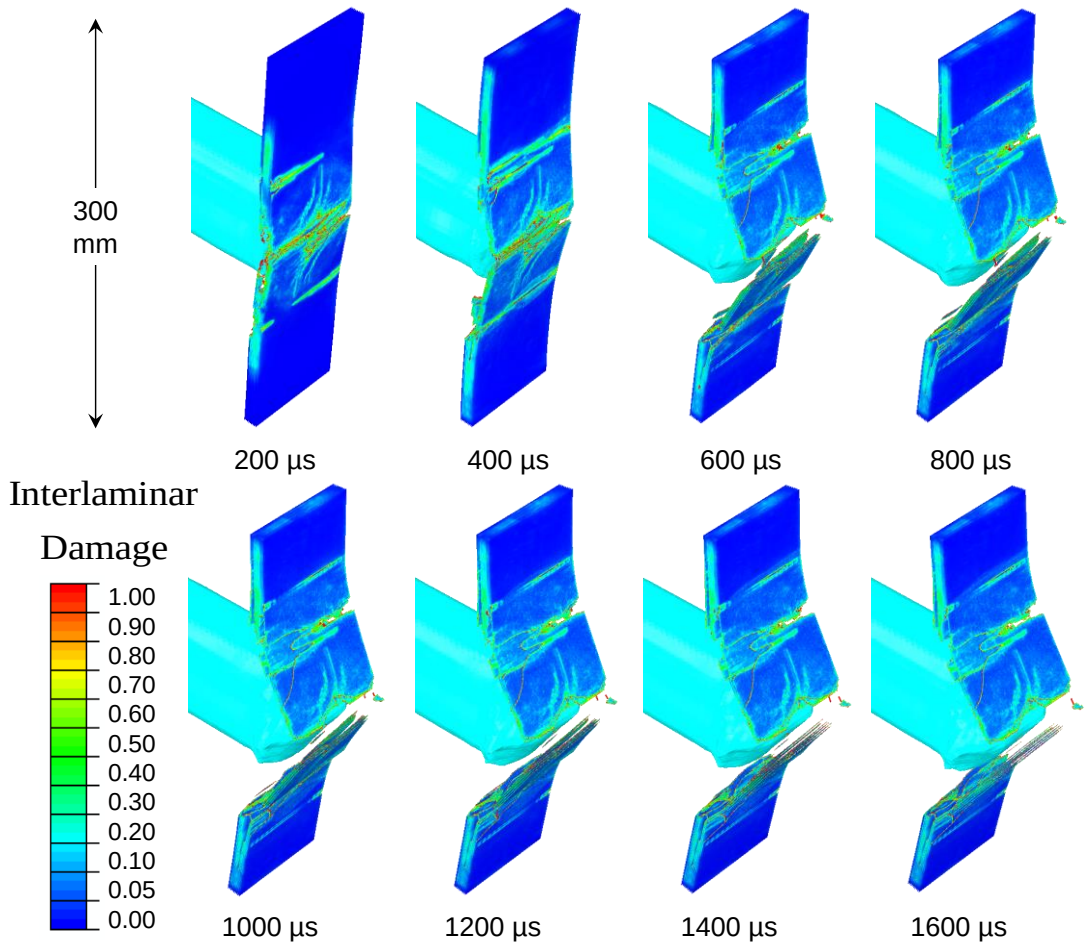


Figure 45 Distributions of inter-ply damage in a quasi-isotropic glass-fiber/epoxy composite laminate subjected to $\bar{I} = 0.20$.

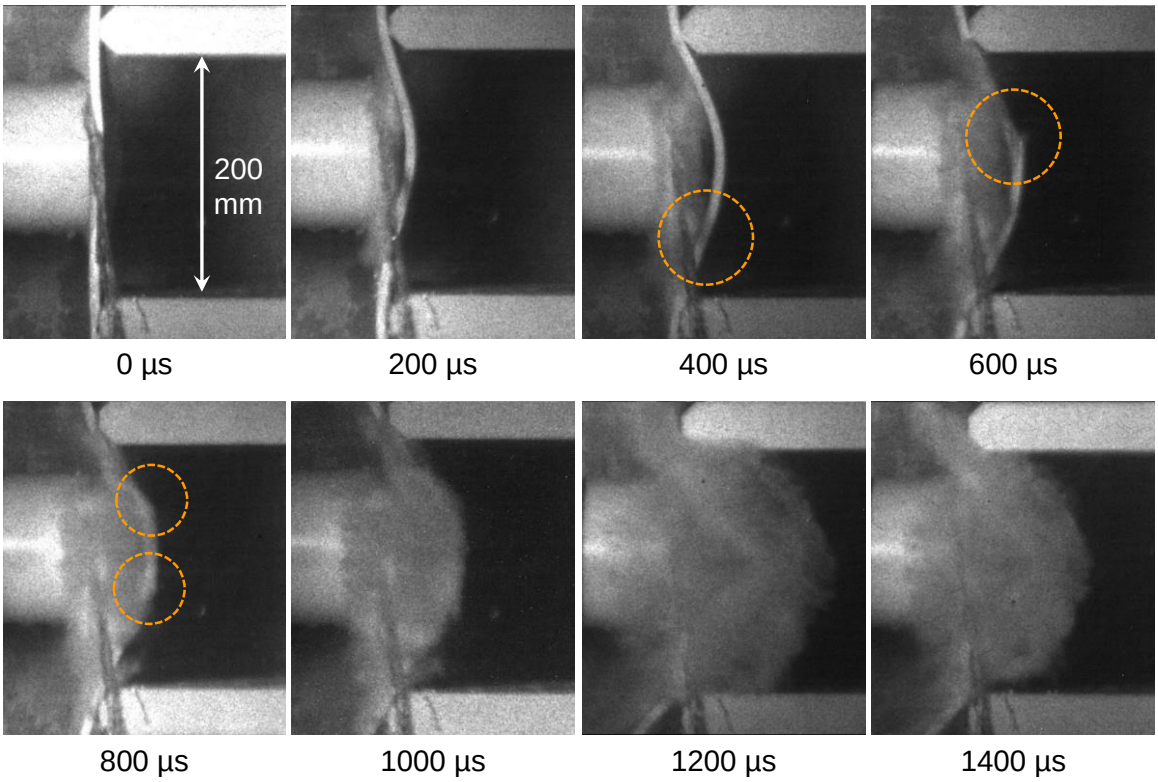


Figure 46 Sequence of high-speed photographs showing the deformation in a monolithic glass-fiber/epoxy composite laminate with fibers oriented parallel to the supports subjected to $\bar{I} = 0.16$.

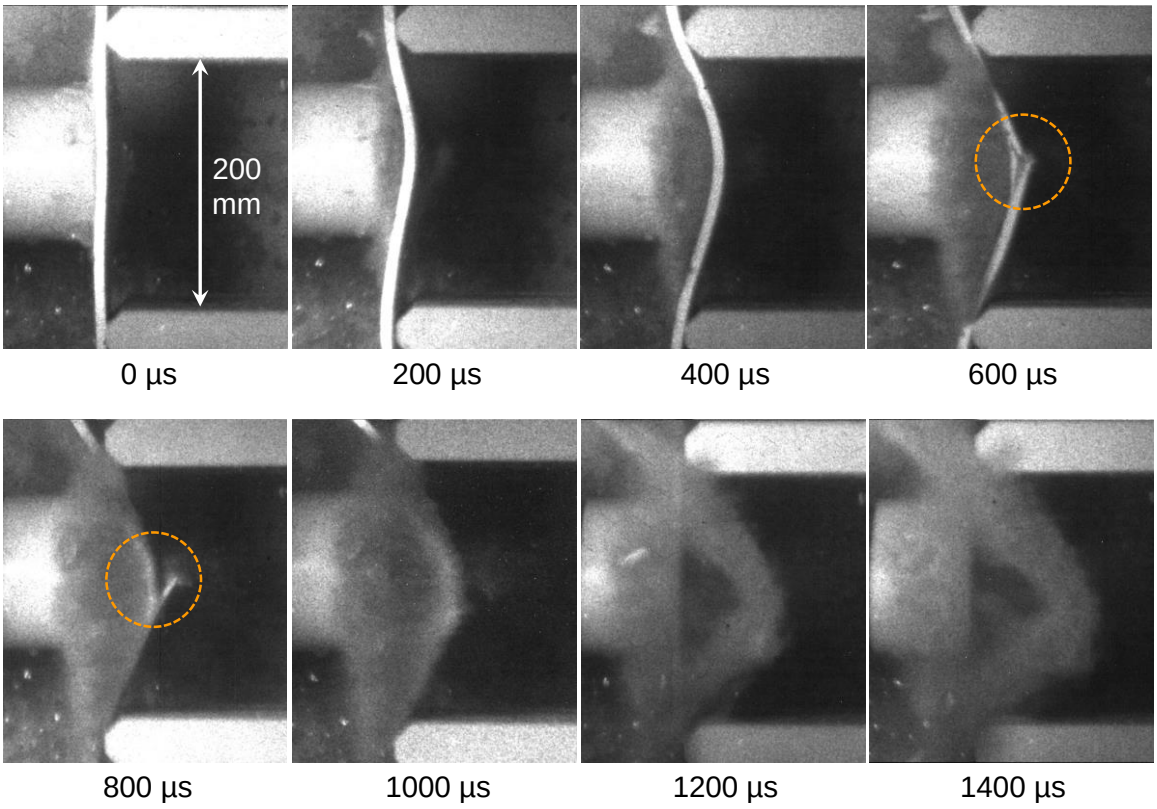


Figure 47 Sequence of high-speed photographs showing the deformation in a monolithic glass-fiber/epoxy composite laminate with fibers oriented perpendicular to the supports subjected to $\bar{I} = 0.16$.

### 6.3.3. Quantification of structural response

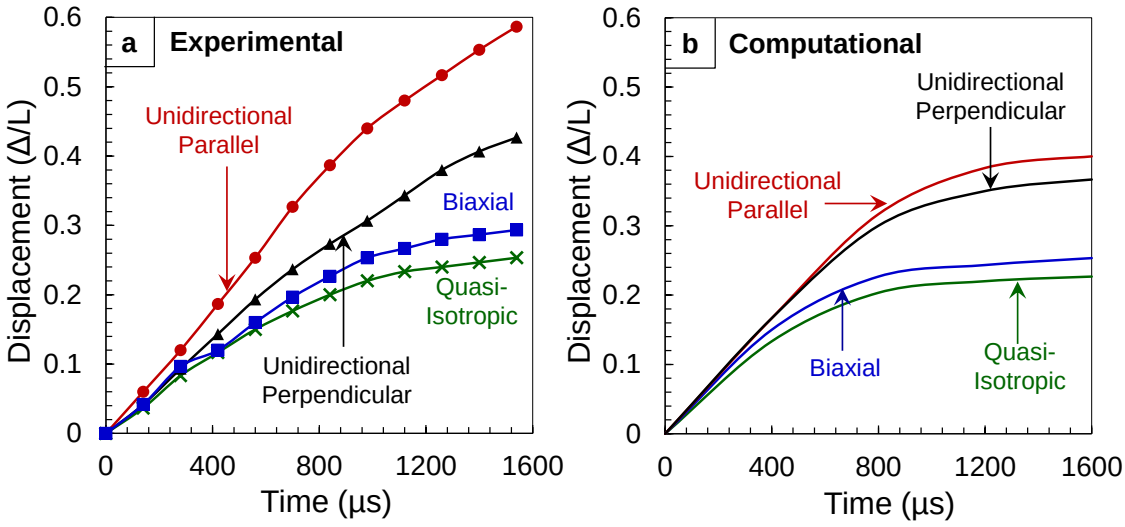


Figure 48 Experimentally measured and numerically calculated midpoint displacements as functions of time for carbon-fiber/epoxy laminates to similar incident impulsive loads.

Figure 48 shows the experimental and computational out-of-plane deflection histories for carbon-fiber/epoxy laminates with different layups. The quasi-isotropic laminate experiences the least deflection, followed by the biaxial laminate, laminate with fibers oriented perpendicular to supports, and parallel to supports, in that order. Initially, the rate of deformation for all plates is similar but as the deformation progresses. As deformation progresses, the quasi-isotropic and biaxial laminates experience a reduction in the rate of bending at $t = 800\,\mu s$. Laminates with fibers oriented parallel to the supports exhibit the least blast resistance, due to their inability to transmit the incident impulse to the supports and mitigate the effects of incident impulsive loads. The laminate with fibers oriented parallel to the supports undergoes the greatest deflection, with a normalized deflection $(\Delta/L)$ of 0.6. The laminate with fibers oriented perpendicular to supports undergoes 60%, the biaxial plate undergoes 50%, and the quasi-isotropic plate

experiences 40% of the deflection experienced by the laminate with fibers oriented parallel to the supports. The computational model accounts for the essential aspects of deformation but the continuum damage framework underestimates the stiffness of the plate resulting in artificial softening which leads to a lower rate of deformation post-failure in comparison to the experiments. However, the model accurately captures the relative blast resistance of each composite laminate.

The out-of-plane deflection histories of glass-fiber/epoxy laminates with different fiber layups are shown in Figure 49. Glass-fibers are inherently more compliant, possessing approximately 30% of the stiffness and strength of carbon-fibers despite being 20% heavier by weight. This is reflected in the deflection of the glass-fiber/epoxy plates which show a clear softening behavior under water-based impulsive loading. The quasi-isotropic laminate experiences the least deflection, with a normalized deflection $\left(\Delta/L\right)$ of 0.35 with the biaxial plate experiencing 10% more deflection, the plate with fibers oriented parallel to supports experiencing 20% more deflection, and fiber oriented perpendicular to supports experiencing 40% more deflection. The finite element model captures the softening effect but slightly underestimates peak deflection due to artificial softening resulting from the continuum damage model.

Minimizing the impulse transmitted to the internal components of marine vessels is of critical importance. For the simply-supported loading configuration discussed here, the target structure transmits an impulse to the supports. The rate of impulse transmission and the magnitude of the transmitted impulse can provide valuable insight into the blast resistance and performance of composite structures. Figure 50(a) shows the reaction forces measured at the supports in finite element simulations while Figure 50(b) shows

the corresponding impulses calculated using $I = \int F \cdot dt$. There is an initial increase in the transmitted force when the incident impulse strikes the specimen and the resulting flexural wave reaches the supports. At this time, there is a small separation between the backface and the supports due to the initiation of bending deformation. The deforming plate strikes the supports a second time and the separates from the supports as the bending deformation eventually causes failure.

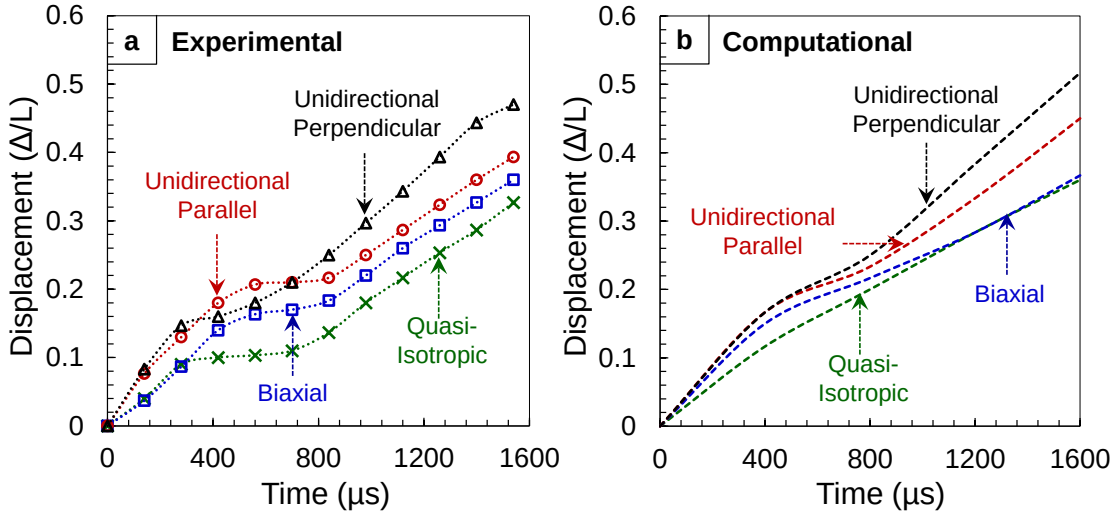


Figure 49 Experimentally measured and numerically calculated midpoint displacements as functions of time for glass-fiber/epoxy laminates to similar incident impulsive loads.

The Hashin damage model used in this computational approach consists of damage modes that encompass tensile matrix cracking, compressive matrix cracking, tensile fiber cracking and compressive matrix cracking. Since cracking initiates due to high tensile stresses caused by bending, the intralaminar damage considered for the purposes of damage quantification is the tensile damage occurring in the matrix and fibers. A cohesive zone model is used to evaluate interlaminar cracking. Evaluating the

rate and extent of damage can provide a deeper insight into the performance of each composite plate.

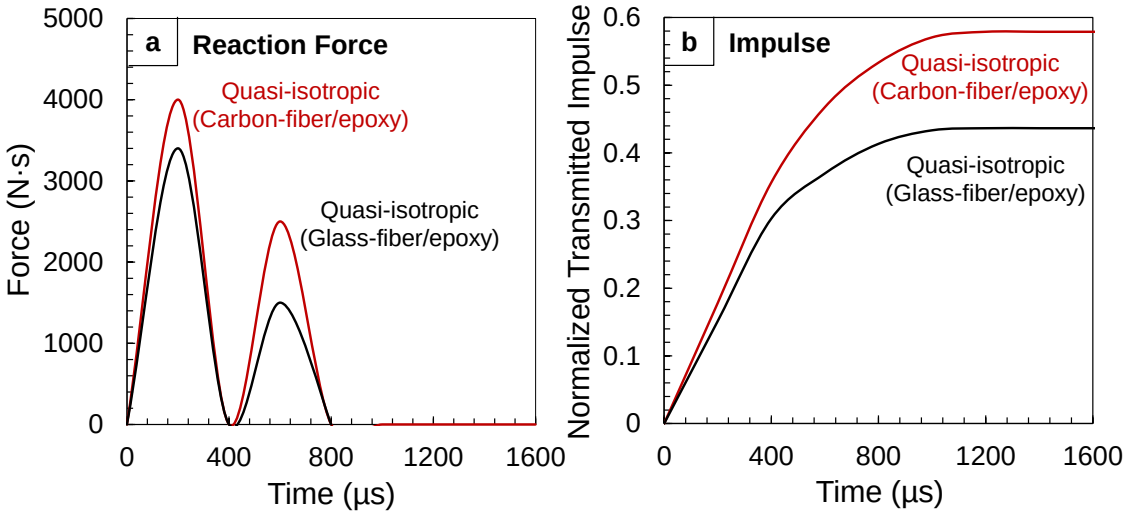


Figure 50 Numerically calculated reaction forces and transmitted impulses as functions of time for carbon-fiber/epoxy and glass-fiber/epoxy laminates subjected to similar incident impulsive loads.

In order to evaluate the total damage in impulsively loaded composite structures, we use a cumulative damage term called "accumulated damage" defined by

$$\bar{N} = \frac{\text{Number of Damaged Elements}}{\text{Total Number of Elements}}. \tag{60}$$

Figure 51(a) shows the ratio of the number of elements undergoing intralaminar damage and the total number of elements described by the Hashin damage model as a function of time for quasi-isotropic carbon-fiber/epoxy and glass-fiber/epoxy laminates subjected to $\bar{I} = 0.20$. The glass-fiber/epoxy specimen experiences damage in ~40% of the laminate while the carbon-fiber/epoxy specimen experiences damage in ~10% of the laminate. Figure 51(b) shows the ratio of the number of elements undergoing interlaminar damage and the total number of cohesive elements as a function of time for quasi-

isotropic carbon-fiber/epoxy and glass-fiber/epoxy laminates subjected to $\bar{I} = 0.20$. The glass-fiber/epoxy specimen experiences damage in ~60% of the interlaminar "resin-rich" regions while the carbon-fiber/epoxy specimen experiences damage in ~10% of the interlaminar regions.

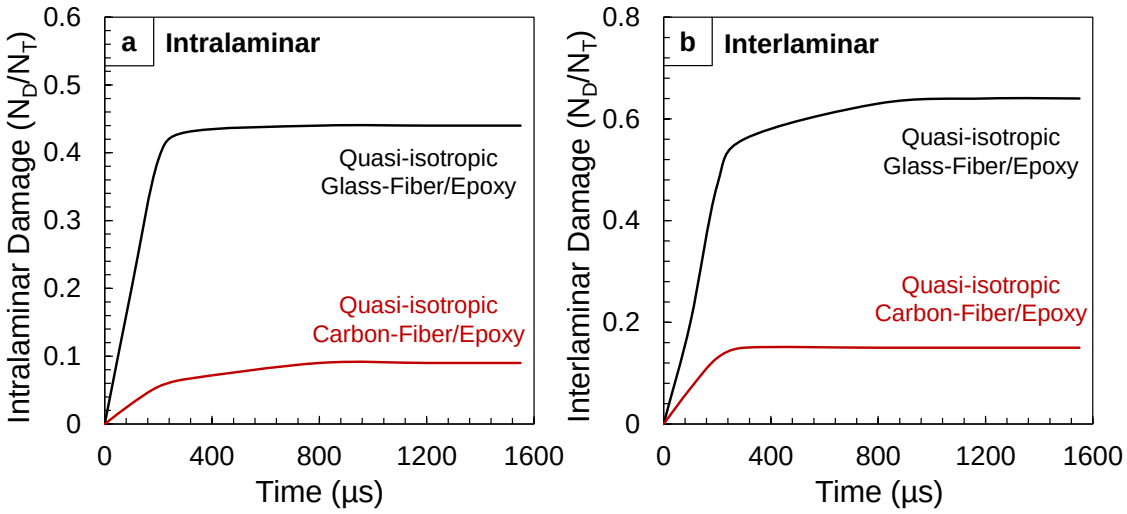


Figure 51 Numerically calculated damage histories for carbon-fiber/epoxy and glass-fiber/epoxy laminates subjected to similar incident impulsive loads.

## 6.4 The effects of load obliquity on structural response

Marine vessels consist of geometrical nonlinearities like inclined and curved surfaces. Such sections of the vessel interact rather differently with high intensity impulsive loads than planar sections. The deformation and damage due such geometric nonlinearities needs to be considered for effective ship structure design. However, this aspect of underwater blast response of marine structures has not been analyzed. To evaluate the effects of load obliquity on the dynamic response of composite laminates, the loading angle is varied from 0° to 10° with increments of 2° and each loading

configuration is subjected to similar incident loads. Figure 52 depicts a loading configuration for a quasi-isotropic laminate subjected to an oblique impulse.

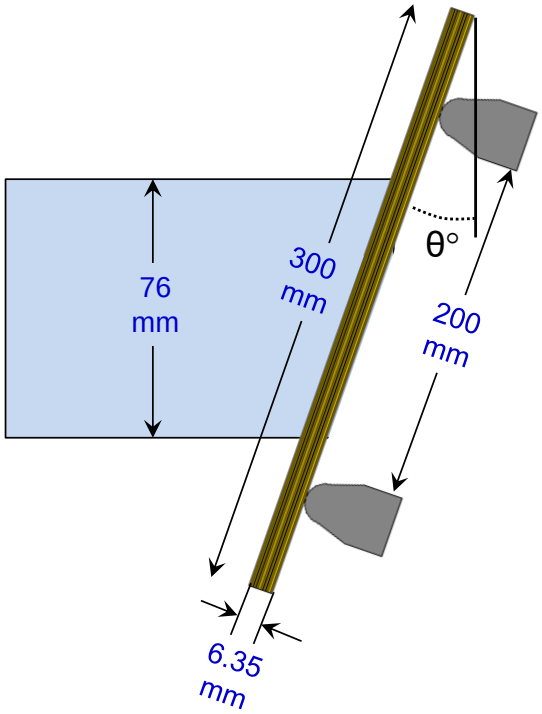


Figure 52 Schematic illustration of the Underwater Shock Loading Simulator (USLS) showing an obliquely loaded simply supported composite plate inclined at an angle $\theta$° to the horizontal.

Figure 53 shows the distributions of damage in an obliquely loaded monolithic composite plate with $\theta = 2^{\circ}$ subjected to $\bar{I} = 0.20$. The different angle of incidence creates complicated loading conditions with the bottom portion of the composite experiencing the incident impulse prior to the upper portion. The uneven incident loading leads to two different regions of highly localized damage. Distributions of damage in an obliquely loaded monolithic composite plate with $\theta = 10^{\circ}$ subjected to $\bar{I} = 0.20$ are shown in Figure 54. The higher angle of obliquity creates multiple locations of localized damage and causes rupture near the upper supports. A comparison of deformation in

planarly loaded plates shown in Figure 36 and obliquely loaded plates in Figure 53 and Figure 54 indicates that higher angles of obliquity increase the number of locations in which localized deformation takes place.

Figure 55 shows the out-of-plane displacement as a function of distance along the impulsively loaded plates at $t =$ 200, 400, 600, 800 and 1000 μs. A major aspect of deformation in a simply-supported bending configuration is the formation of a highly stressed region near the center of the plate which experiences the highest out-of-plane deflection. However, results indicate that increasing angle of obliquity causes localized deformation to be triggered in multiple locations of the plate. The severity of the damage depends on the magnitude of obliquity. Higher obliquity causes an incident wave with the same magnitude to interact with a smaller area leading causing rupture in a localized region which propagates through the rest of the plate. Figure 56 shows the intralaminar and interlaminar damage in quasi-isotropic carbon-fiber/epoxy plates with different angles of obliquity subjected to $\bar{I} = 0.20$. Both interlaminar and intralaminar damage increase with increasing angles of obliquity. There is ~5% increase in damage for every 2° increase in the angle of obliquity.

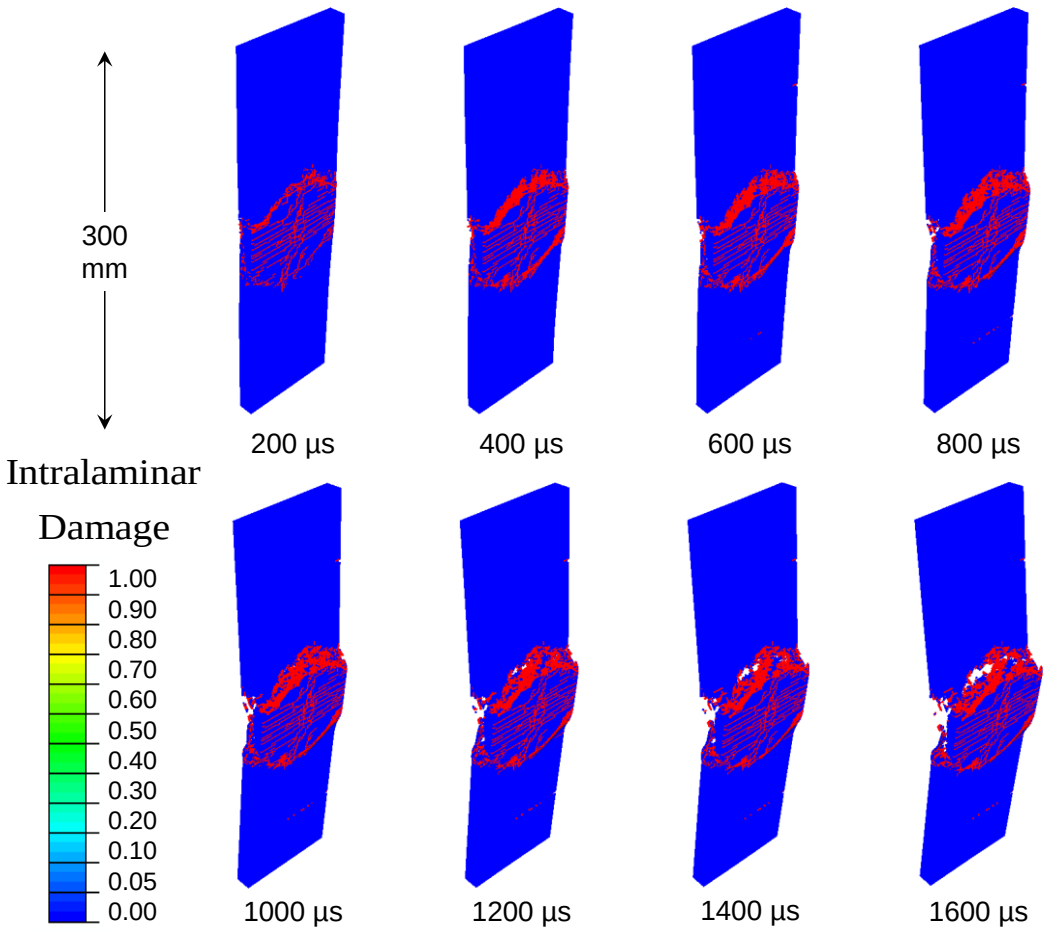


Figure 53 Distributions of in-ply damage in an obliquely loaded quasi-isotropic carbon-fiber/epoxy composite laminate with $\theta = 2^{\circ}$ subjected to $\bar{I} = 0.20$.

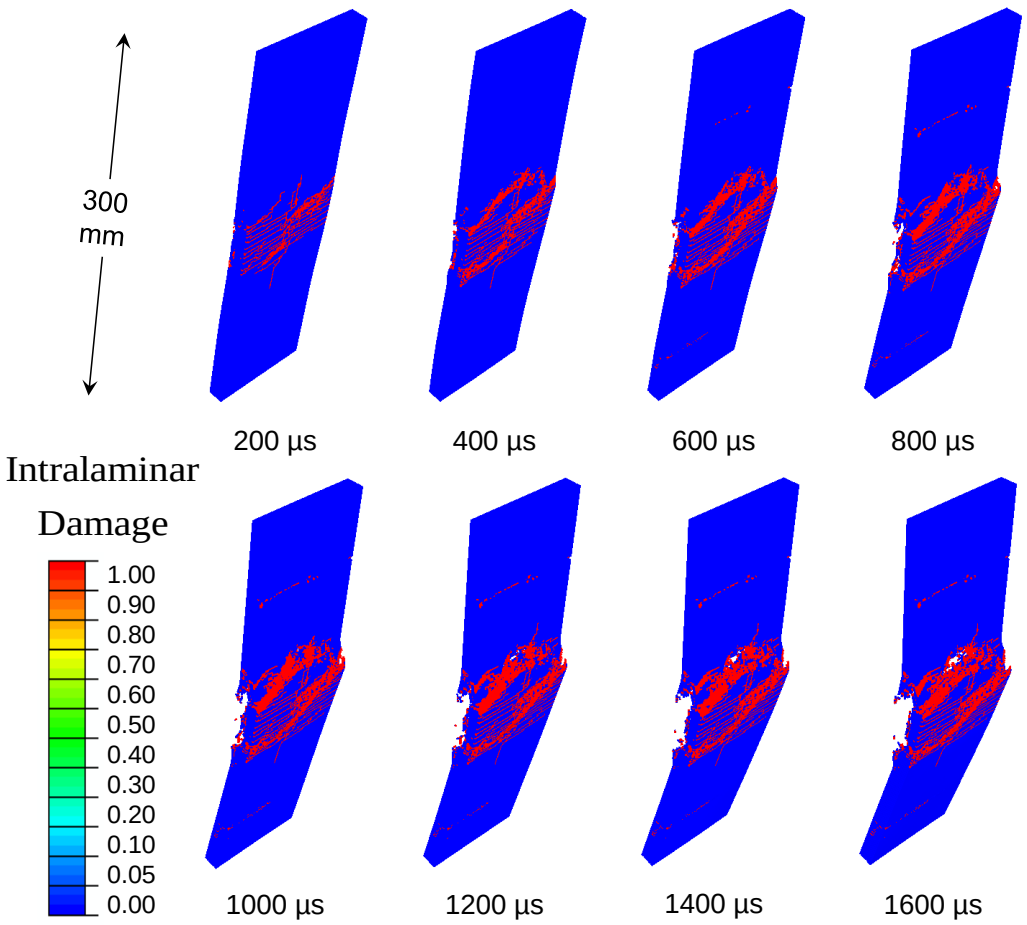


Figure 54 Distributions of in-ply damage in an obliquely loaded quasi-isotropic carbon-fiber/epoxy composite laminate with $\theta = 10^{\circ}$ subjected to $\bar{I} = 0.20$.

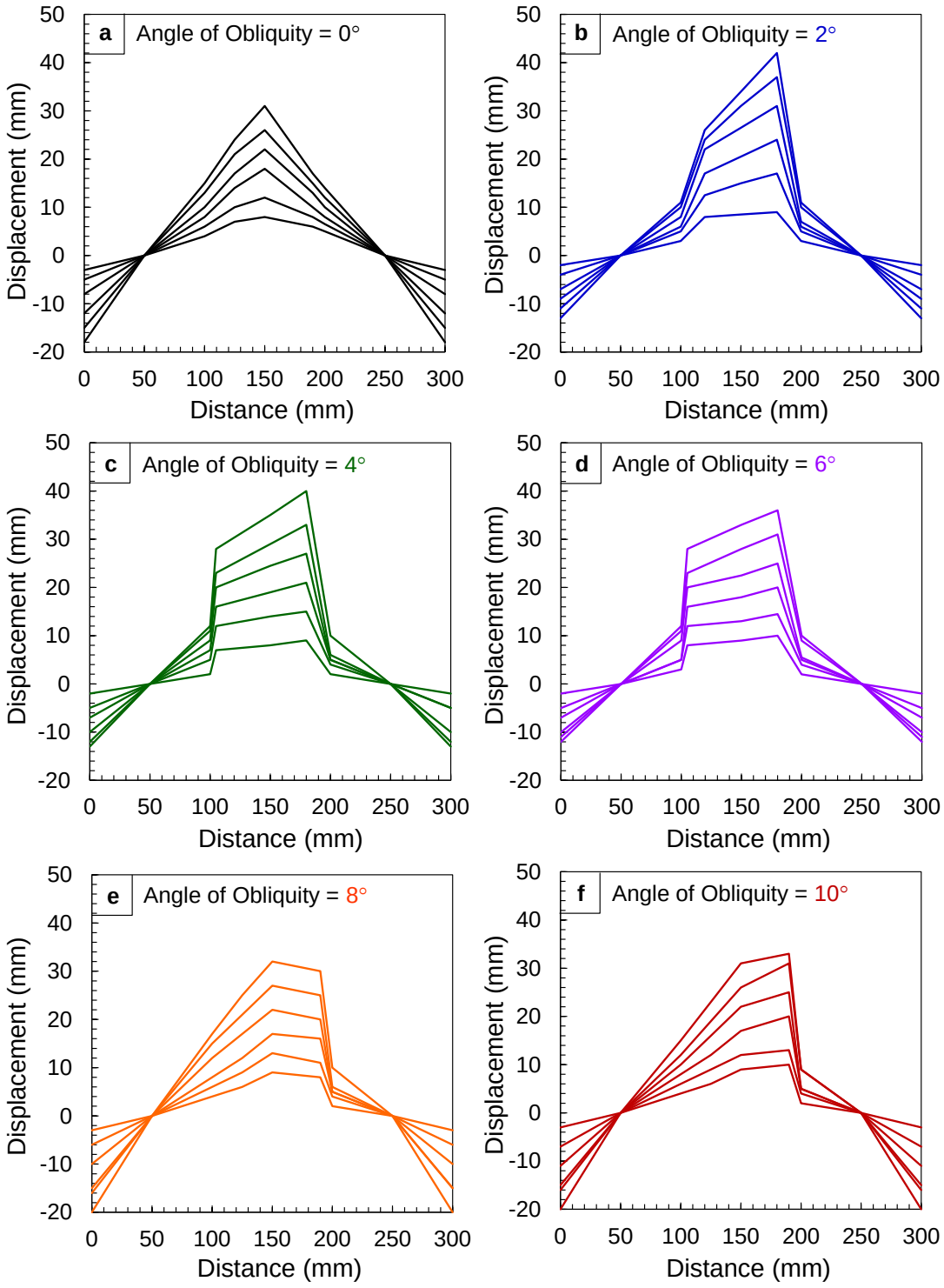


Figure 55 Out-of-plane displacement as a function of distance at $t =$ 200, 400, 600, 800 and 1000 μs for composite laminates with different angles of oblique loading subjected to similar underwater impulsive loads.

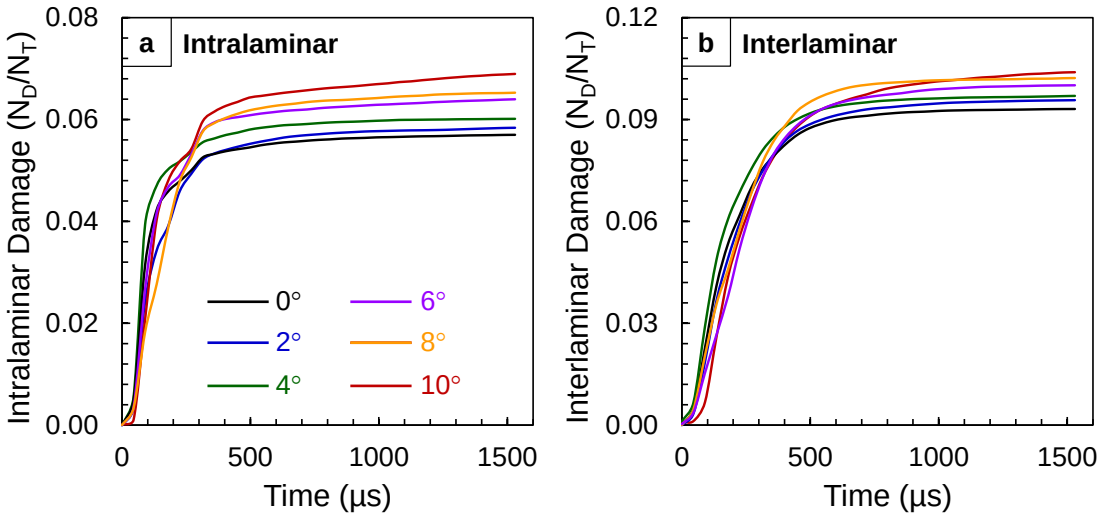


Figure 56 Numerically calculated damage histories for carbon-fiber/epoxy and glass-fiber/epoxy laminates subjected to similar underwater impulsive loads.

## 6.5 Concluding remarks

Marine structures must balance stiffness and load-carrying capacity with the ability to minimize impulse transmission for high blast and impact resistance. Composite structures have higher stiffnesses and high strength-to-weight ratios compared to metallic structures. Additionally, thick composite laminates provide very high bending and shear resistances with relatively small increases in total mass. However, due to the novelty and wide range of structural combinations, the relationships between structural responses and material heterogeneity in composite structures are not well quantified. In particular, the behavior of composite structures under extreme impulsive loading generated by underwater explosions needs to be systematically analyzed.

The composite structures consist of both carbon-fiber and glass-fiber reinforced epoxy resin, and are manufactured by curing commercially available prepregs. The composites consist of 34% epoxy by weight, with the rest containing fibers. Four

different composite layups are analyzed: (1) bi-axial; (2) quasi-isotropic; (3) unidirectional with fibers oriented parallel to supports; and (4) unidirectional with fibers oriented perpendicular to supports. It should be emphasized that the composite panels studied have quite similar overall mass and thickness to enable comparison of performance.

The combined experimental and computational research reported here is an attempt to quantify the underwater blast response of fiber-reinforced epoxy laminates with different material properties and stacking sequences under a range of incident impulsive loads. Since all plates experience failure under an incident impulse of $\bar{I} = 0.16$ with a peak pressure of 196 MPa, this is the highest impulse intensity discussed in this paper. The experiments reported here are supported by a computational framework which employs a Coupled Eulerian Lagrangian (CEL) approach to capture the effects of underwater blasts and fluid-structure interactions (FSI). The results from numerical calculations provide a more in-depth understanding of temporal and spatial evolution of different deformation modes in the structures and the damage mechanisms in different components

Comparison of experiments and simulations shows that numerical calculations provide a reasonable representation of damage and dissipation mechanisms in the composite laminates. The finite element model captures the essential deformation mechanisms observed in both carbon-fiber and glass-fiber/epoxy laminates. Specifically, the following are replicated with reasonable accuracy: fluid-structure interaction effects at the water-structure interface, effects of fiber orientation, in-ply matrix and fiber cracking and rupture, and inter-ply delamination initiation and evolution. The Hashin

damage model overestimates the softening effect resulting from cracking and fracture leading to a slight underestimation of backface deflection.

The unidirectional layups experience splitting due to a lack of stability in the transverse direction, while the bi-axial layups undergo failure near the loading circumference in close proximity to the impulsively loaded region. Quasi-isotropic layups provide the highest blast resistance for both the carbon-fiber and glass-fiber epoxy laminates. Additionally, the quasi-isotropic carbon-fiber/epoxy laminates experience 70% of the deflection experienced by glass-fiber/epoxy laminates.

Since carbon-fiber laminates are nearly four times stiffer than glass-fiber laminates, it is expected that these laminates will transfer higher impulses due to more efficient load spreading. The impulse transmitted by the carbon-fiber laminates is ~130% of that transmitted by glass-fiber laminates, which is relatively modest increase in comparison to superior deflection resistance and reduced in-ply as well as inter-ply damage. In terms of accumulated damage, the carbon-fiber laminates experience 25% of the damage experience by glass-fiber laminates.

To evaluate the effects of load obliquity on the dynamic response of composite laminates, the loading angle is varied from 0° to 10° with increments of 2° and each loading configuration is subjected to similar incident loads. Results indicate that increasing angle of obliquity causes localized deformation to be triggered in multiple locations of the plate. Both interlaminar and intralaminar damage increase with increasing angles of obliquity. There is ~5% increase in damage for every 2° increase in the angle of obliquity.

# 7. DYNAMIC COMPRESSION OF POLYMERIC FOAMS

## 7.1 Introduction

The objective of the present study is to characterize the behavior of structural foams subjected to underwater impulsive loads and delineate the role of core compressibility and facesheet thickness on the response of sandwich plates. The focus is on quantifying the compression and impulse transmission characteristics of PVC foams with a range of densities under loading of water-based high-intensity impulses generated using a recently developed experimental setup called the Underwater Shock Loading Simulator (USLS). The loads mimic the high-pressure, exponentially-decaying impulses that are generated during underwater explosions. As discussed previously, the USLS consists of a projectile-impact-based impulsive loading system, a water chamber, a target holder and a safety enclosure. A range of load intensity with durations between 300 and 1000 μs and peak pressures up to 100 MPa is generated. The impulses are measured using high-dynamic-range-piezoelectric pressure transducers (#109C11 manufactured by PCB Inc.) and a high-frequency data acquisition system from National Instruments Inc. (NI-4432). In-situ measurements of the material response are obtained using high-speed digital imaging and force transducers, providing an opportunity to assess the role of core density and strength on blast resistance during events mimicking an underwater detonation. A complementary numerical model is used to complement the experiments. The analysis uses measures such as compressive strain and transmitted impulse to quantify the blast mitigation capabilities of each configuration. The results are presented

in normalized forms to identify underlying trends in material and structural response and to provide guidance for structural design based on operational requirements. The results from experiments and simulations are compared with analytical predictions. This investigation is expected to reveal insights into the deformation processes in structural foams under the conditions of underwater explosive loading. The combined experimental and computational approach will allow the comparison and validation of constitutive and damage models used in simulations.

For the loading configuration considered here, the frontface is supported by a core and backface. The backface is fitted with a force transducer and the entire assembly is prevented from moving by a heavy steel plate. Xue and Hutchinson [10] provided a correction for Taylor's FSI equation to account for a "pushback" effect when the frontface of areal mass $m_f$ resists motion by virtue of being supported by a core with compressive yield strength $\sigma_Y^c$ such that

$$\bar{I}_T = \frac{I_T}{I_0} = \psi^{\left(\frac{\psi}{1-\psi}\right)} + 0.63\frac{\sigma_Y^c}{p_0}\left(1-\psi^{\left(\frac{\psi}{1-\psi}\right)}\right), \tag{61}$$

with

$$\psi = \frac{\rho_w c_w t_0}{m_f}, \tag{62}$$

and the momentum/area transferred to the core and backface being

$$\bar{I}_B = \frac{I_B}{I_0} = 1.82\frac{\sigma_Y^c}{p_0}\left(1-\psi^{\left(\frac{\psi}{1-\psi}\right)}\right). \tag{63}$$

The impulse acquired by the frontface of a sandwich structure is

$$\bar{I}_F = \frac{I_F}{I_0} = \frac{I_T}{I_0} - \frac{I_B}{I_0}. \tag{64}$$

It should be noted that Xue and Hutchinson's work is applicable to relatively weak, perfectly plastic cores that provide a uniform stress-saturated compressive strain response. Additionally, Taylor's $I_T/I_0$ relation is independent of impulsive load intensity while Xue and Hutchinson's $I_T/I_0$ relation is dependent on the peak pressure of the incident impulse as well as the yield strength of the core, leading to a loss in generality. It is yet to be ascertained if such simplified approaches can sufficiently capture the response of sandwich plates in rather complex cases consisting of different core densities, facesheet thicknessess, high intensity impulsive loads and water-backed conditions.

In the Dynacomp setup, the backface is essentially immovable and the force transducers fitted to the backface enable the calculation of impulse transmitted through the thickness of the sandwich plate. The reaction force histories can be converted to impulses transmitted by the specimen via

$$I_B = \frac{\int F \cdot dt}{A}\ , \tag{65}$$

where $F$ is the reaction force and $A$ is the area under loading. A normalized transmitted impulse is then expressed as

$$\bar{I}_B = \frac{I_B}{I_0}. \tag{66}$$

The transmitted impulse $\bar{I}_B$ is an important metric to evaluate the blast mitigation capability of a sandwich structure. It can be inferred from eqn. (63) that a lower value of $I_B/I_0$ for a specific incident pressure pulse corresponds to better blast mitigation capability of a particular core and the higher the FSI parameter.

For the current analysis, the non-dimensionalized incident impulse $\bar{I}$ in the form of

$$\bar{I} = \frac{I_0}{\rho_w c_w \sqrt{A}} \tag{67}$$

is used, where $A$ is the area of loading. The experiments and numerical modeling for different $\bar{I}$ values simulate the effects of different standoff distances from an explosive source. Swisdak [7, 166, 167] showed that for an underwater explosion using a Tri Nitro Toluene (TNT) explosive source, there exists a power-law relation between the mass $M$ of the explosive and peak pressure $p_0$ (in MPa) such that

$$p_0 = 52.4\left(\frac{M^{1/3}}{r}\right)^{1.13}, \tag{68}$$

where $r$ is the standoff distance in meters. In the experiments reported here, pressures ranging from 10 MPa to 100 MPa can be generated using different projectile velocities. Figure 57 shows a comparison of experimentally measured and numerically calculated pressure histories corresponding to four different projectile velocities. The rise time of the pressure pulses is on the order of 25 μs and the decay time is on the order of 250 μs. The impulsive loads have peak pressures of 18, 28, 43, 59 MPa which approximately

correspond to 100 kg of TNT detonating at distances of 12, 8, 5.5 and 4.2 meters, respectively. The incident impulse magnitudes are $I = \int_0^t p(t)dt =$ 4.8, 8.7, 14.6 and 24.7 kPa·s and the normalized impulse magnitudes calculated using eqn. (67) are $\bar{I} \approx$ 0.05, 0.10, 0.15 and 0.25, respectively.

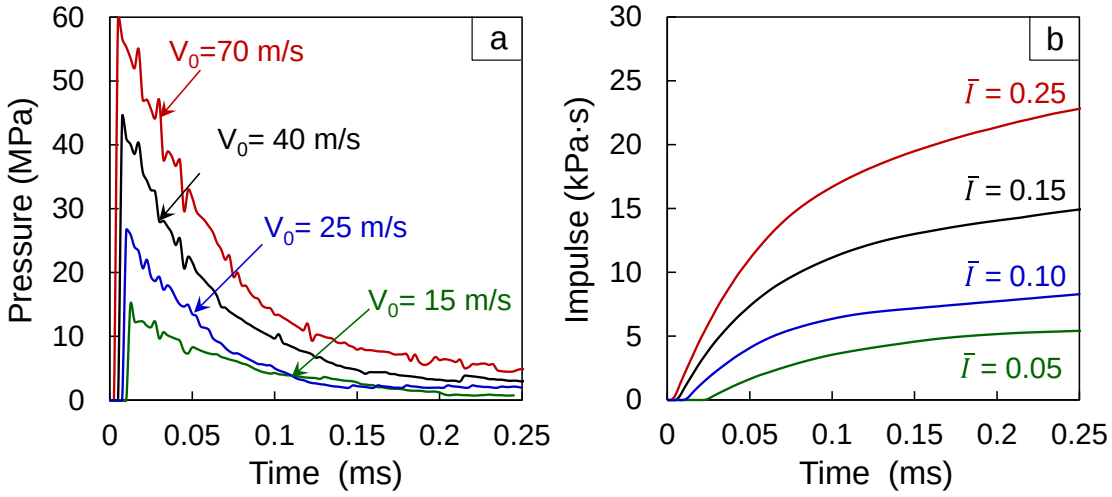


Figure 57 (a) The pressure profiles of impulsive waves in the water chamber measured in experiments for four different projectile velocities; (b) the corresponding normalized incident impulses $(\bar{I})$.

The uniaxial compressive loading setup developed for this analysis is referred to as the "Dynacomp" setup, shown in Figure 58. Here, an aluminum platen is held in contact with water on one side of the platen and a deformable core on the opposite side of the platen. This deformable core is supported by another aluminum platen which rests on a force transducer embedded in a 25 mm thick steel plate. A flange is designed to ensure that the foam core is always in contact with the aluminum platens on both the impulse side and the opposite side and is held normal to the platens. Care is taken to ensure that there is no slippage between the platens and the core. The compressive strain of the foam

core is obtained via high-speed digital imaging and the transmitted impulse is measured using a high dynamic range force transducer. These two parameters provide a description of the compressive response and help quantify the blast mitigation capability of each core configuration. Additionally, the front and backface thicknesses can be varied to evaluate the effect of both variables on the foam core.

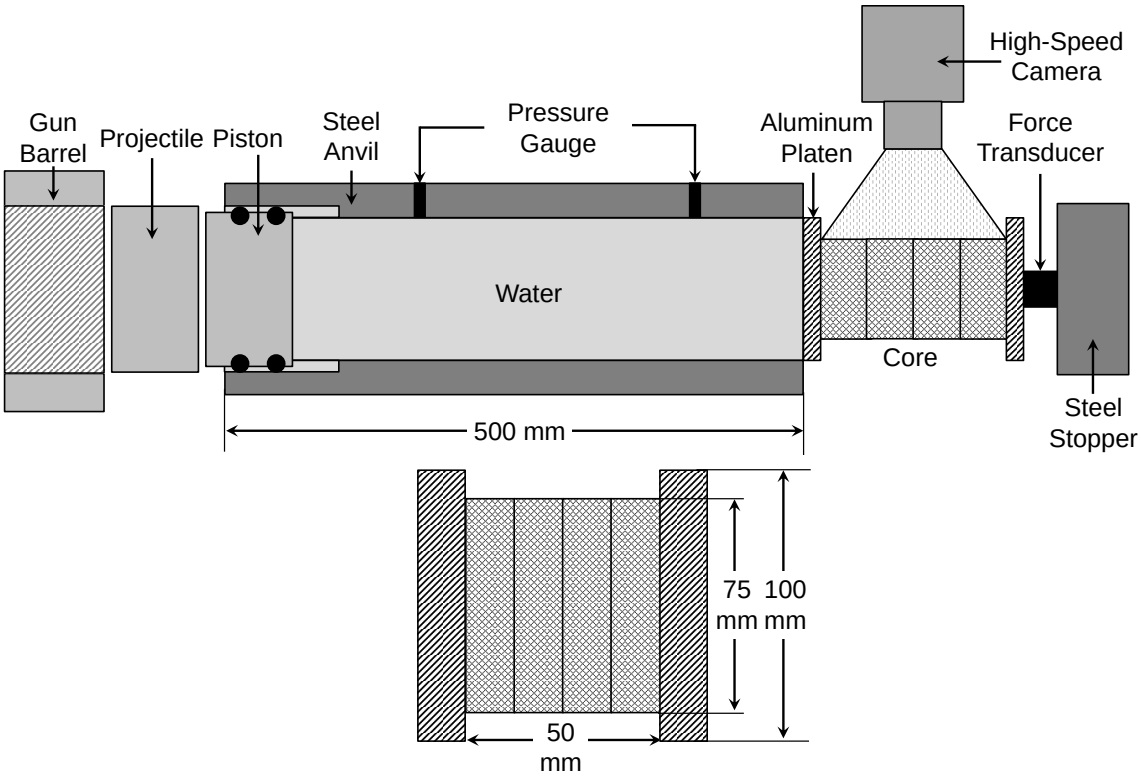


Figure 58 A schematic illustration of the dynamic compression "Dynacomp" test setup within the Underwater Shock Loading Simulator (USLS).

The impulsive waves are planar and produce a uniform pressure over the contact area with the specimen, simplifying the deformation and failure in the material to facilitate measurements using high-speed digital imaging. The loading configuration admits a range of structural dimensions, loading rates and load triaxiality. Two different types of diagnostics are employed as shown in Figure 58. The first uses high-speed

digital imaging to monitor the rate and extent of core compression. The high-speed photographs are analyzed to obtain the compressive strain and strain-recovery in the PVC foams. The compressive strain experienced by the PVC foams is

$$\varepsilon = \frac{L - L_0}{L_0}, \tag{69}$$

where $L_0$ is the initial height and $L$ is the final height.

## 7.2 Underwater impulsive loading experiments

The materials analyzed are structural Poly-Vinyl Chloride (PVC) foams manufactured by DIAB Inc. [143] under the trade name Divinycell HP. These foams are used because their high residual strengths and dimensional stability make them ideal for vacuum bagging and vacuum assisted resin-transfer molding (VARTM). The high strength-to-weight ratio of sandwich structures manufactured using these foams lead to higher vehicle speeds, greater payload capacities, and reduced power demand, all of which result in better operating economy. Additionally, these structural foams possess high chemical resistance, low water absorbency and good thermal insulation and make ideal core materials in sandwich constructions for marine applications. Here, PVC foams with densities of 60, 100, 130, 200 and 250 kg·m$^{-3}$ are studied. The height of the specimen ($T_c$) is 50 mm and the diameter ($D$) is 75 mm. The total thickness of the specimen is $T = T_c + T_f + T_b$ where $T_c$, $T_f$ and $T_b$ are the core, frontface and backface thicknesses, respectively. The compressive stress-strain responses for the core materials, as obtained by George et al. [144], are shown in Figure 10. The stress-strain relations are

linear initially and subsequently show yielding and stress saturation before core densification which leads to a rise in stress. This unique characteristic of the compressive deformation makes the foams especially useful for applications requiring compression and energy absorbency. To compare the effects of different core densities, a normalized density in the form of

$$\bar{\rho} = \frac{\rho_{core}}{\rho_{face}} \tag{70}$$

is used, where $\rho_{core}$ is the density of the foam and $\rho_{face}$ is the density of the facesheet material (aluminum). Foam cores of five different densities are subjected to impulsive loads of four different impulse magnitudes, yielding 20 experimental cases. Finite element simulations are carried out in conjunction with the experiments to ensure that the range of constitutive behaviors captures the essential deformation modes of interest for foam cores expected of sandwich applications.

The circular platens are machined from 12 mm thick 6061 aluminum alloy plates which have a yield strength of 275 MPa and density of 2700 kg $m^{-3}$. This strength is adequate to ensure that the platens undergo negligible plastic deformation under the impulsive loads considered. In the initial set of experiments, the front and backface thicknesses are $T_f = T_b = 12$ mm. To evaluate the effect of frontface mass on the overall response, the thicknesses are increased gradually. The normalized front and backface thicknesses are non-dimensionalized as $T_f/T_c$ and $T_b/T_c$, respectively, where $T_c$ is the core thickness. The facesheet thicknesses are increased gradually and the changes are denoted by $\Delta T_f$ and $\Delta T_b$, respectively. The values for $\Delta T_f$ and $\Delta T_b$ are 4, 6, 8 and 10

mm, giving face thickness-to-core thickness ratios $\left(\Delta T_f / T_c\right)$ and $\left(\Delta T_b / T_c\right)$ of 0.08, 0.12, 0.16 and 0.2. The densities of the platens and the facesheets are much higher than those of the foam cores. For this reason and for the reason that the platens are also much stiffer than the foams, the platens can be considered as effectively rigid. The rigid support behind the force transducer allows higher deformation rates to be obtained under the same incident impulse.

A number of studies have shown that the early-stage response of components of sandwich structures determines the blast resistance to a particular incident impulsive load [69, 145, 168-170]. Deformation modes observed in the earliest stages of the dynamic response are core shear, core indentation, facesheet buckling, and core-face debonding, all of which occur prior to 1000 μs after the onset of loading. For the results reported here, the peak compressive strain, and peak transmitted force and peak transmitted impulse are reached within 1000 μs of the load incidence on the sandwich plate. Since structures must be designed for the greatest possible load-carrying capacity for specified structural attributes, this analysis is focused on the crucial early stage response of the sandwich plates.

## 7.3 Loading-structure-performance maps

To fully utilize the potential of sandwich structures, one consideration is to maximize the performance for a give load setting while minimizing the mass. The weight-efficient designs of blast-resistant structures are determined by a number of factors, such as the expected incident load, facesheet and core materials, structural dimensions, geometry and interfacial effects. To quantify the effect of these factors on

deformation response, structural indices are developed. Non-dimensional variables are used for quantitative evaluation of the compressive response of the PVC foams and the structural response of composite panels as functions of loading and structural attributes. The performance attribute of interest here is the compressive strain $\varepsilon$, transmitted impulse $I_B$ (kPa·s) and normalized transmitted impulse $\bar{I}_B$, the material attribute of interest is the normalized relative density $\bar{\rho}$ and the load is the normalized incident impulse $\bar{I}$. These parameters are varied independently of each other and the performance of each structure is quantified using these parameters. Based on the experiments and numerical simulations reported here, load-structure-performance maps are developed. These maps can be used to inform structural design with the understanding that they should only be used for the specified material, structural parameter ranges and loading conditions specified. For a given combination of core compression and impulse transmitted, the optimum value of relative density for a specific impulsive load level can be achieved by varying material properties of the monolithic plate or sandwich core. To summarize, the variables employed to evaluate blast performance are as follows:

normalized density

$$\bar{\rho} = \frac{\rho_{core}}{\rho_{face}}; \tag{71}$$

normalized incident impulse

$$\bar{I} = \frac{I_0}{\rho_w c_w \sqrt{A}}; \tag{72}$$

compressive strain

$$\varepsilon = \frac{L - L_0}{L_0}; \tag{73}$$

transmitted impulse (kPa·s)

$$I_B = \frac{\int F \cdot dt}{A}; \tag{74}$$

normalized transmitted impulse

$$\bar{I}_B = \frac{I_B}{I_0}; \tag{75}$$

and normalized frontface and backface thickness $\left(\Delta T_f / T_c\right)$ and $\left(\Delta T_b / T_c\right)$, where $\Delta T_f$ and $\Delta T_b$ are the change in frontface and backface thickness respectively.

## 7.4 Results and discussion

The effect of facesheet thickness, core density, loading intensity and loading configuration on blast resistance are analyzed, allowing loading-structure-performance maps to be developed for enhanced structural design. The temporal evolution of selected performance metrics as functions of load intensity and material properties are analyzed. In particular, the two performance metrics studied in detail are core compression and total impulse transmitted through the core. The results from experiments on the compression of polymeric foams are first discussed, followed by the results of experiments on impulsive loading of simply-supported sandwich structures. The experimental results are

used to calibrate the computational model and evaluate response over a wide range of loading and structural attributes.

The results of parametric studies are presented in a format wherein the response variables are functions of the load intensity and structural attributes including relative density and frontface and backface thicknesses. The loading-structure-performance maps allow the identification of specific attributes for any given combination of desired load-carrying capacity and impulse mitigation. They are useful for identifying structural aspects that meet desired performance objectives and allow the trade-offs between conflicting requirements between compressive strain and transmitted impulse to be explored.

### 7.4.1 Experimental results and numerical validation

A coupled Eulerian-Lagrangian framework is used to capture the impulse generation and transfer in the USLS. Figure 59 shows a cross-sectional view of the USLS with a pressure pulse traveling through the water chamber and impinging upon the sandwich core. Also shown are the pressure pulses in the USLS at different locations and different times. The experimentally measured and calculated pressure pulses show good agreement in terms of peak pressures and decay times. The calculated profiles show slightly faster wave attenuation than the measured profiles. Obviously, the coupled Eulerian-Lagrangian framework and the Mie-Gruneisen equation of state allow most essential features of the loading pulses in the experiments to be captured.

Figure 60 shows high-speed photographs and corresponding computational contour plots for strain in the HP60 foam subjected to loading with $\bar{I} = 0.25$. After the

onset of loading, the core undergoes large compressive deformation rather uniformly throughout the thickness. After 750 μs, strain localization occurs near the frontface and backface. At 1000 μs, the core compression is complete and strain localization severe throughout the specimen. Figure 61 shows the compressive response of the HP100 foam subjected to loading with $\bar{I} = 0.25$. In a manner quite similar to the case for the HP60 foam, the strain in the HP100 core is distributed relatively uniformly throughout the thickness and strain localization occurs at multiple locations. The overall compressive strain is lower than that in the HP60 foam and sites of localized straining coalesce into bands. For both the HP60 and HP100 core materials, the bands are not limited to either the frontface or the backface. Rather, they emanate from the frontface and propagate gradually through the thickness, spanning the whole cross-section.

Figure 62 and Figure 63 show high-speed photographs and corresponding calculated strain fields in HP200 and HP250 foam subjected to loading with $\bar{I} = 0.25$, respectively. In both specimens, the strains and resulting strain localization are concentrated at the base of the specimen near the distal face, precipitating inefficient impulse absorption and leading to large impulse transfer through the foam. The experiments and simulations show reasonable agreement in terms of the rate and extent of compression. Additionally, the simulations reveal characteristics of strain localization and deformation response that are difficult to obtain from experiments, thereby adding valuable insight into the response of each sandwich core. However, larger permanent compressions of the foam cores are observed in the experiments than in the calculations. This investigation is focused on the initial, short-term transient response of sandwich cores to high-intensity water-based loading. The homogenized crushable foam

constitutive model and the strain-based damage criterion capture the initial phase of deformation phase which is dominated by compression.

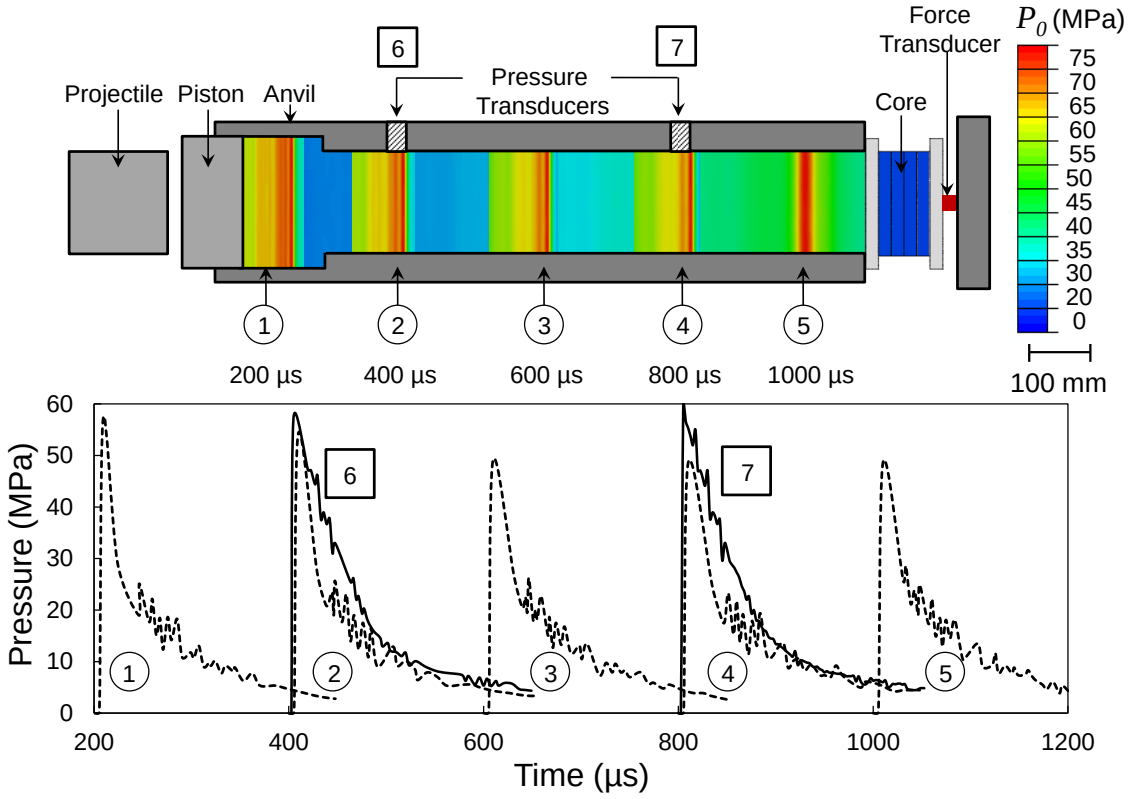


Figure 59 Cross-sectional view of the *Dynacomp* setup showing the distributions of experimentally measured (square-boxed numbers) and numerically calculated (circled numbers) pressure distributions at different locations for an impulsive wave generated with a projectile velocity of 70 $ms^{-1}$ ($\bar{I} = 0.25$).

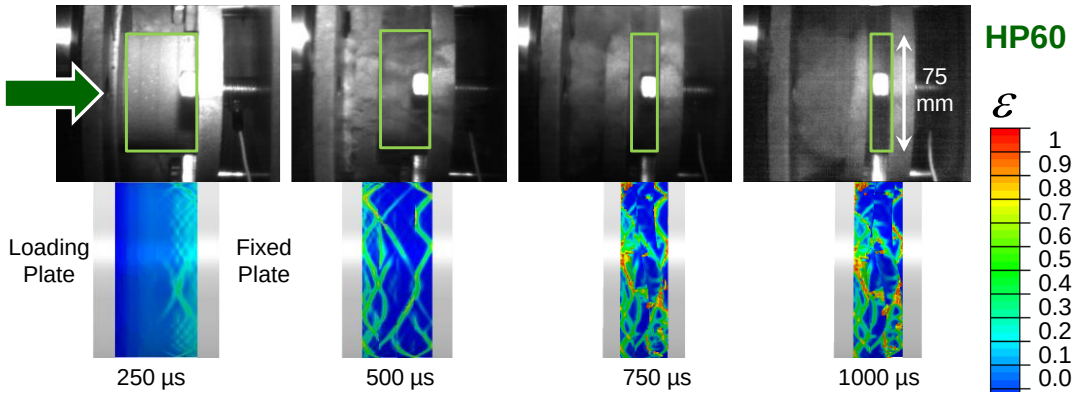


Figure 60 A comparison of experimentally measured and numerically calculated strain fields at different times for a sandwich structure with the HP60 core subjected to $\bar{I} = 0.25$. The distributions show relatively uniform compressive strain throughout the thickness of the sandwich plate.

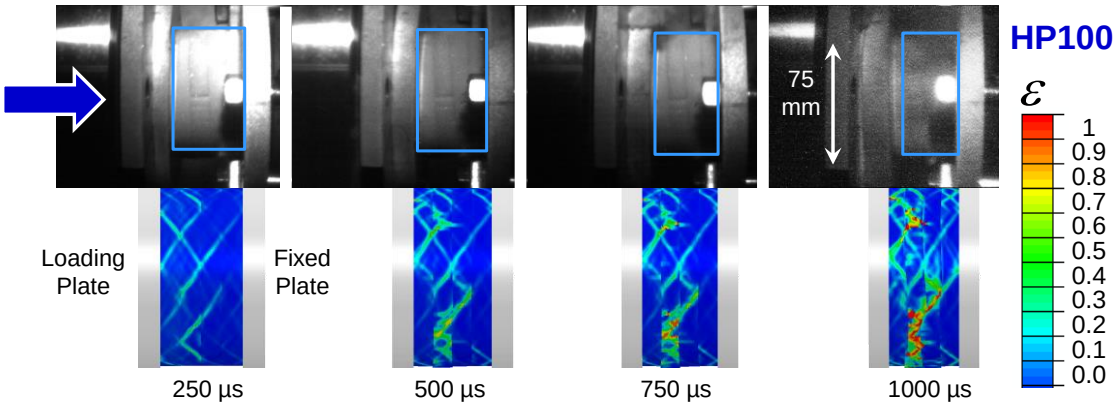


Figure 61 A comparison of experimentally measured and numerically calculated strain fields at different times for a sandwich structure with the HP100 core subjected to $\bar{I} = 0.25$. The distributions show straining throughout the thickness of the sandwich plate.

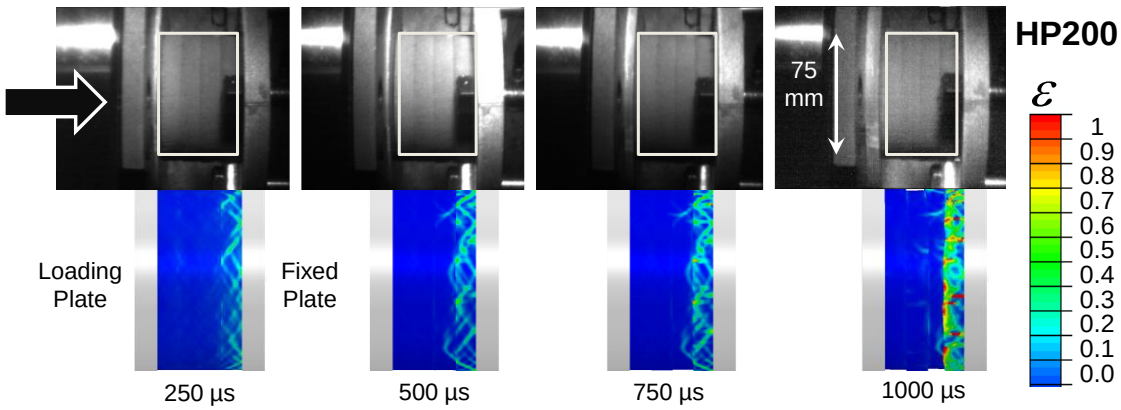


Figure 62 A comparison of experimentally measured and numerically calculated strain fields at different times for a sandwich structure with the HP200 core subjected to $\bar{I} = 0.25$. The extent of compression is significantly lower than that for the structures with HP60, HP100 and HP130 and the strain distributions show localization near the base of the specimen.

### 7.4.2 Deformation in the core

Figure 64(a-d) shows the time histories of the corresponding compressive strain measured from high-speed digital images for all foams analyzed. For the HP60, HP100 and HP130 foams, rapid compression of the sample occurs immediately after the onset of loading, resulting water leaking from the water tank of the USLS. As the density of the foam increases, both the rate and extent of core compression decrease significantly. Specifically, the HP200 and HP250 cores exhibit negligible compression and essentially behave like monolithic plates, indicating that there is no apparent advantage in using these foam materials in applications in which energy absorbency or compliance are desired. Instead, these foams may be desirable for applications that require high stiffness. As the loading intensity increases, both the rate and extent of core compression increase substantially.

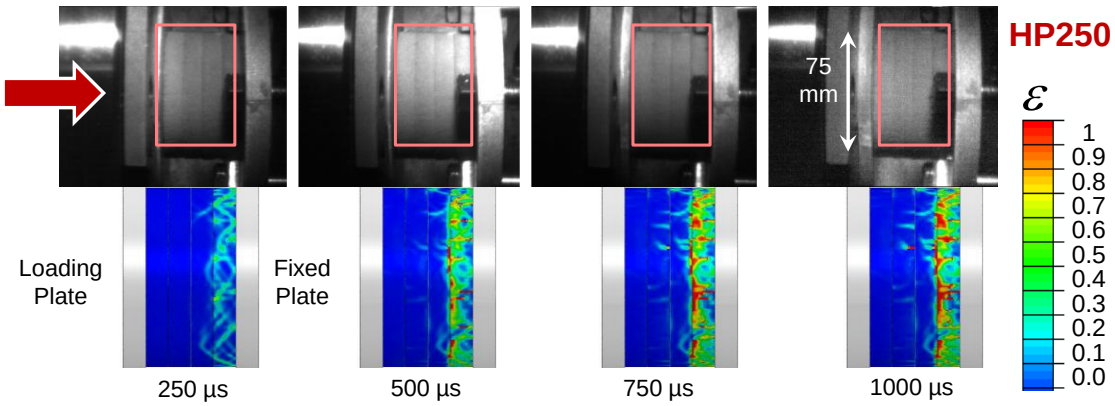


Figure 63 A comparison of experimentally measured and numerically calculated strain fields at different times for a sandwich structure with the HP250 core subjected to $\bar{I} = 0.25$. The core acts like a monolithic plate and, similar to the HP200 case in Fig. 8, the extent of compression is significantly lower than those for HP60, HP100 and HP130. Deformation is mostly near the base of the specimen.

For the highest load intensity considered, i.e. $\bar{I} = 0.25$, the HP60 core experiences maximum compression while the HP100 and HP130 cores show compressions that are 70% and 40% of that observed for HP60, respectively. The compressive strains in the HP200 and HP250 cores are 30% and 10% of that observed in the HP60 core, respectively. Figure 65 shows the loading-structure-performance map of compressive strain $(\varepsilon)$ as a function of the incident impulse $(\bar{I})$ and relative density $(\bar{\rho})$. At all impulse magnitudes, foams with the lowest relative density experience the highest compressive strain. The compressive strain increases as the relative density increases and as the impulse magnitude increases. The HP250 and HP200 cores exhibit significantly higher resistance to crushing compared with the HP60, HP100 and HP130 foam cores. As the core density increases, the maximum core compression increases monotonically up to $\bar{\rho} = 0.05$. With increasing core density, the maximum core compressive strain plateaus at $\bar{I} = 0.12$.

At all loading intensities, lower density yields significantly higher levels of compression. An analysis shows that as the load intensity increases, crushing leads to collapse of the material. As such, it is useful to identify conditions for more uniform load spreading. A major concern for low density cores is the occurrence of localized indentation, which leads to failure of core material and buckling and rupture of the frontface sheet. Furthermore, severe core compression compromises the integrity and lowers the load-bearing capacity of the entire structure. On the other hand, as discussed previously, the high strength associated with high core density can lead to strain localization and failure near the distal face due to non-uniform strain distribution. Therefore, a balance between stiffness and compliance is essential for core materials.

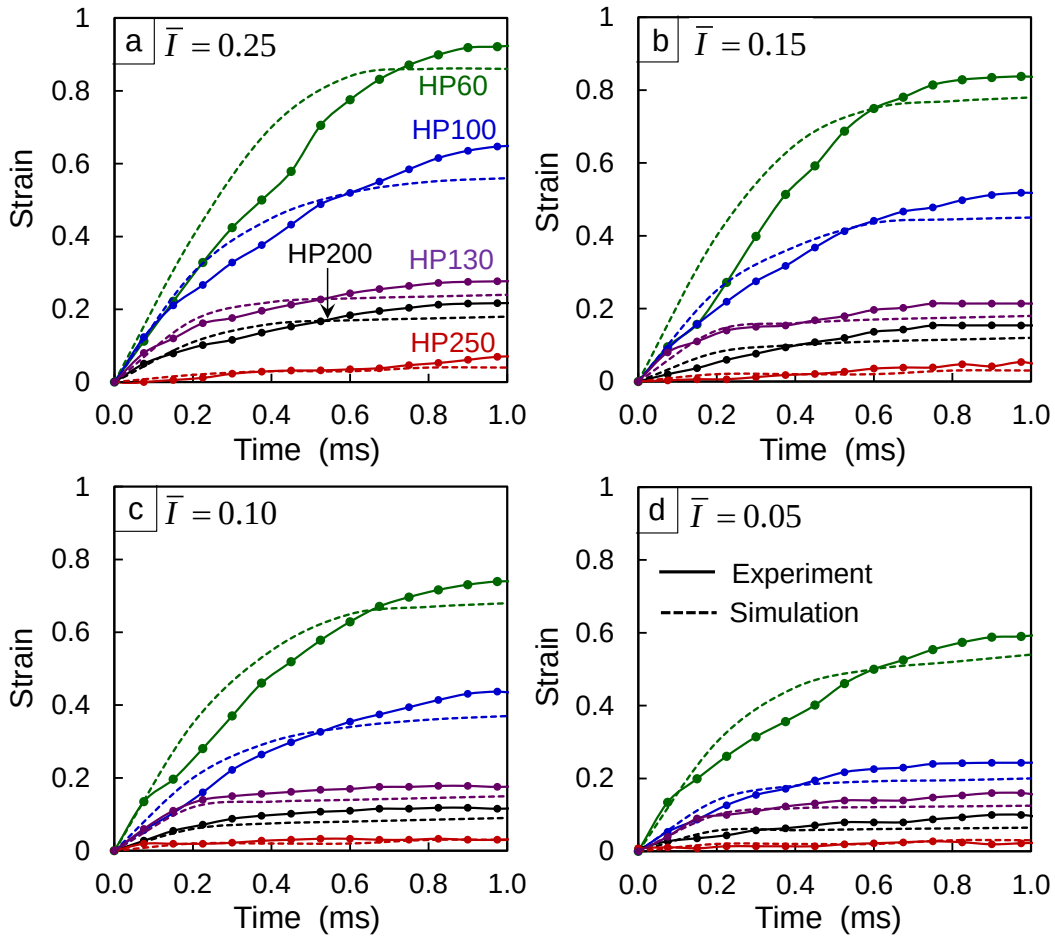


Figure 64 Experimentally measured and numerically calculated strain histories for cases with the HP60, HP100, HP130, HP200 and HP250 cores subjected to loading at different intensities.

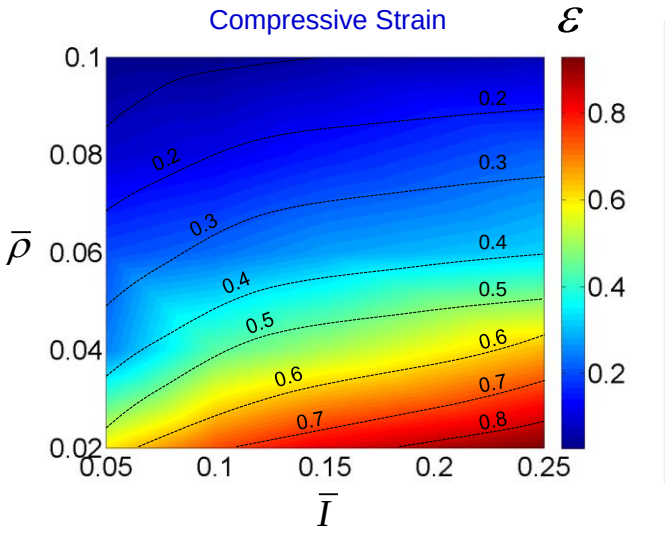

Figure 65 Loading-structure-performance map showing compressive strain in the sandwich core as a function of incident impulsive load intensity $\bar{I}$ and normalized density $\bar{\rho}$. On a unit weight basis, low density cores consistently experience higher compressive strains than high density cores.

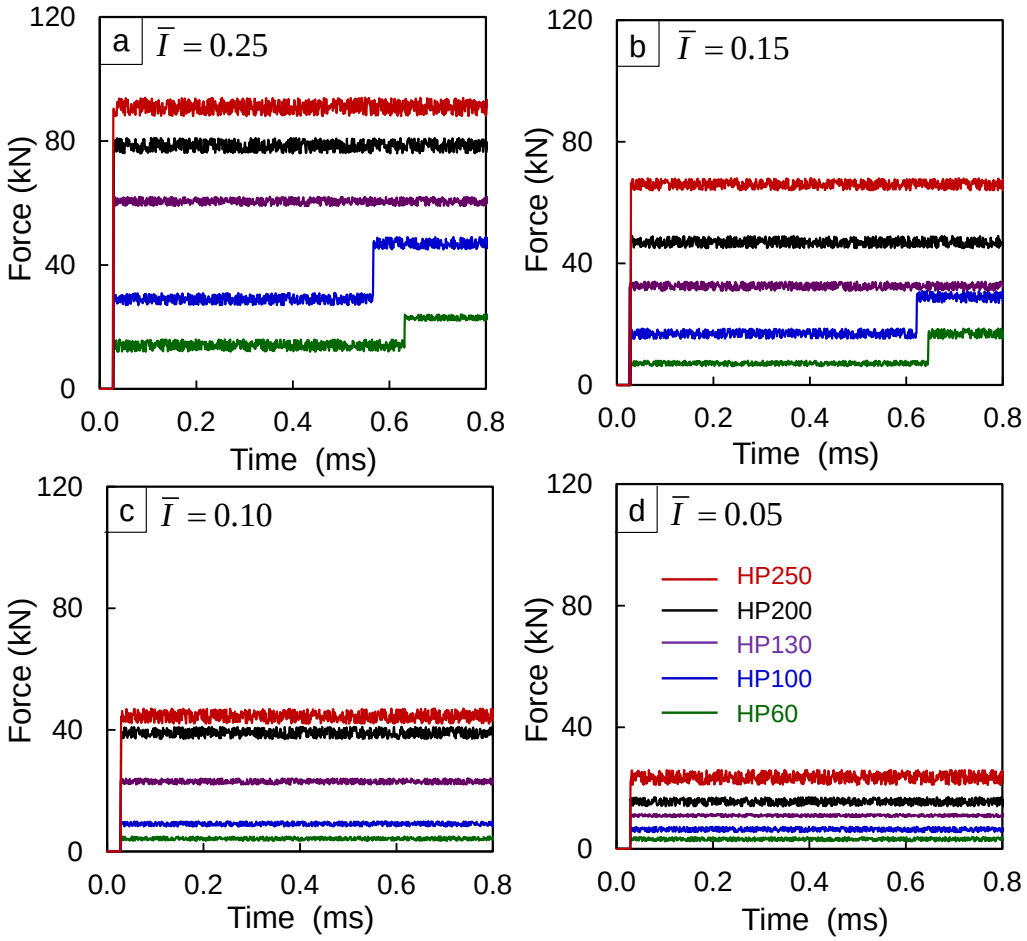


Figure 66 Experimentally measured reaction force histories for sandwich plates subjected to impulsive loading of different intensities.

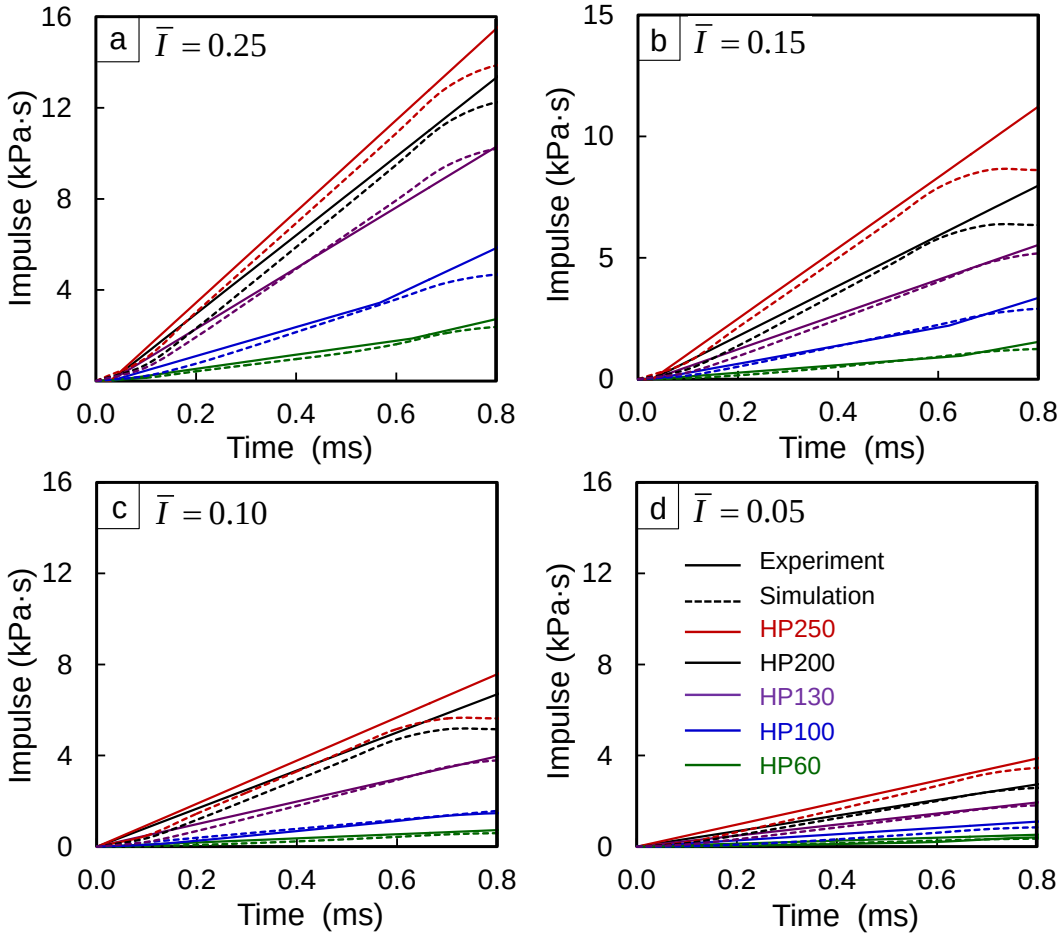


Figure 67 Experimentally measured and numerically calculated transmitted impulse histories for Divinycell HP cores subjected to impulsive loading of different intensities.

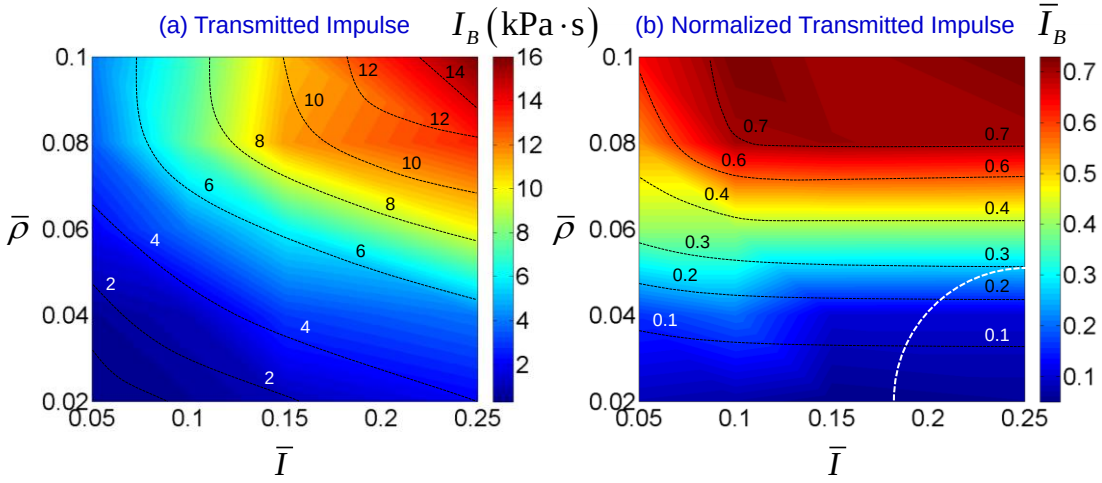


Figure 68 Loading-structure-performance map showing (a) transmitted impulse $I_B$ (kPa·s) and (b) normalized transmitted impulse $\bar{I}_B$ as functions of incident impulsive load $\bar{I}$ and normalized density $\bar{\rho}$. The region encircled by the white dotted line denotes cores that collapsed under impulses exceeding $\bar{I} = 0.10$ as shown in Figure 66.

### 7.4.3 Impulse transmission through the core

Minimizing the impulse transmitted to the downstream section is important for protecting the internal components of marine vessels. The magnitude of the transmitted impulse is therefore an important parameter concerning the blast resistance of composite structures. Clearly, the composite structure that transmits the least impulse at the lowest rate is most desirable. Figure 66(a-d) shows the reaction forces measured by the force transducer for all cores and the input impulse magnitudes. At the higher load intensities $\left(\bar{I} = 0.15 \text{ and } 0.25\right)$, the crushing and collapse of the core material result in high intensities of transmitted impulse. Core indentation is particularly harmful for sandwich structures as it causes instabilities in the frontface which lead buckling and shear failure as well as increased impulse transmission.

Figure 67(a-d) shows the corresponding transmitted impulse histories for all cores and input impulse magnitudes. Lower transmitted impulse indicates better blast mitigation capability. The results show that core density and load intensity both strongly affect impulse transmission. Structures with low density cores consistently outperform structures with high density cores. The effects of core characteristics can be compounded by loading rate. For example, at an incident impulse of $\bar{I} = 0.05$, high density cores transmit slightly higher impulses than low density cores; however, at an incident impulse of $\bar{I} = 0.25$, the structures with the HP250, HP200 and HP130 cores transmit more than thrice the impulse transmitted by the structure with the HP60 core and more than twice the impulse transmitted by the structure with the HP100 core.

A comparison of Figure 64 and Figure 67 reveals that the rate and extent of core compression correlate with the transmitted impulse, with low density cores undergoing high compressive strains and providing higher blast mitigation than high density cores. These trends are observed at all loading intensities with the low density cores (HP60, HP100 and HP130) transmitting significantly lower impulses than the high density cores (HP200 and HP250). This trend is consistent with deformation fields implied in the contour plots for strain shown earlier. Overall, the uniform distribution of strain and high strain levels in low density cores yield low impulse transmission; and non-uniform distribution of strain and lower strain levels in high density cores lead to high impulse transmission. Although the total momentum imparted to the sandwich plates is lower for low density cores, the kinetic energy acquired by the frontface is higher in such cases. This results in greater core compression which is detrimental to residual bending stiffness and strength. Since core compression and impulse transmission can pose opposing requirements on structural parameters, an optimum design must balance the competing requirements. Such a design may be different for different load conditions and intensities.

Figure 68(a) shows the loading-structure-performance map of transmitted impulse $\left(I_B\right)$ as a function of incident impulse $\left(\bar{I}\right)$ and relative density $\left(\bar{\rho}\right)$. At all impulse magnitudes, foams with the lowest relative density transmit the least impulses. The transmitted impulses are strongly dependent on relative density and increase with increasing relative density as well as impulse magnitudes. HP60, HP100 and HP130 foam cores exhibit significantly higher blast mitigation capacity in comparison to HP200 and HP250 foam cores. Figure 68(b) shows the normalized transmitted impulse $\left(\bar{I}_B\right)$ for all

20 foam core specimens as a function of the incident impulse $\left(\bar{I}\right)$ and relative density $\left(\bar{\rho}\right)$. The variation of $\bar{I}_B$ with $\bar{I}$ and $\bar{\rho}$ are quite different from those observed for $I_B$. The transmitted impulse as a fraction of incident impulse seems to be only weakly influenced by the incident impulse magnitude but very strongly influenced by the core density. This highlights the fact that in structural design of sandwich composites, the selection of material for the sandwich core is of utmost importance. The compiled data reveals that at all impulse magnitudes, low density cores transmit a lower fraction of the incident impulses.

It should be noted that although low density cores transmit the least impulses, they also undergo high compressive strains and thereby render the structure more susceptible to collapse. The experiments and calculations are in good agreement, indicating that the homogenized Deshpande and Fleck constitutive model [149] in combination with the Hooputra damage criterion [150] provides a reasonably accurate representation of the deformation in the sandwich core. It should be noted that the Deshpande and Fleck constitutive model slightly overestimates the compliance of the foam core, leading to a higher initial rate of core compression and marginally greater transmitted impulses.

### 7.4.4 Effect of face thickness on deformation and impulse transmission

The effect of facesheet thickness is analyzed by systematically varying both the front and back facesheet thicknesses and by evaluating the response of each sandwich core. The facesheet thicknesses considered are 4, 6, 8 and 10 mm, giving $\left(\Delta T_f / T_c\right)$ and

$\left(\Delta T_b / T_c\right)$ of 0.08, 0.12, 0.16 and 0.2 where $\Delta T_f$ and $\Delta T_b$ are the changes in front and back face thicknesses respectively. Figure 69 shows a comparison of experimentally observed and calculated compressive response of the structure with the HP100 core with $\left(\Delta T_f / T_c\right) = 0.2$. Strain localizes predominantly near the impulse face and near the distal face due to significant wave reverberations. It is instructive to note the differences between the responses of the HP100 core with $\left(\Delta T_f / T_c\right) = 0.2$ and with $\left(\Delta T_f / T_c\right) = 0$ shown in Figure 61. For $\left(\Delta T_f / T_c\right) = 0$, the compressive strain is relatively uniform throughout the thickness. For $\left(\Delta T_f / T_c\right) = 0.2$, the compressive strain tends to localize near the facesheets. Figure 70(a) shows the compressive strain and Figure 70(b) shows the history of the corresponding transmitted impulse for structures with the HP100 core and different frontface thicknesses under loading with $\bar{I} = 0.25$. As the frontface thickness increases, the strains increase and the transmitted impulse increases accordingly. Although thicker frontfaces tend to increase impulse transmission, sufficiently strong frontfaces are necessary for structural integrity. Therefore, sandwich structures must balance the strength and mass of the frontface and allowable core compression to control impulse transmission. Figure 71(b) shows the effect of backface thickness on the transmitted impulse. As the backface thickness increases, the transmitted impulse decreases only slightly. Since the benefit is relatively negligible, the influence of backface thickness on structural response is not analyzed further.

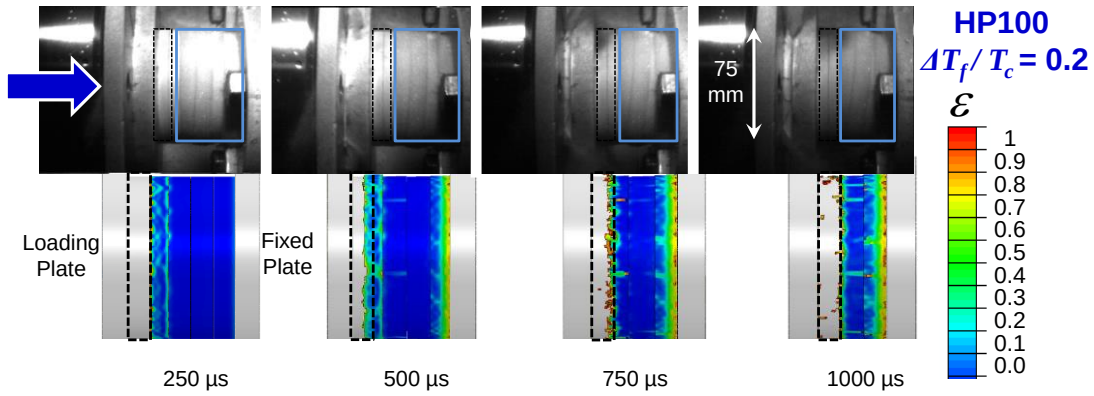


Figure 69 A comparison of experimentally measured and numerically calculated strain fields at different times for a sandwich structure with the HP100 core ($\bar{I} = 0.25$). Note the high strain levels near the front and distal faces in contrast to the relatively uniform strains of the HP100 core with $\left(\Delta T_f / T_c\right) = 0$ in Figure 61.

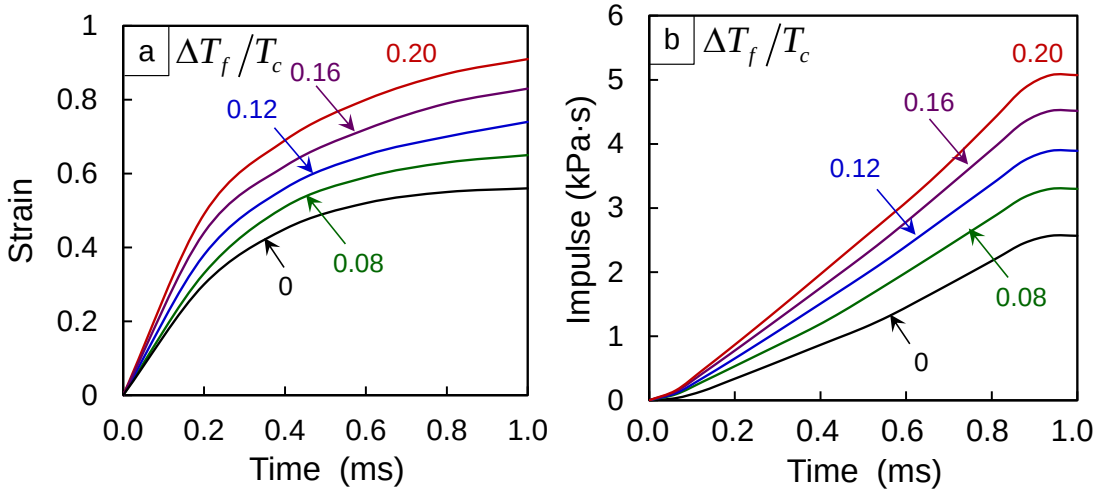


Figure 70 Compressive strain and transmitted impulse histories for different $\left(\Delta T_f / T_c\right)$ values for the HP100 core subjected to $\bar{I} = 0.25$.

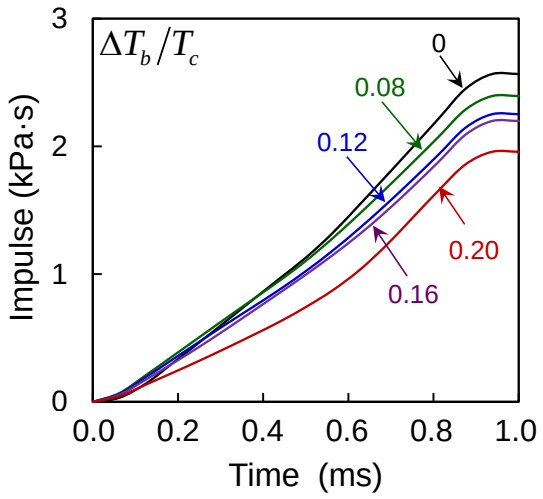


Figure 71 Transmitted impulse histories for different ratios between backface thickness and core thickness $\left(\Delta T_b/T_c\right)$ for the HP100 core subjected to $\bar{I}=0.25$.

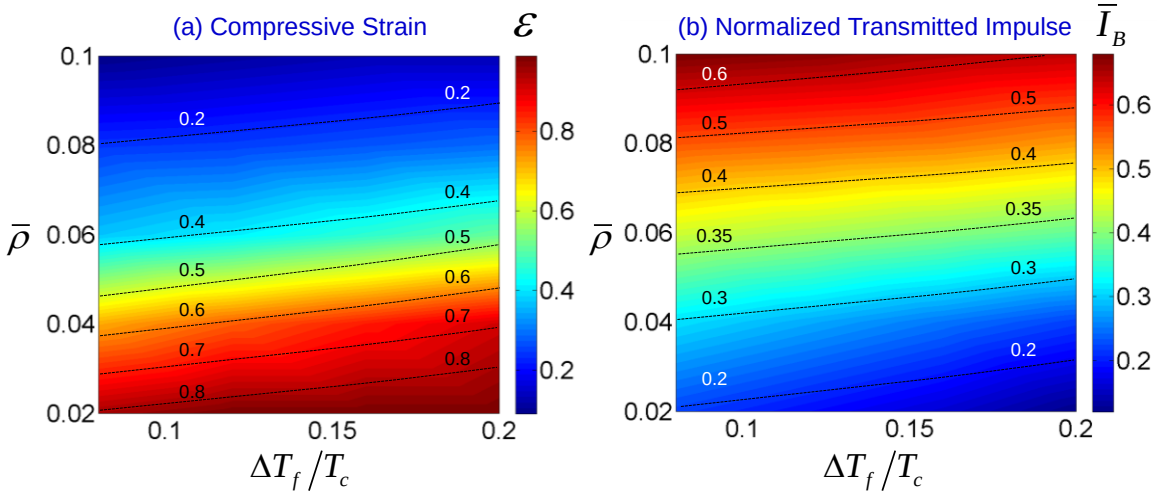


Figure 72 Loading-structure-performance map showing compressive strain $\varepsilon$ and normalized transmitted impulse $\bar{I}_B$ as functions of $\left(\Delta T_f/T_c\right)$ and normalized density $\bar{\rho}$.

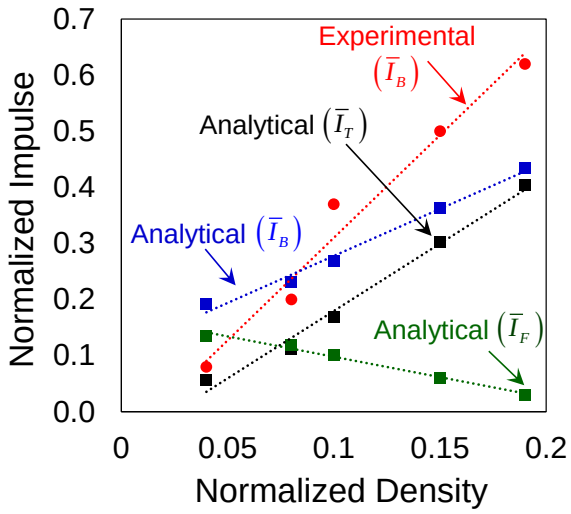


Figure 73 A comparison of normalized transmitted impulse values obtained from experiments and calculated using Xue and Hutchinson's analytical approach [10].

Figure 72(a) shows the peak compressive strain $(\varepsilon)$ and Figure 72(b) shows the normalized transmitted impulse $(\bar{I}_B)$ for all specimens as functions of frontface thickness $(\Delta T_f / T_c)$ and relative density $(\bar{\rho})$ for $\bar{I} = 0.25$. The results reveal that both core compressive strain and normalized transmitted impulse increases with increasing frontface thickness. For a 10% increase in frontface mass, the core compressive strain increases by ~5% and transmitted impulse increases by ~10%. Overall, the core density has a strong influence on blast resistance and the frontface thickness.

### 7.4.5 Comparison with analytical model

A number of analytical models have been developed to extend Taylor's relation for an underwater impulse impinging on a free-standing plate [6]. These relations are generally based on a simplified continuum description of the sandwich core. Figure 73 shows a comparison between the predictions of Xue and Hutchinson's analytical model

[10] and the experimental results obtained in the current study. The Xue and Hutchinson approach clearly delineates the benefit of sandwich plates over monolithic plates of equivalent mass and identifies minimum weight designs. This analytical model, based on a continuum description of the core, accurately predicts the transmitted impulses for low core densities, but significantly underestimates the transmitted impulses for high core densities.

## 7.5 Scaling and structural design

The underwater blast loading problem involves a wide range of length and time scales such as the spatial decay of the blast impulse, blast attenuation, pressure decay time, the size and geometry of the structure, and the area under impulsive loading relative to the total area of the structure. The characteristics of high intensity pressure pulses resulting from underwater blasts have been well established through large-scale experiments. Experimental data relating to underwater explosions supports the use of simple power-law scaling relations between the mass of the explosive, stand-off distance and decay time [4, 163, 166]. More recently, non-dimensionalized performance charts to determine optimal core designs that maximize blast resistance and minimize core mass have been proposed [10, 60, 62, 171, 172].

In the analysis reported here, the underwater blast loading problem is simplified to delineate the performance of the sandwich core and provide a clear understanding of the role of core thickness, core density and facesheet thickness on blast response. The test specimen is designed such that the structure experiences one-dimensional, uniaxial compressive loading. This eliminates the complexities associated with large scale beam

bending and facesheet stretching in blast loaded sandwich plates. Additionally, the performance of the sandwich core and facesheet thickness can be evaluated independently of each other. The height of the specimen is 50 mm and the diameter is 75 mm, which is approximately one order of magnitude smaller than composite sections used in ships. The peak pressure decay time of the incident loads are one order of magnitude smaller than those used in full-scale blast testing [164, 165]. Normalized metrics are used to quantify structural attributes, loading intensities and blast resistance to identify underlying trends and provide design guidance. The following major points can be drawn from this combined experimental and numerical analysis:

a) The momentum transmitted into the sandwich plate is highly dependent on core strength and density. Denser cores $\left(\bar{\rho} > 0.06\right)$ better resist the motion of the frontface and lead to greater momentum transfer.

b) At impulse intensities $\bar{I} > 0.15$, cores with $\bar{\rho} < 0.06$ undergo densification and collapse. On the other hand, for $\bar{I} > 0.15$ and $\bar{\rho} > 0.06$, $\varepsilon$ is 0.2 and almost constant at all loading intensities.

c) The momentum transmitted into the sandwich plates for $\Delta T_f / T_c < 0.1$ is substantially lower than that for $\Delta T_f / T_c > 0.15$. For the same core density, a 100% increase in facesheet thickness leads to a 25% and 50% increase in the core strain and in normalized transmitted impulse, respectively. The greatest momentum transfer occurs in the case of monolithic plates of equivalent mass as sandwich plates.

d) For a given incident impulse, $\Delta T_f / T_c > 0.15$ result in more severe core compression because the impulse acquired by the frontface increases in proportion to mass.

A set of experiments and simulations is carried out to correlate the performance of the sandwich plates under uniaxial compression with the performance under bending of a blast loaded sandwich plate [172]. Figure 74 shows a schematic illustration of the USLS with a simply-supported loading configuration. The sample size considered here is approximately one order of magnitude smaller than composite sections used in ships. The impulsive loads considered in this set of calculations have peak pressures of 40, 90, 140 and 175 MPa, which approximately correspond to 100 kg of TNT detonating at distances of 5.8, 2.83, 1.9 and 1.5 meters, respectively. These impulsive loads are of greater intensity than those analyzed using the Dynacomp setup. The facesheets are made of biaxial E-glass/vinylester composites and the core is PVC foam manufactured by DIAB Inc. [173]. Three PVC foam densities are analyzed: 60, 100 and 200 $kg \cdot m^{-3}$. The facesheets and cores are bonded together using the West System 105 epoxy resin and hardener. The designs considered in this analysis have similar areal masses. To compare the effects of different core densities on response, a relative density $\bar{\rho}$ similar to eqn. (71) is defined such that

$$\bar{\rho} = \frac{\rho_{core}}{\rho_{face}}. \tag{76}$$

Figure 75 shows a sequence of high-speed photographs of the deformation in different composite structures subjected to $p_0 = 175\,\text{MPa}$, which is the highest load intensity

considered in this analysis. Figure 75(a) shows the response of monolithic composite plate. The deformation can be divided into two regimes: (1) flexural wave propagation towards the supports and (2) structural deflection. The flexural wave travels towards the supports in a very short time (~50 μs). Although the resolution of the camera is sufficient to capture this phenomenon, we are more interested in structural response in the form of damage and out-of-plane deflection, which take place over a longer time span. Consequently, the temporal resolution of the camera is selected to capture the behavior over a duration of 2 milliseconds. The displacement of the backface is tracked at the midpoint and compared with that of other structures. Figure 75(b) shows the response of a sandwich structure with HP200 core subjected to $p_0 = 175$ MPa . The core fractures in a direction perpendicular to the planar wave and causes considerable core-face debonding in both the front and the back interfaces. Core compression is negligible and fragmentation is observed near the supports. Figure 75(c) shows the behavior of a sandwich structure with HP100 core. The HP100 core fractures at an inclined angle from the loading direction and simultaneously undergoes core compression and crushing. The response of a sandwich structure with an HP60 core is shown in Figure 75(d). Core compression and frontface wrinkling are observed at $t = 150\,\mu$s. Core indentation occurs at $t = 300\,\mu$s and the core starts to crack at $t = 450\,\mu$s. Damage and deformation in the sandwich structure with a HP60 core is significantly lower than those in the other structures. At high load intensities, it appears that the impulse imparted to the frontface causes it to move away at velocities higher than the allowable dynamic crush rate of the

core, resulting in large differential displacements which cause frontface fracture and core cracking, but negligible core compression.

Figure 76(a) shows the midpoint displacements as functions of time for the four different structures. The sandwich structures with HP200 and HP100 cores and the monolithic structures show relatively similar deformation histories reaching a $\Delta/L$ value of 0.25 at approximately the same rate. The sandwich structure with HP60 cores shows superior blast mitigation, deflecting at a lower rate and reaching a $\Delta/L$ value of 0.17, which is ~60% of that for the other sandwich structures. The results show that core density and load intensity profoundly affect both the rate and the extent of deformation in the composite structures. The study indicates that structure with low density cores consistently outperform structures with high density cores of equal mass. Lower core density and thicker the core correspond to reduction in velocity due to more significant core compression. Additionally, variations in geometric parameters have an effect on flexural rigidity and deformation. Since a fully dynamic computational framework is used to in this analysis, structural effects beyond bending, as well as bending, are captured.

Minimizing the impulse transmitted to the internal components of marine vessels is of critical importance. The rate of impulse transmission and the magnitude of the transmitted impulse can provide valuable insight into the blast resistance and performance of composite structures. Clearly, the composite structure that transmits the least impulse at the lowest rate is most desirable.

Figure 76(b) shows the histories of impulses transmitted by air-backed structures subjected to incident impulsive loads of different magnitudes. For an incident impulse

with $p_0 = 175\,\text{MPa}$, the sandwich structures with HP200, HP100 and HP60 cores transmit ~40%, 30% and 20% of the impulse transmitted by the monolithic composite, respectively. Correlating the rate of impulse transmission with the core characteristics in each case shows that, as the core density decreases and core thickness increases accordingly, the rate of impulse transmission decreases significantly.

Figure 77 shows the normalized deflection $(\Delta/L)$ as a function of impulse $\bar{I}$ for structures with different normalized relative densities $\bar{\rho}$. A monotonically increasing trend of center deflections with increasing core density is seen and shows reasonable agreement with experiments. At all impulse magnitudes, structures with the lowest relative density experience the least deflections. The deflection increases with increasing relative density and impulse magnitude. The structure with the HP200 core performs only marginally better than monolithic structures. The HP100 and HP60 cores yield significantly higher blast resistances in comparison to the HP200 core and the monolithic composite. Figure 78(a) shows the loading-structure-performance map of normalized deflection $(\Delta/L)_{AB}$ as a function of impulse $\bar{I}$ and relative density $\bar{\rho}$. As core density increases, the out-of-plane deflection of the sandwich plates increases dramatically. Figure 78(b) shows the loading-structure-performance map of transmitted impulse for air-backed structures $(\bar{I}_B)$ as a function of normalized incident impulse $\bar{I}$ and normalized relative density $\bar{\rho}$. At all impulse magnitudes, structures with the lowest relative density transmit the least impulse. The transmitted impulse increases with increasing relative density as well as impulse magnitude. HP200 cores perform better than monolithic structures while HP100 and HP60 cores exhibit significantly higher blast mitigation in

comparison to HP200 core and the monolithic composite. Thus, low density cores lead to lower values of deflection as well as lower transmitted impulse at all impulse intensities.

The loading-structure-performance maps for uniaxial compressive loading (Figure 65 and Figure 68) are compared with those for the simply-supported bend loading configuration (Figure 78) to gain insight into the role of core density on bending and failure. Higher core densities $\left(0.06 < \bar{\rho} < 0.1\right)$ limit core crushing, enable higher energy absorption and help maintain the bending strength of a sandwich plate, but result in significantly more momentum being imparted to the structure. This leads to more severe core damage and out-of-plane deflection. Conversely, lower density cores $\left(0.01 < \bar{\rho} < 0.06\right)$ are susceptible to collapse under high intensity loads which can have adverse effects on survivability and residual bending strength. The trade-off between core compression and impulse transmission needs to be considered depending on application. In marine structures supported by stiffeners with water on the impulse side and air on the downstream side, the core has to provide load spreading and impulse absorption capabilities. Since an air-backed sandwich structure is free to deform in the out-of-plane direction, low density cores with $0.01 < \bar{\rho} < 0.06$ can satisfy both requirements and are optimal in such situations [161, 174, 175]. Performance in water-backed conditions is important for the design of parts of ship structures like turbine blades, hull and keel. Water-backed conditions also prevail in underwater pipelines and ducts. Moreover, sections backed by movable equipment and machinery create conditions similar to water-backed loading conditions. In these cases, damage is localized and the structure is relatively undamaged in regions that are away from the loading area. Tensile loads and

fracture in both faces are negligible due to the lack of overall deflection and bending, but the cores undergo severe compression [161, 174, 175]. Consequently, higher core densities are essential in order to maintain structural integrity in case of a blast event. Since minimizing core compression is essential in water-backed conditions, core densities with $0.06 < \bar{\rho} < 0.1$ are most optimal because data in Figure 66(a-d) for $0.01 < \bar{\rho} < 0.06$ suggest that structures are susceptible to collapse under high intensity loads.

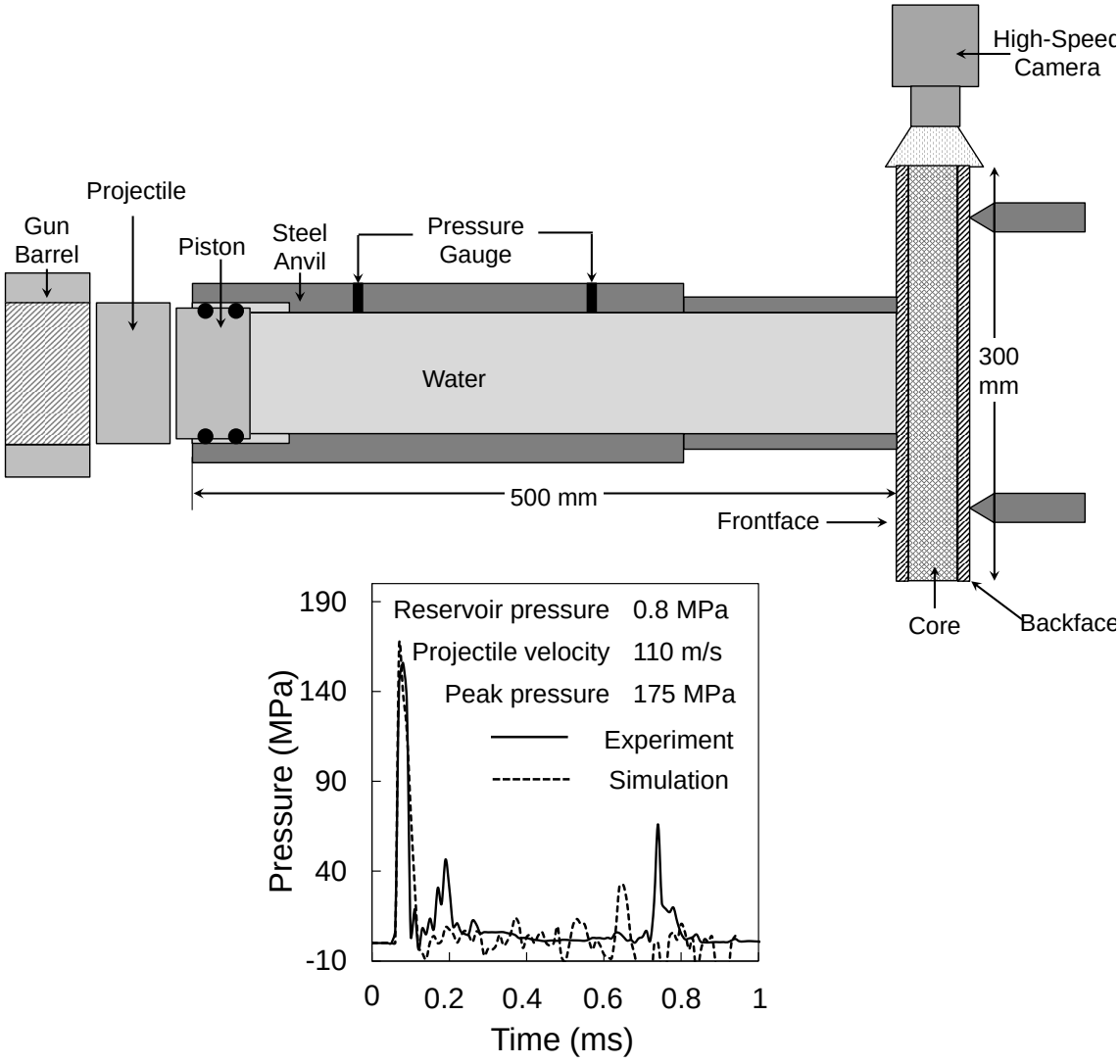


Figure 74 A schematic illustration of the simply-supported air-backed loading configuration within Underwater Shock Loading Simulator (USLS). The incident impulse has a peak pressure of $p_0 = 175$ MPa, which is significantly higher than the peak pressures analyzed using the Dynacomp setup.

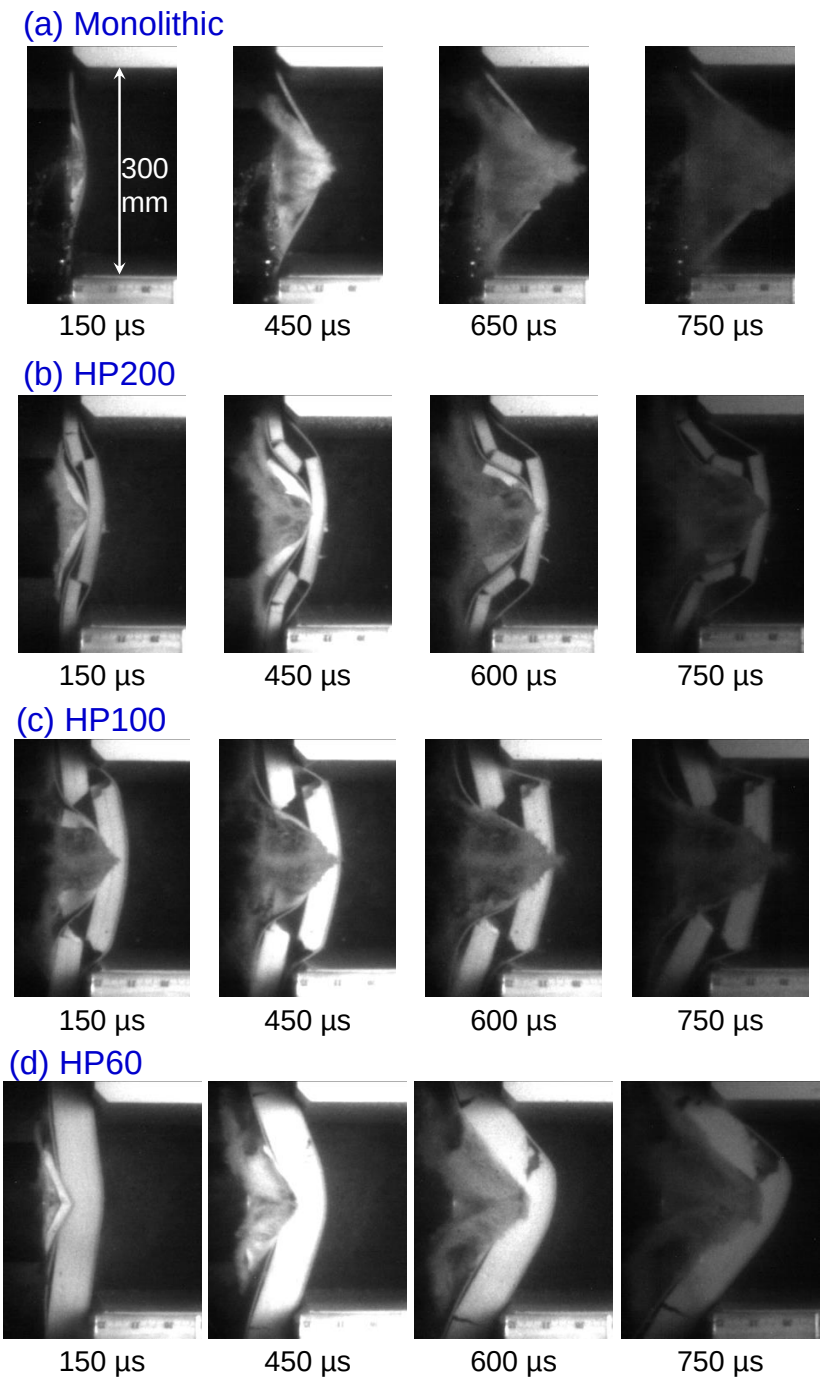


Figure 75 Sequence of high-speed photographs showing the deformation in composite structures subjected to $p_0 = 175$ MPa. The impulse imparted to the frontface causes it to move away at a velocity higher than the allowable dynamic crush rate of the core resulting in large differential displacements which cause frontface fracture and core cracking, but relatively low core compression.

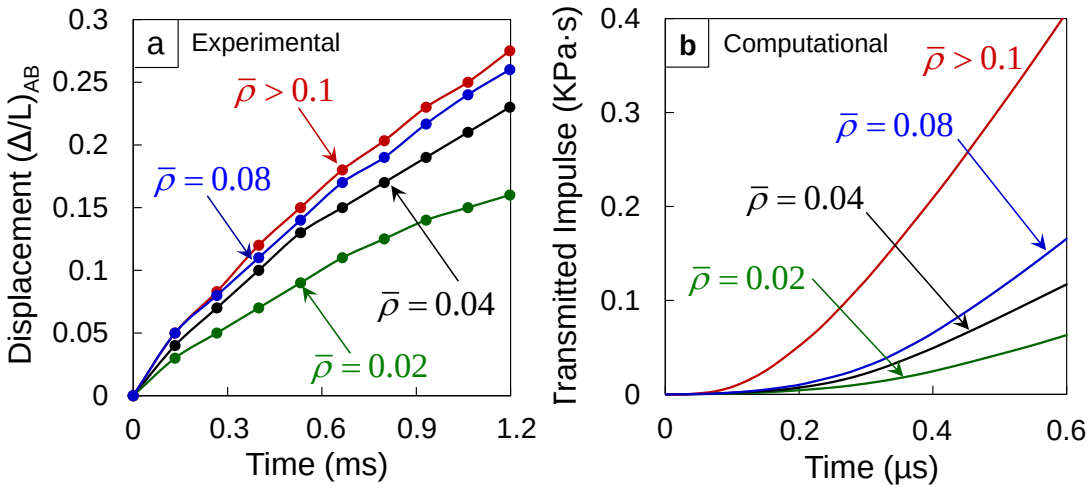


Figure 76 (a) Experimentally measured midpoint displacements and (b) computationally calculated measured transmitted impulses as functions of time for air-backed sandwich structures subjected to an impulse with $p_0 = 175$ MPa.

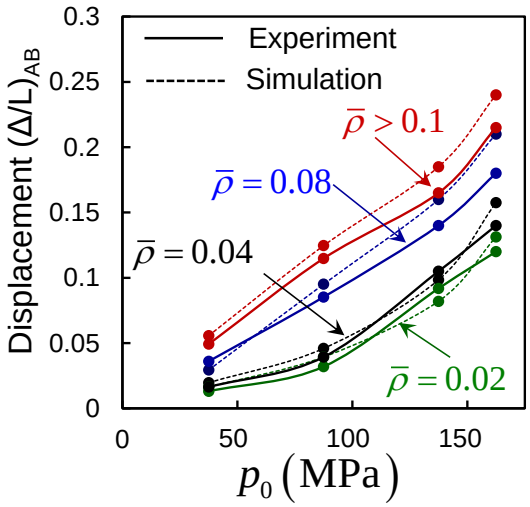


Figure 77 Comparison of experimentally measured and numerically calculated mid-plane deflections at 1000 μs in air-backed structures as functions of normalized incident impulse $p_0$ for different normalized core densities. The results from experiments are in good agreement with those obtained from finite element simulations.

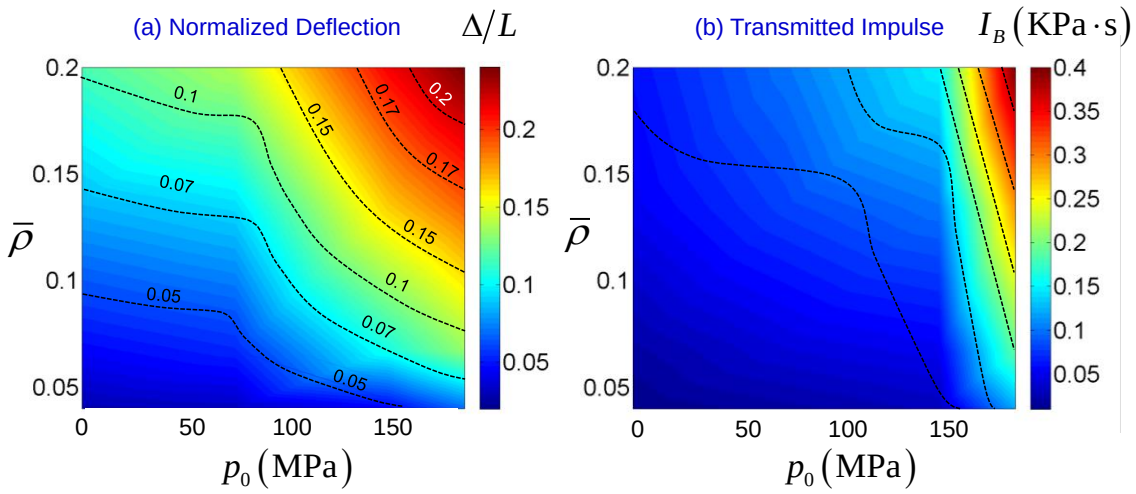


Figure 78 Loading-structure-performance maps for simply-supported sandwich plates showing (a) deflection and (b) transmitted impulse as functions of peak pressure $p_0$ and normalized density $\bar{\rho}$.

## 7.6 Concluding remarks

In addition to providing high bending and shear resistances and enhancing the strength-to-weight ratio of structures, sandwich cores must balance strength and the ability to absorb and retard incoming impulses in order to be effective in protective structures against blast and impact. Polymeric structural foams are especially attractive because of their lightweight, ease of manufacturing, high corrosion resistance, good thermal insulation, and low water absorption. However, due to their wide range of possible densities and structural design attributes, the relationship between the behavior of these foams and incident underwater impulsive loads has yet to be fully established. In an effort to provide quantitative relations for structural design, we have evaluated the load-carrying and impulse transmission capabilities of sandwich structures with PVC foams of a range of density, facesheet thicknesses and incident load intensity. A series of

experiments and numerical simulations are carried out, accounting for effects of structural attributes and loading rates on performance. The loading conditions involve impulsive loads with peak pressures up to 100 MPa, which simulate the effects of an explosive TNT source detonating underwater at different standoff distances from the structure.

The conclusions of this study relating to the load-carrying and blast mitigation capacities of sandwich plates with polymeric foam cores are as follows:

1. The compressive strain experienced by and the impulse transmitted by the sandwich core pose opposing requirements on structural design. Low density cores experience high compressive strains while transmitting lower impulses. On the other hand, high density cores behave like monolithic plates and transmit large fractions of the incident impulse. Although low density cores transmit significantly lower impulses, it should be noted that the kinetic energy acquired by frontfaces in low density cores is much higher, leading to severe core compression. This increased core compression is detrimental to bending stiffness and strength. Structural design must balance the competing requirements.
2. Experiments and simulations are in reasonable agreement in terms of the extent of core compression and impulse transmission. Over the range of impulses and structural configurations considered, the finite element predictions are within 10% of the experimental data. The homogenized, crushable foam constitutive model employed provides accurate tracking of the early stage response of the core material. However, the model slightly overestimates the compliance of the core leading to an increase in core compressive strain and a decrease in the transmitted

impulses in comparison to experiments. The numerical calculations have provided an in-depth understanding of the temporal and spatial evolution of deformation modes in the core material.

3. Cores with different densities show significantly different deformation behaviors. Low density cores like HP60, HP100 and HP130 $\left(0.01 < \bar{\rho} < 0.06\right)$ experience rather uniform straining throughout their thickness and provide high impulse mitigation capacity. High density cores such as HP200 and HP250 $\left(0.06 < \bar{\rho} < 0.1\right)$ experience strain localizations that occur primarily near the facesheets. Such non-uniform distribution of straining leads to high impulse transfer and severe damage in the core material.
4. Loading-structure-performance maps derived from uniaxial compressive loading are compared to those obtained from the simply-supported bend loading configuration to offer insight into the role of core density on bending and failure of sandwich structures. The relative core density is found to be an important parameter determining the performance of sandwich structures in simply-supported conditions. Greater core compressibility minimizes both the deflection and impulse transmission in this configuration. Higher core densities $\left(0.06 < \bar{\rho} < 0.1\right)$ limit core crushing, enable higher energy absorption and help maintain the bending strength of a sandwich plate, but result in significantly more momentum being imparted to the structure. This leads to higher core damage and out-of-plane deflection. Conversely, lower density cores $\left(0.01 < \bar{\rho} < 0.06\right)$ are

susceptible to collapse under high intensity loads which can have adverse effects on survivability and residual bending strength.

5. The frontface and backface masses are varied independently and results indicate that the frontface mass has a significant influence on core compression and impulse transmission, while the backface mass has a negligible effect on structural response. The momentum transmitted into the sandwich plates with $\Delta T_f / T_c < 0.1$ is substantially lower than that for $\Delta T_f / T_c > 0.15$. For the same core density, a 100% increase in facesheet thickness leads to a 25% and 50% increase in the core strain and normalized transmitted impulse, respectively. The greatest momentum transfer occurs in the case of monolithic plates of equivalent mass as sandwich plates. For a given incident impulse, $\Delta T_f / T_c > 0.15$ results in severe core compression and collapse because the impulse acquired by the frontface increases in proportion to mass.

In this combined experimental and numerical study, a parametric approach is employed to develop loading-structure-performance maps to quantify core compression, deflection and impulse transmission as a function of incident load (air-backed or water-backed conditions, load intensity), structural attributes, and loading configurations. The insight gained here provides guidelines for the design of structures for which response to water-based impulsive loading is an important consideration. Finally, it should be noted that the design maps described in this paper are applicable only for the structural attributes and loading conditions considered herein.

# 8. GLASS-FIBER/PVC FOAM SANDWICH STRUCTURES

## 8.1 Introduction

The objective of the present study is to characterize the damage response of sandwich composites with different core densities but similar total masses. The focus of this analysis is on understanding the deformation and failure mechanisms, and quantifying the damage in composite structures as a function of structural attributes, material properties, loading conditions and loading rates. The loading of interest is high intensity water-based impulsive loads. Planar impulses resembling those resulting from underwater explosions are generated using the Underwater Shock Loading Simulator (USLS), a novel experimental setup developed recently. The USLS consists of a projectile-impact-based impulsive loading system, a water chamber, a target holder, and a safety enclosure. The target holder allows clamped and simply-supported boundary conditions. The experiments are designed to quantify the resistance of each structural configuration to underwater impulsive loads The response and failure mechanisms studied include overall deflection, face wrinkling, core-face debonding, core compression, core shear cracking and rupture. Of particular interest is the influence of load intensity and sandwich core characteristics on deformation and failure.

This is a combined experimental and computational study. Finite element simulations are carried out, accounting for the experimental conditions and material properties which are measured independently. The simulations also account for the fluid-structure interaction (FSI) effect at the water-composite interface. Failure mechanisms

considered include shear cracking and fragmentation in the core, cracking in the face sheets, and core-face interfacial debonding. The simulations focus on damage initiation and evolution in the early stage of deformation (~1000 μs) since the load-carrying capacity is most critically reflected then. This combined experimental and numerical approach enables the identification of factors that play important roles in determining the dynamic response of the materials. The analysis uses metrics such as deflection, energy absorbed and impulse transmitted to quantify blast resistance. The results are presented in normalized forms to identify underlying trends in material and structural response.

Figure 79(a-d) shows the comparison of experimentally measured and numerically calculated pressure histories corresponding to four different projectile velocities. The rise time of the pressure pulses is on the order of 25 μs and the decay time is on the order of 800 μs. The impulsive loads considered in this set of calculations have peak pressures of 40, 90, 140, 175, and 245 MPa which approximately correspond to 100 kg of TNT detonating at distances of 5.8, 2.83, 1.9 and 1.5 meters respectively. The incident impulse magnitudes are $I = \int_0^t p(t)dt =$ 0.11,0. 228, 0.359 and 0.424 kPa·s. The normalized impulse magnitudes calculated using eqn. (67) are .. 0.015, 0.035, 0.055 and 0.065, respectively.

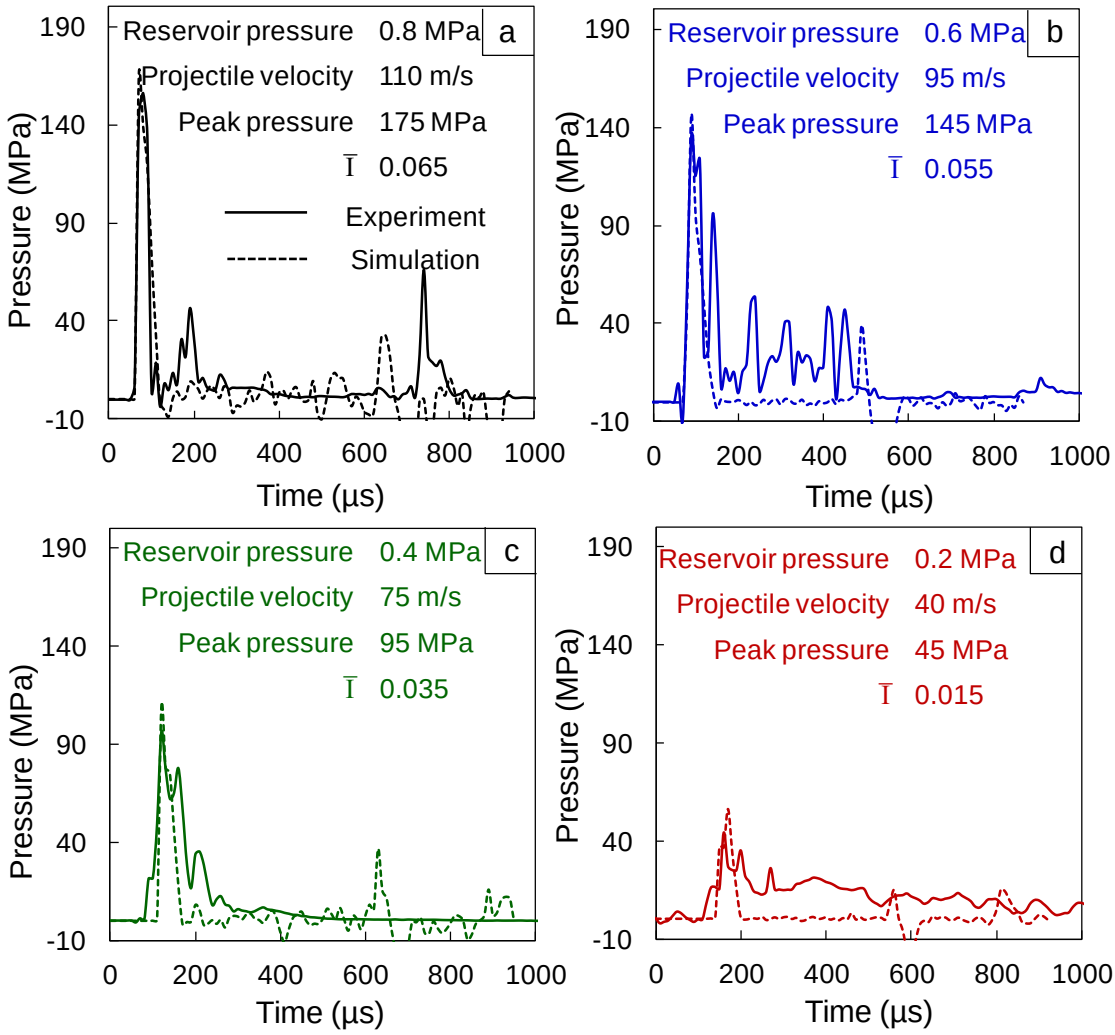


Figure 79 Experimentally measured and numerically calculated pressure histories in the water chamber for four different projectile velocities and impulse magnitudes $\bar{I} = 0.015, 0.035, 0.055$ and $0.065$.

## 8.2 Materials and panel construction

The facesheets are made of biaxial E-glass/vinylester composites and the core is PVC foam manufactured by DIAB Inc. [173]. Three PVC foam densities are used: 60, 100 and 200 kg·m$^{-3}$. The sandwich structures analyzed here are in the form of beam

specimens 300 mm in length and 80 mm in width. The four different specimen designs are as follows:

1. Composite monolithic panel consisting of biaxially oriented $\left[(0/90/0/90)_S\right]$ glass fabric infiltrated with West System 105 epoxy resin. The panel thickness is 6 mm.
2. Sandwich structure with glass fiber reinforced facesheets of thickness 2.5 mm and Divinycell HP60 core with a thickness of 30 mm for a total thickness of 35 mm.
3. Sandwich structure with glass fiber reinforced facesheets of thickness 2.5 mm and Divinycell HP100 core with a thickness of 20 mm for a total thickness of 25 mm.
4. Sandwich structure with glass fiber reinforced facesheets of thickness 2.5 mm and Divinycell HP200 core with a thickness of 10 mm for a total thickness of 15 mm.

The facesheets and cores are bonded together using the West System 105 epoxy resin and hardener. The four designs considered in this analysis have similar areal masses. This sample size is approximately one order of magnitude smaller than composite sections used in ships. To compare the effects of different core densities on response, a relative density defined as

$$\bar{\rho} = \frac{\rho_{core}}{\rho_{PVC}} \tag{77}$$

is used. For the monolithic composite (which does not have a PVC foam core), the relative density is calculated by

$$\bar{\rho} = \frac{f_{matrix} \cdot \rho_{matrix}}{f_{fiber} \cdot \rho_{fiber}}, \tag{78}$$

where $f_{matrix}$ and $\rho_{matrix}$ are the volume fraction and density of the matrix, respective, and $f_{fiber}$ and $\rho_{fiber}$ are the volume fraction and density of the reinforcement, respectively. In a large naval structure, such as a ship or a submarine, structural components are in different service environments and are subject to different loading conditions. For example, ship hulls and superstructures are in contact with water on the outer side (impulse side) and air on the inner side. On the other hand, the keel, rudder, propeller blades and underwater pipelines are in contact with water on both sides (the impulse side and the protected side). For the purpose of the current study, the former is called the air-backed configuration [Figure 80(a)] and the latter is called the water-backed configuration [Figure 80(b)]. The different composite structures and the corresponding geometrical dimensions and areal masses are presented in Table 9.

Table 9 Experiment schedule. The thicknesses of the facesheets are varied to maintain similar areal masses in the composite structures.

| **Beam Designation** | **Core Density ($kgm^{-3}$)** | **Core Thickness (mm)** | **Facesheet Thickness (mm)** | **Areal Mass ($kgm^{-2}$)** |
|---|---|---|---|---|
| M 1,2,3,4 | - | - | 6 | 10.5 |
| HP60 1,2,3,4 | 60 | 30 | 3 | 10.7 |
| HP100 1,2,3,4 | 100 | 20 | 3 | 10.9 |
| HP200 1,2,3,4 | 200 | 10 | 3 | 10.9 |

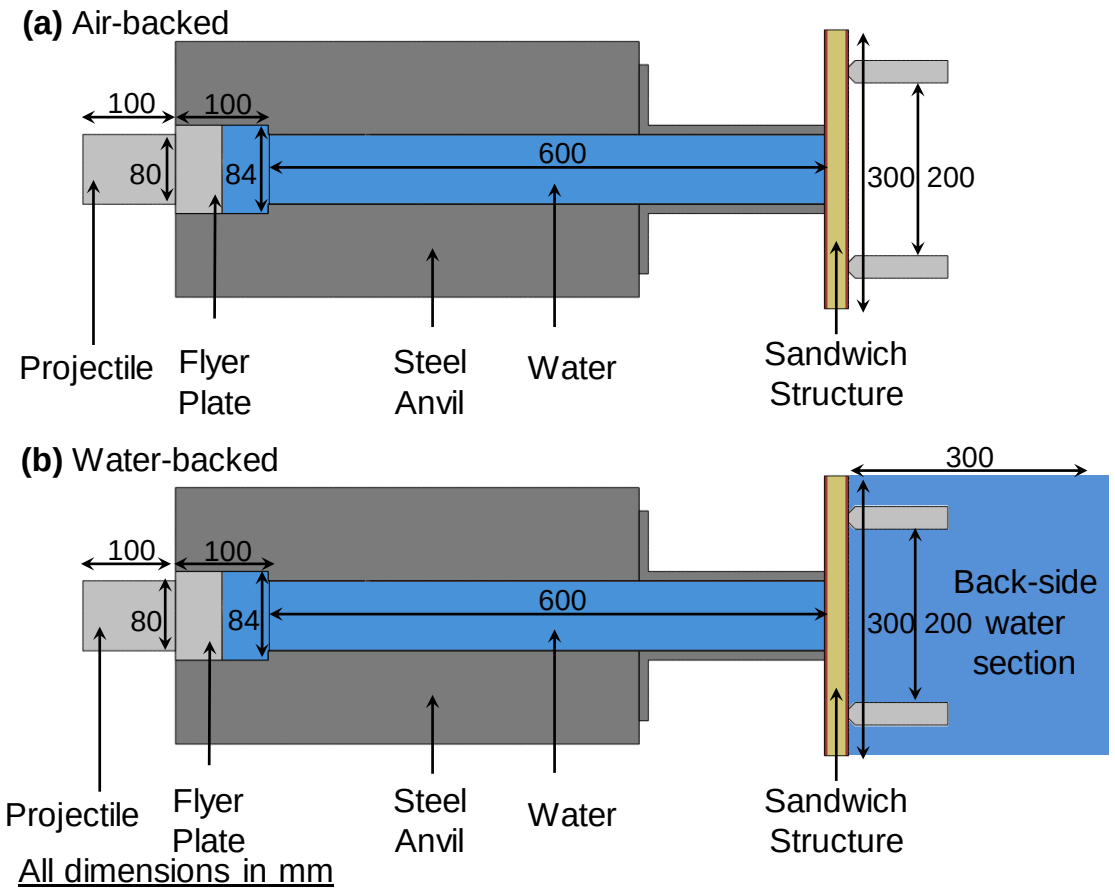


Figure 80 Schematic illustration of the USLS and simply-supported sandwich structure in (a) air-backed and (b) water-backed configurations.

## 8.3 Experimental results

### 8.3.1 Deformation modes and failure mechanisms

When the underwater impulsive wave impinges on the target, a number of deformation and failure modes are observed in the sandwich composite. Due to structural deflection and bending, the frontface experiences compressive loading which causes face wrinkling which is resisted by the core. Frontface buckling can ultimately lead to matrix cracking and fiber-matrix debonding followed by rupture. Failure in the frontface is followed by core compression, core shear cracking and fragmentation. Initially, the core

undergoes rapid compression near the load region, a phenomenon called "core indentation". Triantafillou and Gibson [176, 177] showed that the indentation load is set by plastic yielding in the core and simultaneous inelastic deformation in the frontface. Since the facesheets in this set of experiments are relatively thin, it can be assumed that the core collapses at uniform shear strength with negligible additional strength provided by the facesheets. Due to the simply-supported loading configuration, the backface experiences maximum stresses near the midplane and fails under tensile loading. The interfaces between the core and facesheets are subjected to multi-axial loads due to the complicated deformation modes in both the facesheets and the core.

### 8.3.2 Effect of core density

Figure 81 shows a sequence of high-speed digital images of a monolithic composite plate subjected to an underwater impulsive load in the USLS. The projectile velocity is 75 $ms^{-1}$, the peak pressure is 95 MPa and the resulting impulse corresponds to $\bar{I} = 0.035$ shown in Figure 79(c). In addition to the water flowing out of the water-chamber, a thin Mylar film used for sealing the water-chamber can be seen to the left of the panel. The deformation can be divided into two regimes: (1) flexural wave propagation towards the supports and (2) structural deflection. The flexural wave travels towards the supports in a very short time (~50 μs). Although the resolution of the camera is sufficient to capture this phenomenon, we are more interested in structural response in the form of damage and out-of-plane deflection, which take place over a longer time span. Consequently, the temporal resolution of the camera is selected to capture the behavior over a duration of 2 milliseconds.

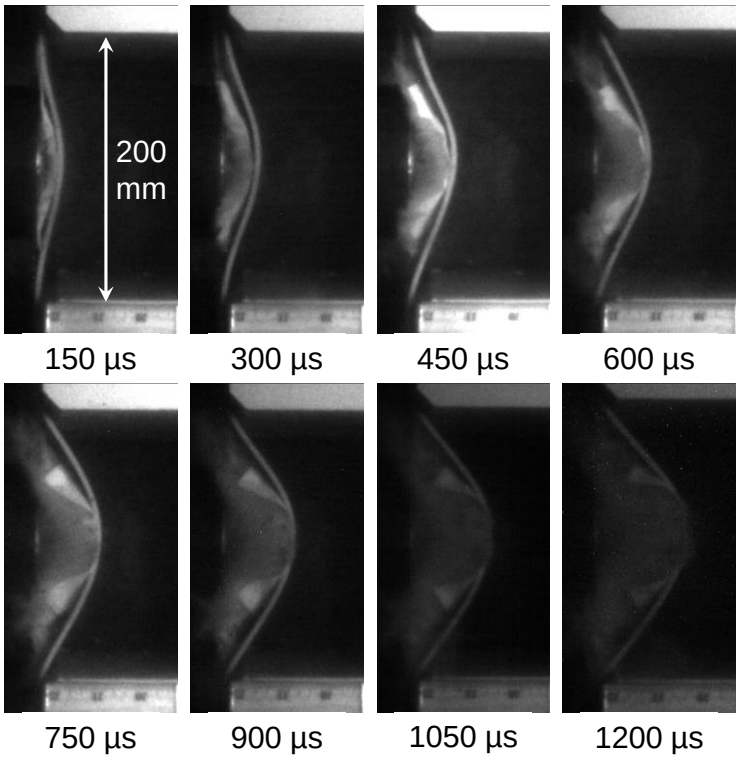


Figure 81 Sequence of high-speed photographs showing the deformation in a monolithic composite plate subjected to underwater impulsive loading with $\bar{I} = 0.035$.

The displacement of the backface is tracked at the midpoint and compared with that of other structures. Although the deformation and damage in sandwich structures can be tracked using high-speed digital imaging, the monolithic composite plate is quite thin and damage mechanisms are hard to discern from high-speed photographs. These damage mechanisms are revealed in post mortem photographs of the monolithic composite plate shown in Figure 82(a-c). Figure 82(a) shows the deformed monolithic plate with clearly formed hinges near the load site which experiences the highest impulsive load. Figure 82(b) and (c) show delamination between successive layers in the laminate, matrix cracking, fiber pullout and rupture. While the deflection is relatively uniform over the length of the composite plate, damage mechanisms are predominantly observed near the

circumference of the shock tube and near the supports, indicating significant influence of shear effects in damage creation.

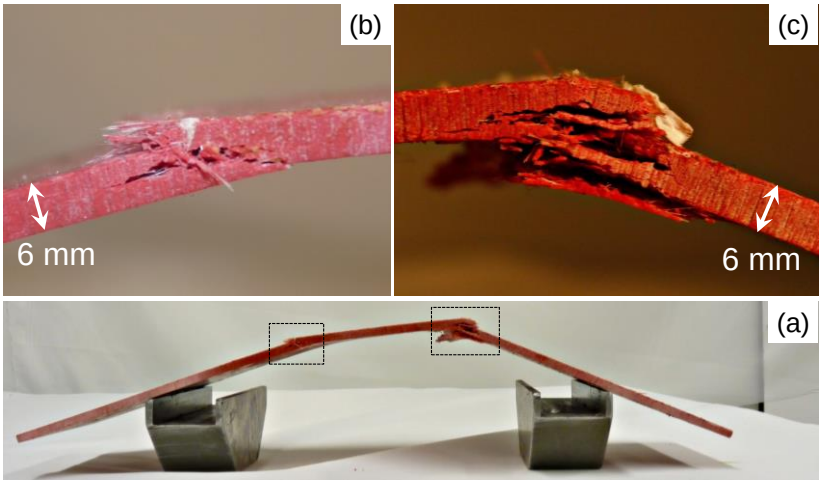


Figure 82 Post mortem photographs of impulsively loaded composite plates with cross sections showing inter laminar delamination, matrix cracking, fiber matrix debonding, fiber pullout and intra laminar cracking.

Figure 83 shows a sequence of high-speed photographs of a composite sandwich structure with a Divinycell HP200 core subjected to $\bar{I} = 0.035$ as shown in Figure 57(c). Initially, flexural waves travel through the frontface, severing the core facesheet bond. In cases where the core facesheet bond is stronger than the PVC foam, a layer of core material is separated by the facesheet due to the low tensile strength of PVC foam. Core-face debonding and core failure due to cracking and fragmentation are observed at $t = 50\,\mu s$. Core crushing commences at $t = 150\,\mu s$ and is restricted to the region close to the loading area. Core cracking and fragmentation occurs and the structure experiences complete failure at $t = 1200\,\mu s$.

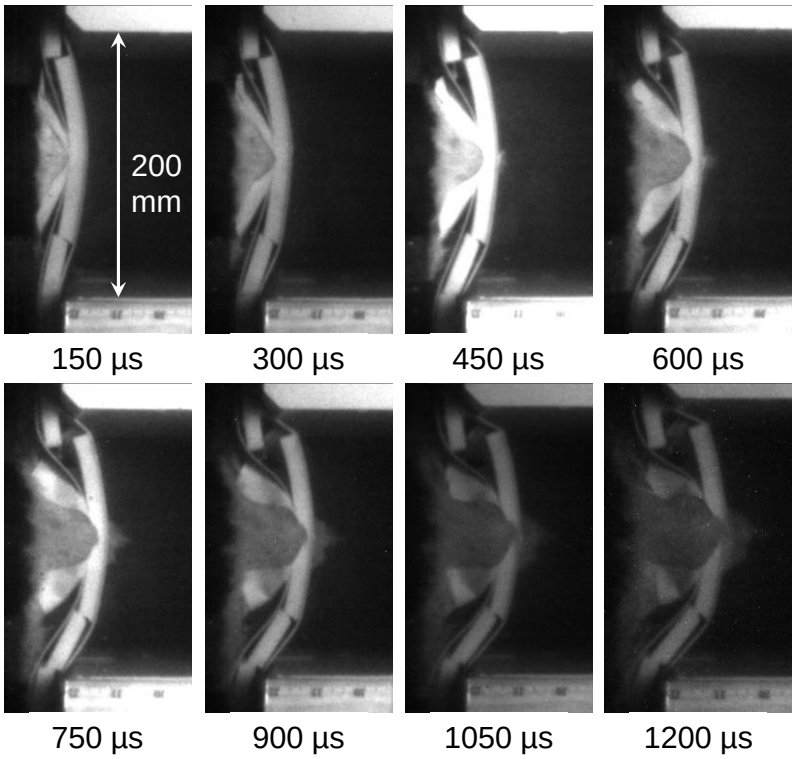


Figure 83 Sequence of high-speed photographs showing the deformation in a sandwich structure with HP200 core subjected to underwater impulsive loading with $\bar{I} = 0.035$. Large scale core frontface debonding and core fragmentation can be observed. The core fractures prior to core compression and rupture occurs at $t = 900\,\mu s$.

Figure 84 shows a sequence of high-speed photographs of a composite sandwich structure with a Divinycell HP100 core subjected to $\bar{I} = 0.035$. Core-facesheet debonding and frontface wrinkling failure occur at $t = 50\,\mu s$ followed by core indentation at $t = 150\,\mu s$. In core indentation failure, the core material fails in a highly localized region, leading to compressive stresses in the frontface which cause frontface buckling. The damage mechanisms in the frontface for this type of deformation are in the form of fiber rupture and matrix cracking. Shear dominated cracks originate near the supports at $t = 300\,\mu s$ followed by core cracking $t = 900\,\mu s$. This structure does not experience rupture.

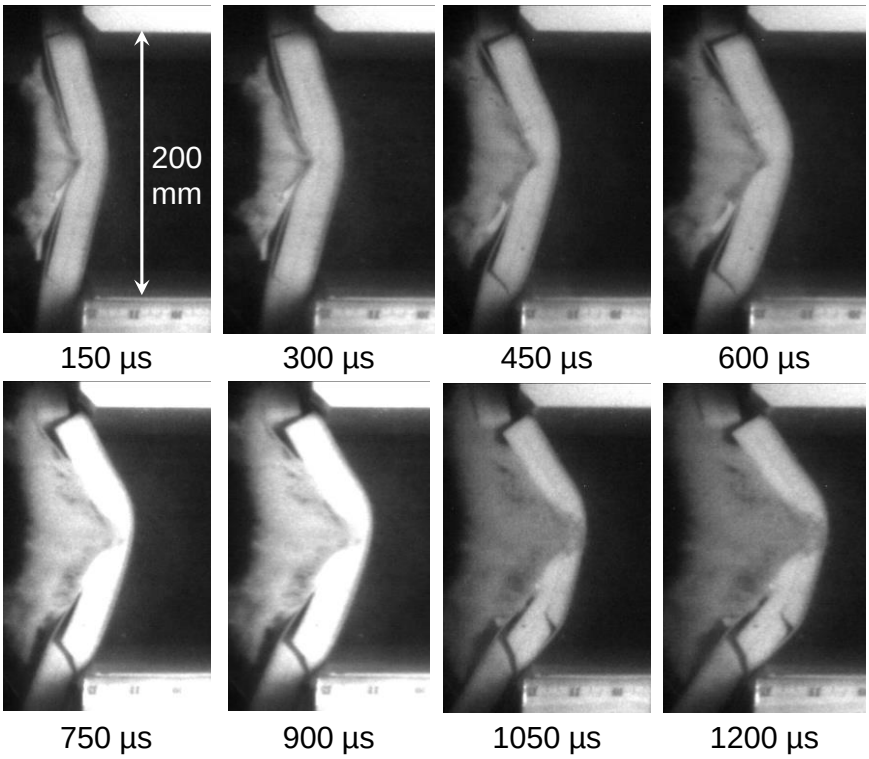


Figure 84 Sequence of high-speed photographs showing the deformation in a sandwich composite with HP100 core subjected to underwater impulsive loading with $\bar{I} = 0.035$. Frontface wrinkling and core indentation occurs at $t = 300\,\mu s$. Inclined cracks initiated at $t = 600\,\mu s$ and were followed by rupture at $t = 900\,\mu s$.

Figure 85 shows a sequence of high-speed photographs of a composite sandwich structure with a Divinycell HP60 core subjected to $\bar{I} = 0.035$. The response of the sandwich structure with a HP60 core is quite different from those with HP100 or HP200 cores in that there is no core shear cracking, frontface wrinkling and core face debonding. Core compression commences immediately after the onset of loading at $t = 150\,\mu s$ and inclined cracks originate near the loading circumference area.

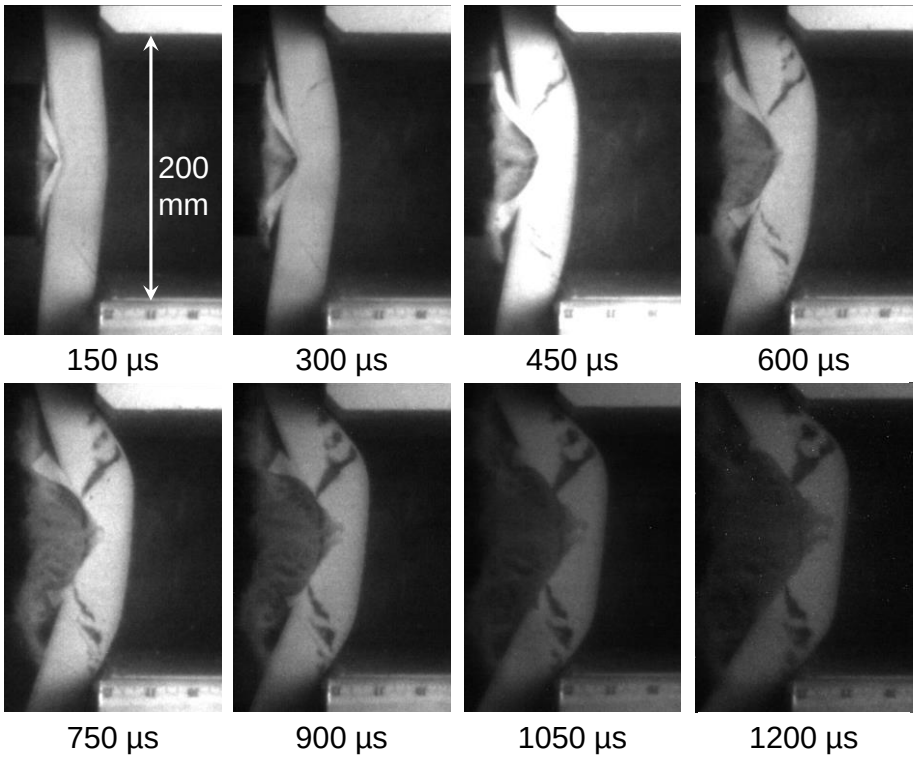


Figure 85 Sequence of high-speed photographs showing the deformation in a sandwich composite with HP60 core subjected to underwater impulsive loading with $\bar{I} = 0.035$. Deformation in the core is quite uniform and bending deformation occurs prior to core cracking. Core face debonding is relatively less widespread and facesheet wrinkling does not occur.

These cracks propagate from the frontface to the backface and branch into multiple cracks (at $t = 450\,\mu s$) near the backface, causing core backface debonding. After core face debonding, core fragmentation initiates. Core compression and core cracking occur simultaneously with crack propagation through the core. Core indentation (localized compressive failure) in HP60 cores occurs to a greater extent than HP100, primarily due to the fact that HP60 compresses at a much lower load than HP100. This indicates that there is a lower limit on core density for a blast-resistant structures. It should be noted that among all the structures studied here, HP60 is the only core for which no catastrophic failure is observed at any load intensity studied.

The midpoint deflections for each composite structure are shown in Figure 86. The monolithic composite structure is used as a benchmark for comparison with sandwich structures. It is determined that the lower the deflection when compared to that of the monolithic composite plate at a particular time, the better is the blast resistance. Figure 86(a) and (b) show the normalized deflection $\Delta/L$ (where $\Delta$ is deflection and $L$ is the span of the composite panel) of composite structures subjected to $\bar{I} = 0.035$ and $\bar{I} = 0.055$, respectively. A comparison of the initial slopes of the deflection vs. time plots shows that the structures with higher relative densities move most rapidly in the direction away from the impulsive load direction. As the loading rate increases, the rate of deflection also increases monotonically. The monolithic composite experiences the highest deflection at the highest rate compared with the sandwich structures. The sandwich structure with HP100 core initially exhibits a rate of deformation that is similar to the sandwich structure with HP200 core but the response of HP100 core diverges at $t = 400\,\mu s$ and the rate of deflection increase decreases. For the sandwich structure with HP60 core, the rate of deflection increase is the lowest among all three structures studied for both load intensities.

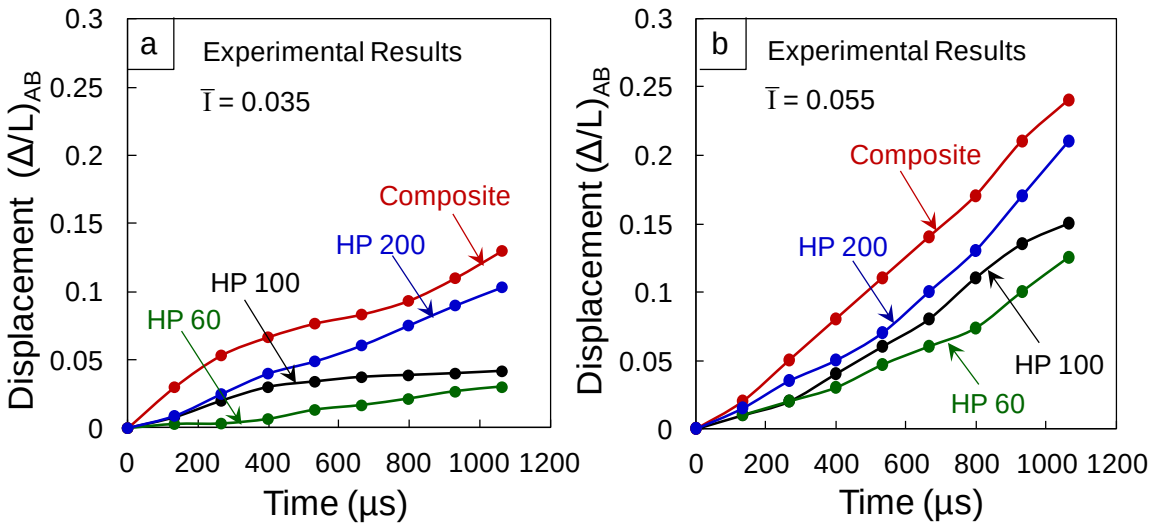


Figure 86 Experimentally measured midpoint displacements as functions of time for sandwich structures subjected to (a) $\bar{I} = 0.035$ and (b) $\bar{I} = 0.055$.

### 8.3.3 Effect of load intensity

The effect of loading rate on blast resistance is evaluated through a range of incident impulsive load intensities shown in Figure 79. Figure 87 presents a sequence of high-speed photographs showing the deformation in different composite structures subjected to $\bar{I} = 0.065$, which is the highest load intensity considered in this analysis. Figure 87(a) shows the response of monolithic composite plate which is similar to what is seen in the high-speed photographs of a monolithic composite subjected to $\bar{I} = 0.035$ discussed earlier. The effect of load intensity is much more significant for sandwich structures due to the nature of the dynamic behavior of the core materials. Figure 87(b) shows the response of a sandwich structure with HP200 core subjected to $\bar{I} = 0.065$. The core fractures in a direction perpendicular to the planar wave and causes considerable core-face debonding in both the front and the back interfaces. Core compression is negligible and fragmentation is observed near the supports. Figure 87(c) shows the

behavior of a sandwich structure with HP100 core. The HP100 core fractures at an inclined angle from the loading direction and simultaneously undergoes core compression and crushing. The response of a sandwich structure with an HP60 core is shown in Figure 87(d). Core compression and frontface wrinkling are observed at $t = 150\,\mu s$. Core indentation occurs at $t = 300\,\mu s$ and the core starts to crack at $t = 450\,\mu s$. Damage and deformation in the sandwich structure with a HP60 core is significantly lower than those in other composite structures. At high load intensities, it appears that the impulse imparted to the frontface causes it to move away at velocities higher than the allowable dynamic crush rate of the core, resulting in large differential displacements which cause frontface fracture and core cracking, but negligible core compression. Figure 88(a) shows the midpoint displacements and velocities as functions of time for the four different structures. The sandwich structures with HP200 and HP100 cores and the monolithic structures show relatively similar deformation histories reaching a $\Delta/L$ value of 0.25 at approximately the same rate. The sandwich structure with HP60 cores shows superior blast mitigation, deflecting at a lower rate and reaching a $\Delta/L$ value of 0.17, which is ~60% of that for the other sandwich structures.

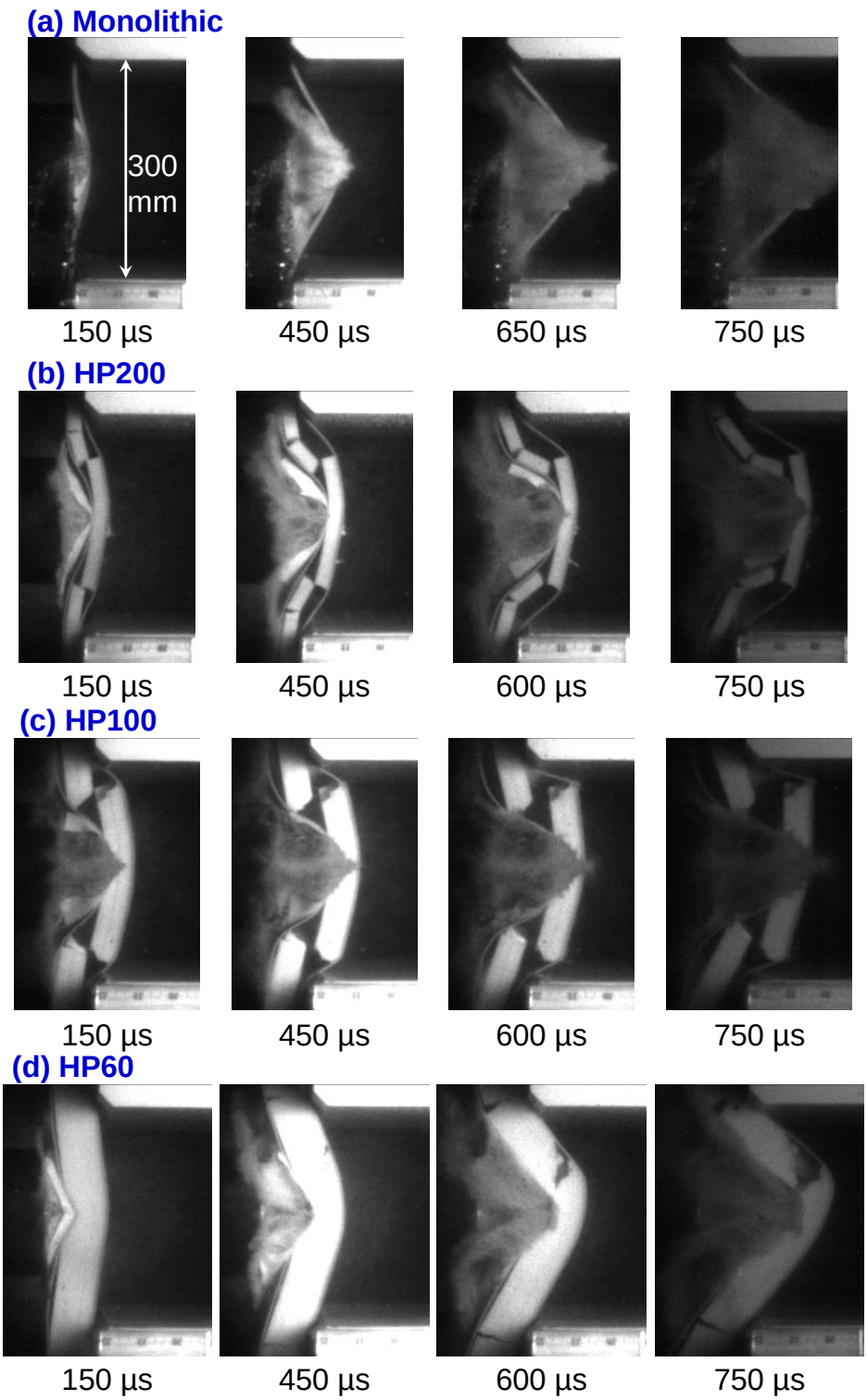


Figure 87 Sequence of high-speed photographs showing the deformation in composite structures subjected to $\bar{I} = 0.065$.

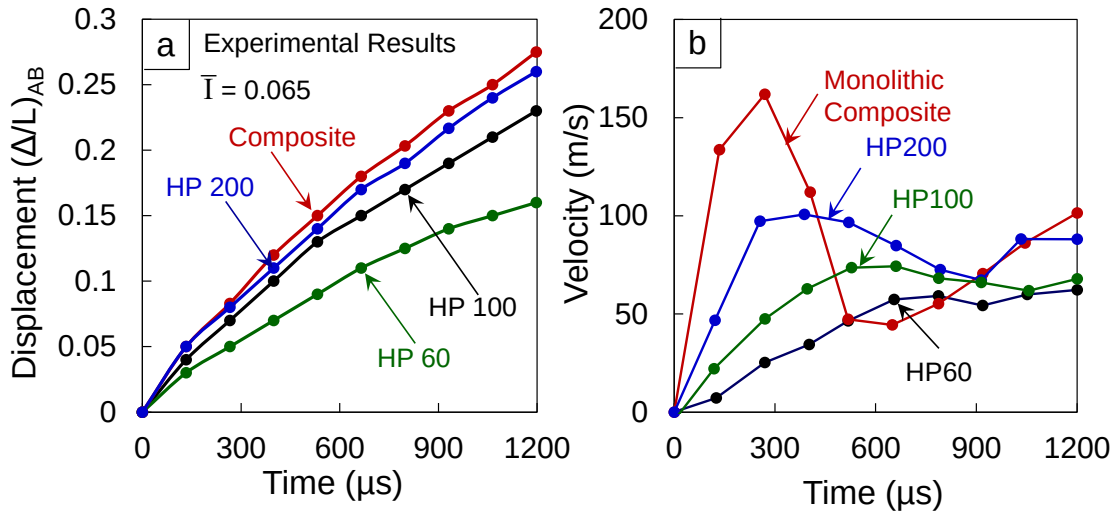


Figure 88 Experimentally measured midpoint displacements and velocities as functions of time for sandwich structures subjected to $\bar{I} = 0.065$.

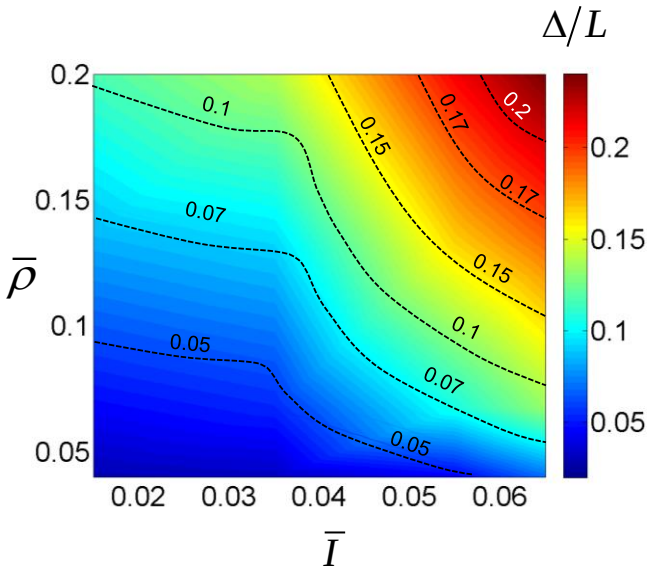


Figure 89 Normalized deflections in air-backed structures as functions of normalized incident impulse $\bar{I}$ and normalized density $\bar{\rho}$. On a unit weight basis, low density cores consistently outperform high density cores. Sandwich structures are superior to monolithic composite plates at all impulse magnitudes.

The results show that core density and load intensity profoundly affect both the rate and the extent of deformation in the composite structures. The study indicates that structure with low density cores consistently outperform structures with high density

cores of equal mass. Figure 88(b) shows the backface velocity histories for all composite panels. The monolithic composite experiences the highest transverse velocities followed by sandwich structures with HP200, HP100 and HP60, in that order. This behavior can be explained by the presence of the sandwich core which reduces the velocity of the deforming composite panel. The lower the core density and thicker the core, the greater the reduction in velocity due to the ability of the core to undergo compression. Additionally, the variations in geometric parameters have an effect on flexural rigidity and deformation in sandwich panels. Since a fully dynamic computational framework is used to in this analysis, structural effects beyond bending, as well as bending, are captured. Figure 89 shows the normalized deflections $\left(\Delta/L\right)_{AB}$ for all 16 air-backed configurations as functions of impulse $\bar{I}$ and relative density $\bar{\rho}$. At all impulse magnitudes, structures with the lowest relative density experience the least deflections. The deflections increase with increasing relative density as well as impulse magnitudes. Structures with HP200 cores perform only marginally better than monolithic structures. Structures with the HP100 and HP60 cores exhibit significantly higher blast resistances in comparison to the structure with the HP200 core and the monolithic composite.

## 8.4 Computational results

### 8.4.1 Validation of numerical approach

A number of failure mechanisms are observed by time-resolved as well as post-mortem inspection of the composite panels. Failure in the monolithic composite panels consists of matrix cracking and fiber pullout, in addition to multiple delaminations

through the cross-section. With increasing load intensity, the severity of matrix cracking increases significantly. In sandwich structures, the failure mechanisms consist of (1) matrix cracking, (2) fiber rupture, (3) fiber-matrix debonding, (4) permanent core compression and core indentation, (5) core shear cracking and rupture, (7) core-face debonding, and (8) rupture of the composite panel. The effects of loading rate are much more significant for sandwich composites with high density cores (HP100 and HP200) than for structures with low density cores (HP60). Concurrent numerical analyses of the response of composite panels provide a more in-depth understanding of the structural response and failure mechanisms. Based on the experiments, a parametric finite element analysis is carried out, focusing on the effects of (i) load intensity, (ii) changes in relative density (monolithic, HP60, HP100, and HP200), and (iii) air-backed and water-backed loading conditions. For all the calculations presented, simply-supported boundary conditions are used, as in the experiments. Also as in experiments, four different projectile velocities are used to generate impulsive loads on the central area of the specimen. Figure 57 shows a comparison of experimentally measured and numerically calculated pressure profiles in the USLS.

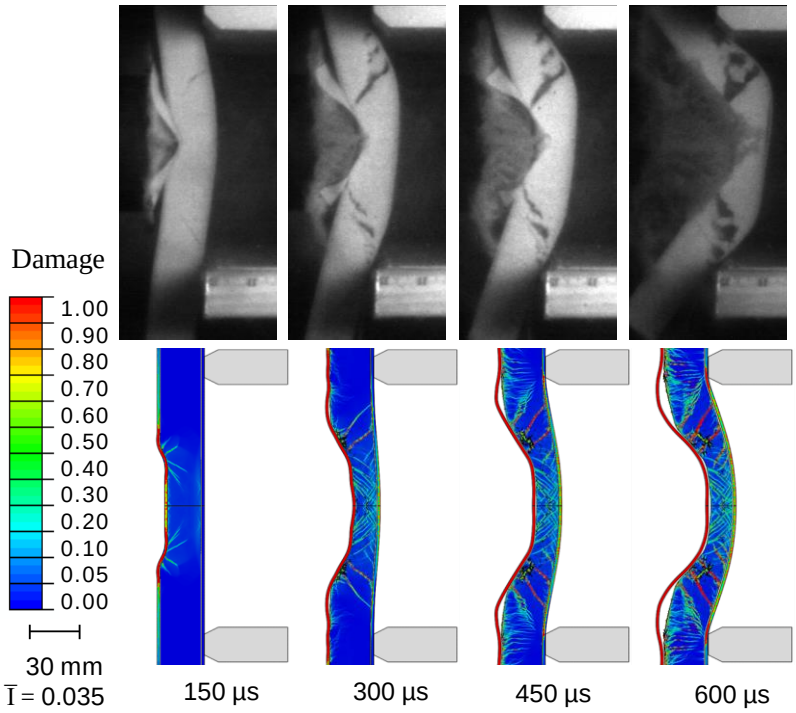


Figure 90 Cross-sectional view showing a comparison of experimentally measured and numerically calculated deformation sequences for a sandwich structure with HP60 core subjected to $\bar{I} = 0.035$. The major deformation mechanisms (core cracking, core frontface debonding and core crushing) are captured in the finite element simulations.

The deflection and impulse transmission in the monolithic plate are taken as benchmarks to which the deflection and impulse transmission in the sandwich structures are compared to gauge relative performance. Figure 90 shows a comparison of high-speed photographs from experiments and contour plots for damage from simulations at different times for a structure with the HP60 core subjected to $\bar{I} = 0.035$. The experiments reveal that core compression commences immediately after the onset of loading at $t = 150\,\mu s$ and inclined cracks originate near the loading circumference. These cracks propagate from the frontface to the backface and branch (at $t = 450\,\mu s$) near the backface, leading to core-backface debonding. Core indentation is observed at the center,

followed by core cracking and finally culminating in fragmentation and collapse. Although damage in the frontface is severe, the backface is relatively undamaged.

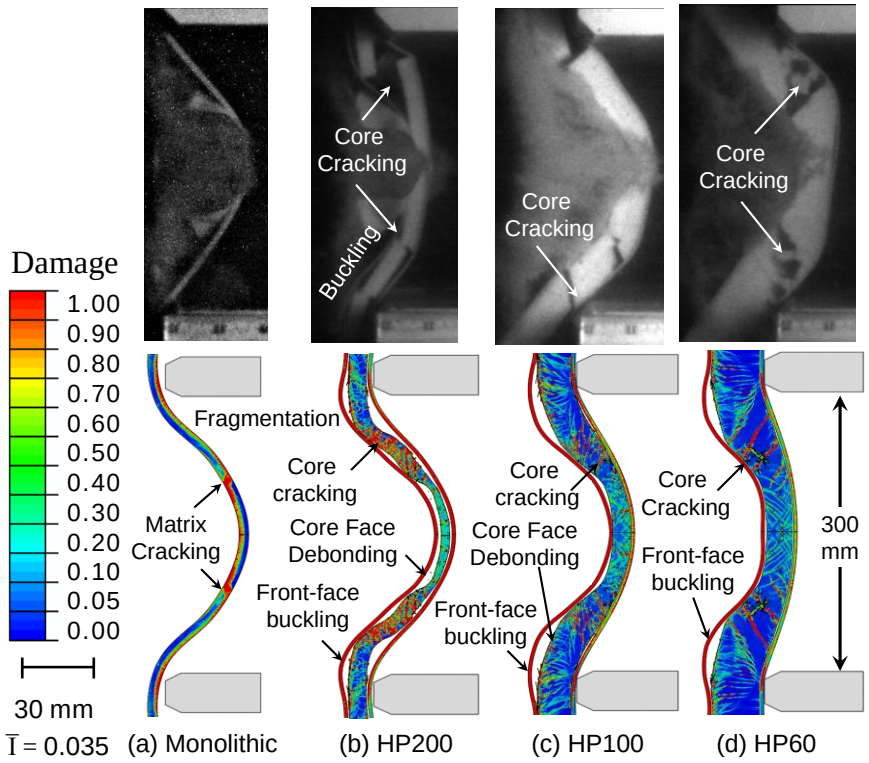


Figure 91 Cross-sectional view showing the distribution of core and facesheet damage in air-backed (a) monolithic composite and (b-d) sandwich structures with HP60, HP100 and HP200 cores. The calculated orientations and locations of failure mechanisms in the face, core and at core-face interfaces are in reasonable agreement with experimental observations. Projectile velocity is 75 $ms^{-1}$ and $\bar{I} = 0.035$.

The entire structure achieves a common velocity at $t = 600\,\mu s$. The numerical simulations capture the different failure modes observed in the experiments. The major deformation modes captured can be divided into distinct regimes based on the time required for each regime: (1) load transfer through frontface and onset of core compression; (2) elastic and inelastic core compression; (3) core cracking and fragmentation and load transfer to backface; and (4) bending in entire structure. The

material properties of the sandwich core determine the duration of each regime. The numerical simulations allow the identification of various damage mechanisms and the chronological sequence in which these mechanisms initiate.

The overall panel deformation and core compression and core cracking closely resemble those observed in high-speed photographs of the experiments reported here. The magnified view of deformation sequences shows that initially, damage is much more severe near the loading area, and as the panel experiences further deformation, core shear and core-face debonding initiate. Strain localization observed in experiments is replicated in the numerical simulations in the form of cracks propagating outwards at ~$45^{o}$ to the loaded region. Extensive cracking and delamination are also observed in the backfaces.

The distributions of damage due to matrix cracking and core cracking and fragmentation in different composite structures are shown in Figure 91(a-d) for $\bar{I} = 0.035$ at $t = 600\,\mu s$. In the monolithic composite [Figure 91(a)], matrix cracking is observed near the circumference of the loading area. Significant damage occurs in the composite layers that are in contact with water but the backface of the monolithic composite is relatively undamaged. For the sandwich composite with the HP200 core [Figure 91(b)], core frontface and backface debonding occurs over the entire structure and the core fails through shear cracking. Both the frontface and the backface experience considerable damage. For the sandwich composite with the HP100 core [Figure 91(c)], the frontface experiences significant damage and core frontface debonding is observed. For the sandwich composite with the HP60 core [Figure 91(d)], frontface buckling and core frontface debonding are observed; but the backface is relatively undamaged. It is apparent that damage in the backface is highly dependent on the properties of the core.

Damage and failure in simply supported sandwich structures occur primarily through the formation of discrete $45^o$ core cracks and separation along the core face interface. Structural failure in all cases is due to shear stresses near the loading area and bending stresses near the supports. Results show reasonable agreement between the experiments and numerical simulations. The compressible foam constitutive model predicts the initial deformation response which is governed by the core compression. Additionally, the damage criterion provides an accurate characterization of damage creation and growth in the composite as well as foam components. However, the numerical model slightly overestimates the compressibility of the foam core, resulting in greater permanent core compression in the simulations as compared to experiments.

### 8.4.2 Deflection

Bending deformation initiates in the structure immediately after the onset of loading. In this configuration, the midpoint of the backface experiences the highest deflection and stresses. Figure 92 shows the histories of center displacements normalized by the length of the structure for front and back faces of the sandwich panels with the (a) HP60, (b) HP100, and (c) HP200 cores along with those of the monolithic composite of equivalent weight. The shaded region shows the core compression at the center. Results show that the center displacement of the monolithic composite is higher than those of all sandwich structures. The velocity acquired by the monolithic plate is very similar to that of the frontface in all three cases. For the three core densities, the frontface acquires much higher velocities than the backface. Therefore, the load spreading capacities of the core are critical for enhancing blast resistance.

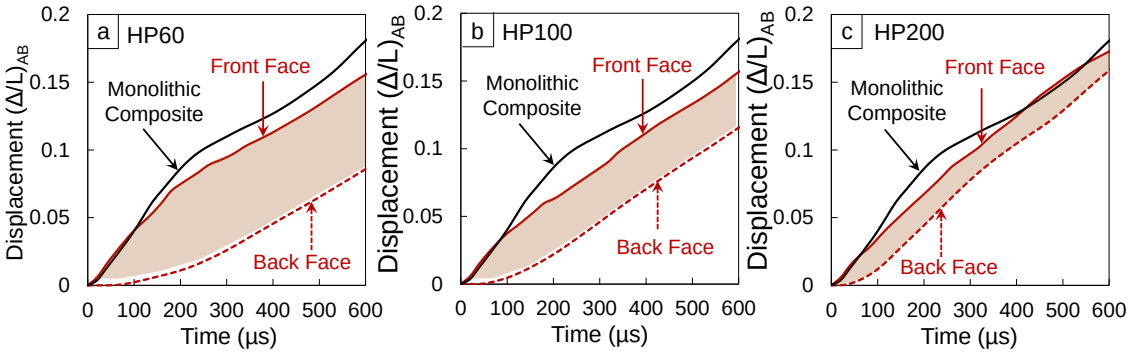


Figure 92 Front and back-face displacements as functions of time for air-backed sandwich structures with (a) HP200, (b) HP100, and (c) HP60 cores subjected to $\bar{I} = 0.035$. The shaded region is the core compression in each case. The solid black line denotes the displacement of the monolithic composite.

Significant deformation in the backface follows core crushing and load transfer through the core. The higher the rate of deformation in the backface, the lower is the blast mitigation capability of the composite. For the HP200 core, the displacement in the backface occurs after a delay of ~50 μs. Comparison of the deflections for front and back faces shows that both faces move with similar velocities. The backface deflection for this case is ~90% of the deflection in the monolithic composite. For the HP100 core, the displacement in the backface occurs after a delay of ~75 μs and the backface experiences ~70% of the displacement in the monolithic composite. For the HP60 core, displacement in the backface occurs after a delay of ~100 μs and the backface deflection is ~40% of the deflection in monolithic composite. The shaded regions in the plots show the core compression for each case. As the relative core density increases, core compression decreases significantly. A comparison of the slopes of the front and back face displacements vs. time plots indicates that thicker, low-density cores provide the greatest reduction in frontface velocity and the longest delay after the onset of loading for structural deflection to initiate.

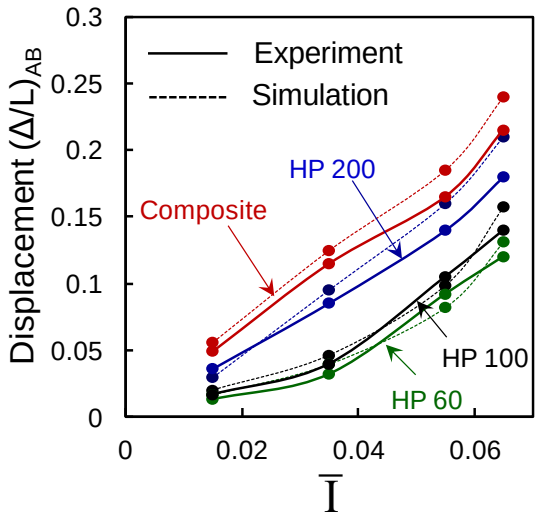


Figure 93 Comparison of experimentally measured and numerically calculated mid-plane deflections at 1000 μs in air-backed structures as functions of normalized incident impulse $\bar{I}$ for different normalized core densities. The results from experiments are in good agreement with those obtained from finite element simulations.

Figure 93 shows the normalized deflection $(\Delta/L)$ as a function of impulse $\bar{I}$ for structures with different relative densities. A monotonically increasing trend of center deflections with increasing core density is observed and shows reasonable agreement with experimental observations. At all impulse magnitudes, structures with the lowest relative density experience the least deflections. The deflections increase with increasing relative density and impulse magnitudes. The structure with the HP200 core performs only marginally better than monolithic structures. The HP100 and HP60 cores yield significantly higher blast resistances in comparison to the HP200 core and the monolithic composite.

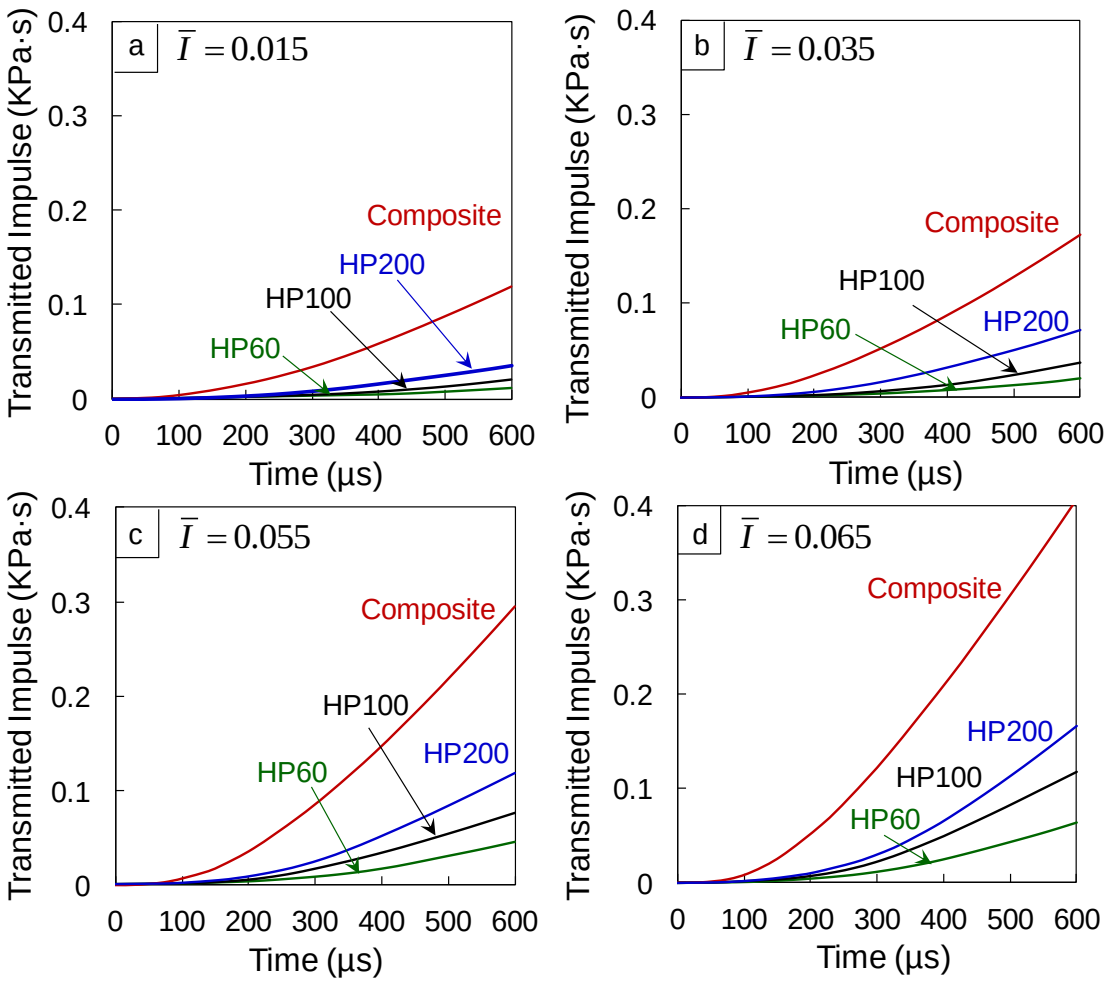


Figure 94 Impulse transmitted to the supports for air-backed composites as function of time for different incident impulsive loads.

### 8.4.3 Impulse transmission

Minimizing the impulse transmitted to the internal components of marine vessels is of critical importance. For the simply-supported loading configuration discussed here, the target structure transmits an impulse to the supports. The rate of impulse transmission and the magnitude of the transmitted impulse can provide valuable insight into the blast resistance and performance of composite structures. Clearly, the composite structure that transmits the least impulse at the lowest rate is most desirable. Figure 94(a-d) shows the

histories of impulses transmitted by air-backed structures subjected to incident impulsive loads of different magnitudes. It can be seen that, compared to the monolithic composite plate, the sandwich structures transmit significantly lower impulses and at much lower rates. In particular, the structure with the HP200 core shows a marked improvement in blast resistance over the monolithic panel. As the core density decreases and the corresponding core thickness increases, the improvements in blast mitigation are more noticeable. For example, for an incident impulse magnitude of $\bar{I} = 0.065$ $\left(I = 0.42\ \text{KPa}\cdot\text{s}\right)$ shown in Figure 94(d), the sandwich structures with HP200, HP100 and HP60 cores transmit ~40%, 30% and 20% of the impulse transmitted by the monolithic composite, respectively. Correlating the rate of impulse transmission with the core characteristics in each case shows that, as the core density decreases and core thickness increases correspondingly, the rate of impulse transmission decreases significantly. For each sandwich structure, the impulses transmitted are significantly lower than those for the monolithic composite. The transmitted impulses increase exponentially with increasing relative density $\bar{I} = 0.065$ and increase monotonically with the increasing incident impulse. The experiments and simulations reveal that the sandwich core is essential for spreading the load uniformly over the entire span of the structure and absorbing the incident impulsive loads to enhance the blast mitigation capabilities of the structures.

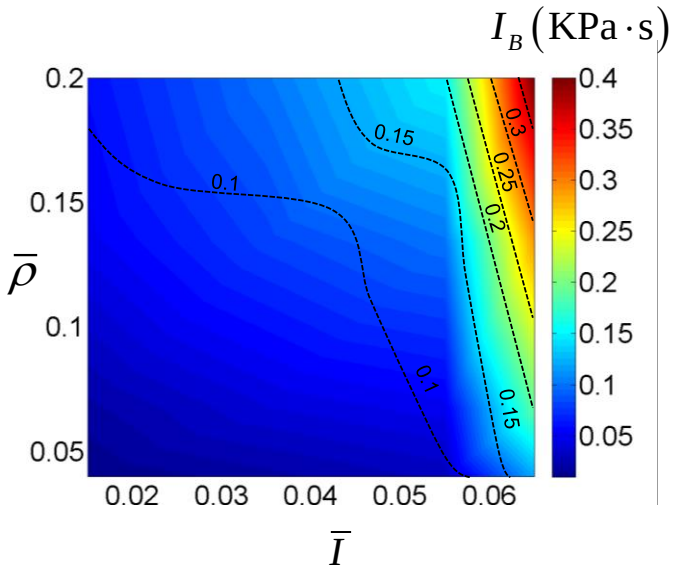


Figure 95 Transmitted impulse in air-backed structures as function of normalized incident impulse $\bar{I}$ and normalized density $\bar{\rho}$.

Figure 95 shows the transmitted impulse for air-backed structures $(I_T)_{AB}$ for all 16 configurations as a function of normalized incident impulse $\bar{I}$ and normalized relative density $\bar{\rho}$. At all impulse magnitudes, structures with the lowest relative density transmit the least impulse. The transmitted impulse increases with increasing relative density as well as impulse magnitude. HP200 cores perform better than monolithic structures while HP100 and HP60 cores exhibit significantly higher blast mitigation in comparison to HP200 core and the monolithic composite.

## 8.5 Response of water-backed structures

An analysis of structural performance in water-backed conditions is important for the design of critical parts of ship structures like turbine blades, hull and keel. Water-backed conditions also prevail in underwater pipelines and ducts. Moreover, a number of sections in the hull of a marine vessel are backed by movable equipment and machinery

which creates conditions similar to water-backed loading conditions. In addition to the results for air-backed structures reported so far, an additional set of simulations is carried out to investigate the role of water in contact with both sides of the structure. The load configuration for this case is shown in Figure 80(b).

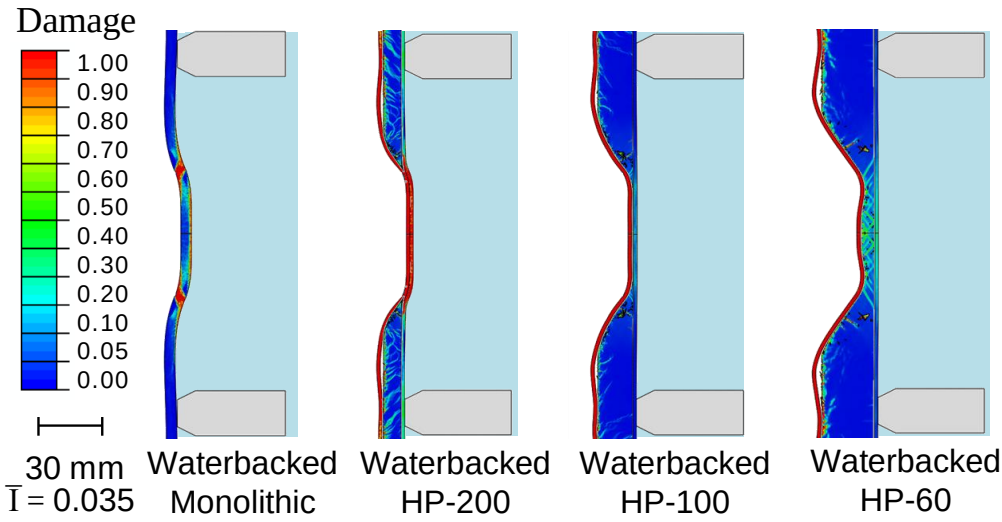


Figure 96 Distributions of damage in water-backed monolithic composite and sandwich structures with HP60, HP100 and HP200 cores. Deformation is highly localized due to the presence of backside water section which affects both deflection and impulse transmission. Design of such structures require different considerations than air-backed structures. Projectile velocity is 75 $ms^{-1}$ and $\bar{I} = 0.035$.

Figure 96 shows the distributions of damage in four different composite structures in water-backed loading for $\bar{I} = 0.035$. These contour plots illustrate the differences in the behavior of air-backed and water-backed structures. For the monolithic composite, high shear stresses develop near the circumference of the loaded area, causing severe damage in the form of matrix cracking. For the sandwich structures, however, flexural waves in the frontface cause core frontface debonding and frontface buckling. Damage is localized and the structure is relatively undamaged in regions that are away from the loading area.

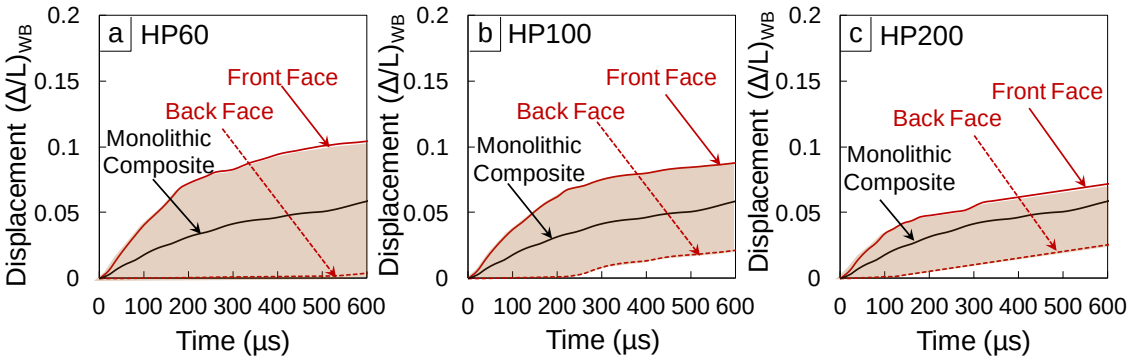


Figure 97 Front and backface displacements as functions of time for water-backed sandwich structures with (a) HP60, (b) HP100, and (c) HP200 cores subjected to an impulse of $\bar{I} = 0.035$. The shaded region is the core compression in each case. The solid black line denotes the displacement of the monolithic composite.

Clearly, for all structures, the overall deflection under water-backed conditions is severely restricted due to the presence of the back side water. Due to the lack of overall deflection and bending, tensile loads in both faces are negligible and the faces undergo significantly lower amount of damage in comparison to the corresponding air-backed cases.

To evaluate the role of relative density on dynamic response, the histories of center displacements experienced by the monolithic composite and both faces in the sandwich structures are shown in Figure 97. The shaded region illustrates the core compression. Core compressive strains for all cores are similar (~100%), but the absolute core compression is significantly higher for HP60 than for HP100 and HP200. For the sandwich structures, due to low relative core densities, the frontface starts to move with a higher velocity than the monolithic plate and the frontface velocity is limited by the core. Therefore, the momentum transferred to the core increases with increasing relative core density.

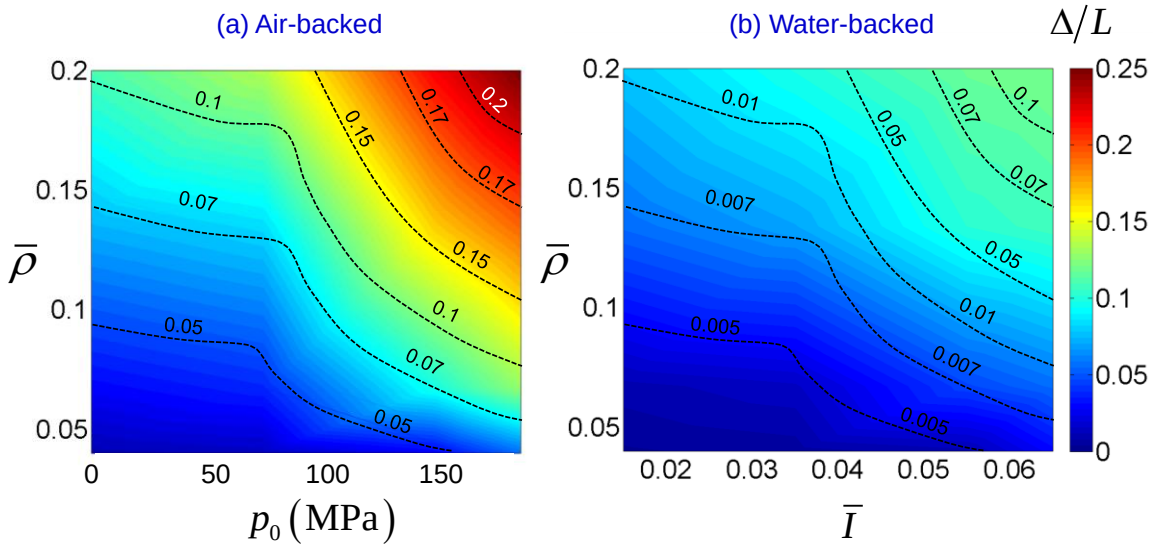


Figure 98 Normalized mid-plane deflection in air-backed and water-backed structures as function of normalized incident impulse $\bar{I}$ and normalized density $\bar{\rho}$.

Figure 98 shows the normalized deflections $(\Delta/L)$ for all 16 cases for the water-backed case as a function of impulse $(\bar{I})$. As observed in air-backed structures, thick cores with low relative density provide the best blast mitigation. In the water-backed case, on average, the deflections are 50% of the deflections in the air-backed case. The resistance of a water-backed structure to applied impulse can be quantified by the magnitude of the impulse transmitted into the back side water section. Figure 99 shows the histories of transmitted impulses for water-backed composite structures subjected to similar impulsive loads. In all cases, the monolithic composite exhibits the least blast mitigation and transmits more than ~80% of the incident impulse into the back side water section. The HP200 core transmits ~40% of the incident impulse. During and up to the core compression stage, or at approximately 100 μs, the impulse transmitted is very low. However, when the core fails completely (at ~400 μs), the frontface "slaps" into the backface and both faces start to move together, causing a pressure pulse to be generated

and transmitted into the back side water. The structure with the HP100 core transmits ~20% of the incident impulse with a low pressure plateau followed by complete impulse at the end of 600 μs. Clearly, blast mitigation in water-backed conditions is relatively insensitive to face thickness and is highly dependent on core density and thickness. The histories of transmitted impulses show that the rate of impulse transmission is highly dependent on the core density. For instance, in Figure 99(d), the monolithic composite transmits the impulse almost instantaneously after the onset of loading while in the sandwich structure, the transmission of the impulse is controlled by core crushing and the impulse is transmitted after complete core collapse. The time duration for failure in each sandwich structure can be clearly identified by the steep rise in transmitted impulse.

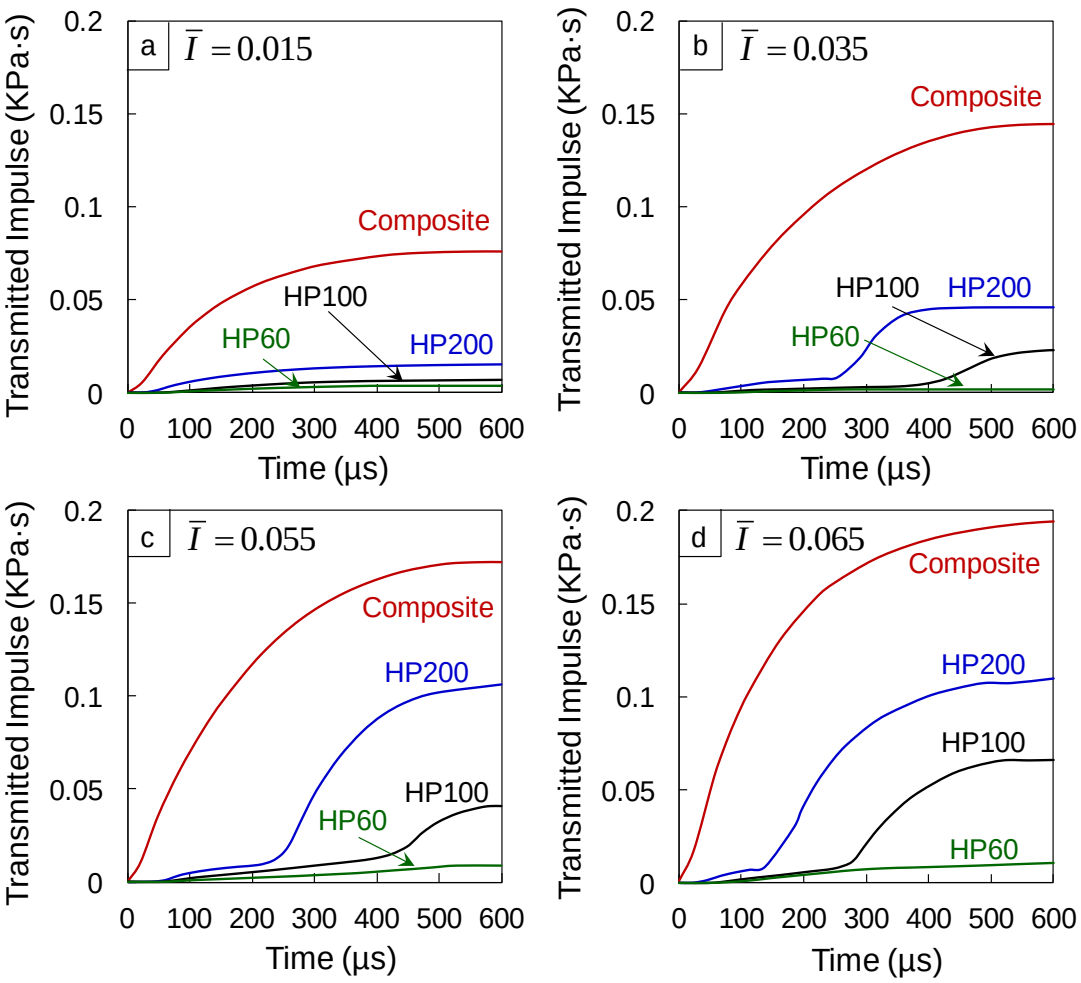


Figure 99 Impulse transmitted to the rear water-section for water-backed composites as function of time for different incident impulses.

Figure 100 shows the transmitted impulse $(I_T)_{WB}$ for all 16 cases as a function of normalized incident impulse $\bar{I}$ and normalized relative density $\bar{\rho}$. The vertical axis shows the transmitted impulse $(I_T)$. At all impulse magnitudes, the magnitude of the transmitted impulse increases monotonically with the relative density. As the core density increases, the fraction of incident impulse transmitted by the structure in a water-backed configuration also increases significantly. Figure 100 shows the transmitted impulse for all 16 cases as a function of normalized incident impulse $\bar{I}$ and normalized relative

density $\bar{\rho}$. The vertical axis shows the normalized deflection $\left(\Delta/L\right)_{WB}$. At all impulse magnitudes, the magnitude of the transmitted impulse increases monotonically with the relative density. As the core density increases, the fraction of incident impulse transmitted by the structure in a water-backed configuration also increases significantly.

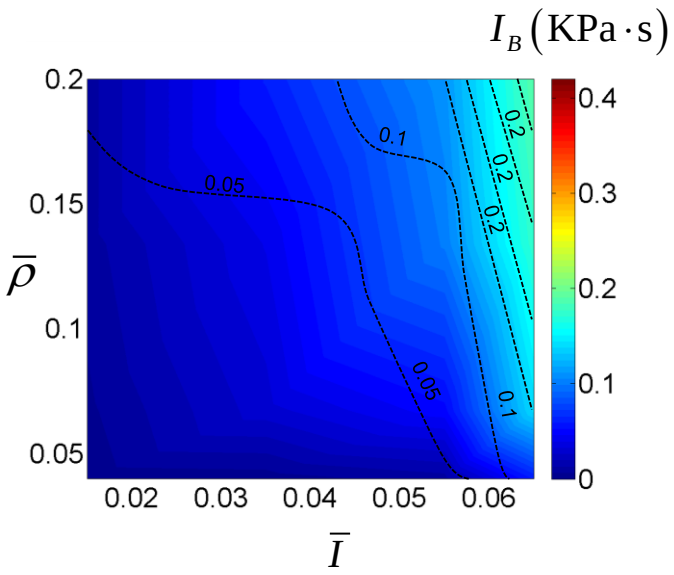


Figure 100 Transmitted impulse in water-backed structures as function of normalized incident impulse $\bar{I}$ and normalized density $\bar{\rho}$.

## 8.6 Conclusions

Marine structures must balance strength and load carrying capacity with the ability to minimize impulse transmission for high blast and impact resistance. Composite structures have higher stiffnesses and high strength-to-weight ratios compared with monolithic structures. Additionally, sandwich structures provide very high bending and shear resistances with slight increases in total mass. However, due to the novelty and wide range of structural combinations, the relationships between structural responses and material heterogeneity in sandwich structures are not well quantified. In particular, the

behavior of composite structures under extreme impulsive loading generated by underwater explosions needs to be systematically analyzed. In an effort to provide useful information for structural design, the load carrying capacity and impulse transmission capabilities of sandwich composites are evaluated over a range of relative densities and impulsive load intensities. The loading conditions involve impulsive loads with peak pressures up to 200 MPa, which simulate the effects of TNT exploding underwater at different standoff distances from the structure. The constitutive and damage models capture the different inelastic deformation and failure mechanisms in composite laminates and sandwich cores. It should be emphasized that the composite panels studied have similar overall mass which necessitates different core thicknesses. The effect of core height on dynamic response is not studied in this analysis.

This study has yielded experimental data on the failure behavior of composites subjected to underwater impulses. Maximal damage was observed near the load circumference in both monolithic and sandwich structures. The analysis of damage modes shows that relative core density is a critical factor in determining structural performance of sandwich structures. Sandwich structures significantly outperform monolithic composites at all impulsive levels and environmental conditions. Low density cores provide higher blast resistance than high density cores. An analysis of the effect of load intensity shows that as the load intensity increases, the deflection of the frontface outpaces the dynamic core crushing capability of the cores, resulting in collapse. In such cases, low density cores provide better load spreading and exhibit better capabilities for compression. However, a major concern for low density cores is the occurrence of core indentation, in which the core fails in a localized region and causes compressive stresses

in the frontface leading to buckling and rupture. Therefore, a balance of core stiffness and softness is essential for optimal blast resistance.

Comparison of experiments and simulations shows that numerical calculations provide a reasonable representation of damage and dissipation mechanisms in the facesheets and core. The compressible foam constitutive model leads to high core compression and a slight overestimate of backface deflection. The finite element model captures the essential deformation mechanisms observed in both the facesheets and the core. Specifically, the following deformation modes are replicated with reasonable accuracy: core indentation, core shear, core-face debonding, facesheet buckling and delamination, structural collapse and rupture. The results from numerical calculations provide a more in-depth understanding of temporal and spatial evolution of different deformation modes in the structure. The deformation in sandwich structures is strongly influenced by core density and loading rate and magnitude. Structures with high relative densities undergo severe damage and exhibit significantly higher core face debonding than structures with low relative densities. For a given impulsive load, structures with low relative densities (HP60 and HP100) experience considerably lower displacements than those with high relative densities (HP200 and monolithic).

In both air-backed and water-backed cases, the maximum impulse transmitted by each structure is used to determine the performance of the composite structure. Sandwich structures exhibit superior blast mitigation capabilities in comparison to monolithic structures at all impulse magnitudes. In particular, thick, low density foam cores made of Divinycell HP60 and HP100 foams provide the highest load spreading and impulse retardation. The temporal histories of impulse transmission show a significant

dependence on core density with a clear increase in transmitted impulse after complete core failure. The transmitted impulses show a monotonic dependence on loading intensity and a power law dependence on the relative density. The effects of high relative density are further exacerbated at higher loading intensities. The insight gained here provides guidelines for the design of structures for which response to water based impulsive loading is an important consideration. Finally, it should be noted that the relations described in this paper are applicable only for the structural attributes and loading conditions considered herein.

# 9. CARBON-FIBER/PVC FOAM SANDWICH STRUCTURES

## 9.1 Introduction

Marine vessels operate in hostile environments which include high and low temperature extremes, transient dynamic loads like hull slamming, and corrosive sea water. Additionally, the structures are expected to withstand hydrodynamic loads resulting from surface and underwater explosions and weapons impact. Sandwich composites can provide good blast mitigation due to their high strength-to-weight ratios and high shear and bending resistances. The lightweight of sandwich composites can also improve speed and fuel economy. Compared with metal, composites are also more corrosion-resistant and have lower repair costs. These attributes make composite sandwich structures attractive materials for marine vessels. However, before such materials can be used, the relationships between their performance, constituent materials and geometric design must be well-understood and quantified.

Investigations have been out on the dynamic deformation and failure of layered materials. Results showed that key damage mechanisms include matrix cracking, fiber breakage and interlaminar delamination. The primary driving forces for the damage processes are transverse shear stresses [38-40]. Interlaminar delamination is the most detrimental to stiffness and strength and, therefore, is a major concern because delamination is not visible on the surface. Chang and co-workers [41-43] have studied the damage behavior of composite laminates under low velocity impact loading, concluding that in-ply matrix cracking precedes delamination growth and shear and bending crack

initiation. The damage behavior of composite laminates is significantly influenced by matrix material, composite layup and geometric aspects such as size, thickness and loading area [44-46]. Minnaar and Zhou [47] used a novel interferometric experimental setup to show that interlaminar crack speeds are significantly higher under shear loading, and that crack speeds are strongly influenced by loading rate in mode II.

However, only limited study has been reported [125, 178] on the dynamic response of composites to water-based impulsive loads. The compressive response and fracture behavior of core material are of primary importance in the structural response of sandwich structures. The stress-strain behavior of cellular foams at high strain rates has been investigated using Split Hopkinson Pressure Bar apparatuses [53, 145-147, 179]. These experiments reveal that PVC foams have mild strain rate sensitivity in the strain rate range of $\dot{\varepsilon} = 10^{-2}$ to $10^{3}\ \mathrm{s}^{-1}$ and negligible strain rate sensitivity in the strain rate range of $\dot{\varepsilon} = 10^{-4}$ to $10^{-2}\ \mathrm{s}^{-1}$. The primary mechanism for energy absorption in foam cores is local wall collapse and volumetric, stress-saturated compression. Constitutive models for foams often rely on homogenized continuum descriptions of the cellular materials [77, 148].

Through the combination of a thick, low-density core and thin facesheets, sandwich structures achieve considerably high shear and bending stiffness to weight ratios than homogeneous plates of equivalent mass made exclusively of either the core or the facesheet material. The primary factors that influence the structural response of a sandwich structure are (1) facesheet thickness, (2) core thickness, and (3) core density. Previous research on the dynamic behavior of sandwich composites has focused on low

velocity contact-based loads such as drop weight and projectile impact [32, 33, 51-55]. It is found that the overall deflection experienced by sandwich plates is significantly lower than monolithic plates of equivalent mass [10, 56-63]. Additionally, the forces and impulses transmitted by sandwich structures are also smaller than those by monolithic structures [56, 59, 60]. Recent assessments of blast-loaded structures show that FSI (fluid-structure interaction) effects play an important role in dynamic response and can be exploited to improve the blast mitigation capability of marine structures [8, 9, 60, 66, 75]. Experiments focusing on different core topologies and specimen sizes have been carried out by Espinosa and co-workers [1, 93, 104] and McShane et al. [105] using underwater pressure impulses generated by gas gun impact and by Dharmasena et al. [64] using planar pressure impulses generated by explosive sheets. Shukla and co-workers [79-83] examined the dynamic response of sandwich structures consisting of woven E-glass composite facesheets and stitched core to air-based shock loading and concluded that stitched cores exhibit superior mechanical performance.

The deformation and failure of composite sandwich structures subjected to underwater impulsive loads are complicated due to competing damage mechanisms, failure modes, interfacial effects and material heterogeneity. The material properties of the different components significantly affect the blast resistance of the structures. In addition, loading (intensity, boundary conditions, and environments) influences the failure modes. Despite recent advances in understanding the dynamic response of sandwich composites, several issues remain. One is the lack of design relations that quantify the response as functions of both materials and geometric parameters. To obtain such relations, experiments that account for proper loading conditions are required.

Diagnostics that provide in-situ, time-resolved response measurements are also required. Until recently, such experiments remained unavailable. Full scale underwater blast experiments have been carried out by Dear and co-workers using C4 explosives to generate the impulsive loads and high-speed photography with Digital Image Correlation (DIC) to evaluate the dynamic response of composite structures [165, 180]. Nurick and co-workers have conducted air-blast experiments using PE4 plastic explosive and a ballistic pendulum apparatus to analyze the damage and energy dissipation in monolithic composite laminates and fiberglass/PVC foam sandwich structures [181, 182].

The objective of the present study is to characterize the damage response of sandwich composites with a range of material and structural attributes including core density, core thickness, facesheet thickness and functionally graded sandwich cores. The focus of this analysis is on understanding the deformation and failure mechanisms, and quantifying the damage in composite structures as a function of structural attributes, material properties, loading conditions and loading rates. The loading of interest is high intensity water-based impulsive loads. Planar impulses resembling those resulting from underwater explosions are generated using the Underwater Shock Loading Simulator (USLS), a novel experimental setup developed recently. The USLS consists of a projectile-impact-based impulsive loading system, a water chamber, a target holder, and a safety enclosure. The target holder allows clamped and simply-supported boundary conditions. The experiments are designed to quantify the resistance of each structural configuration to underwater impulsive loads. The response and failure mechanisms studied include overall deflection, face wrinkling, core-face debonding, core

compression, core shear cracking and rupture. Of particular interest is the influence of load intensity and sandwich core characteristics on deformation and failure.

This is a combined experimental and computational study. Finite element simulations are carried out, accounting for the experimental conditions and material properties which are measured independently. The simulations also account for the fluid-structure interaction (FSI) effect at the water-composite interface. Failure mechanisms considered include shear cracking and fragmentation in the core, cracking in the face sheets, and core-face interfacial debonding. The simulations focus on damage initiation and evolution in the early stage of deformation (~1000 μs) since the load-carrying capacity is most critically reflected then. This combined experimental and numerical approach enables the identification of factors that play important roles in determining the dynamic response of the materials. The analysis uses metrics such as deflection, energy absorbed and impulse transmitted to quantify blast resistance. The results are presented in normalized forms to identify underlying trends in material and structural response.

## 9.2 Water-based impulsive loading experiments

Gas gun impact has been successfully used to generate impulsive loading through water [92, 93, 160, 161, 175]. To obtain controlled loading and simulate different water-structure contact conditions, the Underwater Shock Loading Simulator (USLS) shown in Figure 101 was designed to provide a variety of load configurations with quantitative diagnostics. Important features of this facility include the ability to generate water-based impulsive loading of a wide range of intensity, the ability to simulate the loading of

submerged structures, and integrated high-speed photographic and laser interferometric diagnostics.

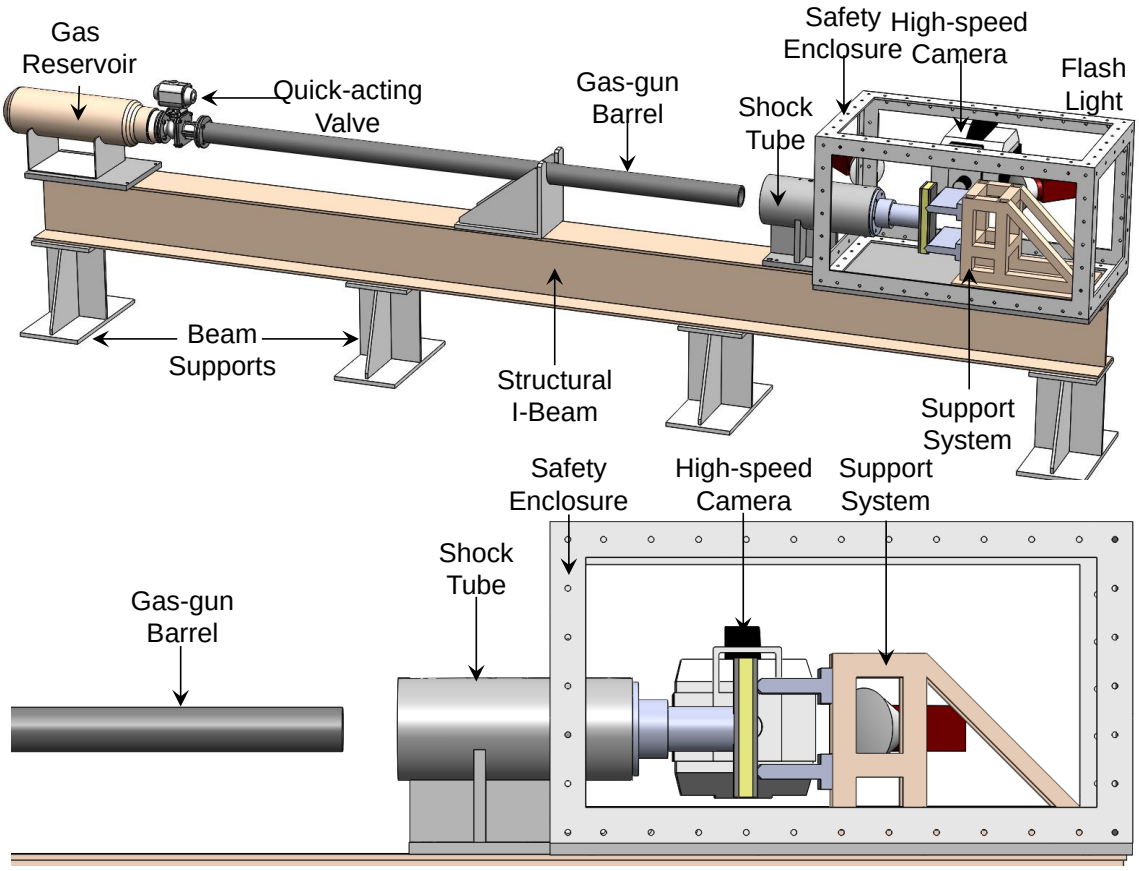


Figure 101 Schematic illustration of the Underwater Shock Loading Simulator (USLS) for testing simply-supported sandwich structures. Pictured are the gas reservoir, gun barrel, water chamber, modular support system, specimen and the Imacon 200D high-speed camera.

The shock tube is an 800 mm long cylinder which is horizontally mounted and filled with water. It is made of steel and has an inside diameter of 80 mm. A thin piston plate is mounted at the front end and the specimen is located at the rear end. A projectile is accelerated by the gas gun and strikes the piston plate, generating a planar pressure pulse in the shock tube. The impulsive load that impinges on the target induces deformation in the specimen at strain rates up to $10^4$ $s^{-1}$. Projectile impact velocities in the

range of 40-115 $ms^{-1}$ are used to delineate the effect of loading rate on the deformation and failure behavior of the structures analyzed. This velocity range corresponds to peak pressures between 40 and 180 MPa, which are comparable to pressures observed in underwater explosions [6, 163]. In all the experiments reported here, a simply-supported beam configuration is used which creates maximum tensile and compressive stresses at the midpoint of the specimen. Additionally, it bears resemblance to the conditions created by hull stiffeners in naval vessels. The impulsive waves are planar and produce a uniform pressure over the contact area with the specimen, simplifying the deformation and failure in the material to a 2-D event.

According to Taylor's analysis of one dimensional blast waves [6, 7, 166] impinging on a free standing plate, the pressure in the fluid at a fixed position follows the relation

$$p(t) = p_0 \exp\left(-\frac{t}{t_0}\right), \tag{79}$$

where $p_0$ is the peak pressure, $t$ is time and $t_0$ is the decay time. The area under this curve is the impulse imparted by the wave

$$I_0 = \int_0^t p(t)\,dt. \tag{80}$$

A non dimensionalized impulse $\bar{I}$ can be expressed as

$$\bar{I} = \frac{I}{\rho_w c_w \sqrt{A}}, \tag{81}$$

where $\rho_w$ is the density of water, $c_w$ is the speed of sound water in water and $A$ is the area of loading. Impulsive waves due to underwater blasts have a characteristic decay time on the order of ~$10^{-4}$ seconds. The experimental facility and numerical modeling simulate the effects of different standoff distances from an explosive source. In experiments involving explosives, Tri Nitro Toluene (TNT) is used to generate underwater blasts. Swisdak [163] showed that for an underwater explosion, the peak pressure (in MPa) scales as

$$p_0 = 52.4\left(\frac{M^{1/3}}{r}\right)^{1.13}, \tag{82}$$

where $p_0$ is the mass of TNT in kilograms and $r$ is the standoff distance in meters. In the experiments reported here, pressures ranging from 10 MPa to 300 MPa can be generated using different projectile velocities. The impulses are measured using high dynamic range piezoelectric pressure transducers (#109C11 manufactured by PCB Inc.) and a high-frequency data acquisition system from National Instruments Inc. (NI-4432). Figure 102(a-f) shows the comparison of experimentally measured and numerically calculated pressure histories corresponding to six different projectile velocities. The rise time of the pressure pulses is on the order of 25 μs and the decay time is on the order of 800 μs. The impulsive loads considered in this set of calculations have peak pressures of 235, 196, 155, 110, 69, and 34 MPa. Based on eqn. (82) these pressures approximately correspond to 100 kg of TNT detonating at distances of 1.5, 1.7, 2.1, 3.8 and 6.5 meters respectively. The normalized impulse magnitudes calculated using eqn. (81) are $\bar{I}$ = 0.3, 0.22, 0.16, 0.12, 0.08, and 0.04 respectively.

A series of tests with gradually increasing impulse magnitudes reveals that a peak pressure of 196 MPa corresponding to $\bar{I} = 0.22$ causes failure in a 6.3 mm thick monolithic plate. In order to set a benchmark and determine the blast resistance of sandwich structures with respect to that of monolithic plates, an impulse of $\bar{I} = 0.22$ is used to in experiments analyze the performance of sandwich structures with different material and structural attributes. The numerical calculations are validated using the experiments, and the simulations are extended to include a range of incident impulsive loads. In simulations, a range of impulse magnitudes shown in Figure 102(a-f) is utilized to identify the role of impulse intensity on structural response and to develop loading-structure-performance relationships between the different aspects considered in this analysis.

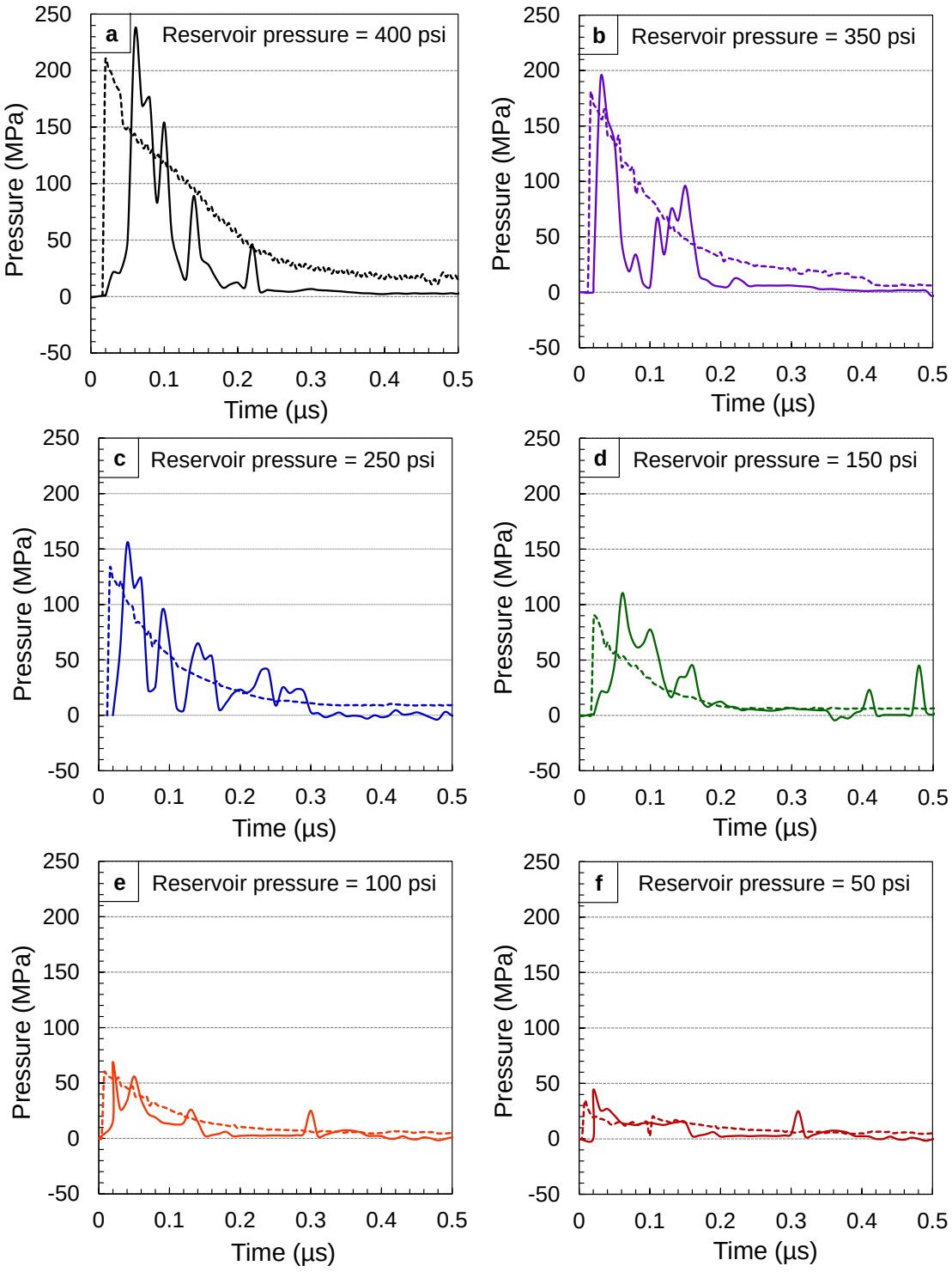


Figure 102 Experimentally measured and numerically calculated pressure histories in the water chamber for six different gas reservoir pressures, and projectile velocities. The impulse magnitude $\bar{I}$ = 0.3, 0.22, 0.16, 0.12, 0.08, and 0.04.

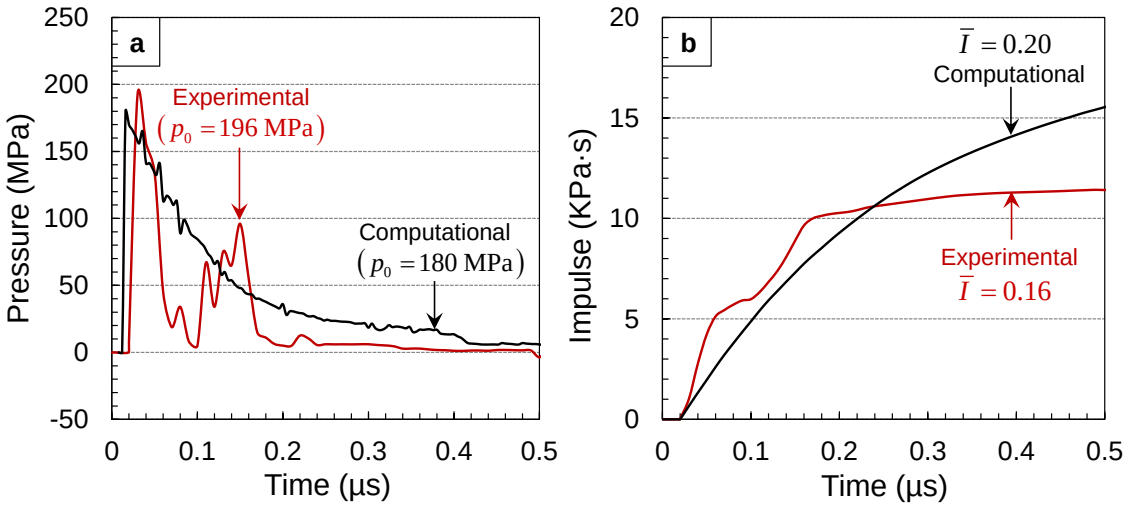


Figure 103 Experimentally measured and numerically calculated pressure and impulse histories in the water chamber for a gas reservoir base pressure of 250 psi and a projectile velocity of ~110 $ms^{-1}$.

## 9.3 Materials and panel construction

The facesheets are made of quasi-isotropic carbon-fiber/epoxy composites and the core is Divinycell HP PVC foam manufactured by DIAB Inc. [173]. Three PVC foam densities are used: 60, 100 and 250 $kg \cdot m^{-3}$. The sandwich structures analyzed here are in the form of beam specimens 300 mm in length and 80 mm in width. Figure 104 shows a schematic illustration of sandwich structure with facesheets consisting of carbon-fiber/epoxy laminates, core-facesheet adhesive from 3M, and core made of DIAB Divinycell HP structural PVC foams. The different specimen designs are shown in Table 10. The details for each specimen are as follows:

1. Monolithic

    a. Composite monolithic panel consisting of carbon-fiber/epoxy plies stacked in a quasi-isotropic layup $(0°/-45°/45°/90°)_s$. The panel thickness is ~6 mm and areal mass of 9.89 $kg \cdot m^{-2}$.

2. Equivalent core mass designs

    a. Sandwich structure with carbon-fiber/epoxy facesheets of thickness ~3 mm and Divinycell HP60 core with a thickness of 30 mm for a total areal mass 11.60 $kg \cdot m^{-2}$.

    b. Sandwich structure with carbon-fiber/epoxy facesheets of thickness ~3 mm and Divinycell HP100 core with a thickness of 20 mm for a total areal mass 11.36 $kg \cdot m^{-2}$.

    c. Sandwich structure with carbon-fiber/epoxy facesheets of thickness ~3 mm and Divinycell HP250 core with a thickness of 10 mm for a total areal mass 11.86 $kg \cdot m^{-2}$.

3. Equivalent core thickness designs

    a. Sandwich structure with carbon-fiber/epoxy facesheets of thickness ~3 mm and Divinycell HP60 core with a thickness of 30 mm for a total thickness of 36 mm.

    b. Sandwich structure with carbon-fiber/epoxy facesheets of thickness ~3 mm and Divinycell HP100 core with a thickness of 30 mm for a total thickness of 36 mm.

    c. Sandwich structure with carbon-fiber/epoxy facesheets of thickness ~3 mm and Divinycell HP250 core with a thickness of 30 mm for a total thickness of 36 mm.

4. Graded core designs

    a. Sandwich structure with carbon-fiber/epoxy facesheets of thickness ~3 mm and a graded core with constructed with 10 mm thick sections of

HP60 + HP100 + HP250 with respect to the impulse side for a total thickness of 36 mm.

b. Sandwich structure with carbon-fiber/epoxy facesheets of thickness ~3 mm and a graded core with constructed with 10 mm thick sections of HP250 + HP100 + HP60 with respect to the impulse side for a total thickness of 36 mm.

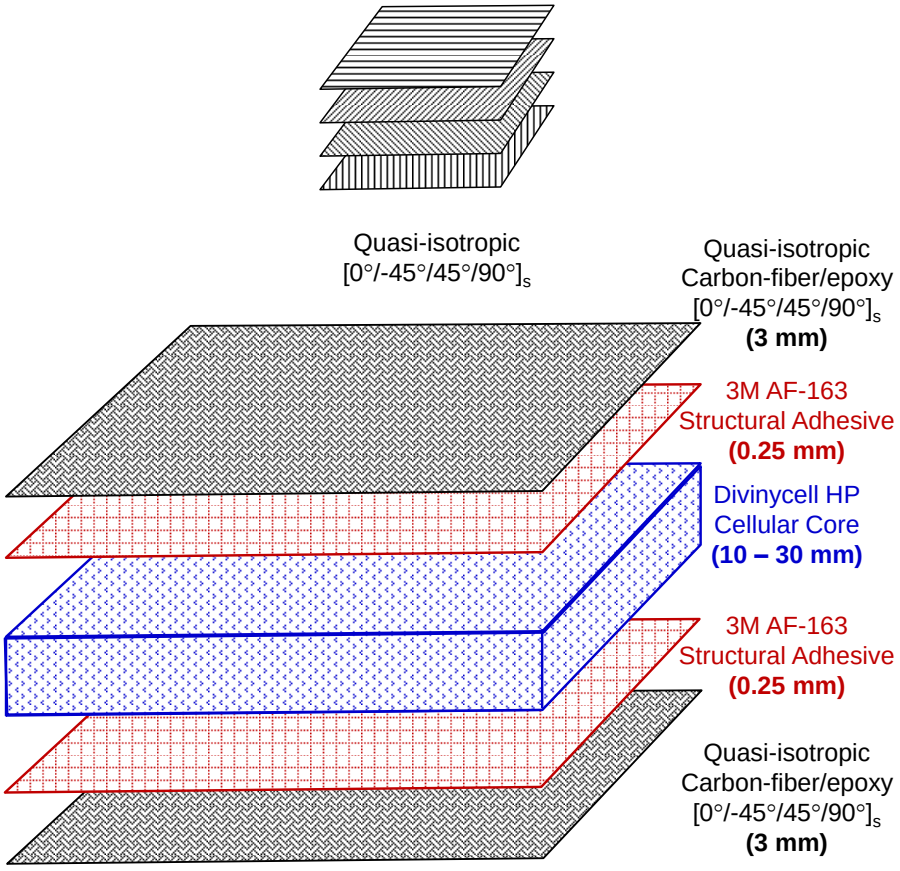


Figure 104 Schematic illustration of sandwich structure with facesheets consisting of carbon-fiber/epoxy laminates, core-facesheet adhesive from 3M, and core made of DIAB Divinycell HP structural PVC foam.

Table 10 Design of experiments for testing.

| | Beam Designation | Core Density ($kgm^{-3}$) | $\bar{\rho}$ | Core Thickness (mm) | Face Thickness (mm) | Areal Mass ($kgm^{-2}$) |
|---|---|---|---|---|---|---|
| **Monolithic** | Monolithic | - | 0.3 | - | ~6 | 9.86 |
| **Equivalent core mass** | HP60 30 mm | 60 | 0.06 | 30 | 3 | 11.60 |
| | HP100 20 mm | 100 | .10 | 20 | 3 | 11.36 |
| | HP250 10 mm | 200 | .25 | 10 | 3 | 11.86 |
| **Equivalent core thickness** | HP60 30 mm | 60 | 0.06 | 30 | 3 | 11.60 |
| | HP100 30 mm | 100 | 0.10 | 30 | 3 | 12.36 |
| | HP250 30 mm | 250 | 0.25 | 30 | 3 | 16.86 |
| **Graded core** | HP60-HP100-HP250 30 mm | 140 (avg) | 0.14 | 30 | 3 | 13.47 |
| | HP250-HP100-HP60 30 mm | 140 (avg) | 0.14 | 30 | 3 | 13.47 |

The facesheets and cores are bonded together using AF-163 structural adhesive from 3M. Figure 104 illustrates the makeup of composite structures analyzed. This sample size is approximately one order of magnitude smaller than composite sections

used in ships. To compare the effects of different core densities on response, a relative density defined as

$$\bar{\rho} = \frac{\rho_{core}}{\rho_{PVC}} \tag{83}$$

is used. For the monolithic composite (which does not have a PVC foam core), the relative density is calculated by

$$\bar{\rho} = \frac{f_{matrix} \cdot \rho_{matrix}}{f_{fiber} \cdot \rho_{fiber}}, \tag{84}$$

where $f_{matrix}$ and $\rho_{matrix}$ are the volume fraction and density of the matrix, respective, and $f_{fiber}$ and $\rho_{fiber}$ are the volume fraction and density of the reinforcement, respectively. In a large naval structure, such as a ship or a submarine, structural components are in different service environments and are subject to different loading conditions. Figure 105 presents a schematic of the USLS showing the loading configuration of a simply-supported sandwich structure subjected to planar impulsive loading. The different composite structures and the corresponding geometrical dimensions and areal masses are presented in Table 10.

## 9.4 Design of experiments and structural design guidance

Non-dimensional variables are used for quantitative evaluation of the dynamic response of the composite panels as a function of loading and structural attributes. In structural design, necessary performance requirements are specified and the structural characteristics that fulfill these objectives are ascertained. The material attribute of

particular interest here is the normalized relative density $\bar{\rho}$ and the loading intensity is the normalized incident impulse $\bar{I}$. These parameters are varied independently of each other and the performance of each structure is quantified using the normalized deflection $\Delta/L$ and normalized transmitted impulse $I_T$.

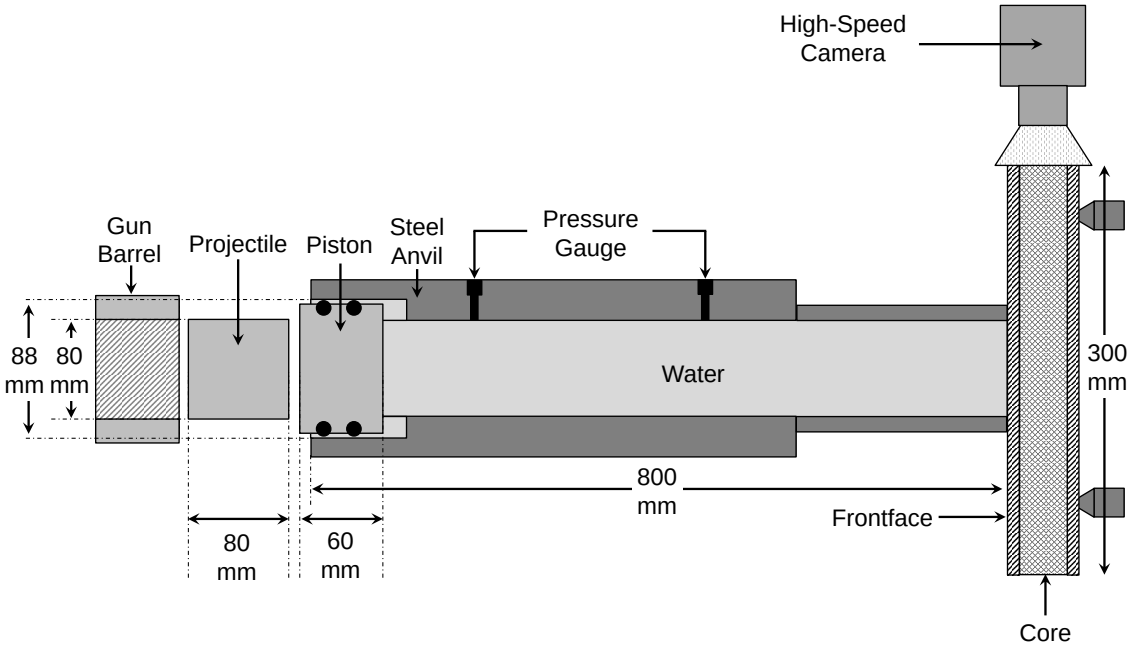


Figure 105 Schematic illustration of the an air-backed loading configuration for an impulsively loaded sandwich structure.

Based on the experiments and numerical simulations reported here, four material-structure-performance relations have been developed. These relations are in the form of a power law in the form of $z = \left[ A \cdot \bar{\rho}^{(m)} \cdot \bar{I}^{(n)} \right]$, where $z$ is the acceptable deflection and transmitted impulse levels and $A, m$ and $n$ are constants. These relations can be used to inform structural design with the understanding that they should only be used for the specified material, structural parameter ranges and loading conditions. For a given combination of deflection and impulse transmitted, the optimum value of relative density

for a specific impulsive load level can be achieved by varying material properties of the monolithic plate or sandwich core.

A number of failure mechanisms are observed by time-resolved as well as post-mortem inspection of the composite panels. Failure in the monolithic composite panels consists of matrix cracking and fiber pullout, in addition to multiple delaminations through the cross-section. With increasing load intensity, the severity of matrix cracking increases significantly. In sandwich structures, the failure mechanisms consist of (1) matrix cracking, (2) fiber rupture, (3) fiber-matrix debonding, (4) permanent core compression and core indentation, (5) core shear cracking and rupture, (7) core-face debonding, and (8) rupture of the composite panel. The effects of loading rate are much more significant for sandwich composites with high density cores (HP100 and HP250) than for structures with low density cores (HP60). Concurrent numerical analyses of the response of composite panels provide a more in-depth understanding of the structural response and failure mechanisms. Based on the experiments, a parametric finite element analysis is carried out, focusing on the effects of (i) load intensity, (ii) changes in relative density (monolithic, HP60, HP100, and HP250), and (iii) air-backed and water-backed loading conditions. For all the calculations presented, simply-supported boundary conditions are used, as in the experiments. The blast resistance of composite structures is quantified through the use of three different measures:

$$\text{Normalized displacement: } \bar{U} = \frac{\text{Out-of-plane Displacement } (\text{mm})}{\text{Lenght of the Structure } (\text{mm})} = \frac{\Delta}{L}; \tag{85}$$

Normalized transmitted impulse: $\bar{I}_B = \dfrac{\text{Transmitted Impulse } (\text{kPa}\cdot\text{s})}{\text{Incident Impulse } (\text{kPa}\cdot\text{s})} = \dfrac{I_T}{I_0}$; (86)

Damage: $\bar{N} = \dfrac{\text{Number of Damaged Elements in All Components}}{\text{Total Number of Elements in All Components}} = \dfrac{N_C}{N_T}$. (87)

## 9.5 Composite structures with equivalent mass

In this analysis, the total mass of the structure is kept relatively constant while the material properties of the composite structures are varied. The structures considered in this analysis are represented in Table 10, column (1), rows (1-2). The effect of material properties, stacking sequences, core geometry, load intensity and loading conditions on blast resistance are analyzed experimentally and computationally. The temporal evolution of selected performance metrics as functions of load intensity and material properties are obtained. In particular, the performance metrics studied in detail are out-of-plane deflection, impulse transmission and accumulated damage. Failure modes are evaluated qualitatively to facilitate comparison of dynamic behavior of the different structures. The experimental results are used to calibrate the computational model and evaluate response over a wide range of loading and structural attributes.

When the underwater impulsive wave impinges on the target, a number of deformation and failure modes are observed in the sandwich composite. Due to structural deflection and bending, the frontface experiences compressive loading which causes face wrinkling which is resisted by the core. Frontface buckling can ultimately lead to matrix cracking and fiber-matrix debonding followed by rupture. Failure in the frontface is followed by core compression, core shear cracking and fragmentation. Initially, the core

undergoes rapid compression near the load region, a phenomenon called "core indentation". Triantafillou and Gibson [176, 177] showed that the indentation load is set by plastic yielding in the core and simultaneous inelastic deformation in the frontface. Since the facesheets in this set of experiments are relatively thin, it can be assumed that the core collapses at uniform shear strength with negligible additional strength provided by the facesheets. Due to the simply-supported loading configuration, the backface experiences maximum stresses near the midplane and fails under tensile loading. The interfaces between the core and facesheets are subjected to multi-axial loads due to the complicated deformation modes in both the facesheets and the core.

### 9.5.1 Experimental results and numerical validation

Figure 106 shows a sequence of high-speed photographs of a composite sandwich structure with carbon-fiber/epoxy faces and a 30 mm thick Divinycell HP60 core subjected to $\bar{I} = 0.16$. Core compression commences immediately after the onset of loading at $t = 200\,\mu s$, and inclined cracks originate near the loading circumference area at $t = 400\,\mu s$. The backface of the sandwich structure, which experiences tensile loading at the mid-section, wrinkles and debonds from the core at $t = 600\,\mu s$. Since the carbon-fiber/epoxy facesheets are rather stiff, they enhance load spreading by uniformly compressing the core throughout the loaded section. Although the overall deflection plateaus at $t = 1000\,\mu s$, the core compressive strain increases continuously up to $t = 1600\,\mu s$, allowing the sandwich structure to minimize the impulse transmitted to the supports. It should be noted that damage in the backface and core-face debonding is strongly dependent on out-of-plane deflection and the compliant HP60 core is much more

susceptible to this type of failure. Figure 107 shows the contour plots of damage from finite element calculations superimposed on high-speed photograph to allow comparison of experimental and numerical results for a 30 mm thick HP60 core. Simulations show that after the onset of loading, the central region of the sandwich core undergoes rapid compression followed by core crushing and cracking. As discussed previously, the computational model underestimates the stiffness of structural foam cores leading to a greater localization of damage compared to experiments. The compressive strain in the core increases continuously up to $t = 1400\,\mu s$.

An analysis of the dynamic compressive response of polymeric foams and the effect face mass (and thickness) on structural response indicates that lighter frontfaces can help mitigate the effects of blast loads by decreasing the momentum gained by the frontface and reducing the impulse transmitted through the core. In order to test this hypothesis on a structural scale involving the interaction of multiple damage modes and failure mechanisms, a sandwich structure consisting of a 30 mm HP60 core, a 1.6 mm thick carbon-fiber/epoxy frontface, and a 3 mm thick carbon-fiber/epoxy backface is subjected to $\bar{I} = 0.16,$ as shown in Figure 108. The structure starts deforming at $t = 200\,\mu s$ and almost instantly undergoes localized failure in the core due to a sudden loss in stiffness near the loading proximity. This phenomenon is also called "core indentation" and involves buckling and kinking of the frontface and debonding of the frontface and the core. As a consequence of core indentation failure, the deformation in the sandwich structure is overwhelmingly concentrated near the mid-section of the structure which results is severe deformation in the core at $t = 600\,\mu s.$ Due to the lack of

uniform load-spreading on the sandwich core, the core fails and water ejects out of the backface at $t = 800\,\mu s$. The plate undergoes shear cracking near the supports at $t = 1200\,\mu s$, resulting in complete rupture and collapse. Although results for uniaxial compression of foams show that a lower frontface mass decreases the impulses transmitted to the core, it is quite clear that multiaxial loads in realistic conditions necessitate a strong and stiff frontface to ensure adequate load spreading and prevent localized failure and collapse.

Figure 109 shows a sequence of high-speed photographs of a composite sandwich structure with carbon-fiber/epoxy faces and a 20 mm thick Divinycell HP100 core subjected to $\bar{I} = 0.16$. Bending deformation initiates in the sandwich structure at $t = 200\,\mu s$, prior to discernible core compression. At $t = 400\,\mu s$, the core experiences compressive strain and the flexural wave traveling from the loading region to the supports causes the frontface-core interface to debond. The core undergoes failure and collapses at $t = 1200\,\mu s$. At such incident impulse intensities, it appears that the impulse imparted to the frontface causes it to move away at velocities higher than the allowable dynamic crush rate of the core, resulting in core failure and rupture. Results from finite element simulations are presented in Figure 110. Initially, the primary deformation mode in the sandwich structure is core compression. At $t = 600\,\mu s$, the core undergoes shear cracking and core-face debonding near the supports. As the sandwich structure deforms continuously, the core compressive strain increases until the composite structure fails at $t = 1200\,\mu s$.

Figure 111 shows a sequence of high-speed photographs of a composite sandwich structure with a Divinycell HP200 core subjected to $\bar{I} = 0.16$. Initially, flexural waves travel through the frontface, severing the core facesheet bond. Specifically, the incident impulse causes severe core-backface debonding due to multi-axial loading. In cases where the core facesheet bond is stronger than the PVC foam, a layer of core material is separated by the facesheet due to the low tensile strength of PVC foam. Core-face debonding and core crushing are observed at $t = 200\,\mu s$. Core cracking commences at $t = 400\,\mu s$ and is restricted to the region close to the loading area. More core cracking and fragmentation occurs at $t = 600\,\mu s$, with cracks initiating at the frontface and traveling in a diagonal fashion to the backface near the supports. The sandwich structure experiences complete failure and the backface undergoes fragmentation and rupture at $t = 1200\,\mu s$. Figure 112 shows the contour plots of damage from finite element calculations superimposed on high-speed photographs to allow comparison of experimental and numerical results for a 10 mm thick HP250 core. Core frontface and backface debonding occurs over the entire structure. Initially, core cracking results from shear stresses due to the high stiffness of the HP250 core. The core fails through a combination of shear cracking, fragmentation and large scale debonding. Both the frontface and the backface experience considerable damage, much greater than the 30 mm thick HP60 core or the 20 mm thick HP100 core.

Overall, results indicate that the numerical simulations capture the different failure modes observed in experiments, including core compression and indentation, damage in the front and back faces, and core-face debonding. It is apparent that damage

in the backface is highly dependent on the properties of the core. Results show reasonable agreement between the experiments and numerical simulations. The compressible foam constitutive model predicts the initial deformation response which is governed by the core compression and the late term response which involves unloading and elastic recovery. Additionally, the damage criterion provides an accurate characterization of damage creation and growth in the composite as well as foam components. However, the numerical model slightly overestimates the compressibility of the foam core, resulting in greater permanent core compression prior to failure in the simulations as compared to experiments.

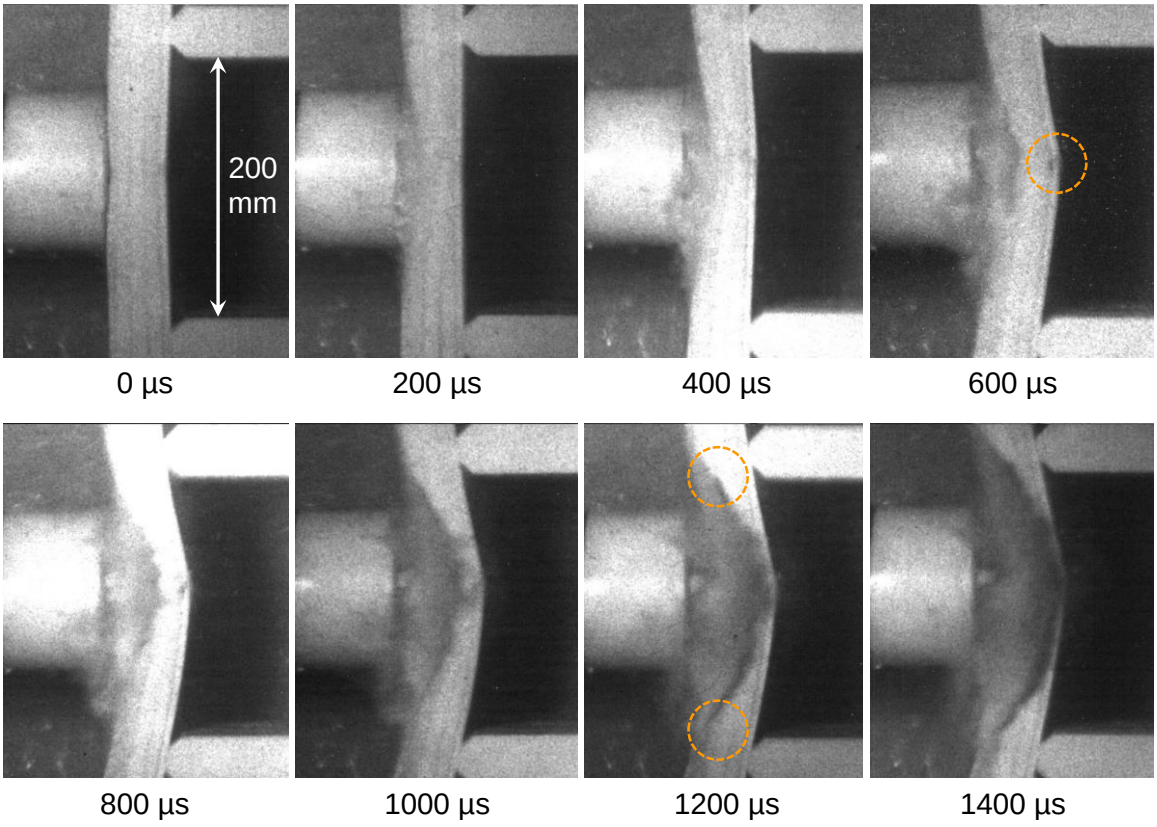


Figure 106 Sequence of high-speed photographs showing the deformation in a sandwich structure with carbon-fiber/epoxy faces and HP60 core subjected to underwater impulsive loading with $\bar{I} = 0.16$. The faces are ~3 mm thick and the core is 30 mm thick.

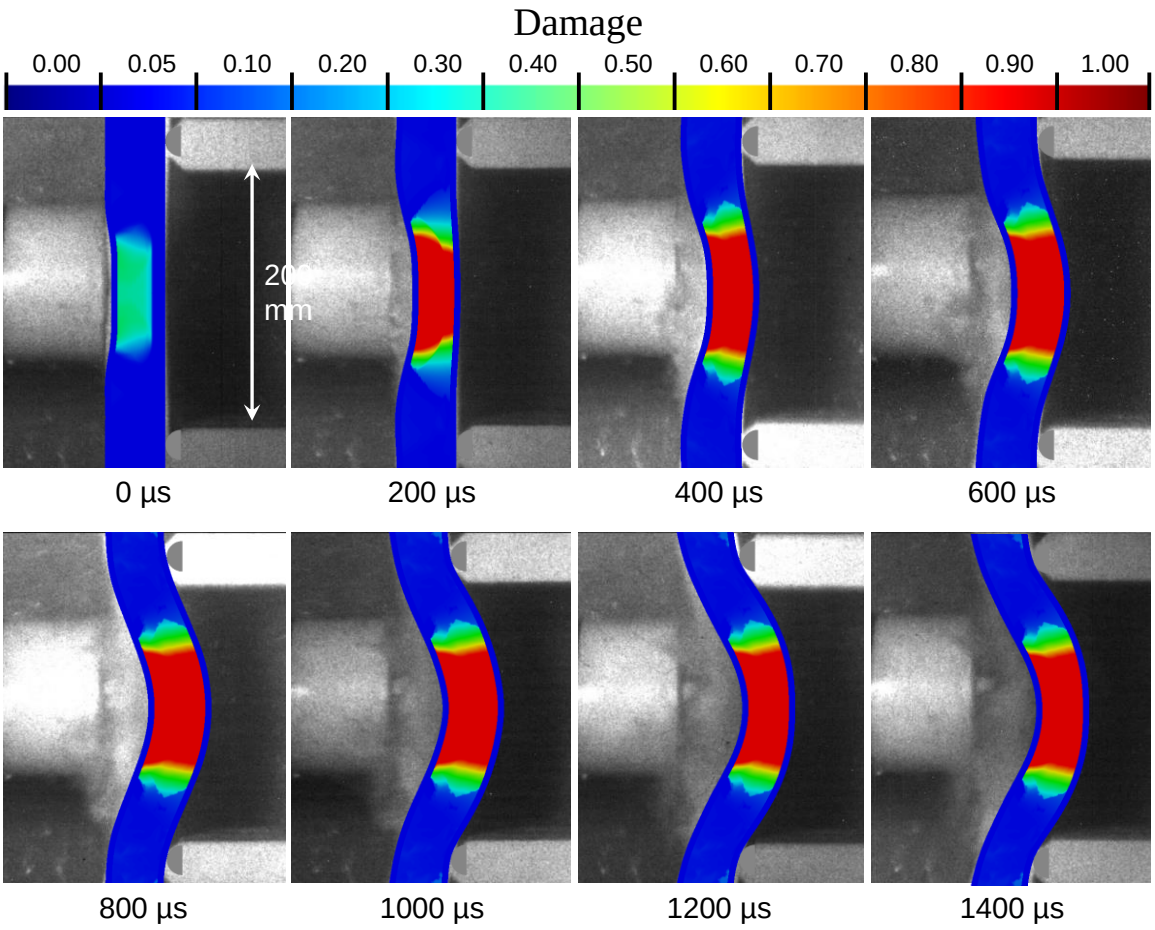


Figure 107 Distributions of damage obtained from finite element simulations superimposed on high-speed photographs showing the deformation in a continuous-core sandwich structure with carbon-fiber/epoxy faces and HP60 core subjected to underwater impulsive loading with $\bar{I} = 0.16$. The faces are ~3 mm thick and the core is 30 mm thick.

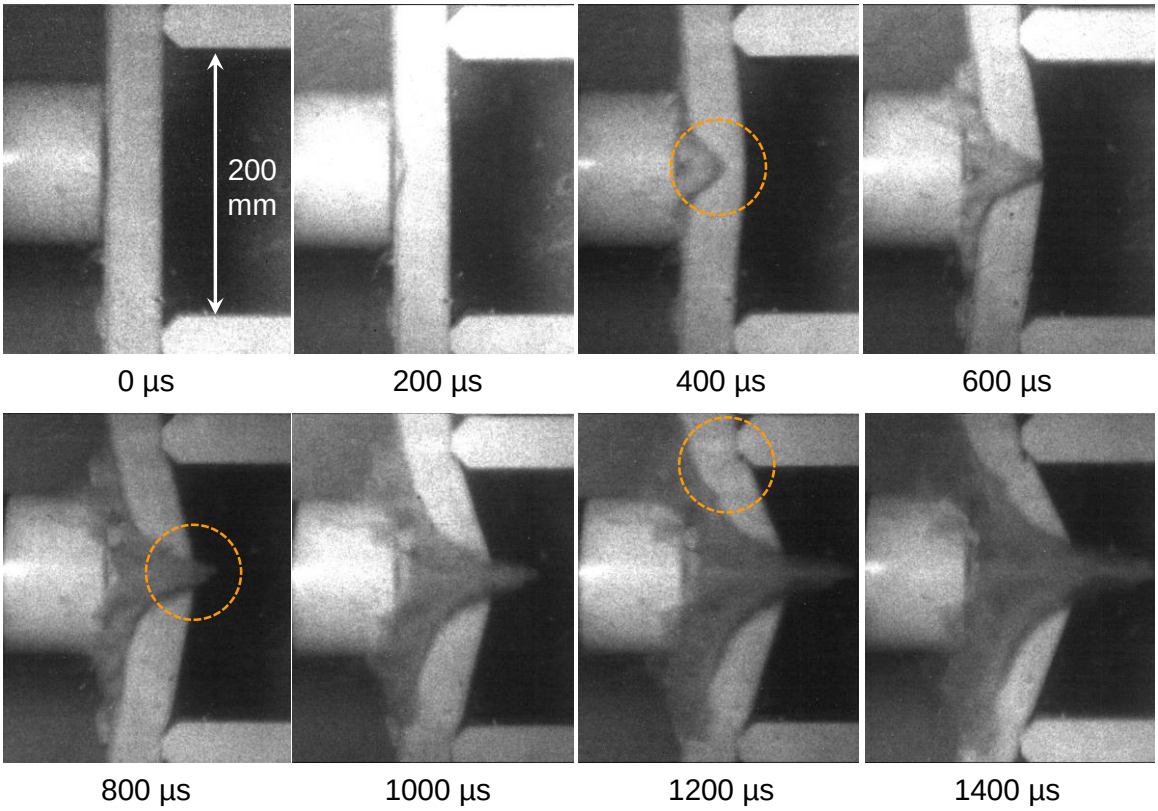


Figure 108 Sequence of high-speed photographs showing the deformation in a sandwich structure with carbon-fiber/epoxy faces and HP60 core subjected to underwater impulsive loading with $\bar{I} = 0.16$. The frontface is 1.6 mm thick, the backface is ~3 mm thick and the core is 30 mm thick.

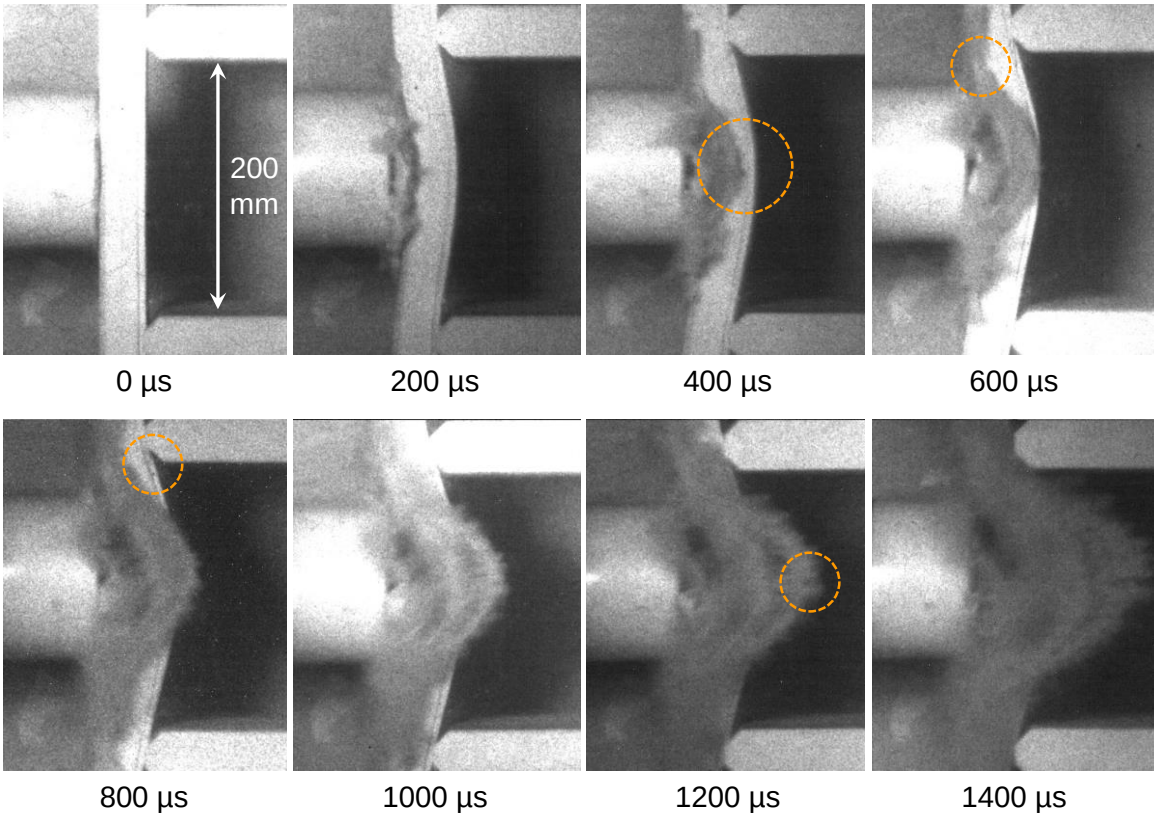


Figure 109 Sequence of high-speed photographs showing the deformation in a sandwich structure with carbon-fiber/epoxy faces and HP100 core subjected to underwater impulsive loading with $\bar{I} = 0.16$. The faces are ~3 mm thick and the core is 20 mm thick.

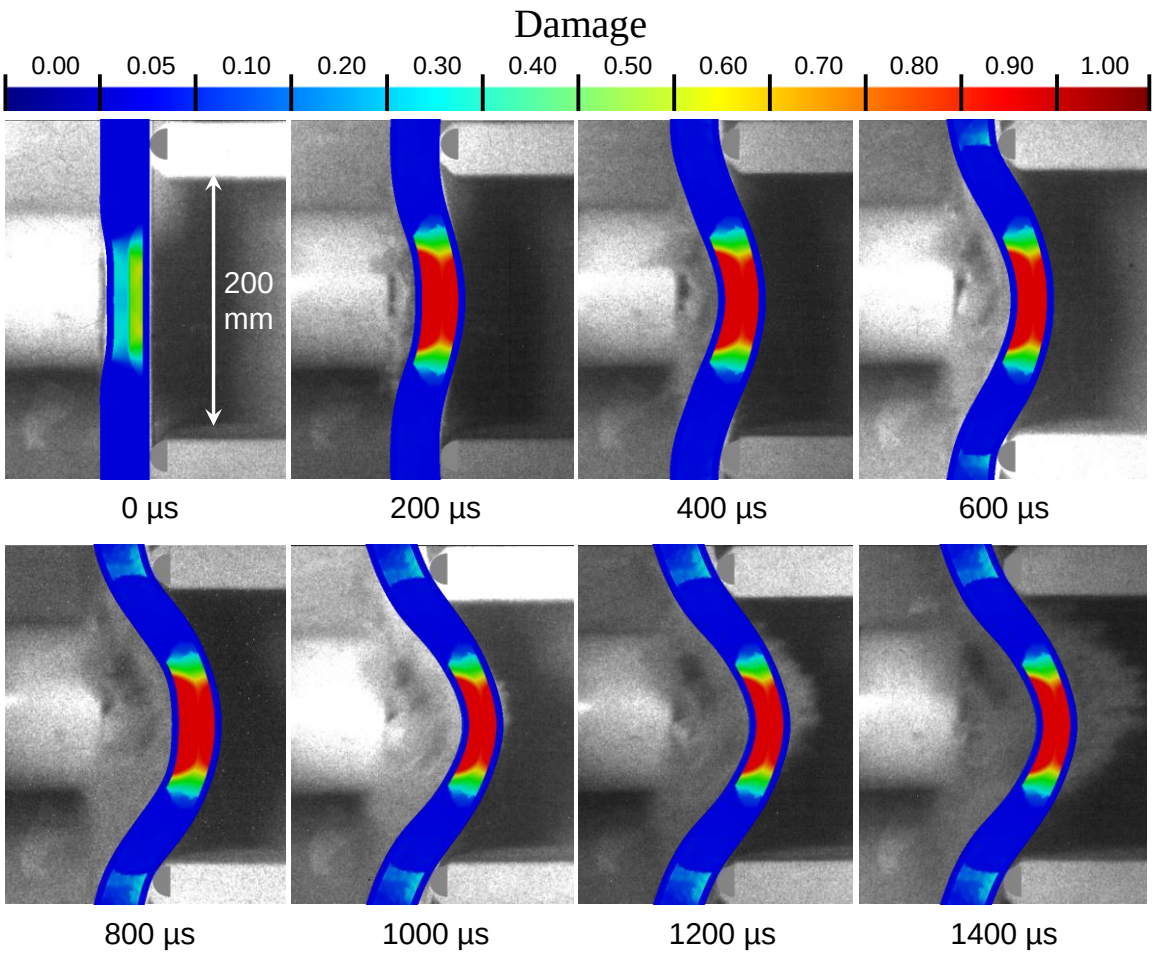


Figure 110 Distributions of damage obtained from finite element simulations superimposed on high-speed photographs showing the deformation in a continuous-core sandwich structure with carbon-fiber/epoxy faces and HP100 core subjected to underwater impulsive loading with $\bar{I} = 0.16$. The faces are ~3 mm thick and the core is 20 mm thick.

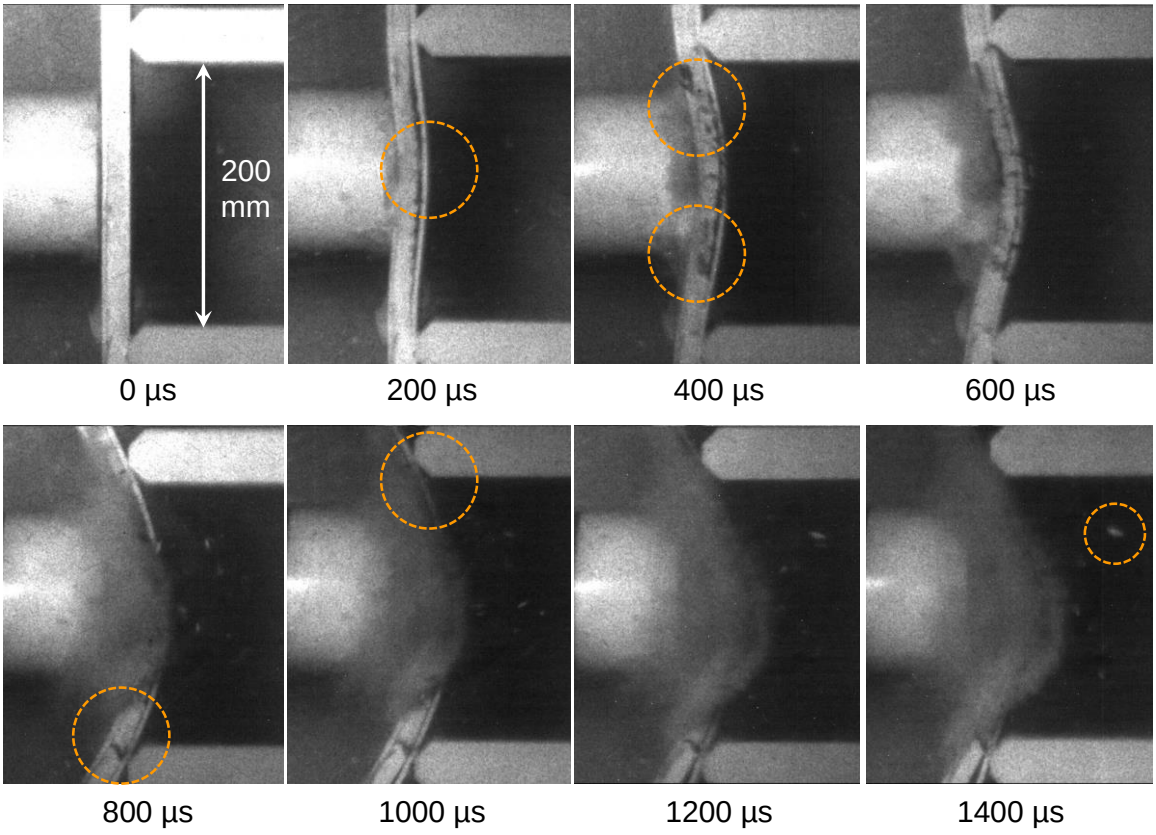


Figure 111 Sequence of high-speed photographs showing the deformation in a sandwich structure with carbon-fiber/epoxy faces and HP2500 core subjected to underwater impulsive loading with $\bar{I} = 0.16$. The faces are ~3 mm thick and the core is 10 mm thick.

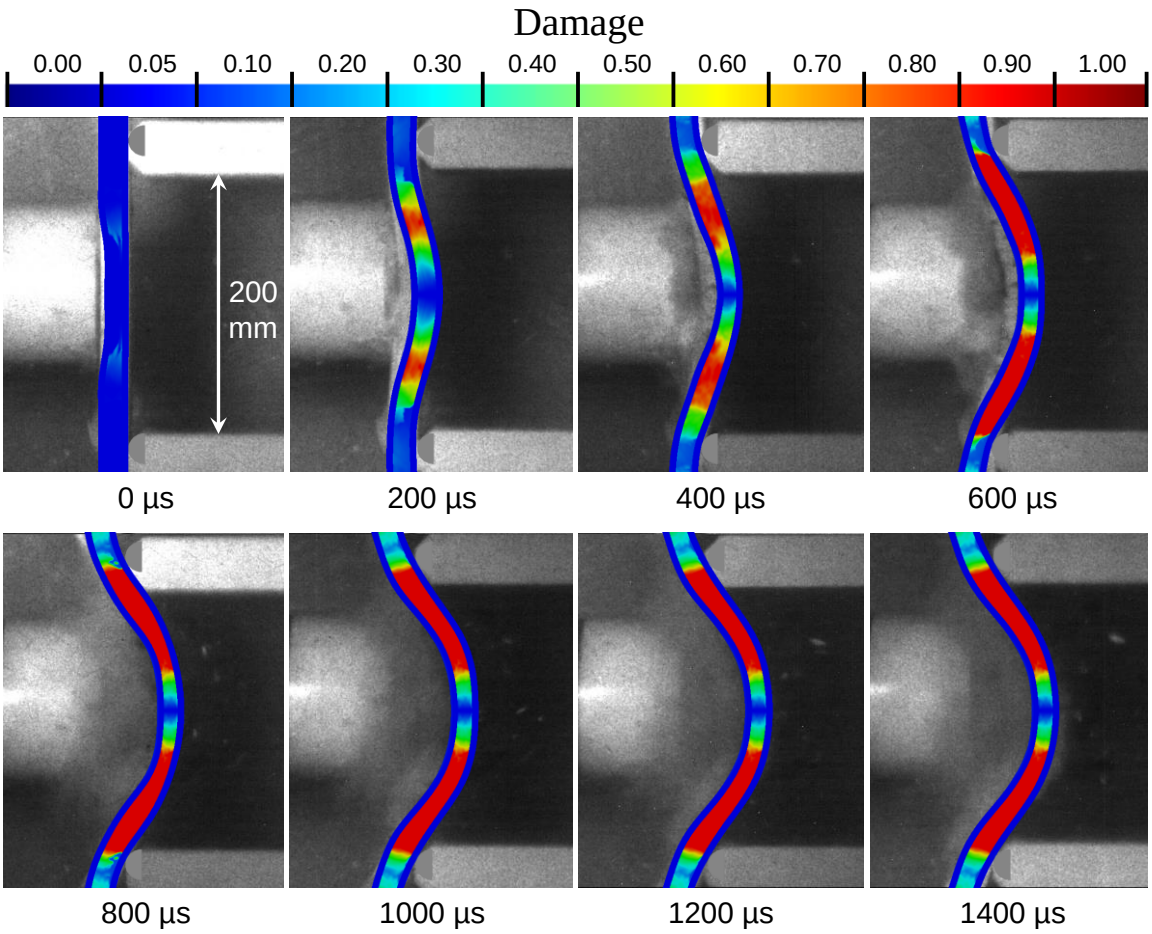


Figure 112 Distributions of damage obtained from finite element simulations superimposed on high-speed photographs showing the deformation in a continuous-core sandwich structure with carbon-fiber/epoxy faces and HP250 core subjected to underwater impulsive loading with $\bar{I} = 0.16$. The faces are ~3 mm thick and the core is 10 mm thick.

### 9.5.2 Out-of-plane deflection

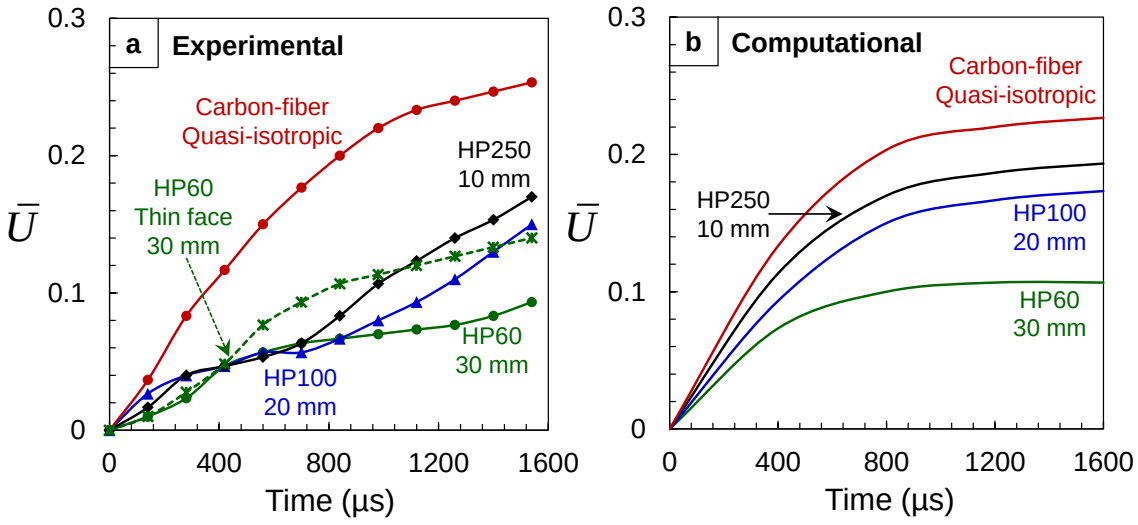


Figure 113 (a) Experimentally measured; and (b) numerically calculated midpoint displacements as functions of time for sandwich structures with equivalent areal mass subjected to $\bar{I} = 0.20$ and $0.16$ respectively.

In the simply-supported configuration, the midpoint of the backface experiences the highest deflection and stresses. Bending deformation initiates in the structure immediately after the onset of loading. Significant deformation in the backface follows core crushing and load transfer through the core. The monolithic composite structure is used as a benchmark for comparison with sandwich structures. It is determined that the lower the deflection when compared to that of the monolithic composite plate at a particular time, the better is the blast resistance. Additionally, the higher the rate of deformation in the backface, the lower is the blast mitigation capability of that particular sandwich structure. For the three core densities, the frontface acquires much higher velocities than the backface. Therefore, the load spreading capacities of the core are critical for enhancing blast resistance. Figure 113(a) and (b) shows the experimentally

measured and computationally calculated histories of center displacements normalized by the length of the composite structure panels respectively. Results for the (a) HP60, (b) HP100, and (c) HP200 cores along with those of the monolithic composite of equivalent mass are presented. Also shown in the same plot is the back displacement experienced by a 30 mm thick HP60 core with a 1.6 mm thick face. All the sandwich structures are subjected to similar impulsive loads with $\bar{I} =\sim 0.20$. The monolithic composite plate undergoes the highest deflection, experiencing a $\bar{U}$ of ~0.26. For the HP200 core, the backface deflection initiates rapidly before plateauing, and the structure experiences ~60% of the deflection in the monolithic composite. For the HP100 core and the HP60 core with the 1.6 mm frontface, the out-of-plane displacement is ~50% of the monolithic plate, while for the 30 mm thick HP60 core, the displacement is ~30% of the monolithic plate. Comparison of the experimental and computational results shows that although the computations do not capture the

Figure 114 shows the core compressive strain in the sandwich structures, calculated by measuring the relative displacements between the frontface and backface. Initially, the core compresses rapidly as the stress wave generated due to the incident impulse causes rapid core strain. When the compressive wave reaches the backface, the backface acquires momentum and starts deforming away from the frontface, stretching the core. At $t = 1200\,\mu s$, the backface velocity reduces and the frontface further compresses the core. Results indicate that as the relative core density increases, core compression decreases significantly. Additionally, thicker low-density cores provide the

greatest reduction in frontface displacement and the longest delay after the onset of loading for structural deflection to initiate.

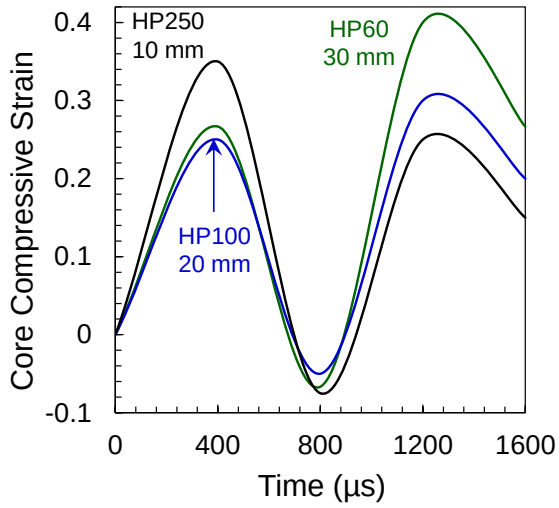


Figure 114 Core compressive strain as a function of time for sandwich structures with equivalent areal mass subjected to $\bar{I} = 0.16$.

The results show that core density profoundly affects both the rate and the extent of deformation in the composite structures. The study indicates that structure with low density, thick cores consistently outperform structures with high density cores of equal mass (and lower thickness). Additionally, the variations in geometric parameters have an effect on flexural rigidity and deformation in sandwich panels. Since a fully dynamic computational framework is used to in this analysis, structural effects beyond bending, as well as bending, are captured.

### 9.5.3 Impulse transmission

Minimizing the impulse transmitted to the internal components of marine vessels is of critical importance. For the simply-supported loading configuration discussed here, the target structure transmits an impulse to the supports. The rate of impulse transmission

and the magnitude of the transmitted impulse can provide valuable insight into the blast resistance and performance of composite structures. Clearly, the composite structure that transmits the least impulse at the lowest rate is most desirable.

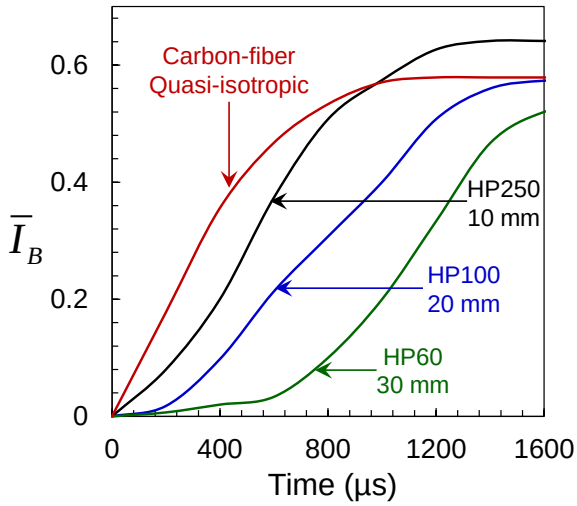


Figure 115 Normalized transmitted impulse as a function of time for sandwich structures with equivalent areal mass subjected to $\bar{I} = 0.16$.

Figure 115 shows the histories of impulses transmitted by composite structures with similar areal masses subjected to an incident impulsive load $\bar{I} = 0.16$. It can be seen that, compared to the monolithic composite plate, the sandwich structures with HP200 and HP100 cores transmit similar impulses but at a significantly lower rate. The 30 mm HP60 core provides the highest impulse mitigation by dramatically reducing the rate of impulse transmission in the initial stages of deformation up to $t = 800\,\mu s$ and also decreasing the total transmitted impulse by ~20%. As the core density decreases and the corresponding core thickness increases, the improvements in blast mitigation are more noticeable.

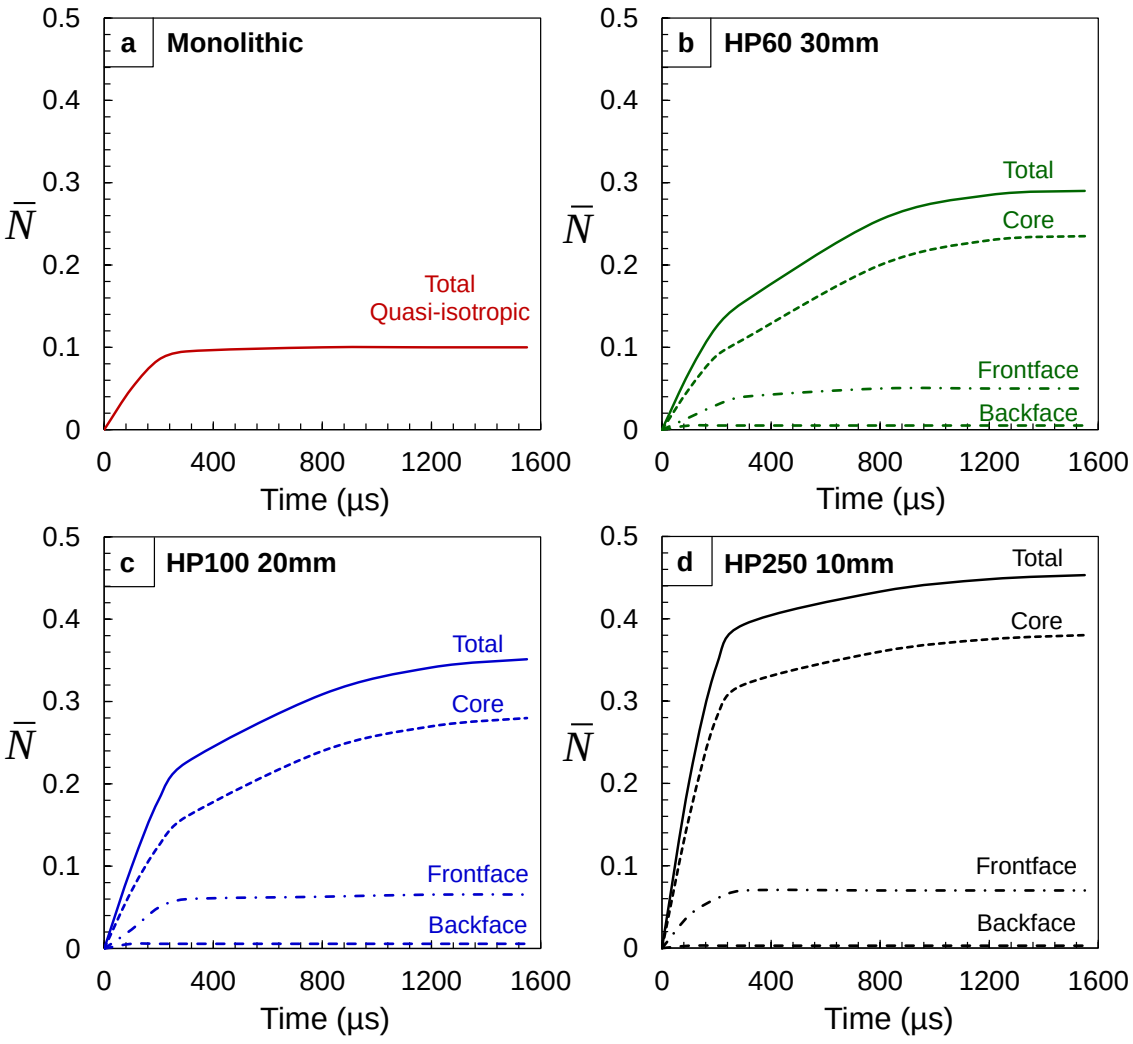


Figure 116 Accumulated damage histories for sandwich structures with equivalent areal mass subjected to $\bar{I} = 0.16$.

### 9.5.4 Accumulated damage

The computational framework developed in this research allows the tracking of damage and failure in different components of the sandwich structure through the use of three constitutive and damage approaches: (1) Hashin damage in the facesheets; (2) cohesive damage in the interfacial regions including interlaminar regions and core-face interfaces; and (3) damage in the sandwich structure core due to severe shear and

compressive stresses through the Deshpande and Fleck criterion [149]. It is essential to quantify the damage in different components to accurately evaluate the deformation response and blast resistance of each structural configuration, and to determine post-blast survivability under a range of loads and material properties.

Figure 116(a-d) shows the histories of damage in the different components of composite structures with varying core densities but similar areal masses subjected to $\bar{I} = 0.16$. The key difference in damage evolution with respect to core density is the fact as the core density increases, the majority of the damage occurs in the early stages of deformation. The HP60 and HP100 cores experience steadily increasing damage throughout the deformation process, while HP250 core experiences the majority of damage in the initial stages of deformation. The inflection of the $\bar{N}$ vs. time curve at $t = \sim 300\,\mu s$ indicates that damage creation seems to be divided into two regimes: (1) impulse transmission regime: which occurs when the incident impulse interacts with the test specimen; and (2) out-of-plane deflection regime: which occurs when the incident impulse travels through the structure and the structure acquires momentum and begins deflecting. Since the impulse transmission regime involves deformation in an extremely short duration, damage is created at a very high rate. Figure 107, Figure 110, and Figure 112 show that when the structure starts deflecting, the damage created during the impulse transmission regime evolves and propagates but no new damage mechanisms are activated. Consequently, although the total damage increases during the deflection regime, the rate of damage creation is significantly lower than in the impulse transmission regime. Damage in the frontface occurs in the impulse transmission regime but does not increase appreciably in the deflection regime. Additionally, as the core

density increases, the damage in the frontface increases while the damage in the backface remains relatively constant.

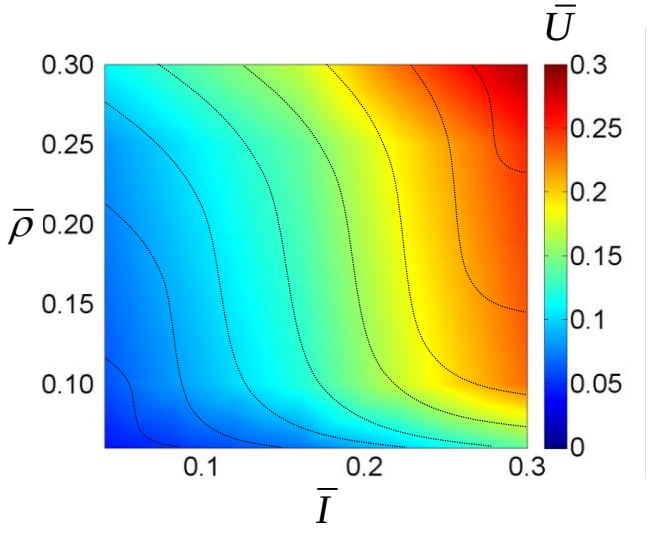


Figure 117 Loading-structure-performance map showing normalized displacement $\bar{U}$ as a function of normalized incident impulse $\bar{I}$ and normalized core density $\bar{\rho}$ for composite structures with equivalent mass.

### 9.5.5 Loading-Structure-Performance maps

Structural design involves selecting materials and designing structures that match the performance profile required by a particular application. A performance profile defines the characteristics required by a structure to excel in its application and defines material indices that capture stated design objectives: minimizing weight, deflection, impulse transmission, cost or maximizing energy absorption, efficiency, bending strength and so on. It is identified by examining the function of the component, the objectives that the designer wishes to fulfill and constraints that the component must meet to perform adequately. Some commonly used indices in more conventional material and structural design research consist of specific stiffness $E/\rho$ , specific strength $\sigma_Y/\rho$ and many

others. These material indices guide the optimal selection of material for component level design. It should be noted that previous design approaches are based on uniaxial compressive loading which is a well-established and quantified loading case. Conversely, in the current scenario consisting of a multitude of loading conditions, structures and materials, the indices must account for a greater number of constraints and variables. Rather simple indices used in previous approaches will be insufficient in this particular case.

Figure 117 shows the loading-structure-performance map of normalized out-of-plane deflection $\bar{U}$ as a function of normalized incident impulse $\bar{I}$ and normalized relative density $\bar{\rho}$ for composite structures with equivalent mass. Results show that low density cores with sufficient thickness have exceptional blast resistance at all load intensities, including failure loads. As the core density increases, the displacement experienced by the structure increases rapidly, especially at failure loads. Figure 118 shows the loading-structure-performance map of normalized transmitted impulse $\bar{I}_B$ as a function of normalized incident impulse $\bar{I}$ and normalized relative density $\bar{\rho}$. In a manner quite similar to out-of-plane deflection, the transmitted impulses are significantly higher for greater core densities. The slight reduction at very high core densities can be attributed to the fact that dense, thin composite plates deflect instantaneously and lose contact with the supports, while sandwich structures resist deflection for a greater period of time and stay in contact with the supports. This causes the monolithic plates to transmit lower impulses for similar incident loads but does not necessarily indicate higher blast resistance.

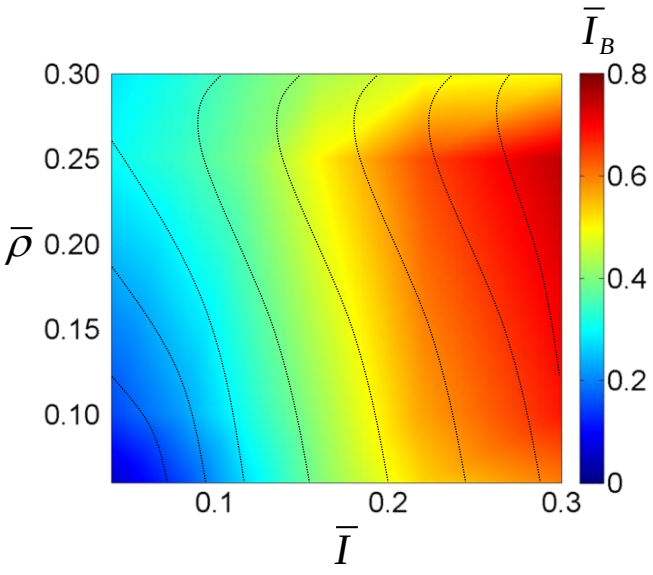


Figure 118 Loading-structure-performance map showing normalized transmitted impulse $\bar{I}_B$ as a function of normalized incident impulse $\bar{I}$ and normalized core density $\bar{\rho}$ for composite structures with equivalent mass.

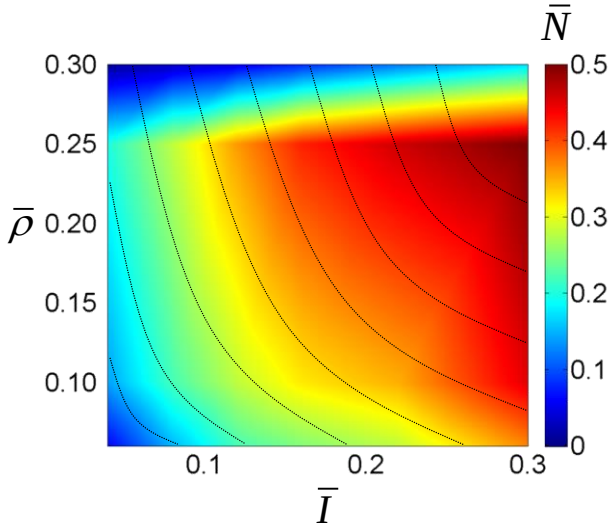


Figure 119 Loading-structure-performance map showing normalized accumulated damage $\bar{N}$ as a function of normalized incident impulse $\bar{I}$ and normalized core density $\bar{\rho}$ for composite structures with equivalent mass.

Figure 119 shows the loading-structure-performance map of normalized damage parameter $\bar{N}$ as a function of normalized incident impulse $\bar{I}$ and normalized relative

density $\bar{\rho}$ for composite structures with equivalent mass. As the incident impulse increases, the damage created in the composite structure increases exponentially.

## 9.6 Composite structures with equivalent thickness

In this analysis, the total mass of the structure is kept relatively constant while the material properties of the composite structures are varied. The structures considered in this analysis are represented in Table 10, column (1), rows (3-4). The effect of material properties, stacking sequences, core geometry, load intensity and loading conditions on blast resistance are analyzed experimentally and computationally. The temporal evolution of selected performance metrics as functions of load intensity and material properties are obtained. In particular, the performance metrics studied in detail are out-of-plane deflection, impulse transmission and accumulated damage. Failure modes are evaluated qualitatively to facilitate comparison of dynamic behavior of the different structures. The experimental results are used to calibrate the computational model and evaluate response over a wide range of loading and structural attributes.

When the underwater impulsive wave impinges on the target, a number of deformation and failure modes are observed in the sandwich composite. Due to structural deflection and bending, the frontface experiences compressive loading which causes face wrinkling which is resisted by the core. Frontface buckling can ultimately lead to matrix cracking and fiber-matrix debonding followed by rupture. Failure in the frontface is followed by core compression, core shear cracking and fragmentation. Initially, the core undergoes rapid compression near the load region, a phenomenon called "core indentation". Triantafillou and Gibson [176, 177] showed that the indentation load is set

by plastic yielding in the core and simultaneous inelastic deformation in the frontface. Since the facesheets in this set of experiments are relatively thin, it can be assumed that the core collapses at uniform shear strength with negligible additional strength provided by the facesheets. Due to the simply-supported loading configuration, the backface experiences maximum stresses near the midplane and fails under tensile loading. The interfaces between the core and facesheets are subjected to multi-axial loads due to the complicated deformation modes in both the facesheets and the core.

### 9.6.1 Experiments and numerical validation

Figure 120 shows a sequence of high-speed photographs of a composite sandwich structure with carbon-fiber/epoxy faces and a 30 mm thick Divinycell HP100 core subjected to $\bar{I} = 0.16$. Initially, flexural waves travel through the frontface, severing the core facesheet bond. In cases where the core facesheet bond is stronger than the PVC foam, a layer of core material is separated by the facesheet due to the low tensile strength of PVC foam. Immediately after the onset of loading, the core compresses in a small region close to the loading area. At $t = 400\,\mu s,$ inclined cracks originate near the loading circumference area. These cracks propagate from the frontface to the backface and branch into multiple cracks in the middle of the core prior to reaching the backface. As deformation progresses, the crack faces widen up to $t = 1000\,\mu s,$ but the structure survives the incident impulse without undergoing catastrophic failure or collapse. Core compression and core cracking occur simultaneously with crack propagation through the core. Tracking the movement of the water exiting the barrel reveals that unlike the HP250 10 mm thick H250 or 20 mm thick HP100 sandwich structures, the water in this case

initially impinges on the structure but travels sideways because the test specimen provides high blast resistance. At $t = 1200\,\mu s,$ the out-of-plane deflection reaches a peak and the structure recovers a significant portion of the deformation. Figure 121 shows the contour plots of damage from finite element calculations superimposed on high-speed photograph to allow comparison of experimental and numerical results for a 30 mm thick HP100 core.

Figure 122 shows a sequence of high-speed photographs of a composite sandwich structure with carbon-fiber/epoxy faces and a 30 mm thick Divinycell HP250 core subjected to $\bar{I} = 0.16$. The deformation in this sandwich plate is involves negligible core crushing and the incident load is directly transmitted to the backface which gathers momentum at $t = 400\,\mu s.$ Following the movement of water exiting the barrel shows that after being unable to penetrate the structure, the water travels sideways (towards the high-speed camera) at $t = 800\,\mu s.$ Figure 123 shows the contour plots of damage from finite element calculations superimposed on high-speed photograph to allow comparison of experimental and numerical results for a 30 mm thick HP100 core. Compared to finite element simulations of other sandwich structures subjected to $\bar{I} = 0.20,$ the 30 mm thick HP250 sandwich structure shows excellent blast resistance and exceptionally high survivability, showing negligible core compression and no major cracking in any of the sandwich components.

Since HP60 cores undergo large deflections while transmitting low impulses, and HP250 cores undergo very low deflection but transmit large impulses, we take a novel approach to sandwich structure core construction. Instead of using a core consisting of a

single continuous material, the core is designed by stacking sections with different relative densities. Two designs are studied, as shown in Table 10, column (1), rows (3-4). Figure 124 shows a sequence of high-speed photographs of a composite sandwich structure with carbon-fiber/epoxy faces and a 30 mm thick Divinycell HP60-HP100-HP250 core subjected to $\bar{I} = 0.16,$ and Figure 125 shows finite element simulations corresponding to the high-speed images. Since the HP60 core section is near the impulsively loaded face, the sandwich core undergoes severe core compression up to $t = 400\,\mu s,$ in a manner similar to the continuous HP60 core (Figure 106). When the impulse is transmitted through the core, inclined cracks originate in the high density core sections (HP250) at $t = 600\,\mu s.$ These cracks propagate towards the backface and cause interfacial separation between the core and backface. Core crushing and cracking occur simultaneously, but core indentation (localized compressive failure) in HP60 section occurs to a greater extent than in the HP100 section. Figure 126 shows a sequence of high-speed photographs of a composite sandwich structure with carbon-fiber/epoxy faces and a 30 mm thick Divinycell HP250-HP100-HP60 core subjected to $\bar{I} = 0.16,$ and Figure 126 shows finite element simulations corresponding to the high-speed images. The HP250 section experiences loading prior to the rest of the core, and the incident impulse is transmitted instantaneously causing the entire sandwich structure to begin deflecting. Unlike the HP60 sandwich structure, the HP250 sandwich structure shows rather negligible core compressive strains in the initial stages of deformation. The response of the HP250 section is reminiscent of the 10 mm thick HP250 core in Figure 111. Since the highest stresses in a simply-supported beam configuration are created near the mid-

section, cracks originate in the HP250 section at $t = 200\,\mu s$ and propagate towards the backface. The specimen reaches its highest deflection at $t = 800\,\mu s,$ before decelerating and recovering the deformation. Although both the graded core structural configurations exhibit high survivability, the HP60-HP100-HP250 layup provides higher blast mitigation due to enhanced core compressibility leading to a reduction in transmitted impulse.

Overall, results indicate that the numerical simulations capture the different failure modes observed in experiments, including core compression and indentation, damage in the front and back faces, and core-face debonding. It is apparent that damage in the backface is highly dependent on the properties of the core. Results show reasonable agreement between the experiments and numerical simulations. The compressible foam constitutive model predicts the initial deformation response which is governed by the core compression and the late term response which involves unloading and elastic recovery. Additionally, the damage criterion provides an accurate characterization of damage creation and growth in the composite as well as foam components. However, the numerical model slightly overestimates the compressibility of the foam core, resulting in greater permanent core compression prior to failure in the simulations as compared to experiments.

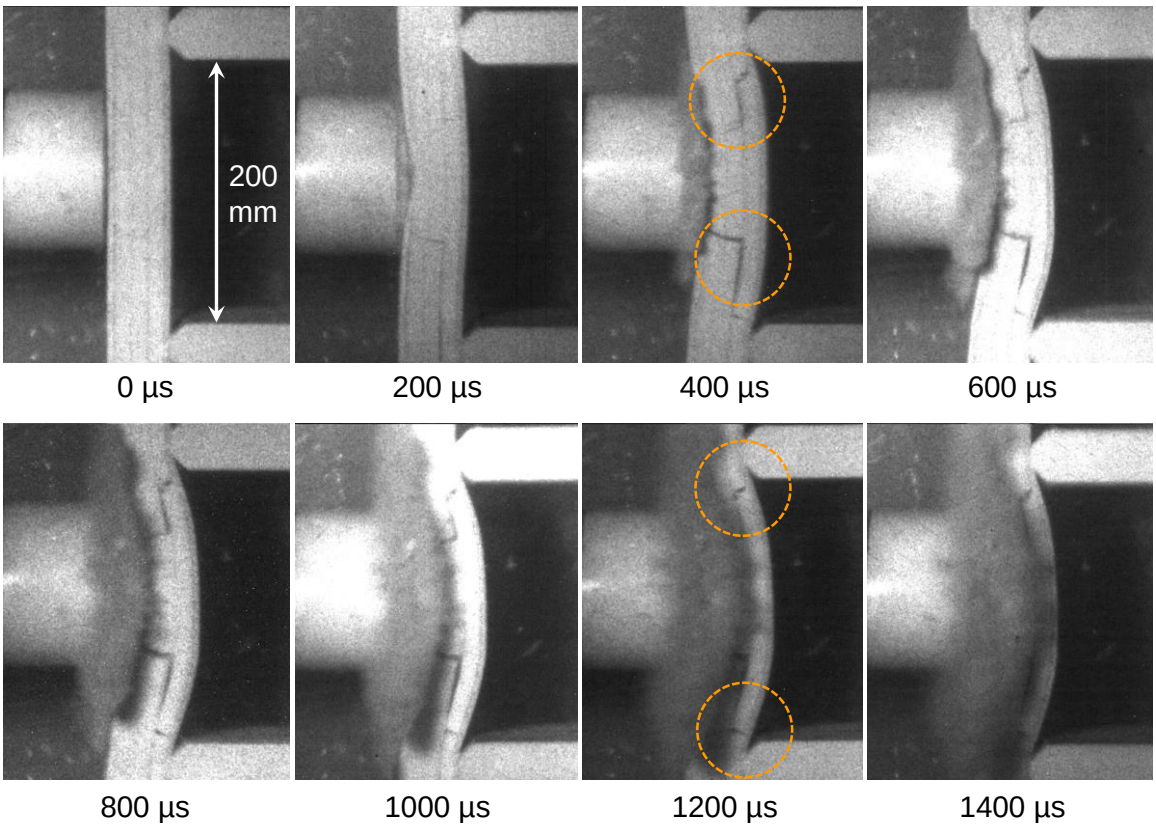


Figure 120 Sequence of high-speed photographs showing the deformation in a sandwich structure with carbon-fiber/epoxy faces and HP100 core subjected to underwater impulsive loading with $\bar{I} = 0.16$. The faces are ~3 mm thick and the core is 30 mm thick.

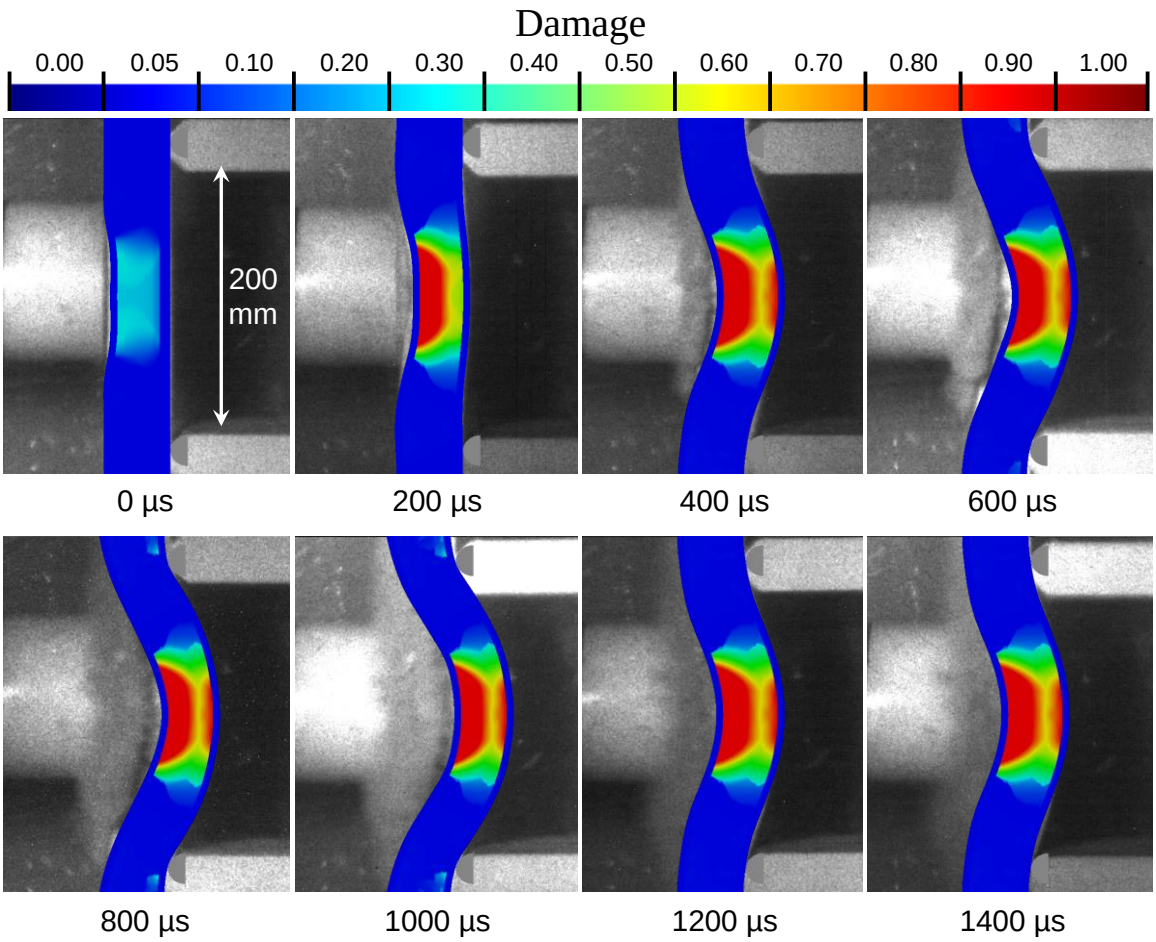


Figure 121 Distributions of damage obtained from finite element simulations superimposed on high-speed photographs showing the deformation in a continuous-core sandwich structure with carbon-fiber/epoxy faces and HP100 core subjected to underwater impulsive loading with $\bar{I} = 0.16$. The faces are ~3 mm thick and the core is 30 mm thick.

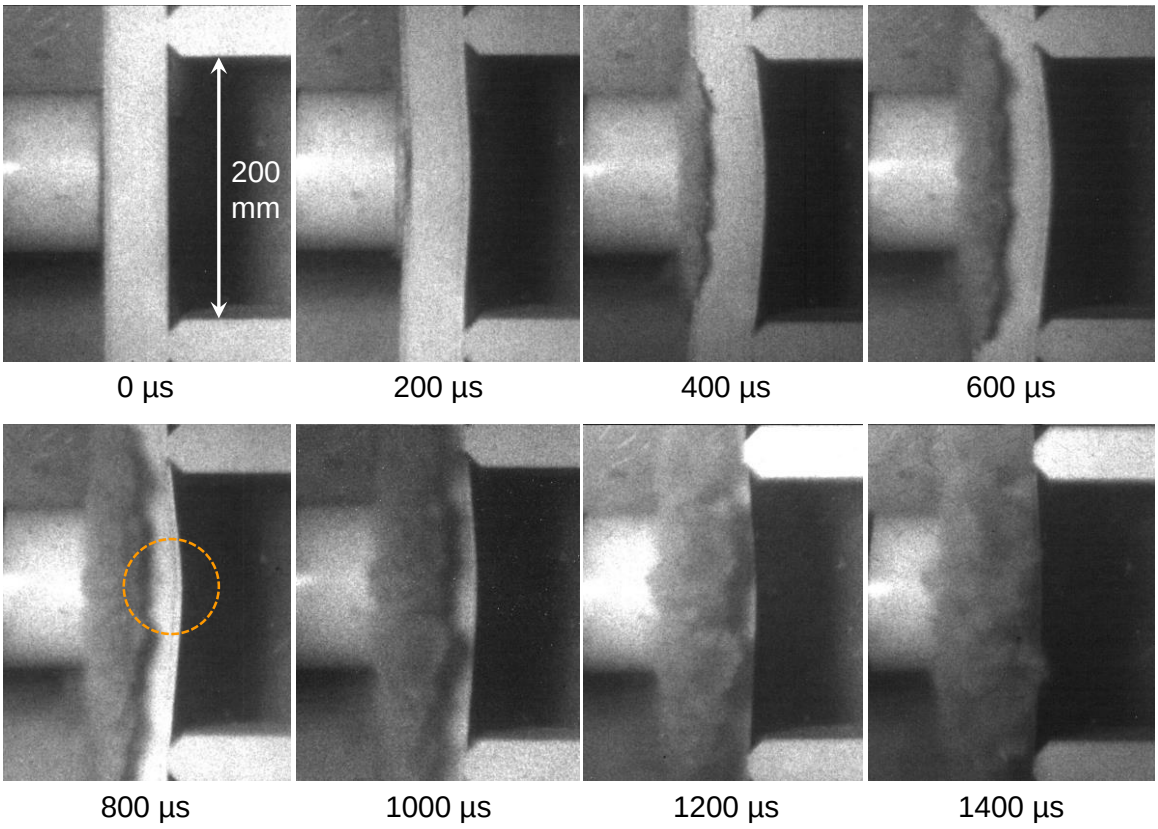


Figure 122 Sequence of high-speed photographs showing the deformation in a sandwich structure with carbon-fiber/epoxy faces and HP250 core subjected to underwater impulsive loading with $\bar{I} = 0.16$. The faces are ~3 mm thick and the core is 30 mm thick.

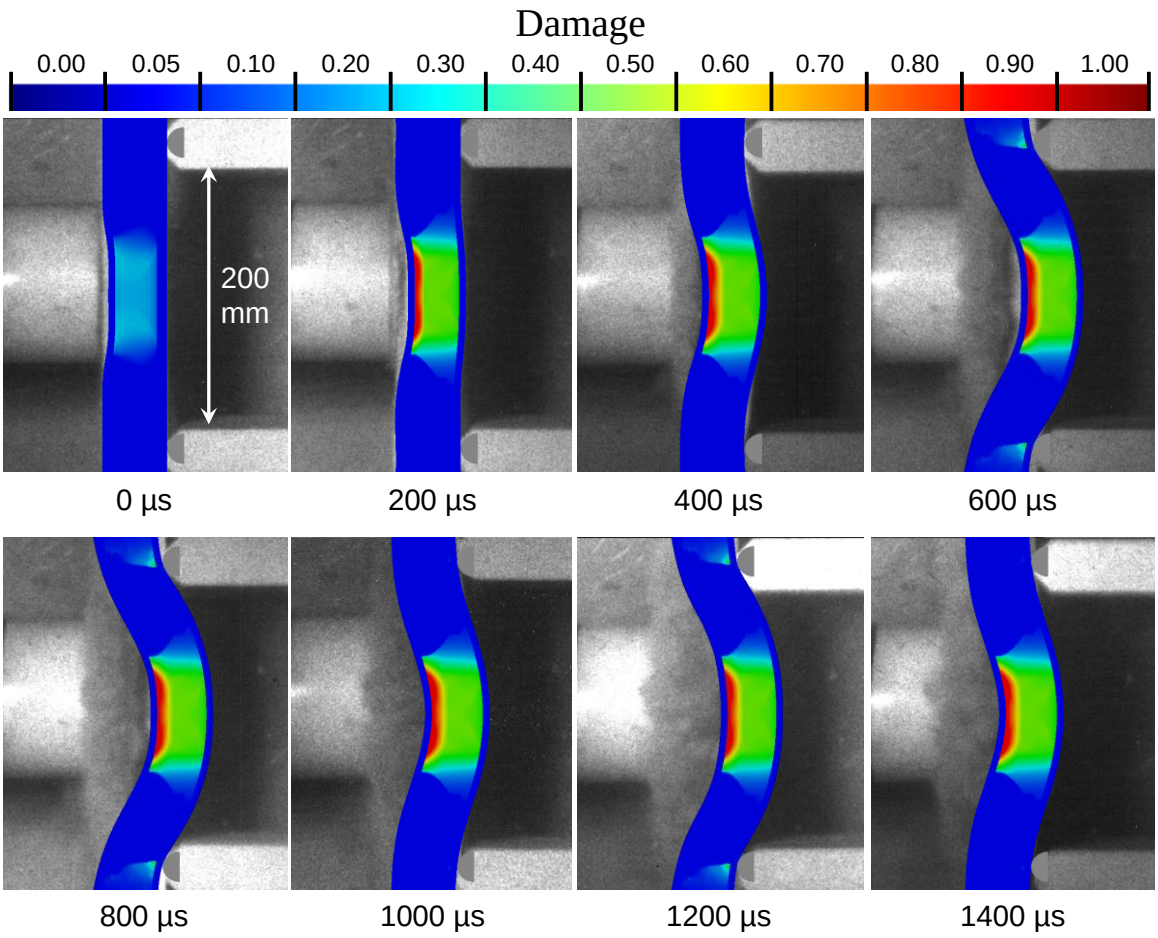


Figure 123 Distributions of damage obtained from finite element simulations superimposed on high-speed photographs showing the deformation in a continuous-core sandwich structure with carbon-fiber/epoxy faces and HP250 core subjected to underwater impulsive loading with $\bar{I} = 0.16$. The faces are ~3 mm thick and the core is 30 mm thick.

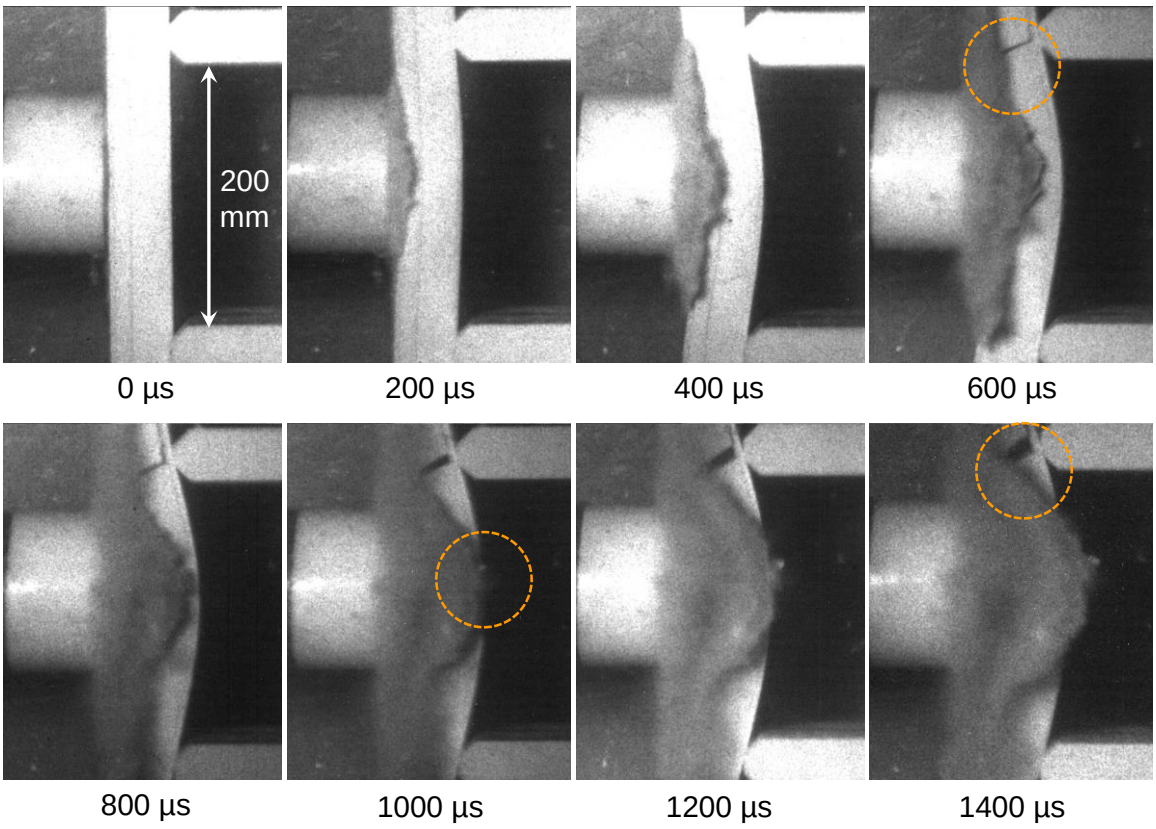


Figure 124 Sequence of high-speed photographs showing the deformation in a graded-core sandwich structure with carbon-fiber/epoxy faces and HP60-HP100-HP250 core subjected to underwater impulsive loading with $\bar{I} = 0.16$. The faces are ~3 mm thick and each layer in the core is 10 mm thick for a total core thickness of 30 mm.

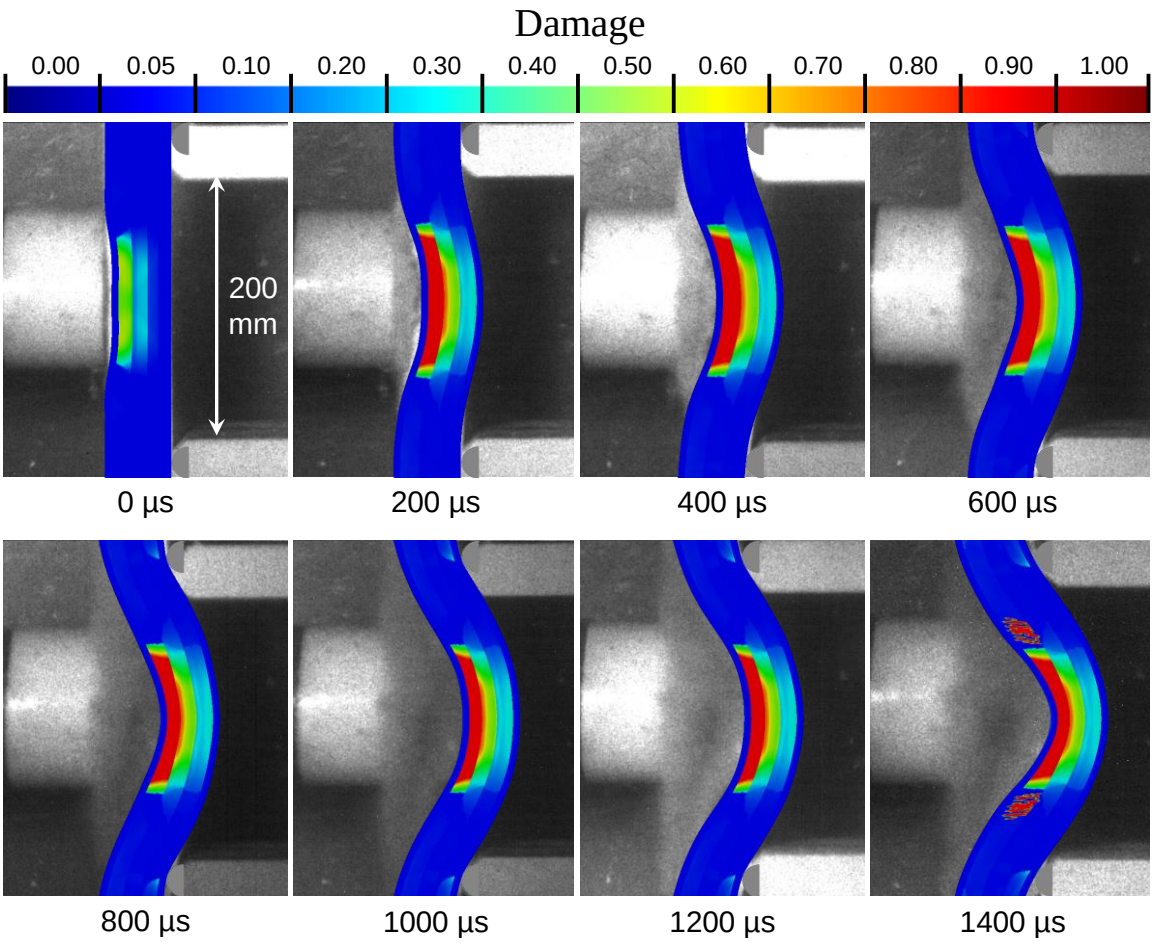


Figure 125 Distributions of damage obtained from finite element simulations superimposed on high-speed photographs showing the deformation in a graded-core sandwich structure with carbon-fiber/epoxy faces and HP60-HP100-HP250 core subjected to underwater impulsive loading with $\bar{I} = 0.16$. The faces are ~3 mm thick and each layer in the core is 10 mm thick for a total core thickness of 30 mm.

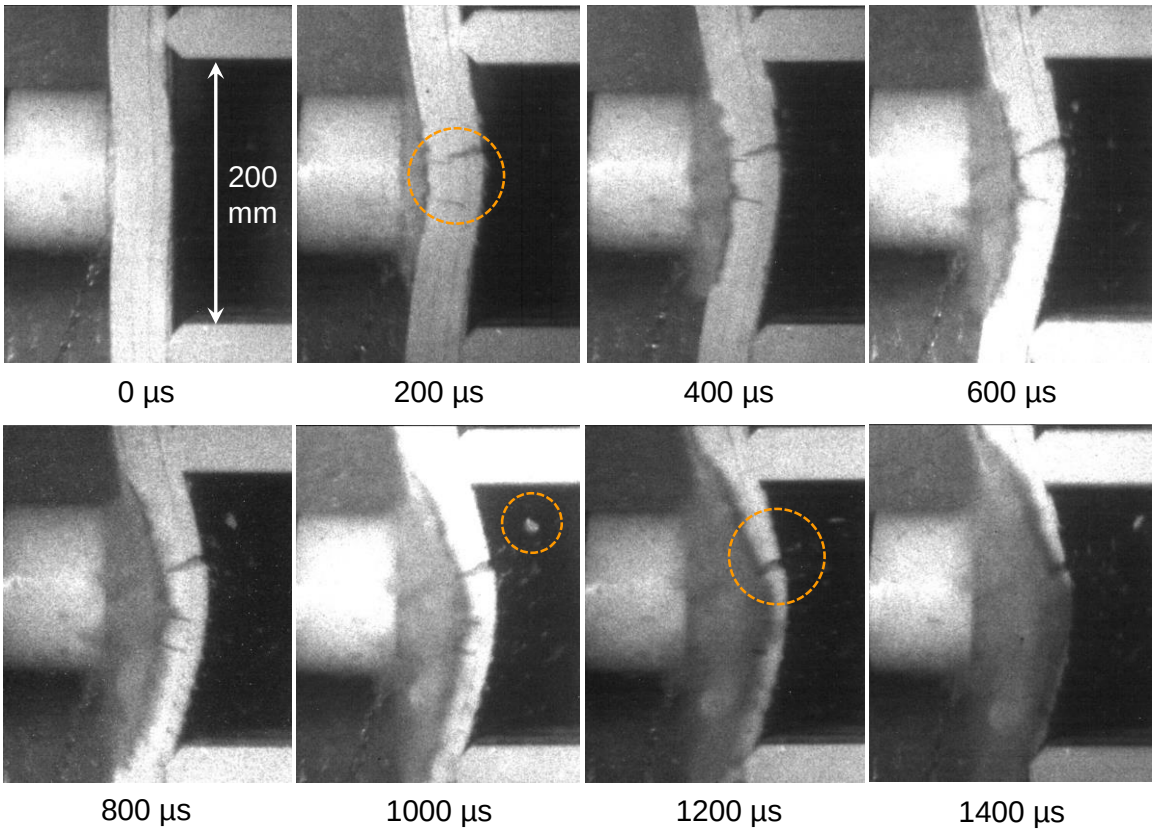


Figure 126 Sequence of high-speed photographs showing the deformation in a graded-core sandwich structure with carbon-fiber/epoxy faces and HP250-HP100-HP60 core subjected to underwater impulsive loading with $\bar{I} = 0.16$. The faces are ~3 mm thick and each layer in the core is 10 mm thick for a total core thickness of 30 mm.

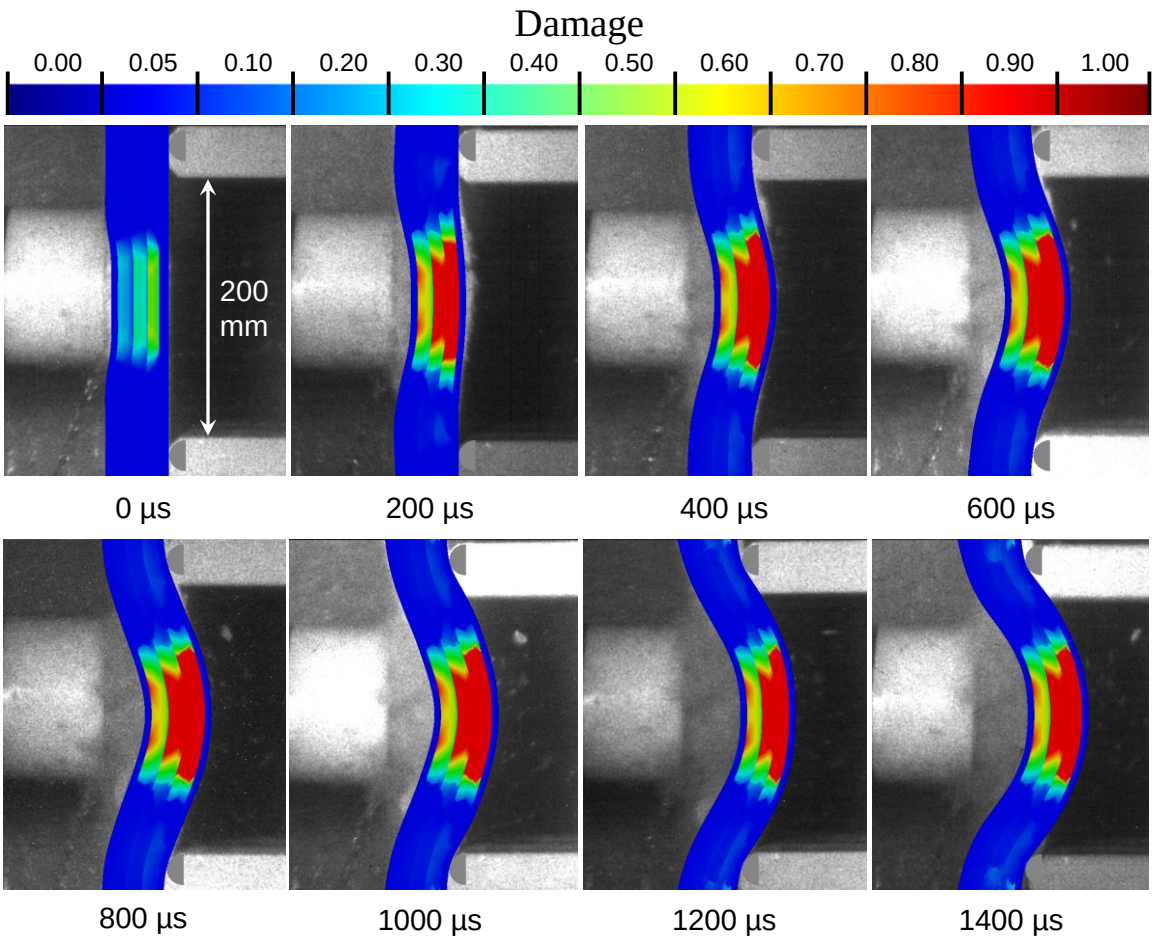


Figure 127 Distributions of damage obtained from finite element simulations superimposed on high-speed photographs showing the deformation in a graded-core sandwich structure with carbon-fiber/epoxy faces and HP250-HP100-HP60 core subjected to underwater impulsive loading with $\bar{I} = 0.16$. The faces are ~3 mm thick and each layer in the core is 10 mm thick for a total core thickness of 30 mm.

### 9.6.2 Out-of-plane deflection

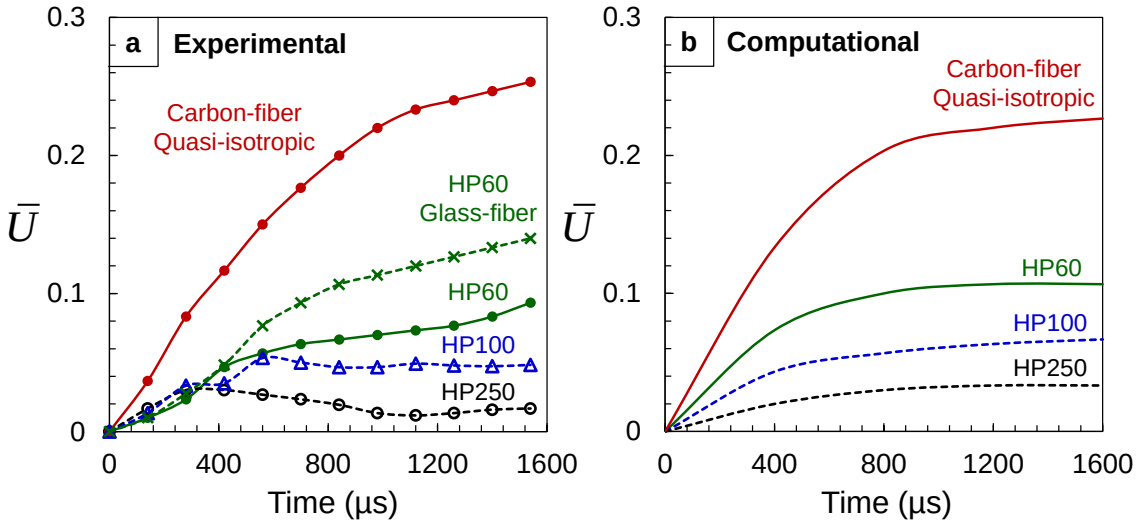


Figure 128 (a) Experimentally measured; and (b) numerically calculated midpoint displacements as functions of time for sandwich structures with equivalent thickness subjected to $\bar{I} = 0.20$ and $0.16$ respectively.

In the simply-supported configuration, the midpoint of the backface experiences the highest deflection and stresses. Bending deformation initiates in the structure immediately after the onset of loading. Significant deformation in the backface follows core crushing and load transfer through the core. The monolithic composite structure is used as a benchmark for comparison with sandwich structures. It is determined that the lower the deflection when compared to that of the monolithic composite plate at a particular time, the better is the blast resistance. Additionally, the higher the rate of deformation in the backface, the lower is the blast mitigation capability of that particular sandwich structure. For the three core densities, the frontface acquires much higher velocities than the backface. Therefore, the load spreading capacities of the core are critical for enhancing blast resistance.

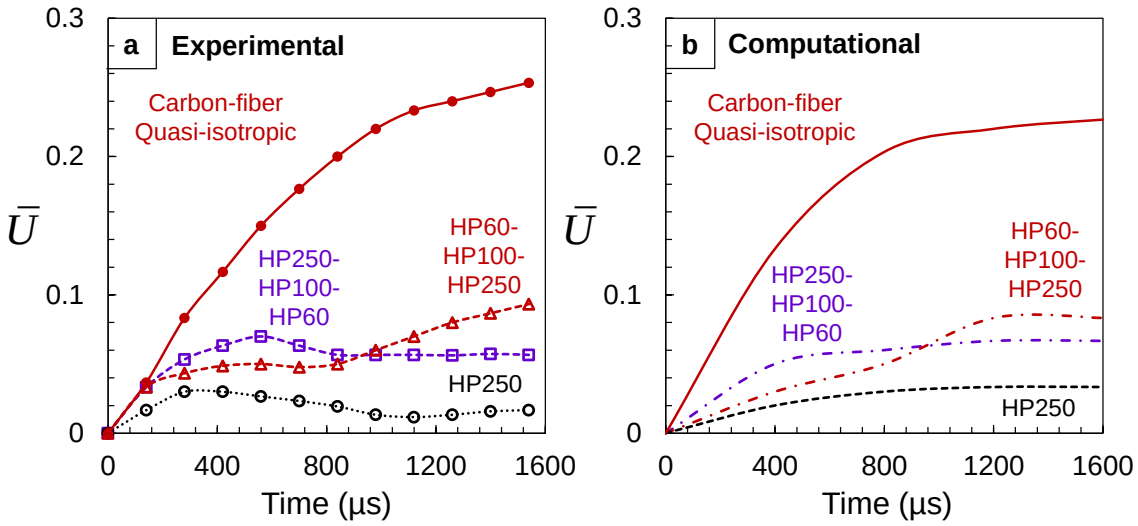


Figure 129 (a) Experimentally measured; and (b) numerically calculated midpoint displacements as functions of time for graded-core sandwich structures with equivalent thickness subjected to $\bar{I} = 0.20$ and 0.16 respectively.

Figure 128 (a) and (b) shows the experimentally measured and computationally calculated histories of center displacements normalized by the length of the composite structure panels for sandwich structures with continuous cores. Out-of-plane deflection in the monolithic plates is also included as a benchmark for comparison. In the initial stages of deformation $(t < 400\,\mu s)$, the rate of deflection increases with increasing core density. However, results indicate that increasing core stiffness dramatically improves post-blast survivability. The deformation in the HP60 sandwich structure increases steadily up to $t = 1600\,\mu s$, experiencing 50% of the deflection in the monolithic plate. However, the deformation in sandwich structures for the HP250 and HP100 cores is arrested at $t = 400\,\mu s$, and continuously decelerates up to $t = 1600\,\mu s$. The HP250 core undergoes ~15% of the peak deflection and 5% of the total deflection experienced by the monolithic plate; while the HP100 core undergoes 25% of the peak and 20% of the total deflection

experienced by the monolithic plate. The numerical simulations capture the out-of-plane deflection in the experiments accurately, but do not capture the significant recovery in the HP250 core.

Figure 129(a) and (b) shows the experimentally measured and computationally calculated histories of center displacements normalized by the length of the composite structure panels for sandwich structures with graded cores. Also included in the plots are structures with the least blast resistance (monolithic composite) and the highest blast resistance (30 mm thick PH250) for comparison. With respect to graded core structures, due to its inability to undergo rapid core compression, the HP250-HP100-HP60 core deflects at a greater rate than the HP60-HP100-HP250. However, deflection in the HP250-HP100-HP60 core plateaus at $t = 600\,\mu s$, while that in the HP60-HP100-HP250 core increases steadily up to $t = 1600\,\mu s$. The simulations account for the differences in core density in the sandwich structure and accurately predict peak and total displacement in both cases.

Figure 130(a) and (b) shows core compressive strain in 30 mm thick continuous and graded cores, calculated by measuring the relative displacements between the frontface and backface. In continuous cores, the HP60 core undergoes the highest core compressive strain, followed by the HP100 and HP250 cores. Both graded cores experience similar core compression in the initial stages of deformation, but the HP60-HP100-HP250 core undergoes greater compression in later stages.

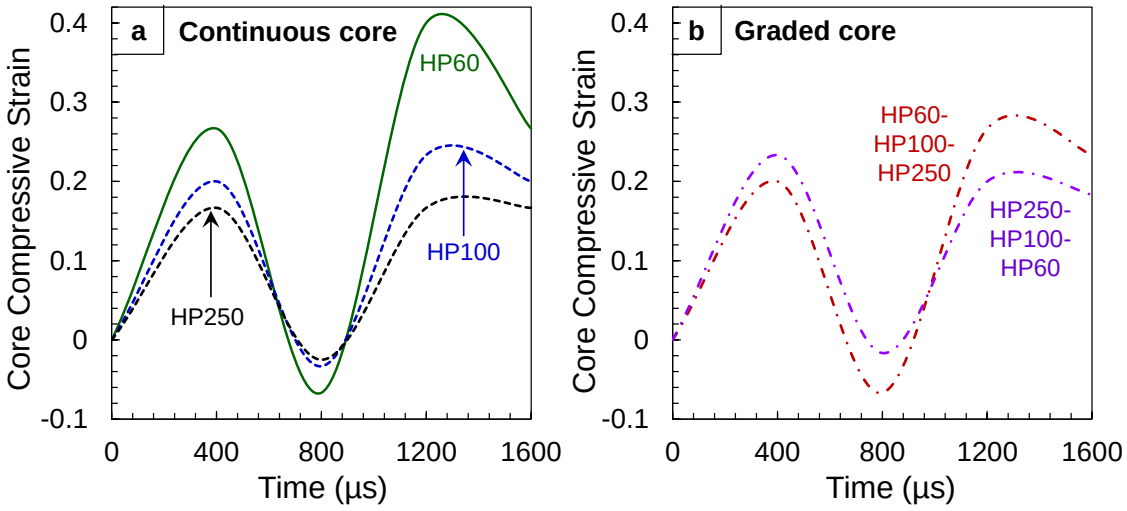


Figure 130 Core compressive strain as a function of time for (a) continuous-core and (b) graded-core sandwich structures with equivalent thickness subjected to $\bar{I} = 0.16$.

### 9.6.3 Impulse transmission

Minimizing the impulse transmitted to the internal components of marine vessels is of critical importance. For the simply-supported loading configuration discussed here, the target structure transmits an impulse to the supports. The rate of impulse transmission and the magnitude of the transmitted impulse can provide valuable insight into the blast resistance and performance of composite structures. Clearly, the composite structure that transmits the least impulse at the lowest rate is most desirable. Figure 131(a) and (b) shows the histories of impulses transmitted by composite structures with similar areal masses subjected to an incident impulsive load $\bar{I} = 0.16$. It is evident that the core density has a considerable influence on the impulse transmitted to the supports. The HP60 core transmits the least impulse because of a balance of high core compressibility and load transfer. Additionally, HP60 The HP100 core transmits ~150%, while the HP200 core transmits ~300% of the impulse transmitted by the HP60 core. With respect

to the graded cores, similar impulses are transmitted in both cases with the total impulse transmitted nearly 200% of the impulse transmitted by the HP60 core.

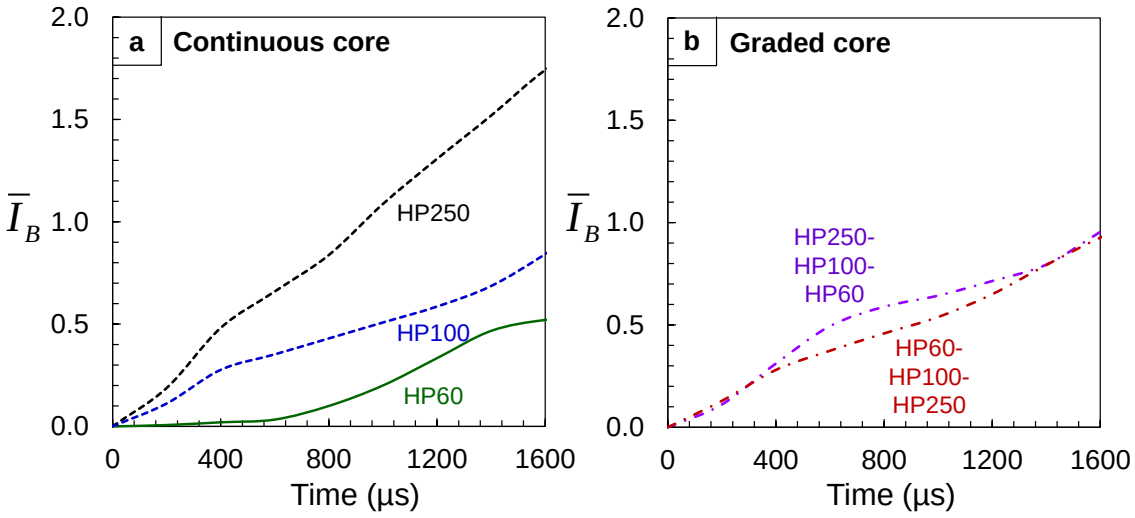


Figure 131 Normalized transmitted impulse as a function of time for (a) continuous-core and (b) graded-core sandwich structures with equivalent thickness subjected to $\overline{I} = 0.16$.

### 9.6.4 Accumulated damage

The computational framework developed in this research allows the tracking of damage and failure in different components of the sandwich structure through the use of three constitutive and damage approaches: (1) Hashin damage in the facesheets; (2) cohesive damage in the interfacial regions including interlaminar regions and core-face interfaces; and (3) damage in the sandwich structure core due to severe shear and compressive stresses through the Deshpande and Fleck criterion [149]. It is essential to quantify the damage in different components to accurately evaluate the deformation response and blast resistance of each structural configuration, and to determine post-blast survivability under a range of loads and material properties.

Figure 132(a-e) shows the histories of damage in the different components of composite structures with varying core densities but similar areal masses subjected to $\bar{I} = 0.16.$ The key difference in damage evolution with respect to core density is the fact as the core density increases, the majority of the damage occurs in the early stages of deformation. The HP60 and HP100 cores experience steadily increasing damage throughout the deformation process, while HP250 core experiences the majority of damage in the initial stages of deformation. Additionally, as the core density increases, the damage in the frontface as a fraction of total damage increases drastically. For the HP60 core, frontface damage is ~20% of the total damage; for the HP100 core, frontface damage is ~40% of the total damage; and for the HP250 core, frontface damage is ~70% of the total damage.

For the graded cores, the HP250-HP100-HP60 structure experiences greater damage, primarily due to increased damage in the core in comparison to the HP60-HP100-HP250 core. There is also a slight increase in both frontface and backface damage for the HP250-HP100-HP60 core. This can be attributed to the fact that the incoming wave interacts with the HP250 section first, leading to greater impulse transfer. The inflection of the $\bar{N}$ vs. time curve at $t = \sim 300\,\mu s$ for all sandwich cores indicates that damage creation seems to be divided into two regimes: (1) impulse transmission regime: which occurs in the initial stages when the incident impulse interacts with the test specimen; and (2) out-of-plane deflection regime: which occurs when the incident impulse travels through the structure to the backface, and the structure acquires momentum and begins deflecting. Since the impulse transmission regime involves deformation in an extremely short duration, damage is created at a very high rate.

Computational results show that when the structure starts deflecting, the damage created during the impulse transmission regime evolves and propagates but new damage mechanisms are not activated. Consequently, although the total damage increases during the deflection regime, the rate of damage creation is significantly lower than in the impulse transmission regime. Damage in the frontface occurs in the impulse transmission regime but does not increase appreciably in the deflection regime.

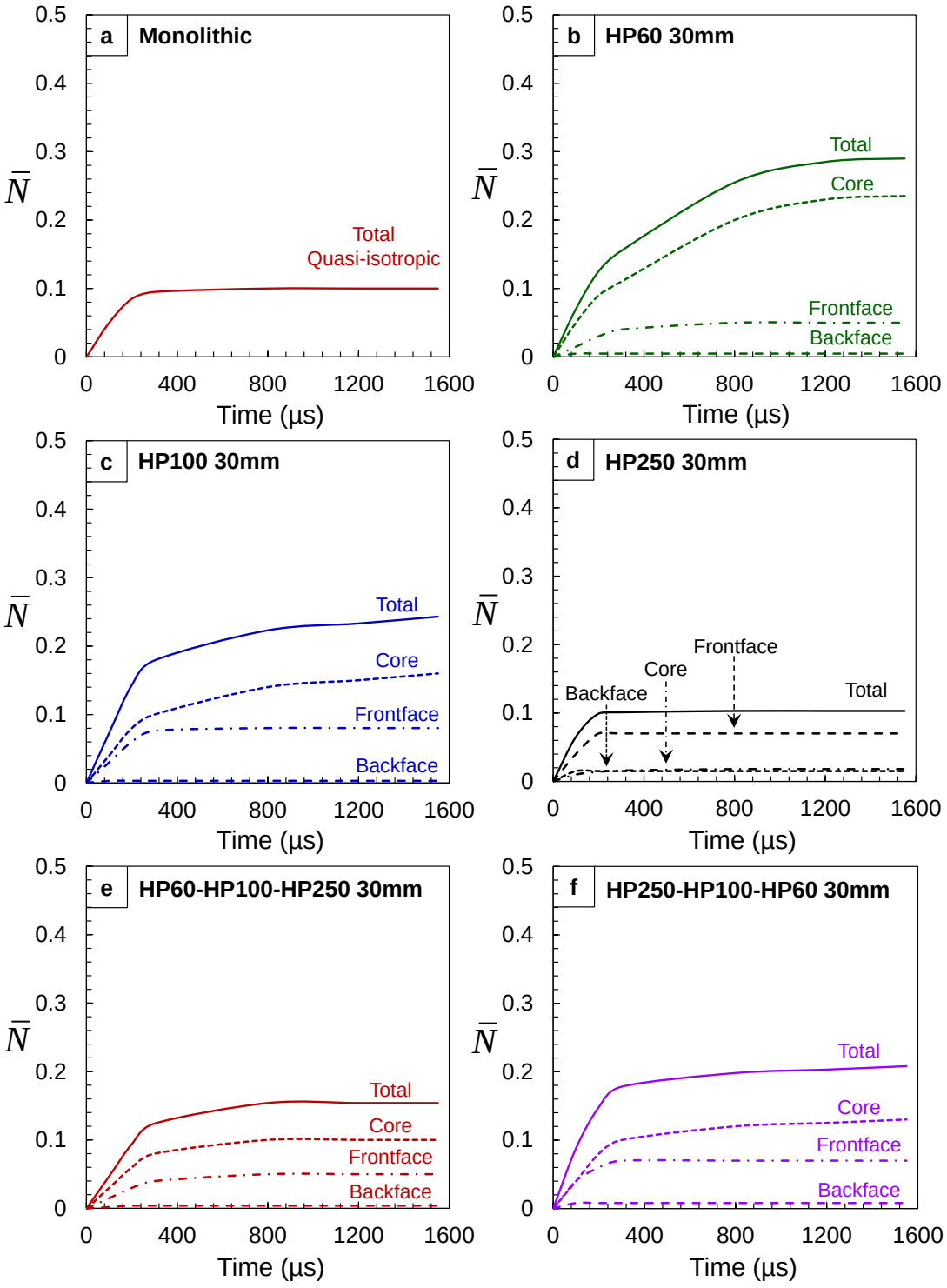


Figure 132 Accumulated damage histories for different sandwich structures with equivalent thickness subjected to $\bar{I} = 0.16$.

### 9.6.5 Loading-Structure-Performance maps

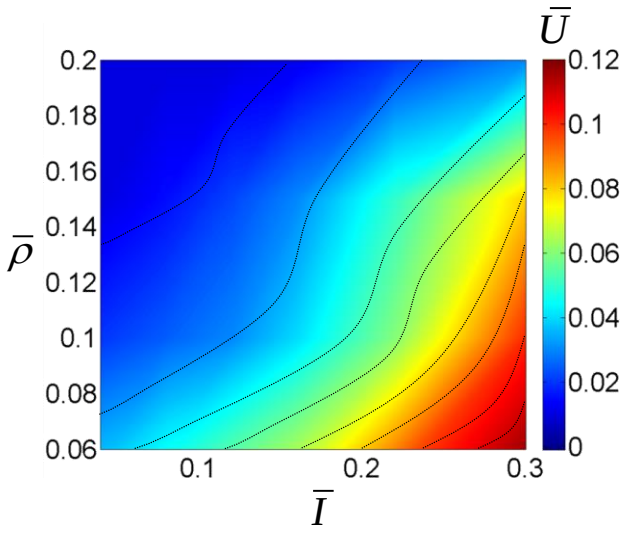


Figure 133 Loading-structure-performance map showing normalized displacment $\bar{U}$ as a function of normalized incident impulse $\bar{I}$ and normalized core density $\bar{\rho}$ for composite structures with equivalent thickness.

Structural design involves selecting materials and designing structures that match the performance profile required by a particular application. A performance profile defines the characteristics required by a structure to excel in its application and defines material indices that capture stated design objectives: minimizing weight, deflection, impulse transmission, cost or maximizing energy absorption, efficiency, bending strength and so on. It is identified by examining the function of the component, the objectives that the designer wishes to fulfill and constraints that the component must meet to perform adequately. Some commonly used indices in more conventional material and structural design research consist of specific stiffness $E/\rho$ , specific strength $\sigma_Y/\rho$ and many others. These material indices guide the optimal selection of material for component level design. It should be noted that previous design approaches are based on uniaxial

compressive loading which is a well-established and quantified loading case. Conversely, in the current scenario consisting of a multitude of loading conditions, structures and materials, the indices must account for a greater number of constraints and variables. Rather simple indices used in previous approaches will be insufficient in this particular case.

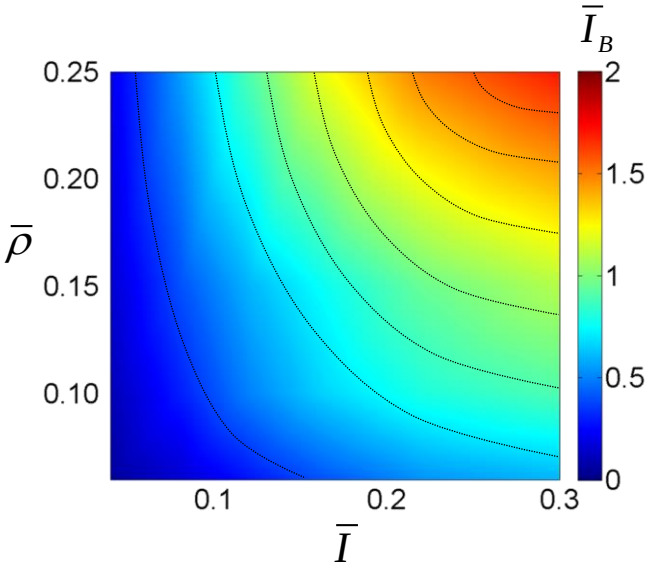


Figure 134 Loading-structure-performance map showing normalized transmitted impulse $\bar{I}_B$ as a function of normalized incident impulse $\bar{I}$ and normalized core density $\bar{\rho}$ for composite structures with equivalent thickness.

Figure 133 shows the loading-structure-performance map of normalized out-of-plane deflection $\bar{U}$ as a function of normalized incident impulse $\bar{I}$ and normalized relative density $\bar{\rho}$ for composite structures with equivalent mass. Results show that low density cores with sufficient thickness have exceptional blast resistance at all load intensities, including failure loads. As the core density increases, the displacement experienced by the structure increases rapidly, especially at failure loads.

Figure 134 shows the loading-structure-performance map of normalized transmitted impulse $\bar{I}_B$ as a function of normalized incident impulse $\bar{I}$ and normalized relative density $\bar{\rho}$. In a manner quite similar to out-of-plane deflection, the transmitted impulses are significantly higher for greater core densities. The slight reduction at very high core densities can be attributed to the fact that dense, thin composite plates deflect instantaneously and lose contact with the supports, while sandwich structures resist deflection for a greater period of time and stay in contact with the supports. This causes the monolithic plates to transmit lower impulses for similar incident loads but does not necessarily indicate higher blast resistance.

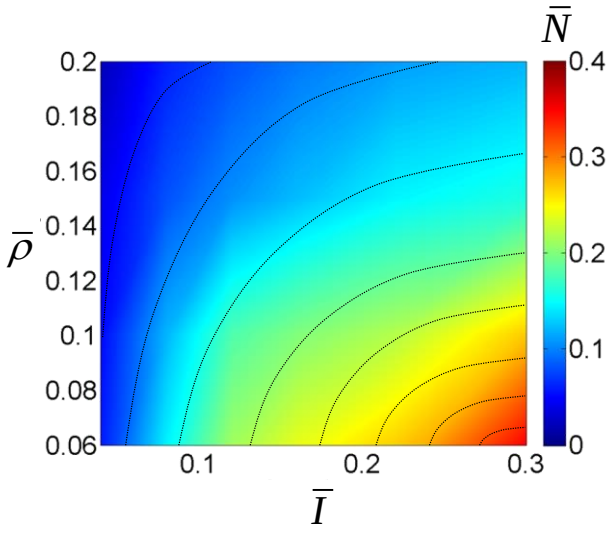


Figure 135 Loading-structure-performance map showing normalized accumulated damage $\bar{N}$ as a function of normalized incident impulse $\bar{I}$ and normalized core density $\bar{\rho}$ for composite structures with equivalent thickness.

Figure 135 shows the loading-structure-performance map of normalized damage parameter $\bar{N}$ as a function of normalized incident impulse $\bar{I}$ and normalized relative density $\bar{\rho}$ for composite structures with equivalent mass. As the incident impulse

increases, the damage created in the composite structure decreases exponentially. This shows that sandwich structures with higher core densities exhibit superior blast resistance and survivability under all loading intensities.

## 9.7 Summary and conclusions

Marine structures must balance strength and load carrying capacity with the ability to minimize impulse transmission for high blast and impact resistance. Composite structures have higher stiffnesses and high strength-to-weight ratios compared with monolithic structures. Additionally, sandwich structures provide very high bending and shear resistances with slight increases in total mass. However, due to the novelty and wide range of structural combinations, the relationships between structural responses and material heterogeneity in sandwich structures are not well quantified. In particular, the behavior of composite structures under extreme impulsive loading generated by underwater explosions needs to be systematically analyzed. In an effort to provide useful information for structural design, the load carrying capacity and impulse transmission capabilities of sandwich composites are evaluated over a range of relative densities and impulsive load intensities. The loading conditions involve impulsive loads with peak pressures up to 200 MPa, which simulate the effects of TNT exploding underwater at different standoff distances from the structure. The constitutive and damage models capture the different inelastic deformation and failure mechanisms in composite laminates and sandwich cores. It should be emphasized that the composite panels studied have similar overall mass which necessitates different core thicknesses. The effect of core height on dynamic response is not studied in this analysis.

This study has yielded experimental data on the failure behavior of composites subjected to underwater impulses. Maximal damage was observed near the load circumference in both monolithic and sandwich structures. The analysis of damage modes shows that relative core density is a critical factor in determining structural performance of sandwich structures. Sandwich structures significantly outperform monolithic composites at all impulsive levels and environmental conditions. Low density cores provide higher blast resistance than high density cores. An analysis of the effect of load intensity shows that as the load intensity increases, the deflection of the frontface outpaces the dynamic core crushing capability of the cores, resulting in collapse. In such cases, low density cores provide better load spreading and exhibit better capabilities for compression. However, a major concern for low density cores is the occurrence of core indentation, in which the core fails in a localized region and causes compressive stresses in the frontface leading to buckling and rupture. Therefore, a balance of core stiffness and softness is essential for optimal blast resistance.

Comparison of experiments and simulations shows that numerical calculations provide a reasonable representation of damage and dissipation mechanisms in the facesheets and core. The compressible foam constitutive model leads to high core compression and a slight overestimate of backface deflection. The finite element model captures the essential deformation mechanisms observed in both the facesheets and the core. Specifically, the following deformation modes are replicated with reasonable accuracy: core indentation, core shear, core-face debonding, facesheet buckling and delamination, structural collapse and rupture. The results from numerical calculations provide a more in-depth understanding of temporal and spatial evolution of different

deformation modes in the structure. The deformation in sandwich structures is strongly influenced by core density and loading rate and magnitude. Structures with high relative densities undergo severe damage and exhibit significantly higher core face debonding than structures with low relative densities. For a given impulsive load, structures with low relative densities (HP60 and HP100) experience considerably lower displacements than those with high relative densities (HP200 and monolithic).

In both air-backed and water-backed cases, the maximum impulse transmitted by each structure is used to determine the performance of the composite structure. Sandwich structures exhibit superior blast mitigation capabilities in comparison to monolithic structures at all impulse magnitudes. In particular, thick, low density foam cores made of Divinycell HP60 and HP100 foams provide the highest load spreading and impulse retardation. The temporal histories of impulse transmission show a significant dependence on core density with a clear increase in transmitted impulse after complete core failure. The transmitted impulses show a monotonic dependence on loading intensity and a power law dependence on the relative density. The effects of high relative density are further exacerbated at higher loading intensities.

The insight gained here provides guidelines for the design of structures for which response to water based impulsive loading is an important consideration. Finally, it should be noted that the relations described in this paper are applicable only for the structural attributes and loading conditions considered herein.

# 10. EFFECT OF FACE STIFFNESS ON DYNAMIC RESPONSE

## 10.1 Introduction

The objective of this study is to examine the effect of the ratio between facesheet thickness and core thickness on the dynamic response of composite sandwich structures. To this end, the core thickness and core density are kept constant and the thickness of the facesheets is varied. Under this condition, the total mass of the structure changes with the thickness of the facesheets. Another approach is to keep the total weight constant and vary the thicknesses of the core and the facesheets accordingly. The second approach can lead to unrealistic sandwich designs and, therefore, is not followed here. We quantify the response of the structures using fiber and matrix damage, facesheet deflections and energy absorbed. The results are analyzed in both normalized and non-normalized forms to gain insight into underlying trends that can be explored in the design of materials and structures.

## 10.2 Structures Analyzed

The load configuration analyzed consists of a sandwich plate subject to impulsive loading at its center. The plate can be regarded as a portion of a ship's hull. The exponentially decaying pressure pulse has an impulse consistent with what is first proposed by Taylor [9]. Figure 136 shows a schematic illustration of a square sandwich plate 300 × 300 mm in size with a loading area of 76 mm in diameter at the center. The load area is 5% of the total area of the plate.

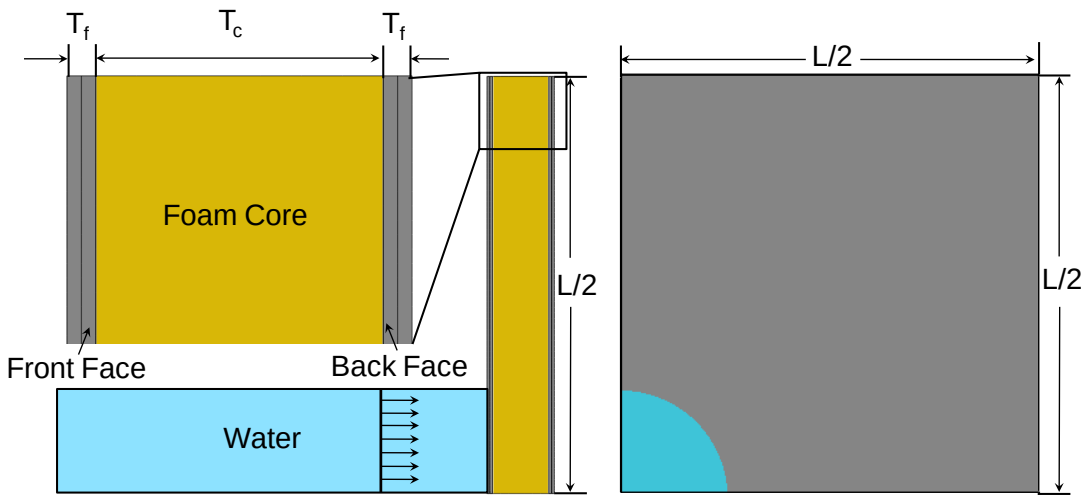


Figure 136 Configuration of planar sandwich structures subject to water-based impulsive

The outer boundaries of the plate are clamped. The symmetries of the plate and loading allow a quarter of the total plate to be considered in the simulations. All panels have a core thickness of $M_c$ mm and a core density of 100 kg·m$^{-3}$, giving a core unit areal mass of $M_c$ = 2 kg/m$^2$. The side length of the plate is $L$ = 300 mm. The facesheets, consisting of plies 0.25 mm in thickness each, are modeled with continuum shell elements. The total facesheet thickness $T_f$ varies from 1 to 20 mm, giving rise to different areal mass values of the sandwich plates. The ratio between the facesheet thickness and the core thickness is $R = T_f / T_c$. All plates have the same material properties. Figure 137 illustrate the sandwich plates analyzed, the $T_f / T_c$ value ranges from 0.05 to 0.4. The insets show magnified views of the plates. In the numerical simulations, the plates are considered to be free of defects due to manufacturing variability and without any pre-stress.

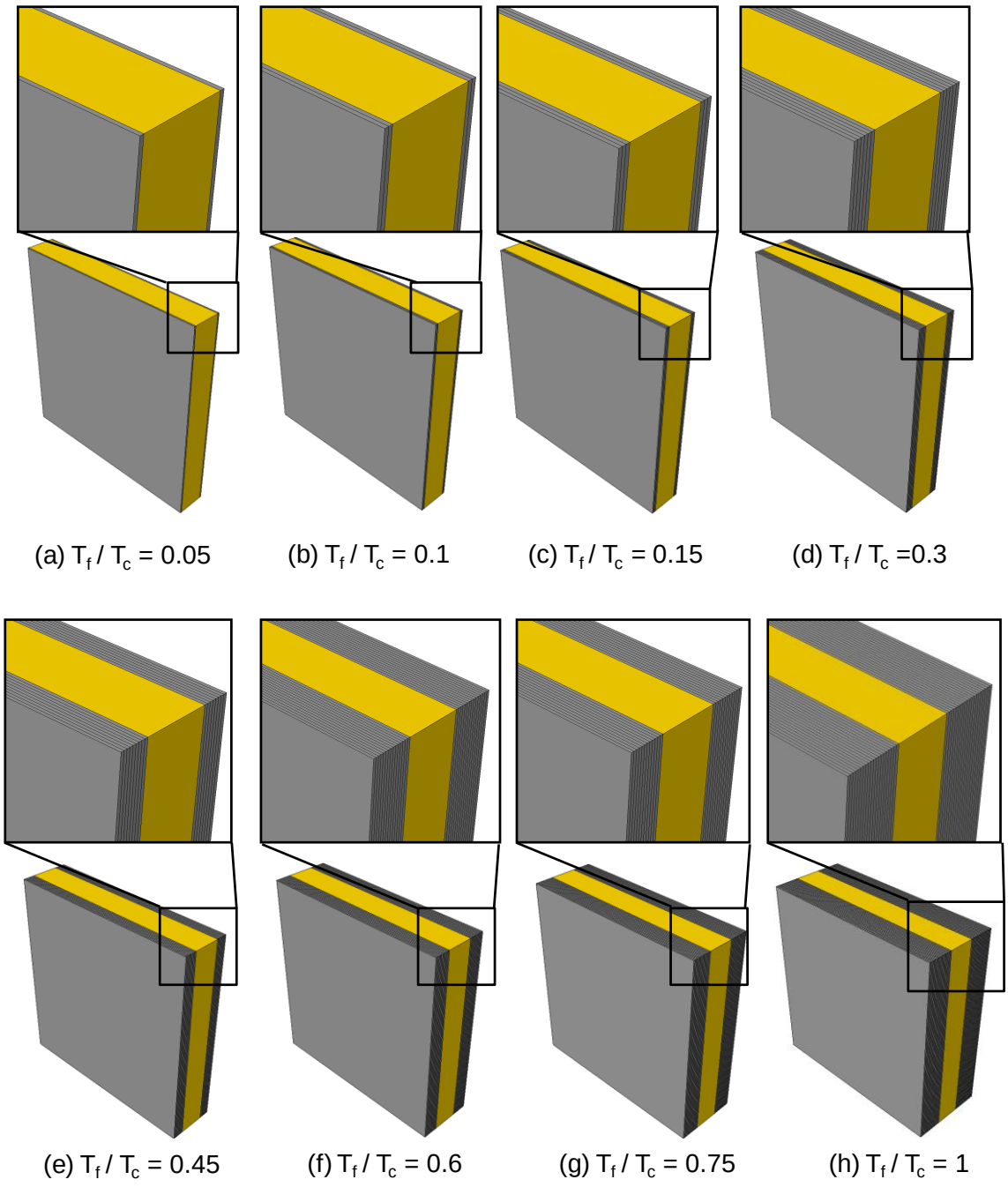


Figure 137 Configurations of composite sandwich structures with different facesheet thicknesses

## 10.3 Dynamic deformation and damage

The deformation of the core shows three distinct stages of response: (1) onset of core crushing, (2) onset of motion of back-face and (3) momentum transfer through the structure. Changes made to the facesheets affect all three stages. In general, all things being equal, structures with thicker facesheets are stronger in an absolute sense, since more material is used. To reveal trends on a per weight basis, we analyze the results in both normalized and non-normalized forms.

Five different impulse levels are considered. The impulses per unit area are $\bar{I} = 0.4, 0.3, 0.2, 0.1 \text{ and } 0.05$ where $\bar{I} = I \Big/ \left( \rho_w c_w \sqrt{A} \right)$. We first consider the results for $\bar{I} = 0.2$ and then compare the results for different impulse levels. Facesheets with thicknesses less than 6 mm $\left( \mathrm{T_f} / \mathrm{T_c} < 0.3 \right)$ are classified as "thin facesheets" and facesheets with thicknesses greater than 6 mm $\left( \mathrm{T_f} / \mathrm{T_c} > 0.3 \right)$ are classified as "thick facesheets".

Figure 138 shows the distribution of tensile damage in the matrix for the last plies of the facesheets 600 μs after onset of deformation in a sandwich plate with a facesheet thickness of 1 mm $\left( \mathrm{T_f} / \mathrm{T_c} = 0.05 \right)$. The load intensity is $\bar{I} = 0.2$. Damage in the front sheet (front-face) is more severe and is dependent on fiber orientation. Maximum damage occurs close to the loading area and spreads outward in later stages of the loading event. Figure 139 shows the corresponding distributions of equivalent plastic strain at three different times for this structure sandwich. The arrival of the load pulse at the target is taken as $t = 0$. Core compression occurs immediately after the onset of loading. Back-

face starts to deform at $t = 100\ \mu s$ and has acquired significant momentum by $t = 500\ \mu s$. Since the facesheets are thin, core crushing is highly localized and the rate of deformation is highly non-uniform in the core. Significant core-facesheet debonding is observed at late stages of the deformation.

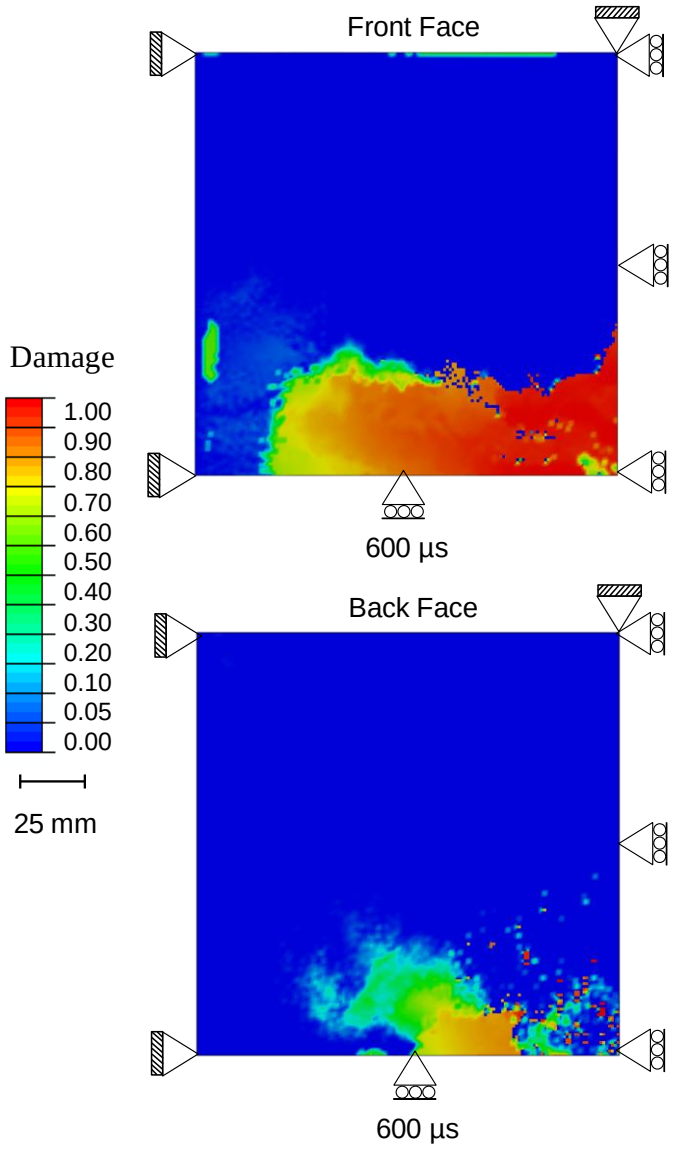


Figure 138 Distributions of tensile damage in the matrix of the facesheets at $t = 600\ \mu s$, $T_f / T_c = 0.05$ and $\bar{I} = 0.2$. The plies shown are oriented horizontally.

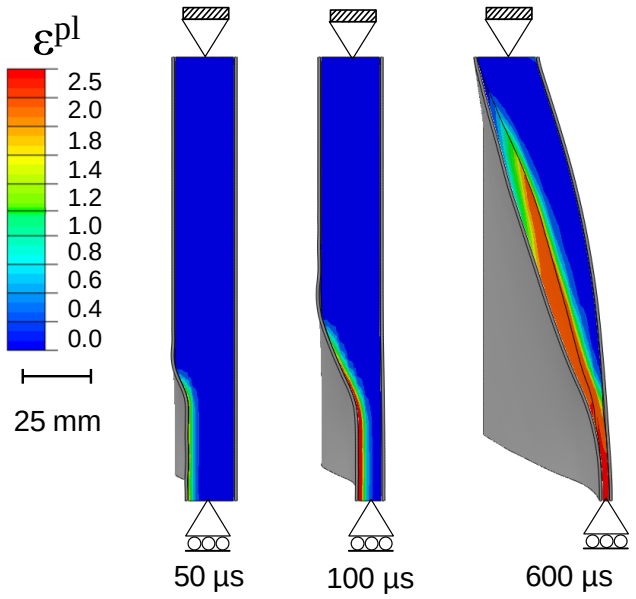


Figure 139 Distributions of equivalent plastic strain in the core at different times for $T_f/T_c = 0.05$ and $\bar{I} = 0.2$.

Figure 141 shows the tensile damage in the matrix for the last plies of the facesheets in a sandwich structure with a facesheet thickness of 8 mm ($T_f/T_c = 0.4$). While the damages in front-face for both $T_f/T_c = 0.05$ (Figure 138) and $T_f/T_c = 0.4$ (Figure 141) are similar, the damages in back-face are quite different, with the damage for $T_f/T_c = 0.4$ being much lower than that for $T_f/T_c = 0.05$. Beyond $T_f/T_c = 0.4$, there is essentially no further improvement in damage resistance. This observation is supported by the analysis of deflections discussed in next section. Figure 140 shows the corresponding distributions of equivalent plastic strain for the sandwich plate in Figure 141. Core deformation is more spread out relative to what is seen in Figure 139 (thinner facesheets) and the motion of back-face starts at a later time of $t = 140\,\mu s$ compared with what is seen in Figure 139. The back-face has acquired significant momentum by

$t = 500\,\mu s$. Figure 139 and Figure 140 show that, as $T_f/T_c$ increases, core compression becomes less localized and the deformation in the core becomes more uniformly distributed. Thicker facesheets also delay the onset of deformation of back-face and the momentum transfer into back-face. After the core is fully compressed, the deformation of the structure occurs primarily through bending. Front-face is in compression and back-face is in tension. The damage in the facesheets (through phenomenological matrix cracking and fiber breakage) provides one mechanism for energy dissipation. Like damage in the facesheets, core-facesheet debonding is more severe for thin facesheets.

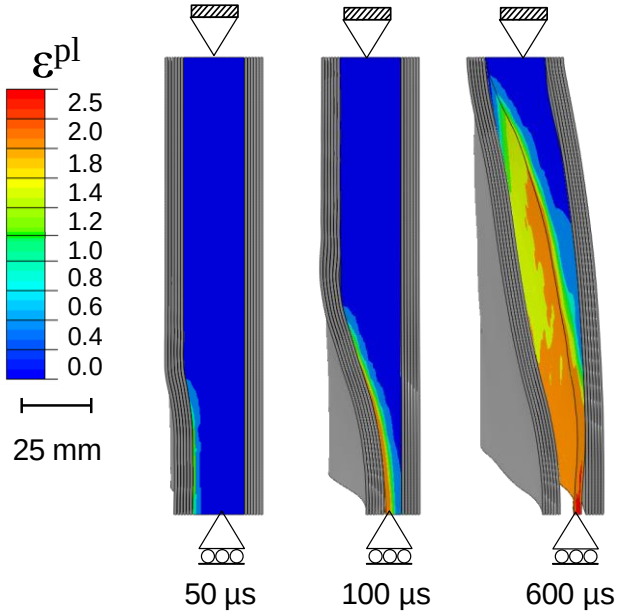


Figure 140 The distributions of equivalent plastic strain in the core at different times. $T_f/T_c = 0.4$ and $\bar{I} = 0.2$.

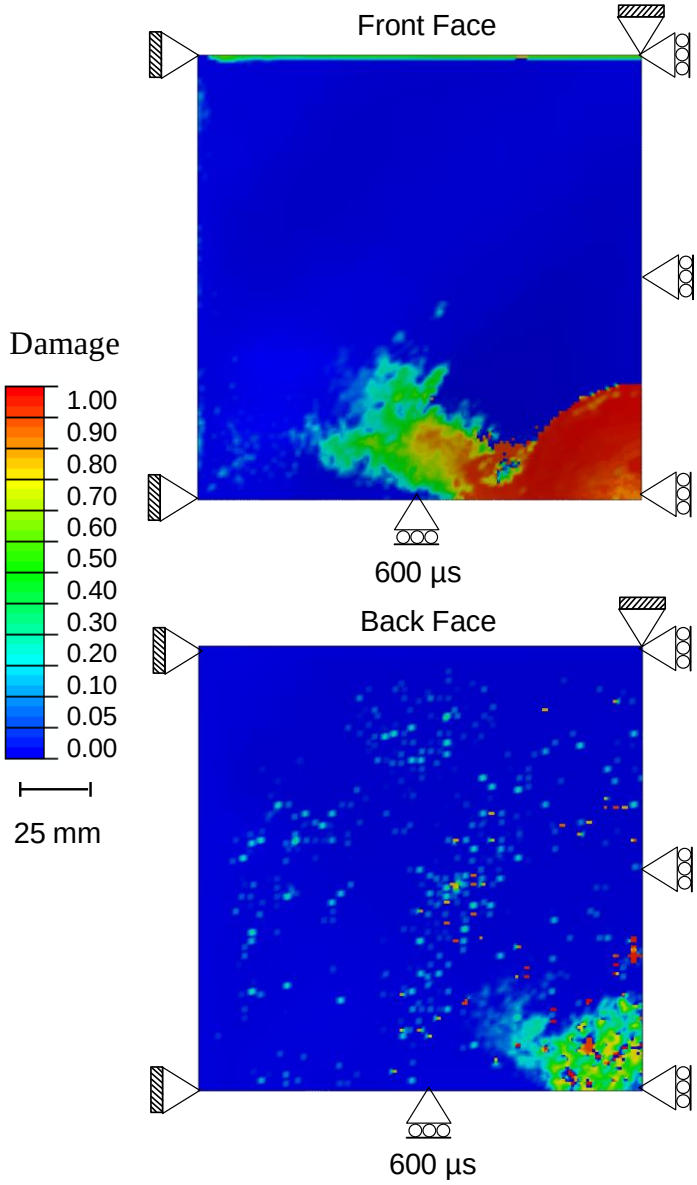


Figure 141 Distributions of tensile damage in the matrix of the facesheets at $t = 600\ \mu s$. $T_f / T_c = 0.4$ and $\bar{I} = 0.2$. The plies shown are oriented horizontally.

## 10.4 Deflection

The displacements at the center of the structures are used to quantify deflection and core compression. In particular, the displacements at the center of the front and back-facesheets ($\Delta$) at 600 μs after the onset of loading are analyzed. The deflections are normalized with the side length (L) of the sandwich plates. Figure 142 (a) shows that $\Delta/L$ increases with $I$ and decreases with the ratio between the thickness of the facesheets and the thickness of the core ($T_f/T_c$) (and therefore decreases with the areal mass of sandwich plates ($M$)). The deflection of back-face is generally lower than that of front-face, due to core compression. As $T_f/T_c$ increases, the decreases in deflections are monotonic. At low impulse magnitudes ($\bar{I} < 0.1$), increasing facesheet thickness does not provide significant reductions in the deflections. As the impulse magnitude increases, the difference between the responses of structures with low $T_f/T_c$ and the responses of those with high $T_f/T_c$ becomes pronounced. For impulse magnitudes above 163 N·s, structures with high $T_f/T_c$ values show markedly lower deflections. For example at $\bar{I} = 0.2, 0.3 \text{ and } 0.4$, as $T_f/T_c$ increases from 0.01 to 0.36, $\Delta/L$ decreases by approximately 56 %. If $T_f/T_c$ increases from 0.6 to 1, $\Delta/L$ decreases by only ~5 %. At all impulse magnitudes, no appreciable reduction in the deflection of front-face is seen for $T_f/T_c > 0.6$. The deflections of back-face shown in Figure 142 (b) are generally lower that the deflections of front-face but exhibit the same trend seen in Figure 13 (a). Overall, increasing the relative thickness of the facesheets up to a certain value (

$T_f/T_c = 0.6$) can significantly decrease the deformation of the structures. Increases beyond this value yields no obvious benefit in terms of structural rigidity. Since the overall weight of the structures is one of the most important aspects in naval structural design, this finding points to a design criterion useful for relevant systems.

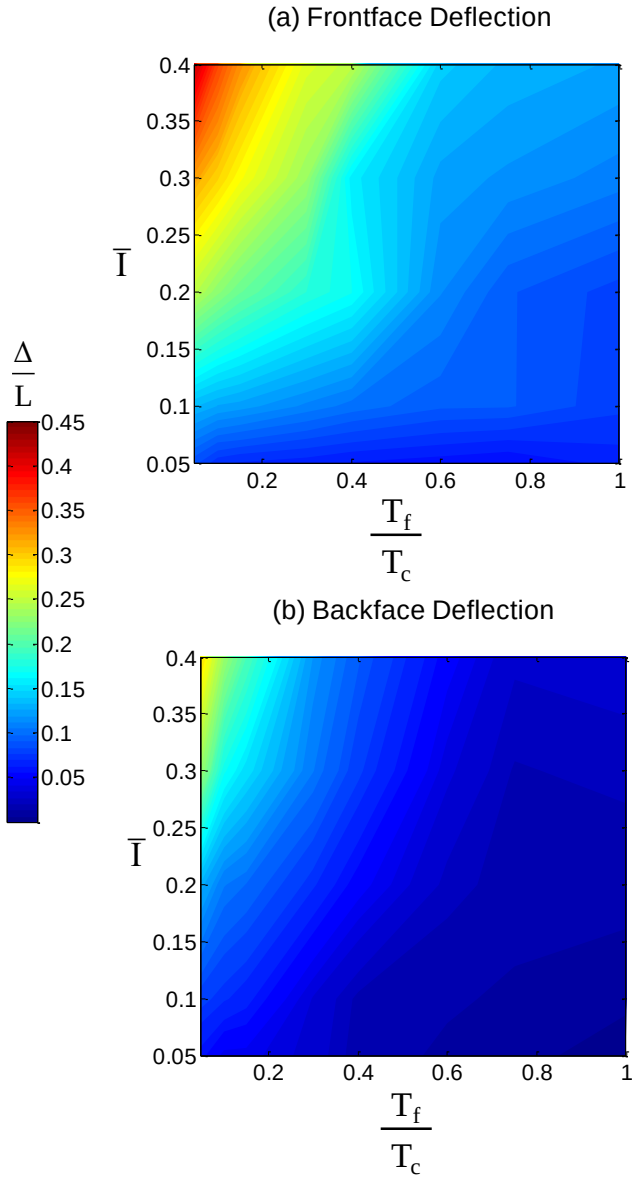


Figure 142 Normalized displacement as a function of $T_f/T_c$ for (a) front-face and (b) back-face.

## 10.5 Energy Absorption

Energy dissipation in glass-fiber reinforced composites is in the form of matrix cracking, fiber breakage and delamination. In the current analysis, only matrix and fiber damages are considered. Energy absorption in the core is in the form of permanent core compression which accounts for the largest portion of overall energy dissipated. For the load conditions analyzed, the primary mode of core deformation is compression with very small amounts of stretching at the supports. Therefore, taking full advantage of core compression is important. Figure 143 shows the total energy dissipated in the structure ( $U$ ) as a function of $T_f/T_c$ . For thin facesheets ($\mathrm{T_f/T_c} < 0.15$), the core compression is highly localized to the load area, leaving large portions of the core relatively intact or underused. For $0.15 < \mathrm{T_f/T_c} < 0.45$, the facesheets are rigid enough to distribute core compression over a larger area, whereby achieving maximum energy dissipation. For $\mathrm{T_f/T_c} > 0.6$, no further improvement in energy dissipation can be gained at all impulse magnitudes, since the core is already fully utilized. An interesting aspect of this plot is that $U$ reaches a maximum at a certain value of $T_f/T_c$, indicating that there is an optimum thickness ratio (approximately $\mathrm{T_f/T_c} = 0.2 - 0.3$) for maximizing energy dissipation. This maximum becomes more obvious at higher load intensities. Figure 144 shows the energy dissipated per unit areal mass ($U/M$ ) as a function of $\mathrm{T_f/T_c}$ for different load intensities. As the $\mathrm{T_f/T_c}$ increases, $U/M$ decreases significantly and eventually levels off at around $\mathrm{T_f/T_c} = 0.6$ . Clearly, the facesheets increase the weight of the structure and provides only limited capability for energy dissipation. This is not

surprising as the primary function of the facesheets is to increase stiffness and strength of the structure.

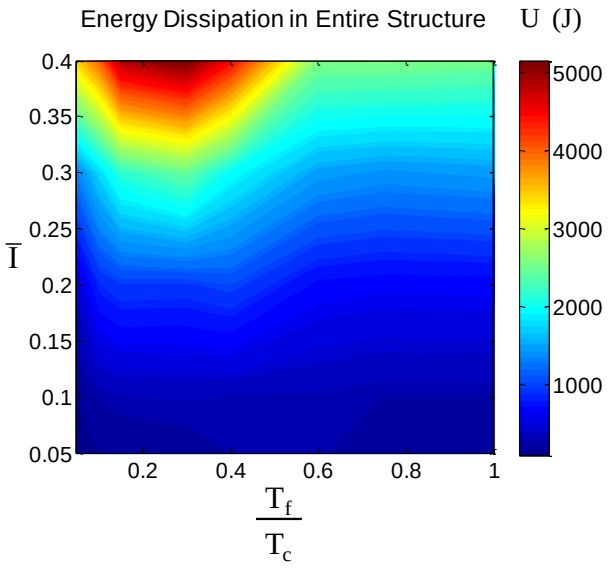


Figure 143 Energy dissipated in the entire structure as a function of $T_f/T_c$.

## 10.6 Performance of Sandwich Core

By keeping the dimensions and material properties of the core the same for all cases, we can assess the performance of the core at different facesheet thicknesses. Figure 145 shows the energy dissipated per unit areal mass in the core as a function of $T_f/T_c$ at different impulse magnitudes. The results are in general agreement with those in Figure 143; the core is responsible for a significant amount of the energy dissipated in the structures.

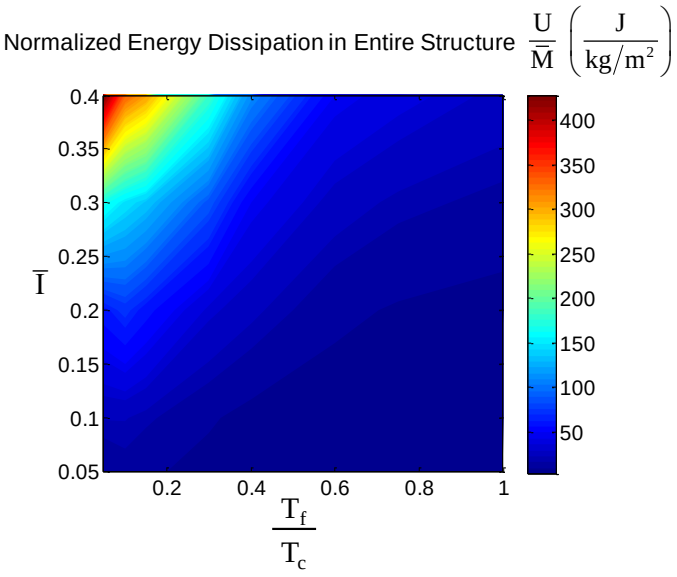


Figure 144 Energy dissipated per unit areal mass as a function of $T_f/T_c$ .

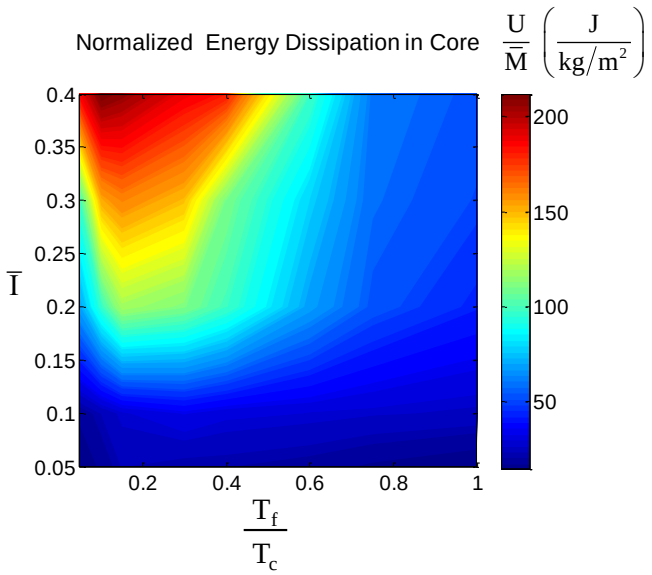


Figure 145 Energy dissipated per unit areal mass as a function of $T_f/T_c$ for the Divinycell H100 foam core. Note that areal mass of core is the same in all calculations.

## 10.7 Desirable Structural Configurations

The desired attributes for a sandwich structure is high energy dissipation capacity and high stiffness (small deflections). For energy dissipation, we consider the energy

dissipated per areal mass. For stiffness, we consider maximum deflection of the structure. Figure 142 and Figure 144 show that there is practically no performance benefit for structures with $T_f/T_c > 0.6$. Figure 144 and Figure 145 show that the highest energy dissipation capacity occurs for $0.15 < T_f/T_c < 0.4$. Figure 142 shows increases in facesheet thickness are most effective for $0.05 < T_f/T_c < 0.3$. Accounting for both factors, the most desirable range for facesheet thickness is $T_f/T_c$ between 0.15 and 0.4 for a given core configuration.

## 10.8 Concluding remarks

The responses to underwater impulsive loads of composite sandwich plates consisting of glass-fiber reinforced epoxy facesheets and PVC foam core with different facesheet-thickness-to-core-thickness ratios are analyzed. The configuration studied is that used in experiments being carried out in the Underwater Shocking Loading Simulator recently developed at Georgia Tech. For comparison purposes, all material properties and core dimensions are kept constant. A fully dynamic finite element model is developed for the experimental configuration, accounting for impulsive loading generation and the dynamic response processes of the structure and water. Deformation and failure mechanisms considered are core crushing, facesheet damage, and core-facesheet separation and contact. Calculations show the distinct response regimes of the structures, as measured by energy dissipated and the maximum deflection. It is found that under the loading conditions and material systems analyzed, there is a range of facesheet thickness in which planar sandwich structures offer the best performance. Specifically,

structures with facesheet-thickness-to-core-thickness ratios between $0.15-0.4$ provide the most efficient use of material in terms of both energy dissipation capacity and rigidity. The insight gained here provides guidelines for the design of structures for which response to water-based impulsive loading is an important consideration. It is important to note that the analysis reported here concerns only one structural configuration, one combination of core and facesheet materials, and one core size. More extensive analyses and experimental verification are needed to determine the applicability of the findings to sandwich structures of different geometries, sizes and materials.

# 11. HYBRID ALUMINUM/CARBON-FIBER STRUCTURES

## 11.1 Introduction

The objective of this combined experimental and computational analysis is to characterize the behavior of monolithic and hybrid plates subjected to underwater impulsive loads and delineate the role of FSI, material properties, interfacial effects and stacking sequence in determining the structural response. The focus is on quantifying the damage and deformation in axis-symmetrically clamped plates subjected to impulsive load of a range of intensities and identifying structural configurations that enhance blast resistance. Previous studies involving hybrid structures have focused on FMLs manufactured using alternating layers of composites and metals. Since the role of individual layers in structural response is unclear, the hybrid plates in this analysis have bilayer configurations consisting of only two layers of respective materials. The configurations allow the delineation of the effects of stacking sequence of the constituent layers on response.

In the experiments reported here, pressures ranging from 10 MPa to 300 MPa can be generated using different projectile velocities. Figure 146 shows the comparison of experimentally measured and numerically calculated pressure histories corresponding to four different projectile velocities. The resulting impulses in each pressure pulse are plotted on the secondary axis of these plots. The rise time of the pressure pulses is on the order of 25 μs and the decay time is on the order of 1500 μs. The impulsive loads have peak pressures of 56, 110, 160, 198 MPa which approximately correspond to 100 kg of

TNT detonating at distances of 4.5, 2.4, 1.7 and 1.4 meters, respectively. The incident impulse magnitudes are $I = \int_0^t p(t)dt =$ 5.48, 9.33, 11.70 and 14.05 kPa·s and the normalized impulse magnitudes calculated using eqn. (67) are $\bar{I} \approx$ 0.15, 0.12, 0.09, 0.06 respectively.

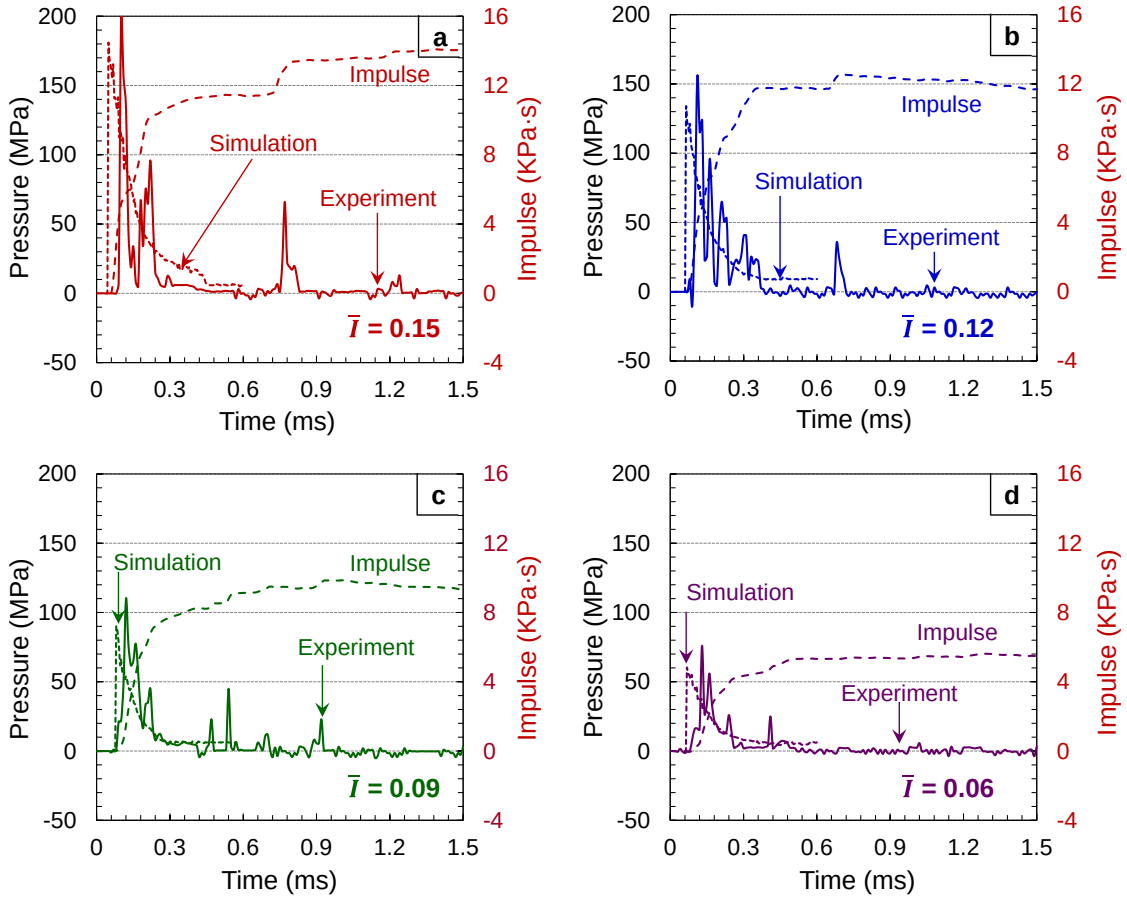


Figure 146 Experimentally measured and numerically calculated pressure histories in the water chamber for four different levels of impulse magnitude $(\bar{I})$.

## 11.2 Specimen construction

Four different structural configurations are studied. Firstly, monolithic aluminum plates are manufactured from 1100 aluminum alloy and have a thickness of 0.812 mm and an areal mass of 2.19 kg/m$^2$. Secondly, monolithic composite plates are manufactured from quasi-isotropic carbon-fiber/epoxy laminates and have a thickness of 1.58 mm and an areal mass of 2.31 kg/m$^2$. The aluminum plates are denoted as "AL" and carbon-fiber/epoxy plates are denoted as "CF" respectively. Finally, hybrid plates are constructed by stacking a 0.406 mm thick aluminum plate and a 0.82 mm thick composite plate in the form of bi-layers bonded with West System 105 epoxy resin. Based on the stacking sequence, the hybrid plates are classified into two types: (1) stacking sequence with aluminum on the impulse side and carbon-fiber/epoxy on the distal side (denoted as "AL/CF") and (2) stacking sequence with carbon-fiber/epoxy on the impulse side and aluminum on the distal side (denoted as "CF/AL"), both with an areal mass of 2.42 kg/m$^2$ including the mass of the adhesive. The different materials and section thicknesses of the specimens studied are summarized in Table 11. The similar areal masses of the different structural configurations enables comparison of their dynamic deformation and blast resistance on an equal mass basis. Figure 147 shows the loading configuration of the clamped configuration to analyze the underwater blast response of plates.

Table 11 Specimens studied. The thicknesses of the different sections are varied to maintain similar areal masses in the hybrid metal-composite structures.

| **Plate** | **Plate designation** | **Aluminum section thickness (mm)** | **Composite section thickness (mm)** | **Areal mass ($kg/m^2$)** |
|---|---|---|---|---|
| Monolithic aluminum | AL | 0.812 | 0 | 2.19 |
| Monolithic Composite | CF | 0 | 1.58 | 2.31 |
| Hybrid plate | AL/CF | 0.406 | 0.82 | 2.42 |
| Hybrid plate | CF/AL | 0.406 | 0.82 | 2.42 |

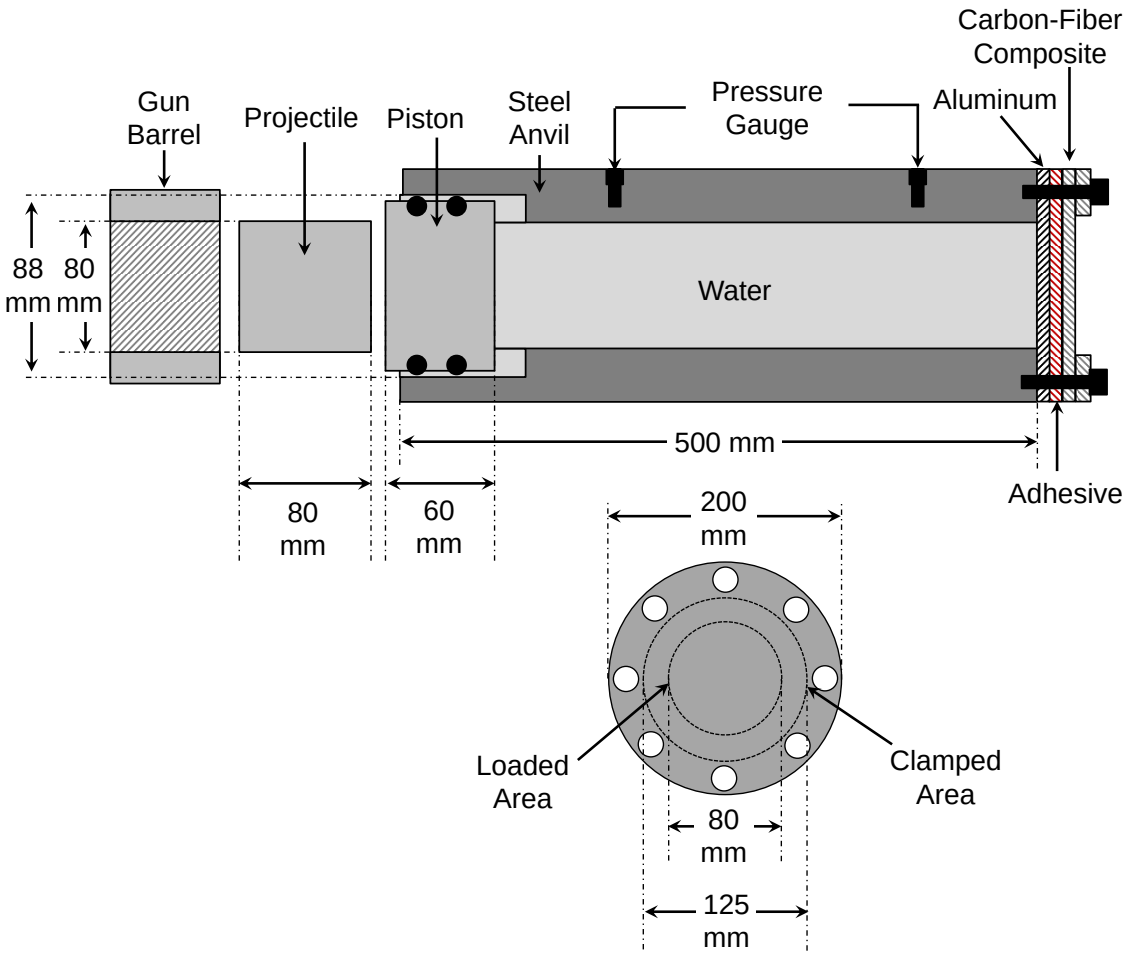


Figure 147 A schematic illustration of the loading mechanism in the Underwater Shock Loading Simulator (USLS) showing the loading configuration used to evaluate the blast resistance of axisymmetrically clamped plates.

The composite laminates are manufactured by curing carbon-fiber epoxy prepregs under vacuum as described in Chapter 3. In hybrid structures, the laminas are stacked in the (0/-45/45/90) sequence until the required mass is achieved. In the finite element simulations, each unidirectional lamina is simulated explicitly to accurately represent the behavior of the entire carbon-fiber/epoxy laminate and capture damage and deformation.

The epoxy layers between two laminas, also called “resin rich layers”, are modeled using cohesive elements to capture interfacial fracture and delamination.

## 11.3 Results and discussion

The effect of material properties, stacking sequences, load intensity and loading condition on blast resistance are analyzed experimentally and computationally. The temporal evolution of selected performance metrics as functions of load intensity and material properties are obtained. In particular, the performance metrics studied in detail are out-of-plane deflection, impulse transmission and energy dissipation. Failure modes are evaluated qualitatively to facilitate comparison of dynamic behavior of the different structures. The results for the monolithic structures are first discussed, followed by the results for the hybrid metal/composite structures. The experimental results are used to calibrate the computational model and evaluate response over a wide range of loading and structural attributes.

### 11.3.1 Experimental results and numerical validation

Figure 148 shows a comparison of high-speed digital photographs and corresponding computational results of the deformation of a monolithic aluminum plate subjected to loading at $\bar{I} = 0.12$. The calculated images show the damage distributions in the material. After the onset of loading, the aluminum plate experiences out-of-plane deflection with the maximum deformation occurring in the central region. At $t = 600\,\mu s$, three cracks initiate and extend outward towards the supports, leading to “petalling”

failure at $t = 1000\,\mu s$. The experiment and simulation are in agreement in terms of failure mode and overall progression of the deformation.

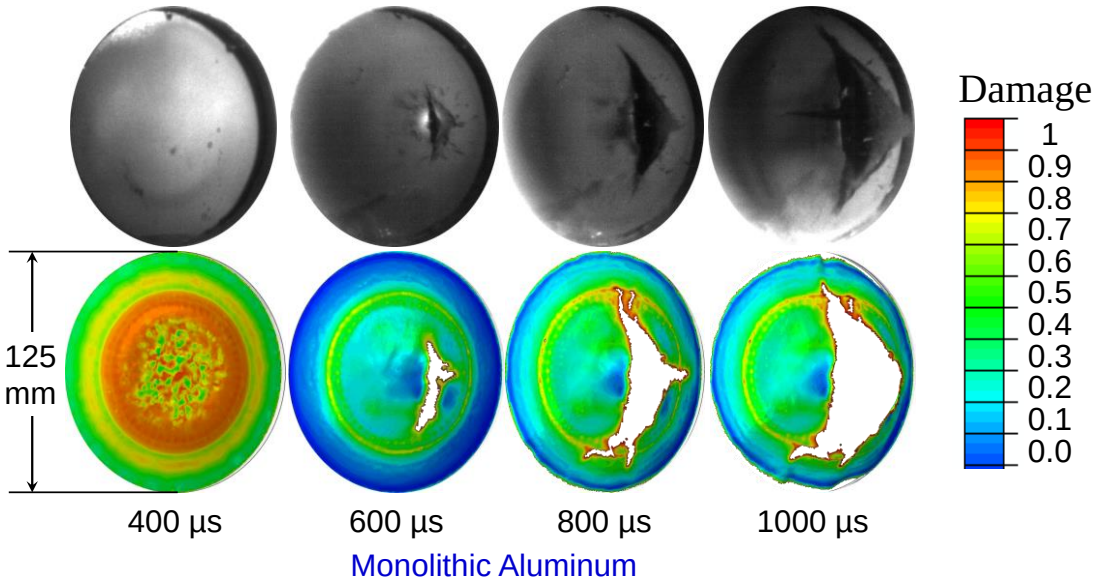


Figure 148 A comparison of experimentally observed and numerically calculated deformation fields with damage distribution at different times for a monolithic aluminum plate subjected to $\bar{I} = 0.12$.

Figure 149 shows experimental images of and corresponding calculated contour plots of Hashin damage parameter in a carbon-fiber/epoxy laminate plate subjected to loading at $\bar{I} = 0.12$. Maximum deformation is observed near the supports in both the experiment and the simulation. Since carbon-fiber/epoxy composite plates have high stiffness, the impulse causes the axisymmetrically clamped plate to undergo shear-dominated deformation and failure near the clamped region. This behavior is in sharp contrast to the bulging and tensile cracking observed in the aluminum plates. The differing deformation and failure behaviors of the metal and composite plates offer an opportunity for their unique strengths to be combined.

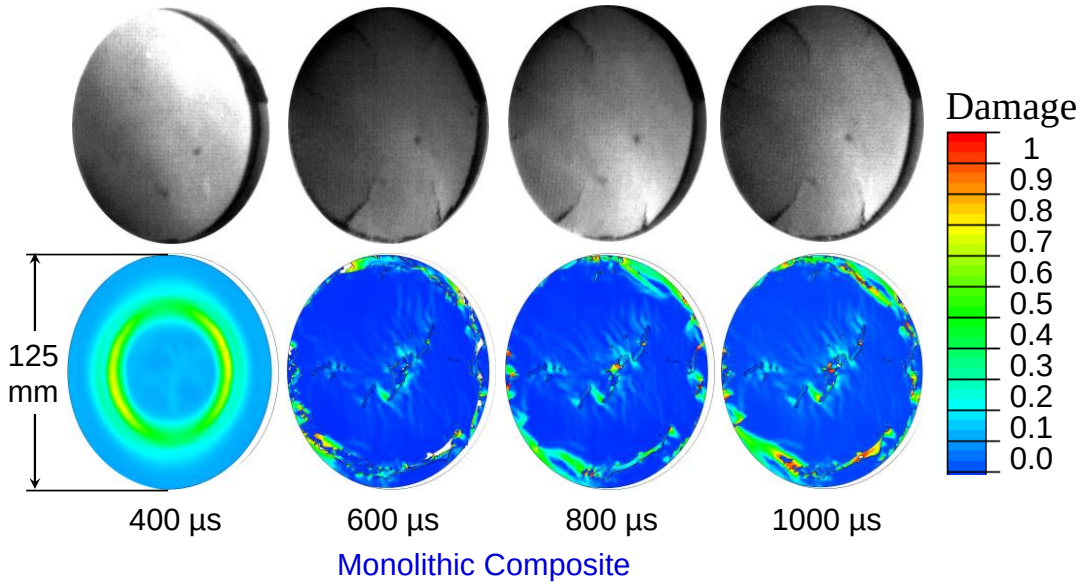


Figure 149 A comparison of experimentally observed and numerically calculated deformation fields with damage distribution at different times for a monolithic carbon fiber/epoxy composite plate subjected to $\bar{I} = 0.12$.

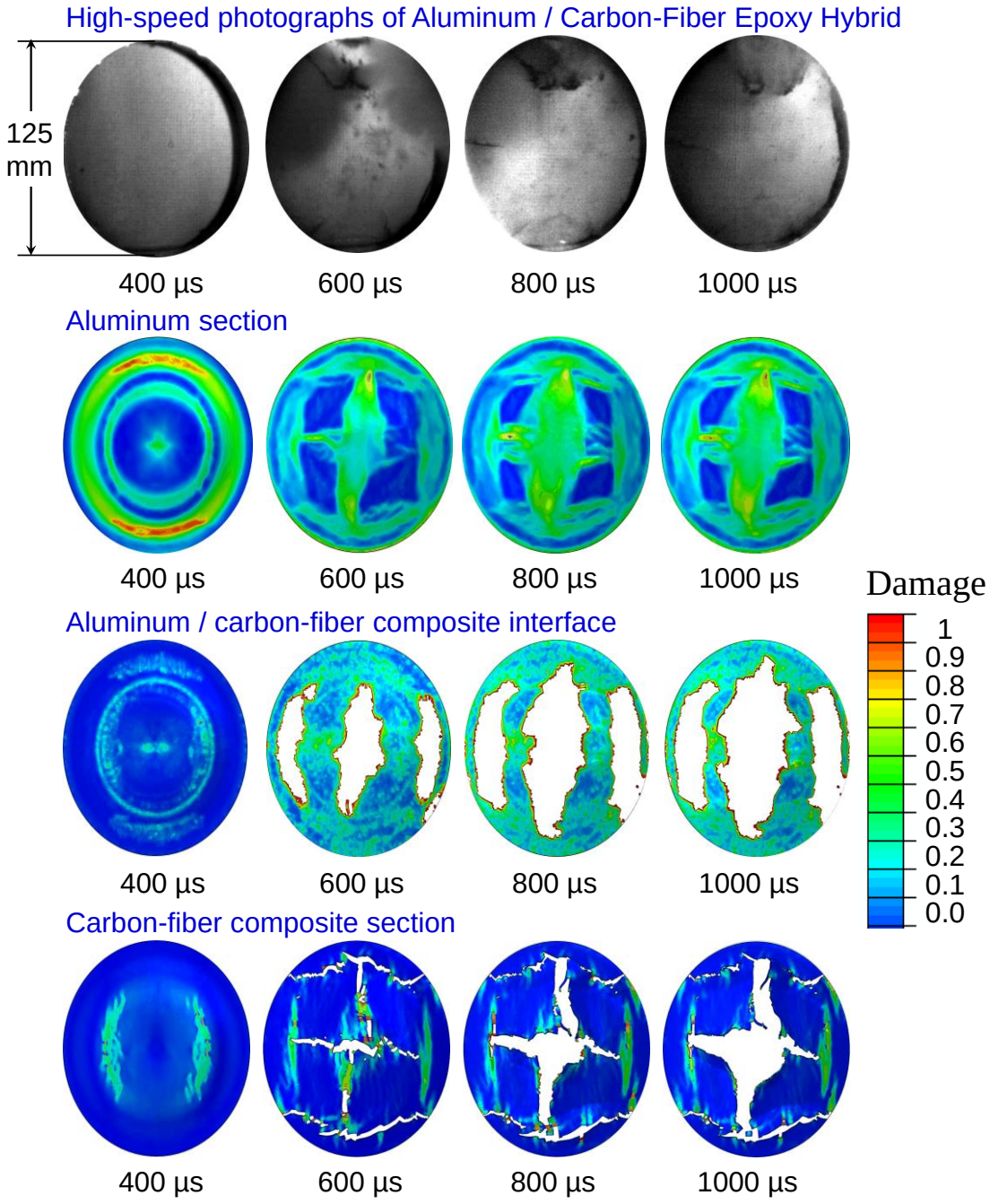


Figure 150 A comparison of experimentally observed and numerically calculated deformation fields with damage distribution at different times for a hybrid plate with the (AL/CF) stacking sequence) subjected to $\bar{I} = 0.12$.

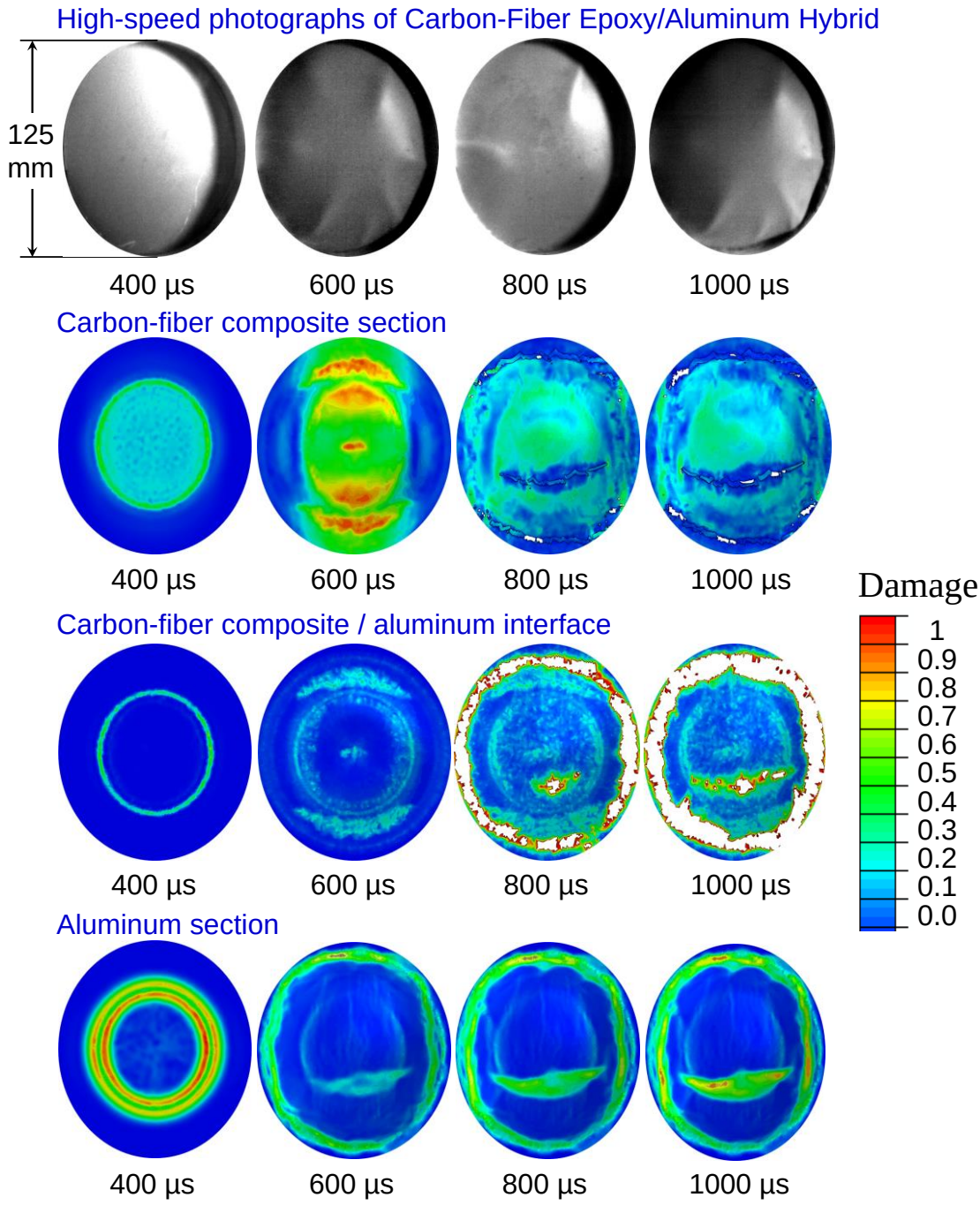


Figure 151 A comparison of experimentally observed and numerically calculated deformation fields at different times for a hybrid plate with the (CF/AL) stacking sequence subjected to $\bar{I} = 0.12$.

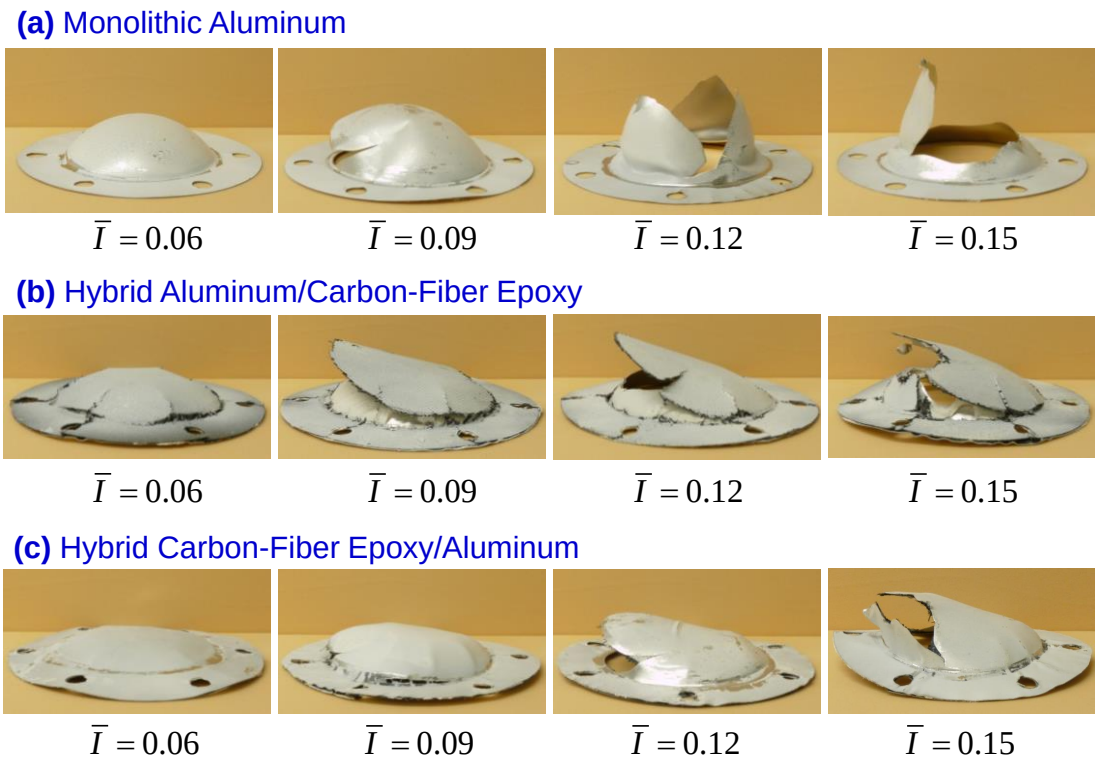


Figure 152 Post-mortem photographs of impulsively loaded (a) monolithic aluminum; (b) hybrid (AL/CF) and (c) hybrid (CF/AL) plates for different incident impulse intensities. Since monolithic composite plates exhibit fragmentation, post-mortem images for these plates are not shown.

Figure 150 shows experimental images and calculated contour plots for the damage of a hybrid metal/composite plate at the same load intensity as that in Figure 7 and Figure 8. The stacking sequence is aluminum/carbon-fiber/epoxy, with the aluminum on the impulse side and the composite on the distal side. The deformation is initially through out-of-plane deflection in the aluminum plate (see, e.g., $t = 400\,\mu s$) and shear near the support in the composite plate (see, e.g., $t = 600\,\mu s$). The bulging in the aluminum plate causes the composite to fail at two locations: near the clamped support and the central region. The impulse breaches the plate at $t = 800\,\mu s$, causing tensile necking and fracture in the aluminum plate and cracking in the composite plate. Figure

151 shows experimental images and calculated contour plots for the damage of a hybrid with a stacking sequence of carbon-fiber/epoxy/aluminum, with the composite on the impulse side and the aluminum on the back side. At $t = 400\,\mu s$, the deformation in the hybrid plate is rather uniform, involving regions of high stresses in the central region and near the clamped boundary. At $t = 600\,\mu s$, the deformation is localized in a small region near the center and near the edge of the clamped periphery. Most importantly, this plate does not experience failure seen in the other three cases already discussed.

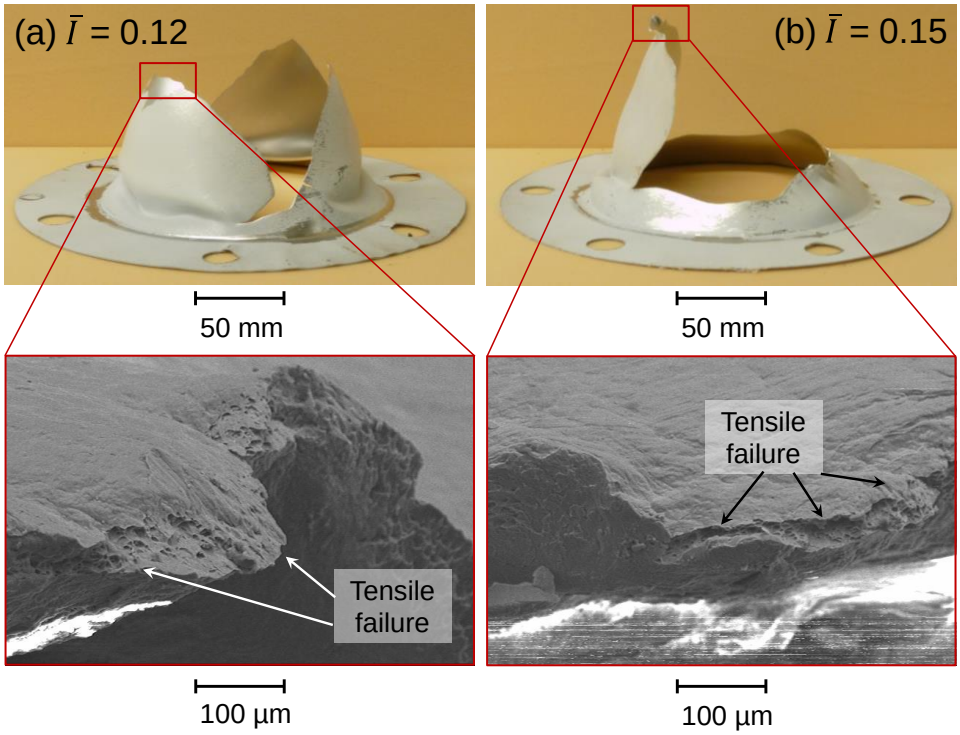


Figure 153 Scanning electron microscope (SEM) micrographs of fractured monolithic aluminum plates subjected to loading at different intensities, (a) $\bar{I} = 0.12$ and (b) $\bar{I} = 0.15$.

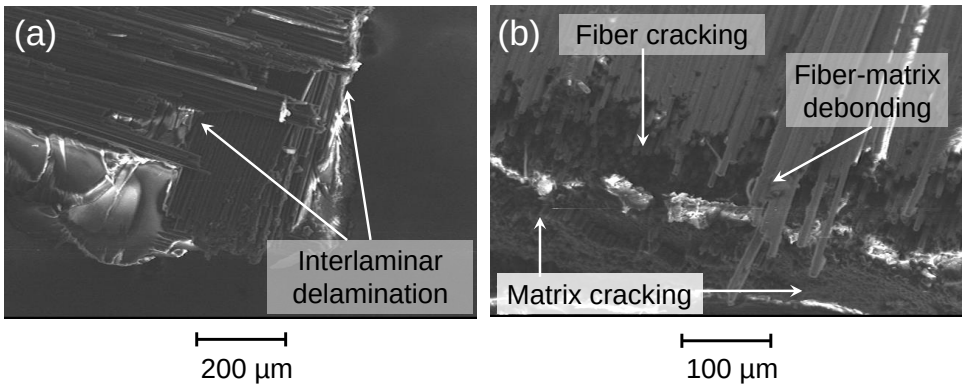


Figure 154 Scanning electron microscope (SEM) micrographs at different magnifications for a fractured monolithic composite plate subjected to $\bar{I} = 0.15$.

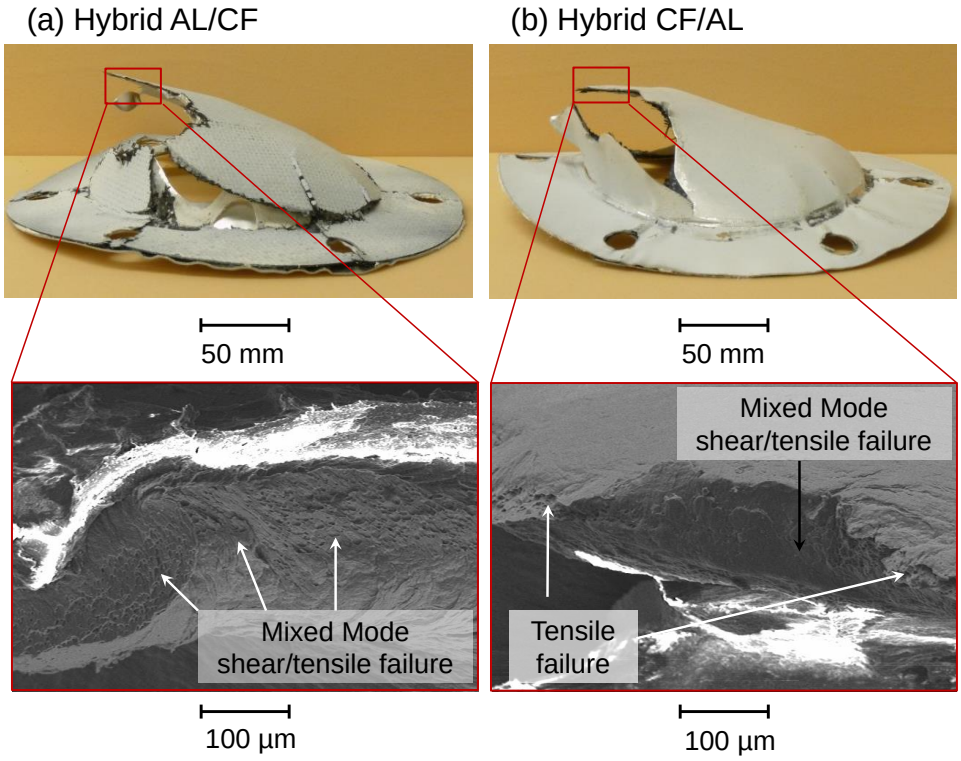


Figure 155 Scanning electron microscope (SEM) micrographs of fractured hybrid metal composite plates with different stacking sequences: (a) hybrid (AL/CF); and (b) hybrid (CF/AL). $\bar{I} = 0.15$ for both cases.

Figure 152(a-c) shows the post-mortem images of monolithic aluminum plates, aluminum/carbon-fiber/epoxy plates and carbon-fiber/epoxy/aluminum plates recovered

after the test. The monolithic composite plates fail due to shear cracking and fragmentation and, therefore, are not especially informative and are not included. The deformation modes in monolithic aluminum plates at different incident load intensities clearly illustrate the effects of loading rate. At $\bar{I} = 0.06$, the monolithic plate experiences out-of-plane deflection and bulging while the hybrid plates experience relatively minor out of plate deflection. At $\bar{I} = 0.09$, the bulging in the aluminum plate is more severe and causes rupture near the clamped periphery. For the same load intensity, the (AL/CF) hybrid plate exhibits bulging and shear rupture of the distal composite plate while the (CF/AL) hybrid plate experiences significantly less deflection and does not show failure in either the aluminum or composite sections. At $\bar{I} = 0.12$, the monolithic aluminum plate experiences petalling failure with rupture initiating at the center and propagating towards the support to create three petals as shown in Figure 148. The (AL/CF) hybrid plate undergoes tensile failure in the metallic section and shear failure in the distal composite section. The (CF/AL) hybrid plate primarily fails due to boundary effects and stress concentrations near the axisymmetrically clamped edge. At $\bar{I} = 0.15$, the aluminum plate fails due to tensile stresses and both hybrid plates exhibit rupture originating near the central region and propagating towards to the support.

At all impulse levels considered in this analysis, the structural response of the monolithic composite laminates consists of shear cracking near the axisymmetrically clamped boundary and failure is primarily in the form of delamination throughout the plate, matrix cracking near the clamped edges and rupture. The structural response of the aluminum plates is dependent on load intensity but fracture in all cases occurs through tensile stretching. At low load intensities, the aluminum plates exhibit bulging but no

rupture; at medium intensities, the aluminum plates undergo petalling failure and rupture; and at high load intensities, the aluminum plates experience localized failure. The results indicate that the response of the hybrid plates is governed by the layup. In the AL/CF plate (with the aluminum section on the impulse side), when the aluminum section bulges, the out-of-plane deflection creates high stresses in the carbon fiber laminate at the center of the plate, leading to significant delamination between the two sections. Conversely, in the CF/AL plate, the carbon fiber composite section prevents the out-of-plane bulging in the aluminum section while the aluminum section prevents shear cracking in the carbon fiber composite section, resulting in a symbiotic effect that enhances blast mitigation at all load intensities while reducing delamination between the two sections. The hybrid plates are mildly sensitive to incident load intensity (primarily because of the aluminum section) and exhibit similar deformation modes at all load intensities.

Figure 153(a) and (b) shows the scanning-electron microscope (SEM) micrographs of fractured aluminum plates subjected to $\bar{I} = 0.12$ and $\bar{I} = 0.15$ respectively. The images show plastic deformation at ~45° to the loading plane, indicating that rupture occurred in tension due to necking. Since the aluminum plates subjected to $\bar{I} = 0.06$ and $\bar{I} = 0.09$ experienced dynamic bulging and rupture near the supports, we conclude that the mode of failure for monolithic aluminum plates is tensile in nature for all incident impulse levels studied. Figure 154 reveals that, in contrast to the aluminum plates, the composite laminates exhibit large-scale delamination and shear-dominated in-ply cracking resulting from matrix damage, fiber rupture and fiber-matrix debonding. The combination of aluminum plates and carbon-fiber/epoxy laminates poses

an interesting problem in terms of failure analysis due to the significantly different failure mechanisms in each section. Figure 155(a) and (b) shows SEM micrographs of hybrid plates with stacking sequences (AL/CF) and (CF/AL) respectively. In both cases, failure in the aluminum sections is in the form of mixed-mode fracture resulting from a combination of shear and stretching. Failure in the carbon-fiber/epoxy laminates is consistent with that observed in the monolithic plates, involving large-scale delamination and shear-dominated in-ply cracking near the support. It is instructive to note that the computational model captures these deformation modes and failure mechanisms in both the metallic and composite sections, and at the interfaces.

### 11.3.2 Out-of-plane deflection

The time-and-space resolved deformation response of the impulsively-loaded plates is evaluated by tracking the out-of-plane deflection, transmitted impulse and energy dissipated cumulatively as well as in each individual component. The maximum values of each performance metric are then compared to evaluate the effect of material properties and stacking sequence on blast resistance. Figure 156(a) shows the out-of-plane displacements of different plates as a function of time with the dotted lines representing the permanent out-of-plane displacements for each plate for $\bar{I} = 0.15$. The results reveal that initially, the deflection in the composite plate increases at the highest rate but is surpassed by the deflection in the aluminum plate at $t = 200\,\mu s$. This can be attributed to the high stiffness of the carbon-fiber/epoxy laminate which arrests the deformation of the plate.

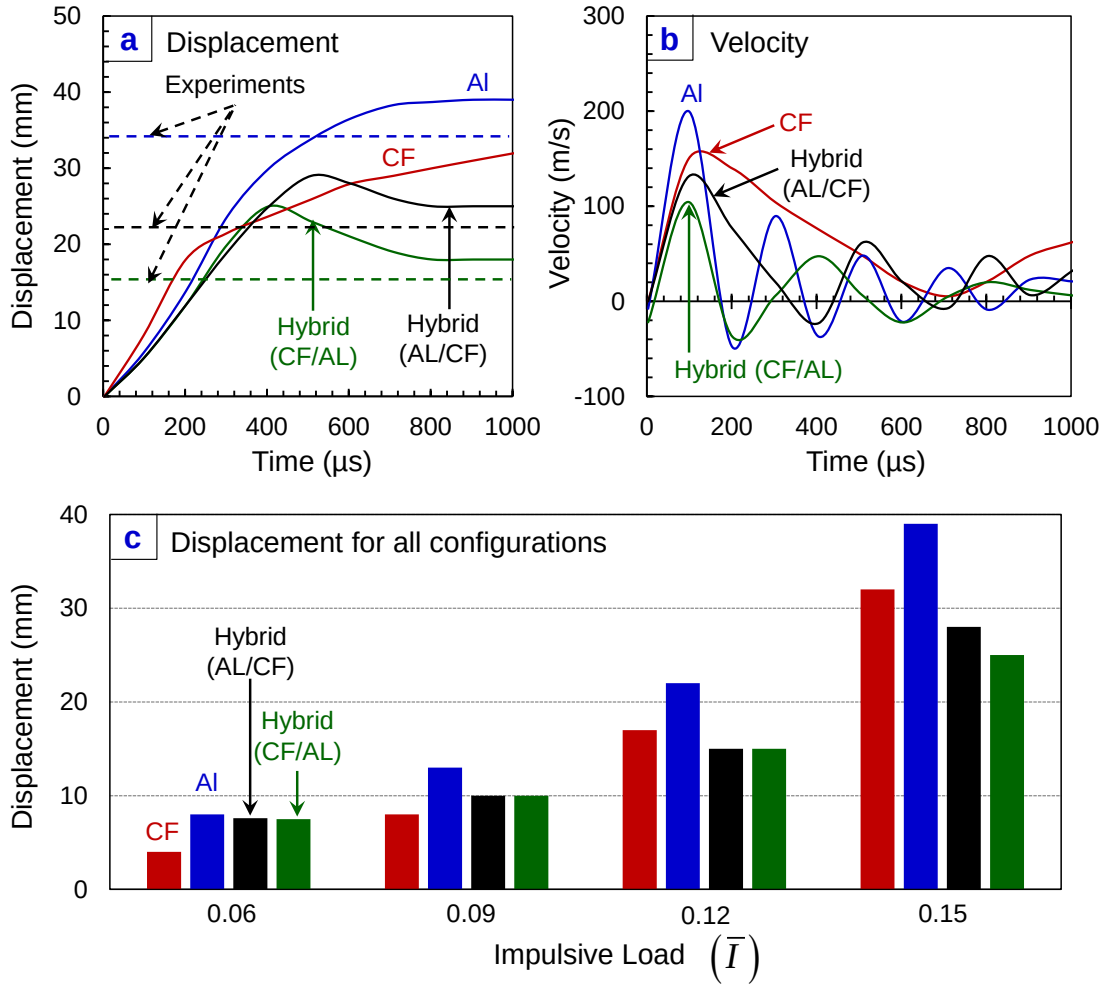


Figure 156 Computational results for (a) out-of-plane displacement and (b) mid-plane velocity as functions of time; and (c) peak out-of-plane displacements for different structures and incident impulsive loads.

On the other hand, the aluminum plate undergoes severe plastic deformation and experiences ~15% higher overall deflection. Both hybrid plates exhibit superior blast resistance, with the (AL/CF) plate undergoing ~70% of the deflection and the (CF/AL) plate undergoing 50% of the deflection experienced by the monolithic aluminum plate, respectively. The results also reveal a slight difference (~10%) between the permanent out-of-plane deflection in the experiments and the peak displacements in simulations, especially for the hybrid structures. This can be attributed to the elastic recovery in the

unloading process. Figure 156(b) shows the velocity acquired by each plate under $\bar{I} = 0.15$, revealing that the hybrid plates achieve steady-state before both monolithic plates. The peak displacements at $t = 1200\,\mu s$ for all structural configurations are shown in Figure 156(c). At low incident impulsive loads, the deflections in monolithic aluminum and composite plates are comparable, while at high incident impulsive loads, the aluminum plates exhibit higher out-of-plane deflection. At all impulsive loads considered, the hybrid plates undergo significantly lower deflection than the monolithic plates, with the (CF/AL) plate showing superior blast resistance in comparison to the (AL/CF) plate.

### 11.3.3 Impulse transmission

A major concern in the design of protective structures is the magnitude of the impulse transmitted through the structures. In evaluating the blast resistance of the monolithic and hybrid plates, the forces and impulses transmitted to the supports can provide an in-depth understanding of the blast mitigation capability. Figure 157(a) and (b) shows the reaction forces measured at supports and the corresponding impulses transmitted by each structure for $\bar{I} = 0.15$. The reaction force histories show that the carbon-fiber/epoxy laminate transmits the highest reaction forces and impulses to the supports because of high stiffness and comparatively low areal mass. After an initial peak, the composite plate reaction forces subside over 1000 μs due to a combination of fragmentation and strain recovery. The monolithic aluminum plate continues to deform plastically up to failure and transmits a relatively uniform reaction force.

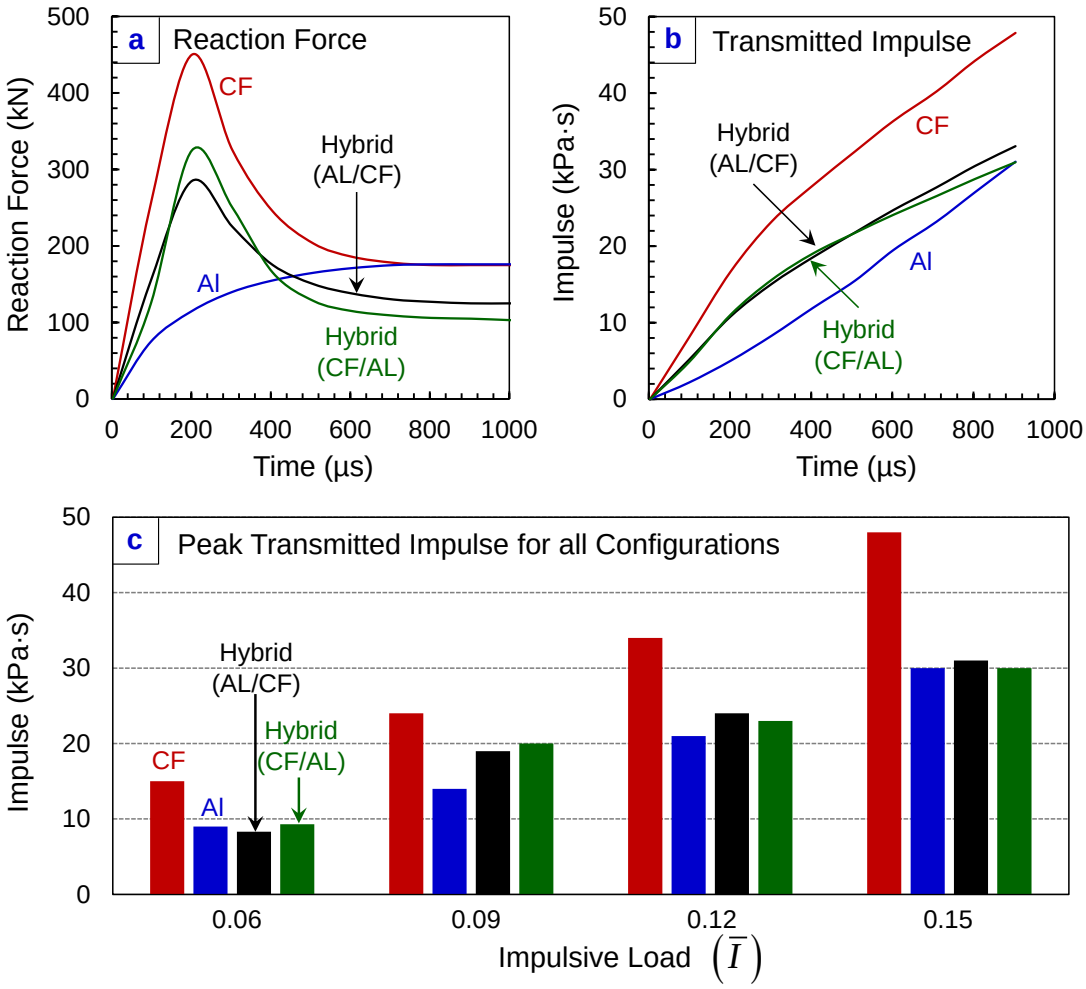


Figure 157 Computational results for (a) reaction force and (b) transmitted impulse as functions of time; and (c) peak transmitted impulses for different structures and incident impulsive loads.

The hybrid plates exhibit an initial peak in transmitted forces followed by strain recovery in both the carbon-fiber/epoxy and aluminum sections. This initial peak surpasses the peak reaction forces transmitted by the aluminum plate but subsides much more rapidly in comparison to the aluminum plate.

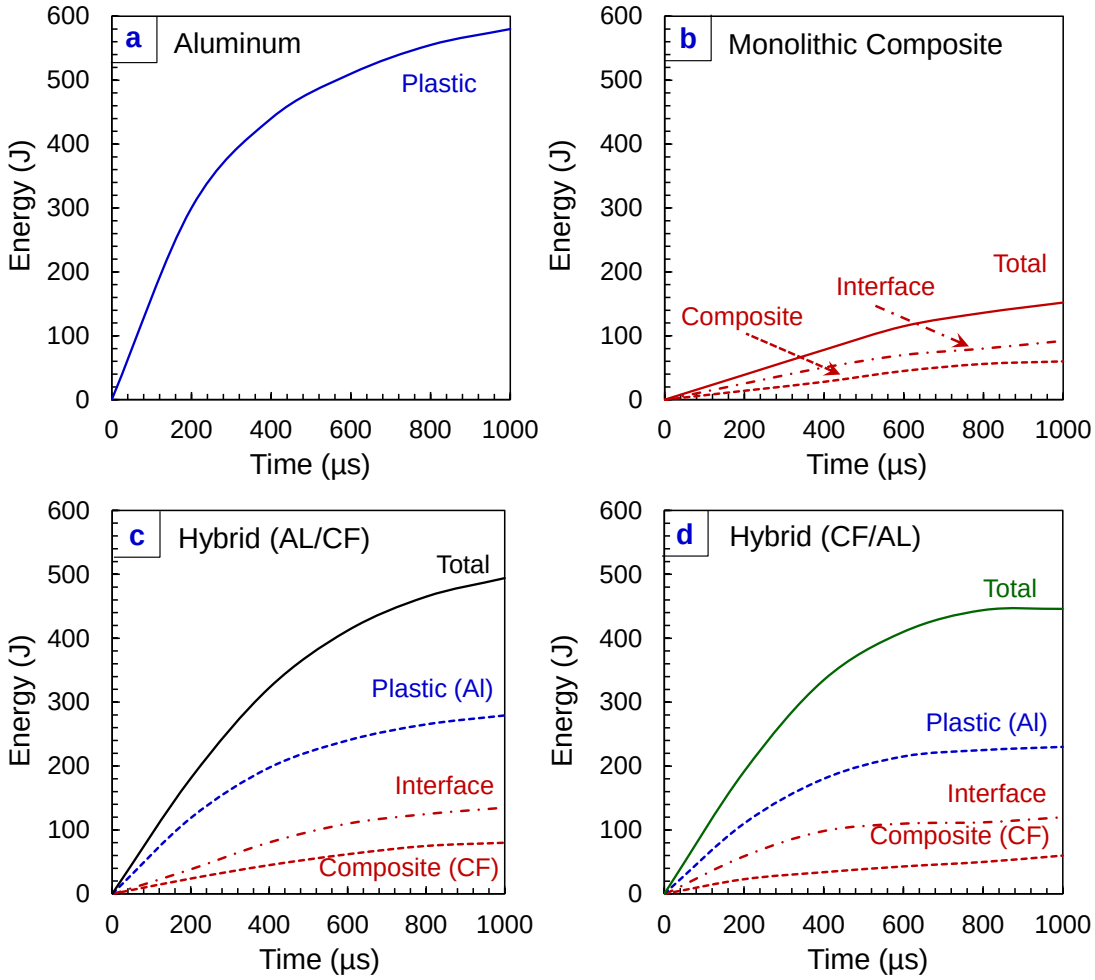


Figure 158Computational results for energy dissipation histories for different components of (a) aluminum; (b) composite; (c) hybrid (AL/CF); and (d) hybrid (CF/AL) plates.

The transmitted impulse histories show that hybrid plates transmit significantly lower impulses than the composite plate, with the (AL/CF) plate transmitting 70% and (CF/AL) plate transmitting 60% of the impulse transmitted by the carbon-fiber/epoxy laminate, respectively. The impulses transmitted by the hybrid plates and the monolithic aluminum plate are rather similar at all incident loads.

### 11.3.4 Energy dissipation

When an impulsive wave interacts with a structure, a number of energy dissipation mechanisms are activated. It is important to understand how the dissipation is distributed in the structures in order to determine effectiveness. A significant fraction of the incident energy is dissipated through plastic deformation via tensile stretching in the aluminum plates, as shown in Figure 153. In composite plates, the energy dissipation primarily occurs through interlaminar delamination and in-ply damage in the form of matrix cracking, fiber cracking and fiber-matrix debonding, as shown in Figure 154. Figure 158(a-d) shows the histories of the energy dissipated in the different components of each structure subjected to $\bar{I} = 0.15$. As expected, the aluminum plates exhibit considerably higher energy dissipation in comparison to the composite laminates. Specifically, plastic deformation in the aluminum plates enables them to dissipate 500% more energy than the composite plates. Within the composite plate, interlaminar damage dissipation surpasses in-ply damage dissipation. The hybrid plates dissipate similar amounts of total energy with minor differences in the component-level dissipation.

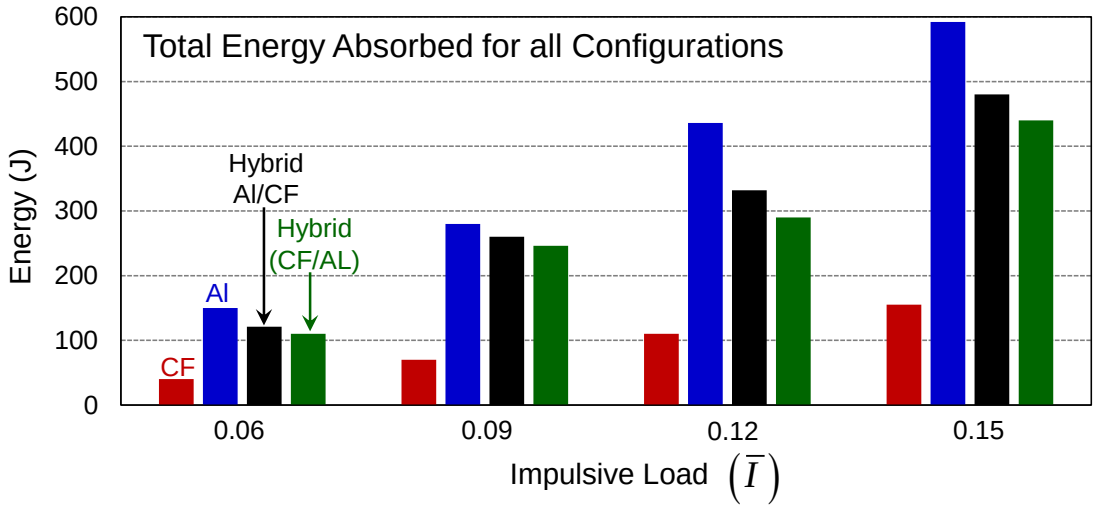


Figure 159 Computational results for total energy dissipation for aluminum, carbon-fiber/epoxy, hybrid (AL/CF) and hybrid (CF/AL) plates.

Specifically, in the hybrid (AL/CF) plate, the aluminum section is responsible for ~60%, the interfacial damage dissipation is responsible for ~25% and in-ply damage dissipation is responsible for ~15% of the total energy dissipation respectively. In the hybrid (CF/AL) plate, the aluminum section is responsible for ~50%, the interfacial damage dissipation is responsible for ~30% and in-ply damage dissipation is responsible for ~20% of the total energy dissipation. It should be noted that the energy dissipation of the hybrid plates is slightly enhanced by an additional layer of adhesives required to bond the aluminum and composite sections. The comparison of total dissipated energy for different structural configurations subjected to a range of incident impulses is shown in Figure 159. The monolithic aluminum plate dissipates the highest amount of energy for all load intensities while both the (AL/CF) and (CF/AL) hybrid plates dissipate ~75% of the energy dissipated by the monolithic aluminum plates. Additionally, the (CF/AL) hybrid plates exhibit lower energy dissipation in both the aluminum and composite

sections in comparison to the (AL/CF) hybrid plate. The monolithic composite plates are relatively inefficient with respect to energy dissipation capacity.

### 11.3.5 Design of hybrid structures for blast mitigation

To fully utilize the potential of hybrid metal composite structures, one consideration is to maximize the performance under a given load condition while maintaining or minimizing the mass. Weight-efficient designs of blast-resistant structures are determined by a number of factors, such as the expected incident load, types of materials, stacking sequences, interfacial effects, structural geometry and loading configuration. To quantify the effect of these factors on deformation response, a performance metric consisting of out-of-plane deflection, transmitted impulse, plastic dissipation and plastic dissipation density is developed.

Experiments and simulations discussed previously have revealed that hybrid structures perform marginally better than monolithic structures at low incident load intensities but exhibit superior blast resistance at higher load intensities where damage and failure play a major role. The stacking sequence consisting of composite on the impulse side and aluminum on the opposite side (CF/AL) provides the highest blast mitigation through a combination of minimum deflection and impulse transmission and maximum energy dissipation among the structures analyzed. It should be noted that the hybrid plates studied consist of equal weight of aluminum and carbon-fiber/epoxy laminate.

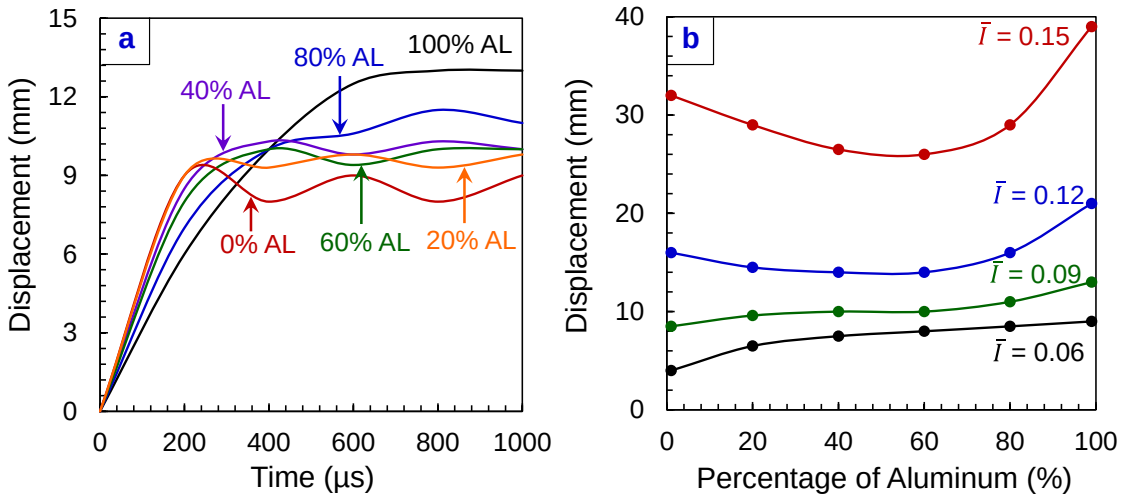


Figure 160 Computational results for (a) out-of-plane displacement as a function of time and (b) peak out-of-plane displacement as a function of the percentage of aluminum in (CF/AL) hybrid plates for different incident impulse levels.

It is important to understand the role of hybrid plate construction and the effects of varying amounts of aluminum and carbon-fiber/epoxy in the design. A computational study is carried out by varying the percentage of aluminum in the (CF/AL) hybrid plate while the total mass is kept constant. The percentage of aluminum is varied from 0% to 100% in increments of 20% and the remaining mass in each case is that of carbon-fiber/epoxy. Table 12 shows the mass and thickness of each section of the hybrid plate in the optimization analysis. The six hybrid plates consisting of varying amounts of aluminum are then subjected to loading under the four different incident impulse levels in Figure 146(a-d).

Figure 160(a) shows the time histories of the out-of-plane deflection at the center of (CF/AL) hybrid plates with varying amounts of aluminum subjected to $\bar{I} = 0.09$. The plate with 0% Al experiences high initial rate of deflection increase followed by vibration. As the amount of aluminum increases, the vibration diminishes, with the 100%

Al plate reaching a non-deforming state at approximately $t = 700\ \mu s$. Figure 160(b) shows the permanent deflection of the (CF/AL) hybrid plates as a function of the percentage of Al for a range of load magnitude. At low impulse magnitudes $\left(\bar{I} \le 0.09\right)$, the composite plate experiences the least deflection, with the permanent deflection increasing with the amount of aluminum. At higher impulse magnitudes $\left(\bar{I} > 0.09\right)$ where fracture and failure are a major consideration, the plate with 60% Al and 40% carbon-fiber/epoxy composition (denoted as 60% Al) exhibits the lowest deflection, undergoing 15% and 25% of the deflections experienced by the 0% Al and 100% Al plates, respectively. The 40% Al plate experiences slightly higher deflections compared with the 60% Al plate.

Table 12 Hybrid structures with different amounts of aluminum and composites.

| Plate Designation | AL Percentage (%) | AL Thickness (mm) | AL Mass (kg) | CF/Epoxy Mass (kg) | CF/Epoxy Thickness (mm) |
|---|---|---|---|---|---|
| 100% AL | 100 | 1 | 2.7 | 0 | 0 |
| 80% AL | 80 | 0.8 | 2.16 | 0.54 | 0.36 |
| 60% AL | 60 | 0.6 | 1.62 | 1.08 | 0.72 |
| 40% AL | 40 | 0.4 | 1.08 | 1.62 | 1.08 |
| 20% AL | 20 | 0.2 | 0.54 | 2.16 | 1.44 |
| 0% AL | 0 | 0 | 0 | 2.7 | 1.8 |

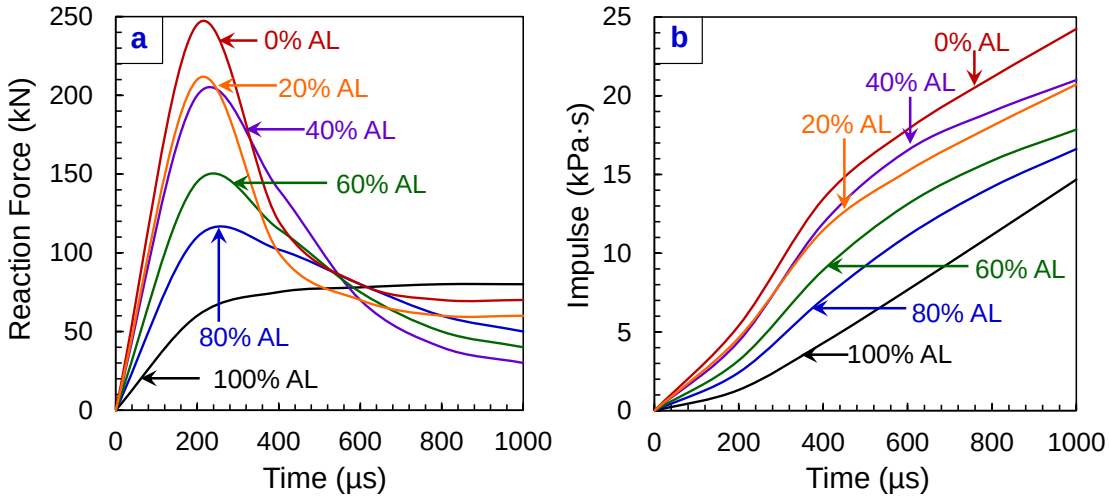


Figure 161 Computational results for (a) reaction force and (b) transmitted impulse as functions of time for (CF/AL) hybrid plates with varying amounts of aluminum.

Minimizing the impulse transmitted to the downstream section is important for protecting the internal components of marine vessels. The magnitude of the transmitted impulse is therefore an important parameter concerning the blast resistance of composite structures. Clearly, the structure that transmits the least impulse at the lowest rate is most desirable. Figure 161(a) shows the reaction forces measured at supports and Figure 161(b) shows the corresponding impulses transmitted through (CF/AL) hybrid plates consisting of varying amounts of aluminum subjected to $\bar{I} = 0.09$. For the 0% Al plate which is exclusively constructed from carbon-fiber/epoxy, the reaction forces show a sharp initial peak which subsides after 600 μs. As the amount of aluminum in the hybrid plate increases, the magnitude of the initial peak gradually decreases until it disappears at 100% Al. Overall, the 0% Al plate transmits the highest impulse while the 100% Al plate transmits the least impulse. Figure 162 shows the transmitted impulses for the hybrid plates as a function of the percentage of aluminum for a range of incident impulse

magnitude. The monolithic aluminum (100% Al) plate transmits the least impulse at all load intensities while the 80% Al and 60% Al plates transmit 105% and 110% of the impulse transmitted by the 100% Al plate, respectively. The results indicate that there is a minor benefit in terms of impulse mitigation in hybrid plates beyond a 40% aluminum/ 60% carbon-fiber/epoxy composition.

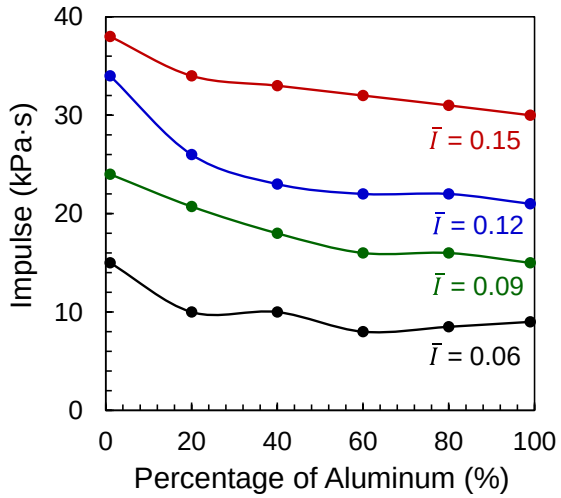


Figure 162 Computational results for transmitted impulse as a function of the percentage of aluminum in (CF/AL) hybrid plates for different incident impulsive loads.

A drawback of composite structures is their significantly lower energy dissipation capacity relative to metallic structures. As discussed previously, composite plates dissipate ~15% of the energy dissipated by monolithic aluminum plates of equal mass. Within the composite plates, adhesives and interfacial effects account for a majority of the inelastic dissipation while in-ply damage mechanisms account for a relatively minor fraction of the energy dissipated. Additionally, in hybrid structures, aluminum sections are responsible for a large fraction of total dissipated energy. An analysis of failure modes reveals the tendency of composite structures to experience fragmentation and failure under high intensity loads. Hybrid structures serve to eliminate this drawback and

provide improved blast mitigation by enhancing the energy dissipation capacity of the structures. Figure 163(a) shows the time histories of plastic dissipation in hybrid plates consisting of different amounts of aluminum while Figure 163(b) shows the dissipation in hybrid plates as a function of the percentage of aluminum for a range of incident loads. The energy dissipated in the hybrid plates increases rapidly with the amount of aluminum up to 60% and plateaus beyond that level. In fact, there is a slight decrease in dissipation for the 80% Al -and 100% Al plates at the lower load intensities.

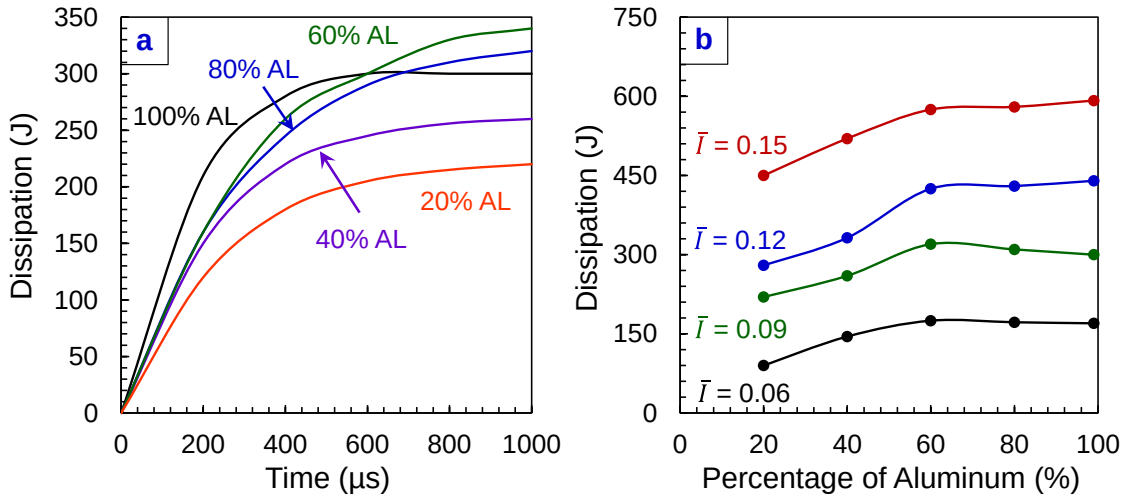


Figure 163 Computational results for (a) plastic dissipation as a function of time and (b) plastic dissipation as a function of the percentage of aluminum in (CF/AL) hybrid plates for different incident impulsive.

To evaluate the efficiency of energy dissipation in the hybrid plates, the ratio between the plastic dissipation in the aluminum to the mass of aluminum is calculated. This ratio, called dissipation density (dissipation per unit mass), is shown in Figure 164(a) as a function of time for the (CF/AL) hybrid plates with varying amounts of aluminum and shown in Figure 164(b) as a function of the percentage of aluminum in the hybrid plates. The results reveal that the dissipation per unit mass is highest for thin

layers of aluminum in the 20% Al and 40% Al plates and decreases drastically as the percentage of aluminum increases.

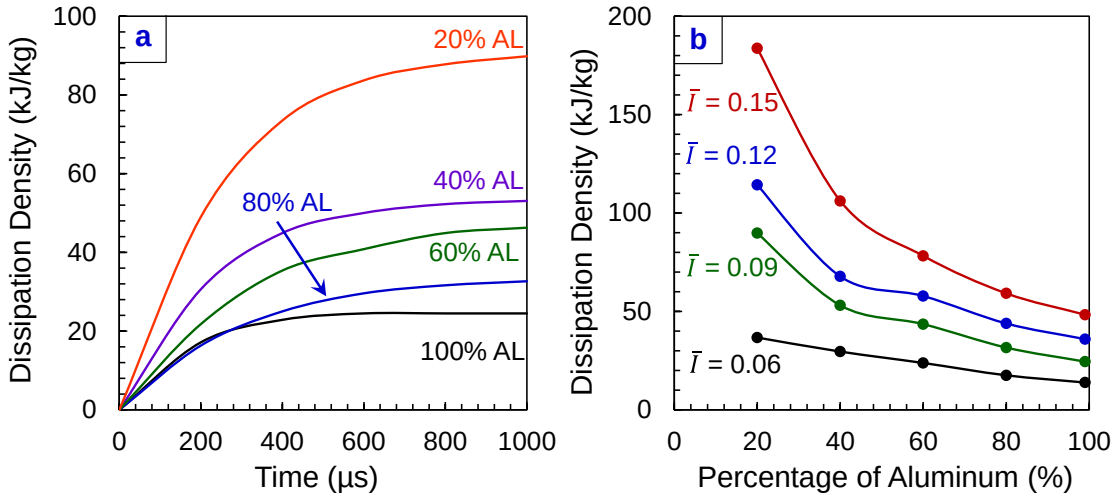


Figure 164 Computational results for (a) plastic dissipation density as a function of time and (b) plastic dissipation density as a function of the percentage of aluminum in (CF/AL) hybrid plates for different incident impulsive loads.

It should be noted that the presence of the aluminum section in a hybrid plate has two main effects: (1) providing confinement for the carbon-fiber/epoxy plate to prevent shear cracking and fragmentation and (2) enhancing impact resistance by improving energy dissipation. The results reported here show that these two effects require conflicting structural modifications. The first effect is best achieved by the presence of a thick aluminum layer while the second effect is best achieved by multiple thin aluminum layers. The design of the aluminum section thickness must then balance these two competing requirements. Further studies on this should explore the effects of stacking sequence involving alternating layers of carbon-fiber/epoxy and aluminum sections in a (CF/AL) configuration.

## 11.4 Concluding remarks

Marine structures must balance strength and load-carrying capacity with the ability to minimize impulse transmission for high blast and impact resistance. The combined experimental and computational research reported here is an attempt to quantify the underwater blast response of hybrid fiber-metal laminates with different stacking sequences under a range of incident impulsive loads. The peak pressures of the incident impulses considered range from 59 MPa to 198 MPa. Since all plates considered fail under an incident impulse of $\bar{I} = 0.15$ with a peak pressure of 198 MPa, this is the highest impulse intensity discussed in this paper. The experiments reported here are supported by fully dynamic finite element calculations. The results from numerical calculations provide a more in-depth understanding of temporal and spatial evolution of different deformation modes in the structures and the partitioning of energy in different components.

The monolithic aluminum plates experience petalling failure and exhibit bulging and tensile necking in the central region under a range of incident impulsive loads. Composite plates undergo extensive delamination at all load intensities and experience in-ply damage in the form of matrix cracking, fiber cracking and fiber-matrix debonding. The failure is predominantly near the clamped boundary, indicating significant shear dependence of damage. The hybrid (AL/CF) plates exhibit bulging and tensile failure in the aluminum sections and large-scale shear cracking in the composite sections. Additionally, the lack of confinement for the composite plate creates large delamination at the interface between the aluminum and composite sections. Conversely, the hybrid (CF/AL) plates exhibit significantly superior blast resistance with minimal shear cracking

in the composite section and significantly lower bulging in the aluminum section. This behavior can be attributed to the confining conditions created by the aluminum section that prevents the composite from deflecting and failing under shear loads in conjunction with the stiff composite section which prevents excessive bulging. Both hybrid structures exhibit superior blast resistance in comparison to monolithic plates of equivalent mass.

With respect to the hybrid plates, it is determined that the stacking sequence consisting of the composite section in contact with water and aluminum section on the opposite side provides marginally higher blast mitigation capability. In stacking sequence, the carbon fiber composite section prevents the out-of-plane bulging in the aluminum section while the aluminum section prevents shear cracking in the carbon fiber composite section resulting in a symbiotic effect that enhances blast mitigation at all loading intensities while reducing delamination between the two sections.

The blast resistance of each plate is evaluated by comparing the impulses transmitted through and the energy dissipated by the plate. The hybrid structures are found to possess superior impulse mitigation capabilities at all impulsive loads, transmitting ~60% of the impulses transmitted by the composite laminates. The monolithic aluminum plates and the aluminum sections of the hybrid plates are responsible for the majority of the energy dissipation at all impulse intensities, absorbing more than 60% of the total energy dissipated in the hybrid plates. Interfacial damage dissipation is found to exceed in-ply damage dissipation in the composite sections. Overall, the hybrid metal/composite structures constitute better alternatives to monolithic structures of either material, due to the combination of high stiffness and strength-to-weight ratio.

In the hybrid plates, the composite section is responsible for restricting the out-of-plane deflection while the aluminum section plays a vital role in impulse mitigation and energy dissipation. It is found that that plates with 40%-60% of aluminum by weight provide an optimal combination of resistance to deflection, impulse mitigation and energy dissipation. Additionally, thinner layers of aluminum lead more efficient energy dissipation on a unit mass basis.

A parametric study is carried to quantify deflection, impulse transmission and energy dissipation as functions of incident load, material properties, and structural attributes. The insight gained provides guidelines for the design of next generation structures and retro-fitting of existing structures for which response to water-based impulsive loading is an important consideration. The exploration of different stacking sequences, adhesive strengths, relative thicknesses and inclusion of low density cellular solids for enhanced blast mitigation should form the basis of future studies.

# 12. SUMMARY AND CONCLUSIONS

Since G. I. Taylor's pioneering work on underwater explosions and the dynamic behavior of free-standing thin-plates, there have been a number of studies to quantify the effects of an underwater blast on marine structures. Due to high shear-and-bending resistances and the ability to modify core-materials to suit applications, sandwich structures are increasingly being used in applications that require cost-effective, durable and blast-resistance structures. Recent investigations in this area have shown that sandwich-structures are very useful for blast-mitigation and consistently outperform monolithic structures of the same mass. The dynamic response of sandwich structures to underwater impulsive loads presents a rich source of engineering problems - experimental, analytical and computational.

Effective design of marine composite structures requires an intimate understanding of dynamic deformation and failure and a capability to predict and control their performance. The complexity of technical issues necessitates detailed experiments that account for realistic service environments and a complementary computational framework that allows a wide range of scenarios to be explored. The input from such parametric technical approaches can be utilized to address the need for better designed, more durable, blast resistant and lightweight marine vessels.

An underwater impulsive loading facility, the Underwater Shock Loading Simulator (USLS) has been designed and fabricated. The facility makes use of a gas-gun based projectile-impact mechanism to generate controlled, planar underwater impulsive loads which impinge on the target structure. A highly modular support system allows in-

situ high-speed digital imaging of the dynamic deformations in marine structures. An Imacon 200D high-speed camera is used to take photographs and dynamic pressure-transducers are used to measure the impulse intensity. The facility can be modified to test oblique and curved structures.

The structural configurations studied include thick monolithic composite plates and sandwich structures manufactured with HP60, HP100 and HP200 cores from DIAB Inc. Simply-supported composite sandwich panels are subjected to underwater impulsive loads of varying magnitudes. The dynamic deformations are tracked using in-situ high-speed digital imaging with an Imacon 200D high-speed camera at a frame rate of ~20000 frames per second. Coupled Eulerian-Lagrangian finite element simulations are carried out, accounting for FSI effects, damage in the form of core-cracking and fragmentation, matrix-cracking and core-face debonding. The dynamic response of composite structures is investigated using this computational approach and shows that the experiments and simulations are in good agreement. The model is then extended to different structural attributes and loading configurations that include planar and oblique loading, cylindrical structures, sandwich cores with different densities and graded cores with increasing and decreasing densities.

In addition to providing high bending and shear resistances and enhancing the strength-to-weight ratio of structures, sandwich cores must balance strength and the ability to absorb and retard incoming impulses in order to be effective in protective structures against blast and impact. Polymeric structural foams are especially attractive because of their lightweight, ease of manufacturing, high corrosion resistance, good thermal insulation, and low water absorption. However, due to their wide range of

possible densities and structural design attributes, the relationship between the behavior of these foams and incident underwater impulsive loads has yet to be fully established. In an effort to provide quantitative relations for structural design, we have evaluated the load-carrying and impulse transmission capabilities of sandwich structures with PVC foams of a range of density, facesheet thicknesses and incident load intensity. A series of experiments and numerical simulations are carried out, accounting for effects of structural attributes and loading rates on performance. The loading conditions involve impulsive loads with peak pressures up to 100 MPa, which simulate the effects of an explosive TNT source detonating underwater at different standoff distances from the structure. The conclusions of this study relating to the load-carrying and blast mitigation capacities of sandwich plates with polymeric foam cores are as follows:

1. The compressive strain experienced by and the impulse transmitted by the sandwich core pose opposing requirements on structural design. Low density cores experience high compressive strains while transmitting lower impulses. On the other hand, high density cores behave like monolithic plates and transmit large fractions of the incident impulse. Although low density cores transmit significantly lower impulses, it should be noted that the kinetic energy acquired by frontfaces in low density cores is much higher, leading to severe core compression. This increased core compression is detrimental to bending stiffness and strength. Structural design must balance the competing requirements.
2. Experiments and simulations are in reasonable agreement in terms of the extent of core compression and impulse transmission. Over the range of impulses and structural configurations considered, the finite element predictions are within 10%

of the experimental data. The homogenized, crushable foam constitutive model employed provides accurate tracking of the early stage response of the core material. However, the model slightly overestimates the compliance of the core leading to an increase in core compressive strain and a decrease in the transmitted impulses in comparison to experiments. The numerical calculations have provided an in-depth understanding of the temporal and spatial evolution of deformation modes in the core material.

3. Cores with different densities show significantly different deformation behaviors. Low density cores like HP60, HP100 and HP130 $\left(0.01 < \bar{\rho} < 0.06\right)$ experience rather uniform straining throughout their thickness and provide high impulse mitigation capacity. High density cores such as HP200 and HP250 $\left(0.06 < \bar{\rho} < 0.1\right)$ experience strain localizations that occur primarily near the facesheets. Such non-uniform distribution of straining leads to high impulse transfer and severe damage in the core material.
4. Loading-structure-performance maps derived from uniaxial compressive loading are compared to those obtained from the simply-supported bend loading configuration to offer insight into the role of core density on bending and failure of sandwich structures. The relative core density is found to be an important parameter determining the performance of sandwich structures in simply-supported conditions. Greater core compressibility minimizes both the deflection and impulse transmission in this configuration. Higher core densities $\left(0.06 < \bar{\rho} < 0.1\right)$ limit core crushing, enable higher energy absorption and help

maintain the bending strength of a sandwich plate, but result in significantly more momentum being imparted to the structure. This leads to higher core damage and out-of-plane deflection. Conversely, lower density cores $\left(0.01 < \bar{\rho} < 0.06\right)$ are susceptible to collapse under high intensity loads which can have adverse effects on survivability and residual bending strength.

5. The frontface and backface masses are varied independently and results indicate that the frontface mass has a significant influence on core compression and impulse transmission, while the backface mass has a negligible effect on structural response. The momentum transmitted into the sandwich plates with $\Delta T_f / T_c < 0.1$ is substantially lower than that for $\Delta T_f / T_c > 0.15$. For the same core density, a 100% increase in facesheet thickness leads to a 25% and 50% increase in the core strain and normalized transmitted impulse, respectively. The greatest momentum transfer occurs in the case of monolithic plates of equivalent mass as sandwich plates. For a given incident impulse, $\Delta T_f / T_c > 0.15$ results in severe core compression and collapse because the impulse acquired by the frontface increases in proportion to mass.

Marine structures must balance stiffness and load-carrying capacity with the ability to minimize impulse transmission for high blast and impact resistance. Composite structures have higher stiffnesses and high strength-to-weight ratios compared with monolithic structures. Additionally, thick composite laminates provide very high bending and shear resistances with slight increases in total mass. However, due to the novelty and wide range of structural combinations, the relationships between structural responses and

material heterogeneity in composite structures are not well quantified. In particular, the behavior of composite structures under extreme impulsive loading generated by underwater explosions is systematically analyzed.

The combined experimental and computational research reported here is an attempt to quantify the underwater blast response of fiber-reinforced epoxy laminates with different material properties and stacking sequences under a range of incident impulsive loads. The peak pressures of the incident impulses considered range from 59 MPa to 198 MPa. Since all plates considered fail under an incident impulse of $\bar{I} = 0.16$ with a peak pressure of 196 MPa, this is the highest impulse intensity discussed in this paper. The experiments reported here are supported by fully dynamic finite element calculations. The results from numerical calculations provide a more in-depth understanding of temporal and spatial evolution of different deformation modes in the structures and the partitioning of energy in different components. It should be emphasized that the composite panels studied have similar overall mass and thickness.

Comparison of experiments and simulations shows that numerical calculations provide a reasonable representation of damage and dissipation mechanisms in the composite laminates. The finite element model captures the essential deformation mechanisms observed in both carbon-fiber and glass-fiber/epoxy laminates. Specifically, the following are replicated with reasonable accuracy: fluid-structure interaction effects at the water-structure interface, effects of fiber orientation, in-ply matrix and fiber cracking and rupture, and inter-ply delamination initiation and evolution. The Hashin damage model overestimates the softening effect resulting from cracking and fracture leading to underestimation of backface deflection. The results from numerical

calculations provide a more in-depth understanding of temporal and spatial evolution of different deformation modes in the structure.

Glass-fiber/polyester PVC foam sandwich structures outperform monolithic composite structures at all load intensities. Failure in the monolithic structure is in the form of shear-cracking in the matrix, fiber-matrix debonding and fiber-fracture. The damage mechanisms in low-density cores are primarily in the form core-indentation, core-crushing and cracking due to bending-stresses while in high-density cores are primarily in the form of face-wrinkling under compressive loads, face-rupture, core-cracking and fragmentation and core-crushing, in that order. An important aspect of the dynamic response of high-density cores is the delayed core-compression - high-density cores undergo large-scale fracture and fragmentation before the onset of core-crushing. Low-density cores undergo fracture simultaneously with core-crushing and fracture is primarily due to tensile loads created by bending deformation. Experiments demonstrate that the dynamic behavior of PVC foams is significantly influenced by rate-effects when loads are complex and multi-axial. All these damage and deformation modes are captured by the finite-element simulations.

In sandwich-composite face-sheets, failure in the front-face (impulse-side) is primarily in the form of compressive buckling failure which causes instantaneous core-face debonding followed by front-face rupture. Failure in the back-face is identical to the failure observed in monolithic-composite, showing matrix-cracking and fiber-matrix debonding under large tensile stretching. The midpoint deflections and reaction-forces transmitted to supports are used as metrics to evaluate blast-resistance of sandwich panels. The lower the values of these metrics, the better is the blast resistance. Results

show that low-density cores are superior to high-density cores or monolithic composite structures, consistently showing lesser deflections and transmitting lower impulses. The sandwich structure with the HP60 core is the only composite structure studied here that does not undergo complete rupture - maintaining better structural integrity than other structures - even at very high intensity loads. Clearly, as long as dimensional constraints are fulfilled, weak-cores and strong faces provide better blast-mitigation in marine structures subjected underwater impulsive loads.

In sandwich structures, core-compression and crushing in the sandwich core is highly localized near the loading region. Since large-scale bending is prevented due to the presence of a dense water-backed condition, no inclined cracks originate at the loaded area and fragmentation is negligible. Damage is primarily in the form of core-crushing and shear-fractures. The deflection and the magnitude of the pressure-wave transmitted to the back-side water-section are used as metrics to evaluate the blast-resistance. Water-backed structures, on average, undergo ~50% lesser deflection than air-backed structures. Thick cores of low-density foams consistently outperform high-density cores and monolithic structures. The transmitted pressure waves show that the monolithic structures transmit ~80%, HP200 core transmits ~40%, HP100 core transmits ~20% and HP60 core transmits negligible pressure into the back-side water-section. Blast-mitigation is relatively insensitive to face properties and highly sensitive to core thickness and density. Weak cores allow a stress-saturated compressive strain regime and greatly reduce the intensity of the transmitted impulse.

The analysis of deformation in blast loaded carbon-fiber/epoxy and PVC foam sandwich structures has yielded experimental data on the failure behavior of composites subjected to underwater impulses. Maximal damage was observed near the load circumference in both monolithic and sandwich structures. The analysis of damage modes shows that relative core density is a critical factor in determining structural performance of sandwich structures. Sandwich structures significantly outperform monolithic composites at all impulsive levels and environmental conditions. Low density cores provide higher blast resistance than high density cores. An analysis of the effect of load intensity shows that as the load intensity increases, the deflection of the frontface outpaces the dynamic core crushing capability of the cores, resulting in collapse. In such cases, low density cores provide better load spreading and exhibit better capabilities for compression. However, a major concern for low density cores is the occurrence of core indentation, in which the core fails in a localized region and causes compressive stresses in the frontface leading to buckling and rupture. Therefore, a balance of core stiffness and softness is essential for optimal blast resistance.

Comparison of experiments and simulations shows that numerical calculations provide a reasonable representation of damage and dissipation mechanisms in the facesheets and core. The compressible foam constitutive model leads to high core compression and a slight overestimate of backface deflection. The finite element model captures the essential deformation mechanisms observed in both the facesheets and the core. Specifically, the following deformation modes are replicated with reasonable accuracy: core indentation, core shear, core-face debonding, facesheet buckling and delamination, structural collapse and rupture. The results from numerical calculations

provide a more in-depth understanding of temporal and spatial evolution of different deformation modes in the structure. The deformation in sandwich structures is strongly influenced by core density and loading rate and magnitude. Structures with high relative densities undergo severe damage and exhibit significantly higher core face debonding than structures with low relative densities. For a given impulsive load, structures with low relative densities (HP60 and HP100) experience considerably lower displacements than those with high relative densities (HP200 and monolithic).

In both air-backed and water-backed cases, the maximum impulse transmitted by each structure is used to determine the performance of the composite structure. Sandwich structures exhibit superior blast mitigation capabilities in comparison to monolithic structures at all impulse magnitudes. In particular, thick, low density foam cores made of Divinycell HP60 and HP100 foams provide the highest load spreading and impulse retardation. The temporal histories of impulse transmission show a significant dependence on core density with a clear increase in transmitted impulse after complete core failure. The transmitted impulses show a monotonic dependence on loading intensity and a power law dependence on the relative density. The effects of high relative density are further exacerbated at higher loading intensities.

The responses to underwater impulsive loads of composite sandwich plates consisting of glass-fiber reinforced epoxy facesheets and PVC foam core with different facesheet-thickness-to-core-thickness ratios are analyzed. The configuration studied is that used in experiments being carried out in the Underwater Shocking Loading Simulator recently developed at Georgia Tech. For comparison purposes, all material properties and core dimensions are kept constant. A fully dynamic finite element model is

developed for the experimental configuration, accounting for impulsive loading generation and the dynamic response processes of the structure and water. Deformation and failure mechanisms considered are core crushing, facesheet damage, and core-facesheet separation and contact. Calculations show the distinct response regimes of the structures, as measured by energy dissipated and the maximum deflection. It is found that under the loading conditions and for the material systems analyzed, there is a range of facesheet thickness in which planar sandwich structures offer the best performance. Specifically, structures with facesheet-thickness-to-core-thickness ratios between provide the most efficient use of material in terms of both energy dissipation capacity and rigidity. The insight gained here provides guidelines for the design of structures for which response to water-based impulsive loading is an important consideration. It is important to note that the analysis reported here concerns only one structural configuration, one combination of core and facesheet materials, and one core size. More extensive analyses and experimental verification are needed to determine the applicability of the findings to sandwich structures of different geometries, sizes and materials.

Marine structures must balance strength and load-carrying capacity with the ability to minimize impulse transmission for high blast and impact resistance. The combined experimental and computational research reported here is an attempt to quantify the underwater blast response of hybrid fiber-metal laminates with different stacking sequences under a range of incident impulsive loads. The peak pressures of the incident impulses considered range from 59 MPa to 198 MPa. Since all plates considered fail under an incident impulse of $\bar{I} = 0.15$ with a peak pressure of 198 MPa, this is the highest impulse intensity discussed in this paper. The experiments reported here are

supported by fully dynamic finite element calculations. The results from numerical calculations provide a more in-depth understanding of temporal and spatial evolution of different deformation modes in the structures and the partitioning of energy in different components.

The monolithic aluminum plates experience petalling failure and exhibit bulging and tensile necking in the central region under a range of incident impulsive loads. Composite plates undergo extensive delamination at all load intensities and experience in-ply damage in the form of matrix cracking, fiber cracking and fiber-matrix debonding. The failure is predominantly near the clamped boundary, indicating significant shear dependence of damage. The hybrid (AL/CF) plates exhibit bulging and tensile failure in the aluminum sections and large-scale shear cracking in the composite sections. Additionally, the lack of confinement for the composite plate creates large delamination at the interface between the aluminum and composite sections. Conversely, the hybrid (CF/AL) plates exhibit significantly superior blast resistance with minimal shear cracking in the composite section and significantly lower bulging in the aluminum section. This behavior can be attributed to the confining conditions created by the aluminum section that prevents the composite from deflecting and failing under shear loads in conjunction with the stiff composite section which prevents excessive bulging. Both hybrid structures exhibit superior blast resistance in comparison to monolithic plates of equivalent mass.

With respect to the hybrid plates, it is determined that the stacking sequence consisting of the composite section in contact with water and aluminum section on the opposite side provides marginally higher blast mitigation capability. In stacking sequence, the carbon fiber composite section prevents the out-of-plane bulging in the

aluminum section while the aluminum section prevents shear cracking in the carbon fiber composite section resulting in a symbiotic effect that enhances blast mitigation at all loading intensities while reducing delamination between the two sections.

The blast resistance of each plate is evaluated by comparing the impulses transmitted through and the energy dissipated by the plate. The hybrid structures are found to possess superior impulse mitigation capabilities at all impulsive loads, transmitting ~60% of the impulses transmitted by the composite laminates. The monolithic aluminum plates and the aluminum sections of the hybrid plates are responsible for the majority of the energy dissipation at all impulse intensities, absorbing more than 60% of the total energy dissipated in the hybrid plates. Interfacial damage dissipation is found to exceed in-ply damage dissipation in the composite sections. Overall, the hybrid metal/composite structures constitute better alternatives to monolithic structures of either material, due to the combination of high stiffness and strength-to-weight ratio.

In the hybrid plates, the composite section is responsible for restricting the out-of-plane deflection while the aluminum section plays a vital role in impulse mitigation and energy dissipation. It is found that that plates with 40%-60% of aluminum by weight provide an optimal combination of resistance to deflection, impulse mitigation and energy dissipation. Additionally, thinner layers of aluminum lead more efficient energy dissipation on a unit mass basis.

The insight gained in this research work provides guidelines for the design of next generation structures and retro-fitting of existing structures for which response to water-based impulsive loading is an important consideration.

# REFERENCES


1. Espinosa, H.D., S. Lee, and N. Moldovan, *A novel fluid structure interaction experiment to investigate deformation of structural elements subjected to impulsive loading.* Experimental Mechanics, 2006. **46**(6): p. 805-824.

2. Wei, Z., et al., *Analysis and interpretation of a test for characterizing the response of sandwich panels to water blast.* International Journal of Impact Engineering, 2007. **34**(10): p. 1602-1618.

3. Dharmasena, K.P., et al., *Response of metallic pyramidal lattice core sandwich panels to high intensity impulsive loading in air.* International Journal of Impact Engineering, 2011. **38**(5): p. 275-289.

4. Cole, R.H., *Underwater Explosions.* Princeton University Press, Princeton, NJ, 1948.

5. Swisdak, M.M., *Explosion Effects and Properties: Part II--Explosion Effects in Water.* NSWC/WOL TR 76-116 1978.

6. Taylor, G.I., *The pressure and impulse of submarine explosion waves on plates.* . The scientific papers of G I Taylor, vol. III, pp. 287–303. Cambridge: Cambridge University Press, 1941

7. Taylor, G.I., *The Scientific Papers of G I Taylor.* Cambridge University Press, Cambridge, 1963.

8. Kambouchev, N., R. Radovitzky, and L. Noels, *Fluid-structure interaction effects in the dynamic response of free-standing plates to uniform shock loading.* Journal of Applied Mechanics-Transactions of the Asme, 2007. **74**(5): p. 1042-1045.

9. Hutchinson, J.W., *Energy and Momentum Transfer in Air Shocks.* Journal of Applied Mechanics-Transactions of the Asme, 2009. **76**(5).

10. Hutchinson, J.W. and Z.Y. Xue, *Metal sandwich plates optimized for pressure impulses.* International Journal of Mechanical Sciences, 2005. **47**(4-5): p. 545-569.

11. Taylor, G.I., *The distortion under pressure of a diaphragm which is clamped along its edge and stressed beyond its elastic limit.* Underwater Explosion Research, Vol. 3, The Damage ProcessOffice of Naval Research (1950), pp. 107–121 originally written 1942, 1942.

12. Travis, F.W. and W. Johnson, *Experiments in the dynamic deformation of clamped circular sheets of various metals subject to an underwater explosive charge.* Sheet Metal Indust., 39 (1961), pp. 456–474, 1961.

13. Johnson, W., et al., *Experiments in the underwater explosive stretch forming of clamped circular blanks.* Int. J. Mech. Sci., 8 (1966), pp. 237–270, 1966.

14. Williams, T., *Some metallurgical aspects of metal forming.* Sheet Metal Indust., 39 (1962), pp. 487–494, 1962.

15. Finnie, T.M., *Explosive forming of circular diaphragms.* Sheet Metal Indust., 39 (1962), pp. 391–398, 1962.

16. Bednarski, T., *The dynamic deformation of a circular membrane.* Int. J. Mech. Sci., 11 (1969), pp. 949–959, 1969.

17. Symonds, P.S. and N. Jones, *Impulsive loading of fully clamped beams with finite plastic deflections and strain-rate sensitivity.* Int. J. Mech. Sci., 14 (1972), pp. 49–69 1972.

18. Bodner, S.R. and P.S. Symonds, *Experiments on dynamic plastic loading of frames.* Int. J. Solids Struct., 15 (1979), pp. 1–13, 1979.

19. Bodner, S.R. and P.S. Symonds, *Experiments on viscoplastic response of circular plates to impulsive loading.* J. Mech. Phys. Solids, 27 (1979), pp. 91–113, 1979.

20. Richardson, R.M. and J.G. Kirkwood, *Theory of the plastic deformation of thin plates by underwater explosions.* Underwater Explosion Research, Vol. 3, The Damage ProcessOffice of Naval Research, pp. 305–421, 1950.

21. Hudson, G.E., *A theory of the dynamic plastic deformation of a thin diaphragm.* J. appl. Phys., 22 (1951), pp. 1-11, 1951.

22. Frederick, D., *A simplified analysis of circular membranes subjected to an impulsive loading producing large plastic deformations.* Proc. 4th Annual Conf. Solid Mechanics, University of Texas (1959), pp. 18–35, 1959.

23. Griffith, J. and H. Vanzant, *Large deformation of circular membranes under static and dynamic loading.* 1st Int. Cong. Exp. Mech. Paper No. 702 (1961), 1961.

24. Hopkins, H.G. and W. Prager, *On the dynamics of plastic circular plates.* ZAMP (J. appl. Math. and Phys.), 5 (1954), pp. 317–330, 1954.

25. Wang, A.J. and H.G. Hopkins, *The plastic deformation of built-in circular plates under impulsive load.* J. Mech. Phys. Solids, 3 (1954), pp. 22–37, 1954.

26. Florence, A.L., *Circular plates under a uniformly distributed impulse.* Int. J. Solids Struct., 2 (1966), pp. 37–47, 1966.

27. Hopkins, H.G., *On the plasticy theory of plates.* Proc. Soc. Lond., A241 (1957), pp. 153–179, 1957.

28. Shapiro, G.S., *On a rigid-plastic annular plate under impulsive loading.* J. appl. Math. Mech. (Pnk. Mat. i Mek), 23 (1959), pp. 234–241, 1959.

29. Jones, N., *Recent progress in the dynamic plastic behaviour of structures. Part I, II and III.* Shock Vib. Dig., 1978, 1978 and 1981.

30. Nurick, G.N. and J.B. Martin, *Deformation of Thin Plates Subjected to Impulsive Loading - a Review .1. Theoretical Considerations.* International Journal of Impact Engineering, 1989. **8**(2): p. 159-170.

31. Nurick, G.N. and J.B. Martin, *Deformation of Thin Plates - Subjected to Impulsive Loading - a Review .2. Experimental Studies.* International Journal of Impact Engineering, 1989. **8**(2): p. 171-186.

32. Steeves, C.A. and N.A. Fleck, *Collapse mechanisms of sandwich beams with composite faces and a foam core, loaded in three-point bending. Part II: experimental investigation and numerical modelling.* International Journal of Mechanical Sciences, 2004. **46**(4): p. 585-608.

33. Tagarielli, V.L., V.S. Deshpande, and N.A. Fleck, *The dynamic response of composite sandwich beams to transverse impact.* International Journal of Solids and Structures, 2007. **44**(7-8): p. 2442-2457.

34. Jorgensen, T.J., et al., *Chemosensitization and radiosensitization of human lung and colon cancers by antimitotic agent, ABT-751, in athymic murine xenograft models of subcutaneous tumor growth.* Cancer Chemotherapy and Pharmacology, 2007. **59**(6): p. 725-732.

35. Kleun, B.J.K. and A.W. Van der Wart, *Misspecification in infinite-dimensional Bayesian statistics.* Annals of Statistics, 2006. **34**(2): p. 837-877.

36. Raftenberg, M.N. and M.J. Scheidler, *Gap Formations in Simulations of Shpb Tests on Elastic Materials Soft in Shear.* Shock Compression of Condensed Matter - 2009, Pts 1 and 2, 2009. **1195**: p. 715-718.

37. Raftenberg, M.N., *A shear banding model for penetration calculations.* International Journal of Impact Engineering, 2001. **25**(2): p. 123-146.

38. Abrate, S., *Impact on laminated composite materials.* Appl. Mech. Rev. 44 (4), 155–190., 1991.

39. Abrate, S., *Impact on laminated composites: recent advances.* Appl. Mech. Rev. 47, 517-544, 1994.

40. Joshi, S.P. and C.T. Sun, *Impact Induced Fracture in a Laminated Composite.* Journal of Composite Materials, 1985. **19**(1): p. 51-66.

41. Chang, F.K., H.Y. Choi, and S.T. Jeng, *Study on Impact Damage in Laminated Composites.* Mechanics of Materials, 1990. **10**(1-2): p. 83-95.

42. Chang, F.K., H.Y. Choi, and S.T. Jeng, *Characterization of Impact Damage in Laminated Composites.* Sampe Journal, 1990. **26**(1): p. 18-25.

43. Lessard, L.B. and F.K. Chang, *Damage Tolerance of Laminated Composites Containing an Open Hole and Subjected to Compressive Loadings .2. Experiment.* Journal of Composite Materials, 1991. **25**(1): p. 44-64.

44. Cantwell, W.J. and J. Morton, *The Impact Resistance of Composite-Materials - a Review.* Composites, 1991. **22**(5): p. 347-362.

45. Hashin, Z., *Analysis of Stiffness Reduction of Cracked Cross-Ply Laminates.* Engineering Fracture Mechanics, 1986. **25**(5-6): p. 771-778.

46. Hashin, Z., *Analysis of Orthogonally Cracked Laminates under Tension.* Journal of Applied Mechanics-Transactions of the Asme, 1987. **54**(4): p. 872-879.

47. Minnaar, K. and M. Zhou, *A novel technique for time-resolved detection and tracking of interfacial and matrix fracture in layered materials.* Journal of the Mechanics and Physics of Solids, 2004. **52**(12): p. 2771-2799.

48. Zenkert, D., *An introduction to sandwich construction.* Engineering Materials Advisory Service, 1995.

49. Plantema, F., *Sandwich construction.* New York: Wiley, 1996.

50. Allen, H., *Analysis and design of structural sandwich panels.* Oxford: Pergamon Press, 1969.

51. Schubel, P.M., J.J. Luo, and I.M. Daniel, *Impact and post impact behavior of composite sandwich panels.* Composites Part A-Applied Science And Manufacturing, 2007. **38**(3): p. 1051-1057.

52. Nemes, J.A. and K.E. Simmonds, *Low-Velocity Impact Response of Foam-Core Sandwich Composites.* Journal of Composite Materials, 1992. **26**(4): p. 500-519.

53. Mines, R.A.W., C.M. Worrall, and A.G. Gibson, *The Static and Impact Behavior of Polymer Composite Sandwich Beams.* Composites, 1994. **25**(2): p. 95-110.

54. J. L. Abot, I.M.D., *Composite sandwich beams under low velocity impact.* Proc. of AIAA Conf. , Seattle, 2001.

55. Schubel, P.M., J.J. Luo, and I.M. Daniel, *Low velocity impact behavior of composite sandwich panels.* Composites Part a-Applied Science and Manufacturing, 2005. **36**(10): p. 1389-1396.

56. Liang, Y.M., et al., *The response of metallic sandwich panels to water blast.* Journal Of Applied Mechanics-Transactions Of The Asme, 2007. **74**(1): p. 81-99.

57. Dharmasena, K.P., et al., *Dynamic compression of metallic sandwich structures during planar impulsive loading in water.* European Journal of Mechanics a-Solids, 2010. **29**(1): p. 56-67.

58. Wei, Z., et al., *The resistance of metallic plates to localized impulse.* Journal of the Mechanics and Physics of Solids, 2008. **56**(5): p. 2074-2091.

59. Xue, Z.Y. and J.W. Hutchinson, *Preliminary assessment of sandwich plates subject to blast loads.* International Journal of Mechanical Sciences, 2003. **45**(4): p. 687-705.

60. Xue, Z.Y. and J.W. Hutchinson, *A comparative study of impulse-resistant metal sandwich plates.* International Journal of Impact Engineering, 2004. **30**(10): p. 1283-1305.

61. Qiu, X., V.S. Deshpande, and N.A. Fleck, *Finite element analysis of the dynamic response of clamped sandwich beams subject to shock loading.* European Journal of Mechanics a-Solids, 2003. **22**(6): p. 801-814.

62. Fleck, N.A. and V.S. Deshpande, *The resistance of clamped sandwich beams to shock loading.* Journal of Applied Mechanics-Transactions of the Asme, 2004. **71**(3): p. 386-401.

63. Qiu, X., V.S. Deshpande, and N.A. Fleck, *Dynamic response of a clamped circular sandwich plate subject to shock loading.* Journal of Applied Mechanics-Transactions of the Asme, 2004. **71**(5): p. 637-645.

64. Dharmasena, K.P., et al., *Mechanical response of metallic honeycomb sandwich panel structures to high-intensity dynamic loading.* International Journal of Impact Engineering, 2008. **35**(9): p. 1063-1074.

65. Cote, F., et al., *The out-of-plane compressive behavior of metallic honeycombs.* Materials Science and Engineering a-Structural Materials Properties Microstructure and Processing, 2004. **380**(1-2): p. 272-280.

66. Deshpande, V.S. and N.A. Fleck, *One-dimensional response of sandwich plates to underwater shock loading.* Journal of the Mechanics and Physics of Solids, 2005. **53**(11): p. 2347-2383.

67. Kazemahvazi, S., et al., *Dynamic failure of clamped circular plates subjected to an underwater shock.* Journal of Mechanics of Materials and Structures, 2007. **2**(10): p. 2007-2023.

68. McMeeking, R.M., et al., *An analytic model for the response to water blast of unsupported metallic sandwich panels.* International Journal of Solids and Structures, 2008. **45**(2): p. 478-496.

69. McShane, G.J., V.S. Deshpande, and N.A. Fleck, *Dynamic Compressive response of stainless-steel square honeycombs.* Journal of Applied Mechanics-Transactions of the Asme, 2007. **74**(4): p. 658-667.

70. Wei, Z., F.W. Zok, and A.G. Evans, *Design of sandwich panels with prismatic cores.* Journal of Engineering Materials and Technology-Transactions of the Asme, 2006. **128**(2): p. 186-192.

71. Wei, Z., M.Y. He, and A.G. Evans, *Application of a dynamic constitutive law to multilayer metallic sandwich panels subject to impulsive loads.* Journal of Applied Mechanics-Transactions of the Asme, 2007. **74**(4): p. 636-644.

72. Valdevit, L., J.W. Hutchinson, and A.G. Evans, *Structurally optimized sandwich panels with prismatic cores.* International Journal of Solids and Structures, 2004. **41**(18-19): p. 5105-5124.

73. Wicks, N. and J.W. Hutchinson, *Performance of sandwich plates with truss cores.* Mechanics of Materials, 2004. **36**(8): p. 739-751.

74. Vaziri, A., Z.Y. Xue, and J.W. Hutchinson, *Performance and failure of metal sandwich plates subjected to shock loading.* Journal of Mechanics of Materials and Structures, 2007. **2**(10): p. 1947-1963.

75. Vaziri, A. and J.W. Hutchinson, *Metal sandwich plates subject to intense air shocks.* International Journal of Solids and Structures, 2007. **44**(6): p. 2021-2035.

76. Spuskanyuk, A.V. and R.M. McMeeking, *Sandwich panels for blast protection in water: simulations.* International Journal of Materials Research, 2007. **98**(12): p. 1250-1255.

77. Deshpande, V.S. and N.A. Fleck, *Isotropic constitutive models for metallic foams.* Journal of the Mechanics and Physics of Solids, 2000. **48**(6-7): p. 1253-1283.

78. Xue, Z.Y. and J.W. Hutchinson, *Constitutive model for quasi-static deformation of metallic sandwich cores.* International Journal for Numerical Methods in Engineering, 2004. **61**(13): p. 2205-2238.

79. Tekalur, S.A., A.E. Bogdanovich, and A. Shukla, *Shock loading response of sandwich panels with 3-D woven E-glass composite skins and stitched foam core.* Composites Science and Technology, 2009. **69**(6): p. 736-753.

80. Tekalur, S.A., A. Shukla, and K. Shivakumar, *Blast resistance of polyurea based layered composite materials.* Composite Structures, 2008. **84**(3): p. 271-281.

81. LeBlanc, J., et al., *Shock loading of three-dimensional woven composite materials.* Composite Structures, 2007. **79**(3): p. 344-355.

82. Grogan, J., et al., *Ballistic resistance of 2D and 3D woven sandwich composites.* Journal of Sandwich Structures & Materials, 2007. **9**(3): p. 283-302.

83. Wang, E.H., N. Gardner, and A. Shukla, *The blast resistance of sandwich composites with stepwise graded cores.* International Journal of Solids and Structures, 2009. **46**(18-19): p. 3492-3502.

84. Rathbun, H.J., et al., *Performance of metallic honeycomb-core sandwich beams under shock loading.* International Journal of Solids and Structures, 2006. **43**(6): p. 1746-1763.

85. Rathbun, H.J., et al., *Structural performance of metallic sandwich beams with hollow truss cores.* Acta Materialia, 2006. **54**(20): p. 5509-5518.

86. Zok, F.W., et al., *Structural performance of metallic sandwich panels with square honeycomb cores.* Philosophical Magazine, 2005. **85**(26-27): p. 3207-3234.

87. Qiu, X., V.S. Deshpande, and N.A. Fleck, *Impulsive loading of clamped monolithic and sandwich beams over a central patch.* Journal of the Mechanics and Physics of Solids, 2005. **53**(5): p. 1015-1046.

88. Radford, D.D., V.S. Deshpande, and N.A. Fleck, *The use of metal foam projectiles to simulate shock loading on a structure.* International Journal of Impact Engineering, 2005. **31**(9): p. 1152-1171.

89. Mori, L.F., et al., *Deformation and fracture modes of sandwich structures subjected to underwater impulsive loads.* Journal of Mechanics of Materials and Structures, 2007. **2**(10): p. 1981-2006.

90. Mori, L.F., et al., *Deformation and Failure Modes of I-Core Sandwich Structures Subjected to Underwater Impulsive Loads.* Experimental Mechanics, 2009. **49**(2): p. 257-275.

91. Horacio D. Espinosa , D.G., Félix Latourte and Ravi S. Bellur-Ramaswamy *Failure Modes in Solid and Sandwich Composite Panels Subjected to Underwater Impulsive Loads.* 9th International Conference on Sandwich Structures, ICSS9, 2010.

92. Wei, X.D., et al., *Three-dimensional numerical modeling of composite panels subjected to underwater blast.* Journal of the Mechanics and Physics of Solids, 2013. **61**(6): p. 1319-1336.

93. Latourte, F., et al., *Failure mechanisms in composite panels subjected to underwater impulsive loads.* Journal of the Mechanics and Physics of Solids, 2011. **59**(8): p. 1623-1646.

94. Wadley, H.N.G., et al., *Dynamic compression of square honeycomb structures during underwater impulsive loading.* Journal of Mechanics of Materials and Structures, 2007. **2**(10): p. 2025-2048.

95. Wadley, H., et al., *Compressive response of multilayered pyramidal lattices during underwater shock loading.* International Journal of Impact Engineering, 2008. **35**(9): p. 1102-1114.

96. LeBlanc, J. and A. Shukla, *Dynamic response and damage evolution in composite materials subjected to underwater explosive loading: An experimental and computational study.* Composite Structures, 2010. **92**(10): p. 2421-2430.

97. Hudson, G.E., *A Theory of the Dynamic Plastic Deformation of a Thin Diaphragm.* Journal of Applied Physics, 1951. **22**(1): p. 1-11.

98. Wang, A.J. and H.G. Hopkins, *On the Plastic Deformation of Built-in Circular Plates under Impulsive Load.* Journal of the Mechanics and Physics of Solids, 1954. **3**(1): p. 22-37.

99. Menkes, S.B. and H.J. Opat, *Broken Beams - Tearing and Shear Failures in Explosively Loaded Clamped Beams.* Experimental Mechanics, 1973. **13**(11): p. 480-486.

100. Nurick, G.N. and G.C. Shave, *The deformation and tearing of thin square plates subjected to impulsive loads - An experimental study.* International Journal of Impact Engineering, 1996. **18**(1): p. 99-116.

101. Lee, Y.W. and T. Wierzbicki, *Fracture prediction of thin plates under localized impulsive loading. Part I: dishing.* International Journal of Impact Engineering, 2005. **31**(10): p. 1253-1276.

102. Wierzbicki, T., et al., *Calibration and evaluation of seven fracture models.* International Journal of Mechanical Sciences, 2005. **47**(4-5): p. 719-743.

103. Balden, V.H. and G.N. Nurick, *Numerical simulation of the post-failure motion of steel plates subjected to blast loading.* International Journal of Impact Engineering, 2005. **32**(1-4): p. 14-34.

104. Wei, X.D., et al., *A new rate-dependent unidirectional composite model - Application to panels subjected to underwater blast.* Journal of the Mechanics and Physics of Solids, 2013. **61**(6): p. 1305-1318.

105. McShane, G.J., et al., *Dynamic rupture of polymer-metal bilayer plates.* International Journal of Solids and Structures, 2008. **45**(16): p. 4407-4426.

106. Battley, M. and T. Allen, *Servo-hydraulic System for Controlled Velocity Water Impact of Marine Sandwich Panels.* Experimental Mechanics, 2012. **52**(1): p. 95-106.

107. Battley, M., et al., *Dynamic characterisation of marine sandwich structures.* Sandwich Structures7: Advancing with Sandwich Structures and Materials, 2005: p. 537-546.

108. Avachat, S. and M. Zhou, *High-speed digital imaging and computational modeling of dynamic failure in composite structures subjected to underwater impulsive loads.* International Journal of Impact Engineering, 2015. **77**: p. 147-165.

109. Vlot, A., *Impact loading on Fibre Metal Laminates.* International Journal of Impact Engineering, 1996. **18**(3): p. 291-307.

110. Yaghoubi, A.S. and B. Liaw, *Effect of lay-up orientation on ballistic impact behaviors of GLARE 5 FML beams.* International Journal of Impact Engineering, 2013. **54**: p. 138-148.

111. Yaghoubi, A.S. and B. Liaw, *Influences of thickness and stacking sequence on ballistic impact behaviors of GLARE 5 FML plates: Part II - Numerical studies.* Journal of Composite Materials, 2014. **48**(19): p. 2363-2374.

112. Yaghoubi, A.S. and B. Liaw, *Influences of thickness and stacking sequence on ballistic impact behaviors of GLARE 5 FML plates: Part I-experimental studies.* Journal of Composite Materials, 2014. **48**(16): p. 2011-2021.

113. Fatt, M.S.H., et al., *Ballistic impact of GLARE (TM) fiber-metal laminates.* Composite Structures, 2003. **61**(1-2): p. 73-88.

114. Abdullah, M.R. and W.J. Cantwell, *The high-velocity impact response of thermoplastic-matrix fibre-metal laminates.* Journal of Strain Analysis for Engineering Design, 2012. **47**(7): p. 432-443.

115. Fan, J., Z.W. Guan, and W.J. Cantwell, *Numerical modelling of perforation failure in fibre metal laminates subjected to low velocity impact loading.* Composite Structures, 2011. **93**(9): p. 2430-2436.

116. Langdon, G.S., et al., *Behaviour of fibre-metal laminates subjected to localised blast loading: Part I - Experimental observations.* International Journal of Impact Engineering, 2007. **34**(7): p. 1202-1222.

117. Lemanski, S.L., et al., *Behaviour of fibre metal laminates subjected to localised blast loading - Part II: Quantitative analysis.* International Journal of Impact Engineering, 2007. **34**(7): p. 1223-1245.

118. Vo, T.P., et al., *Modelling of the low-impulse blast behaviour of fibre-metal laminates based on different aluminium alloys.* Composites Part B-Engineering, 2013. **44**(1): p. 141-151.

119. Vo, T.P., et al., *Low-impulse blast behaviour of fibre-metal laminates.* Composite Structures, 2012. **94**(3): p. 954-965.

120. Karagiozova, D., et al., *Simulation of the response of fibre-metal laminates to localised blast loading.* International Journal of Impact Engineering, 2010. **37**(6): p. 766-782.

121. Langdon, G.S., et al., *Fiber-Metal Laminate Panels Subjected to Blast Loading.* Dynamic Failure of Materials and Structures, 2010: p. 269-296.

122. Johnson, W., *Impact strength of materials*. 1972, London. UK: Edward Arnold (Publishers) Limited.

123. Jones, N., *Structural impact*. 1997: Cambridge UK: Cambridge University Press; .

124. Steeves, C.A. and N.A. Fleck, *Collapse mechanisms of sandwich beams with composite faces and a foam core, loaded in three-point bending. Part 1: analytical models and minimum weight design.* International Journal of Mechanical Sciences, 2004. **46**(4): p. 561-583.

125. Hashin, Z., *Failure Criteria for Unidirectional Fiber Composites.* Journal of Applied Mechanics-Transactions of the Asme, 1980. **47**(2): p. 329-334.

126. Puck, A. and H. Schürmann, *Failure analysis of FRP laminates by means of physically based phenomenological models.* Composites Science and Technology, Volume 62, Issues 12–13, September–October 2002, Pages 1633–1662, 1999.

127. Kiel, A.H., *The Response of Ships to Underwater Explosions.* Department of the Navy, 1961.

128. Chan, S., et al., *Ballistic limit prediction using a numerical model with progressive damage capability.* Composite Structures, 2007. **77**(4): p. 466-474.

129. Pinho, S.T., P. Robinson, and L. Iannucci, *Fracture toughness of the tensile and compressive fibre failure modes in laminated composites.* Composites Science and Technology, 2006. **66**(13): p. 2069-2079.

130. Lapczyk, I. and J.A. Hurtado, *Progressive damage modeling in fiber-reinforced materials.* Composites Part a-Applied Science and Manufacturing, 2007. **38**(11): p. 2333-2341.

131. Needleman, A., *An analysis of tensile decohesion along an interface.* Journal of the Mechanics and Physics of Solids, 1990. **38**(3): p. 289-324.

132. Tvergaard, V. and J.W. Hutchinson, *The Relation between Crack-Growth Resistance and Fracture Process Parameters in Elastic Plastic Solids.* Journal of the Mechanics and Physics of Solids, 1992. **40**(6): p. 1377-1397.

133. Tvergaard, V. and A. Needleman, *Effect of Crack Meandering on Dynamic, Ductile Fracture.* Journal of the Mechanics and Physics of Solids, 1992. **40**(2): p. 447-471.

134. Needleman, A. and V. Tvergaard, *Mesh Effects in the Analysis of Dynamic Ductile Crack-Growth.* Engineering Fracture Mechanics, 1994. **47**(1): p. 75-91.

135. Xu, X.P. and A. Needleman, *Numerical Simulations of Fast Crack-Growth in Brittle Solids.* Journal of the Mechanics and Physics of Solids, 1994. **42**(9): p. 1397-&.

136. Camacho, G.T. and M. Ortiz, *Computational modelling of impact damage in brittle materials.* International Journal of Solids and Structures, 1996. **33**(20-22): p. 2899-2938.

137. Espinosa, H.D., P.D. Zavattieri, and S.K. Dwivedi. *A finite deformation continuum discrete model for the description of fragmentation and damage in brittle materials*. 1998. Pergamon-Elsevier Science Ltd.

138. Camanho, P.P., C.G. Davila, and M.F. de Moura, *Numerical simulation of mixed-mode progressive delamination in composite materials.* Journal of Composite Materials, 2003. **37**(16): p. 1415-1438.

139. Minnaar, K. and M. Zhou, *Characterization of impact in composite laminates.* AIP Conference Proceedings, 2002. **620**(1): p. 1208.

140. Zhai, J. and M. Zhou, *Finite element analysis of micromechanical failure modes in a heterogeneous ceramic material system.* International Journal of Fracture, 2000. **101**(1-2): p. 161-180.

141. Benzeggagh, M.L. and M. Kenane, *Measurement of mixed-mode delamination fracture toughness of unidirectional glass/epoxy composites with mixed-mode bending apparatus.* Composites Science and Technology, 1996. **56**(4): p. 439-449.

142. Abell, A.B. and D.A. Lange, *Fracture mechanics modeling using images of fractured surfaces.* International Journal of Solids and Structures, 1998. **35**(31-32): p. 4025-4033.

143. DIAB Inc., S.D., DeSoto, Texas 75115, USA.

144. George, T., et al., *Hybrid core carbon fiber composite sandwich panels: Fabrication and mechanical response.* Composite Structures, 2014. **108**: p. 696-710.

145. Tagarielli, V.L., V.S. Deshpande, and N.A. Fleck, *The high strain rate response of PVC foams and end-grain balsa wood.* Composites Part B-Engineering, 2008. **39**(1): p. 83-91.

146. Qiao, P.Z., M.J. Yang, and F. Bobaru, *Impact mechanics and high-energy absorbing materials: Review.* Journal of Aerospace Engineering, 2008. **21**(4): p. 235-248.

147. Lee, S., et al., *Deformation rate effects on failure modes of open-cell Al foams and textile cellular materials.* International Journal of Solids and Structures, 2006. **43**(1): p. 53-73.

148. Zhang, J., et al., *Constitutive modeling of polymeric foam material subjected to dynamic crash loading.* International Journal of Impact Engineering, 1998. **21**(5): p. 369-386.

149. Deshpande, V.S. and N.A. Fleck, *Multi-axial yield behaviour of polymer foams.* Acta Materialia, 2001. **49**(10): p. 1859-1866.

150. Hooputra, H., et al., *A comprehensive failure model for crashworthiness simulation of aluminium extrusions.* International Journal of Crashworthiness, 2004. **9**(5): p. 449-463.

151. Poapongsakorn, P. and L.A. Carlsson, *Fracture toughness of closed-cell PVC foam: Effects of loading configuration and cell size.* Composite Structures, 2013. **102**: p. 1-8.

152. Johnson, G.R. and W.H. Cook, *Fracture Characteristics of 3 Metals Subjected to Various Strains, Strain Rates, Temperatures and Pressures.* Engineering Fracture Mechanics, 1985. **21**(1): p. 31-48.

153. Corbett, B.M., *Numerical simulations of target hole diameters for hypervelocity impacts into elevated and room temperature bumpers.* International Journal of Impact Engineering, 2006. **33**(1-12): p. 431-440.

154. Gullerud, A.S., et al., *Simulation of ductile crack growth using computational cells: numerical aspects.* Engineering Fracture Mechanics, 2000. **66**(1): p. 65-92.

155. Pijaudier-Cabot, G. and Z.P. Bazant, *Nonlocal Damage Theory.* Journal of Engineering Mechanics, 1987. **113**(10): p. 1512-1533.

156. Comi, C., *A non-local model with tension and compression damage mechanisms.* European Journal of Mechanics a-Solids, 2001. **20**(1): p. 1-22.

157. D'Alembert, J.R., *Recherches sur la courbe que forme une corde tenduë mise en vibration (Researches on the curve that a tense cord forms [when] set into vibration).* Histoire de l'académie royale des sciences et belles lettres de Berlin, vol. 3, pages 214-219, 1747.

158. Graff, K.F., *Wave Motion in Elastic Solids.* Oxford Universiy Press, 1975.

159. AshbyMF, E.A., Fleck NA, Gibson LJ, Hutchinson JW, WadleyHNG., *Metal foams: a design guide.* Butterworth–Heinemann, 2000.

160. Avachat, S. and M. Zhou, *Effect of Facesheet Thickness on Dynamic Response of Composite Sandwich Plates to Underwater Impulsive Loading.* Experimental Mechanics, 2011. **Volume 52**(Issue 1): p. pp 83-93.

161. Avachat, S. and M. Zhou, *Dynamic Response Of Composite Sandwich Structures Subjected To Underwater Impulsive Loads: Experiments And Simulations* Conference Proceedings of the 16th International Conference on Composite Structures, ICCS-16, A. J. M. Ferreira (Editor), FEUP, Porto, 2011, 2011.

162. Avachat, S. and M. Zhou, *Dynamic Response of Submerged Composite Sandwich Structures to Blast Loading.* Proceedings of the IMPLAST 2010 - SEM Fall Conference, October 12-14 2010 Providence, Rhode Island, USA, Arun Shukla (Editor), 2010.

163. Swisdak, M.M., *Explosion effects and properties: Part II – explosion effects in water.* Technical Report, Naval Surface Weapons Center, Dahlgren, Virginia, USA, 1978.

164. Arora, H., et al., *Compressive strength after blast of sandwich composite materials.* Philosophical Transactions of the Royal Society a-Mathematical Physical and Engineering Sciences, 2014. **372**(2015).

165. Arora, H., P.A. Hooper, and J.P. Dear, *The Effects of Air and Underwater Blast on Composite Sandwich Panels and Tubular Laminate Structures.* Experimental Mechanics, 2012. **52**(1): p. 59-81.

166. Cole, R.H., *Spherical Shock Waves from Underwater Explosions.* Physical Review, 1947. **72**(2): p. 177-177.

167. Kambouchev, N., L. Noels, and R. Radovitzky, *Numerical simulation of the fluid-structure interaction between air blast waves and free-standing plates.* Computers & Structures, 2007. **85**(11-14): p. 923-931.

168. Radford, D.D., et al., *The response of clamped sandwich plates with metallic foam cores to simulated blast loading.* International Journal of Solids and Structures, 2006. **43**(7-8): p. 2243-2259.

169. McShane, G.J., V.S. Deshpande, and N.A. Fleck, *The underwater blast resistance of metallic sandwich beams with prismatic lattice cores.* Journal of Applied Mechanics-Transactions of the Asme, 2007. **74**(2): p. 352-364.

170. Tagarielli, V.L. and N.A. Fleck, *A comparison of the structural response of clamped and simply supported sandwich beams with aluminium faces and a metal foam core.* Journal of Applied Mechanics-Transactions of the Asme, 2005. **72**(3): p. 408-417.

171. Chiras, S., et al., *The structural performance of near-optimized truss core panels.* International Journal of Solids and Structures, 2002. **39**(15): p. 4093-4115.

172. Avachat, S. and M. Zhou, *High-speed digital imaging and computational modeling of dynamic failure in composite structures subjected to underwater impulsive loads.* International Journal of Impact Engineering, 2015. **77**(0): p. 147-165.

173. DIAB Inc., S.D., DeSoto, Texas 75115, USA http://www.diabgroup.com/europe/literature/e_pdf_files/man_pdf/H_man.pdf Accessed 5 May 2011.

174. Avachat, S. and M. Zhou, *Effect of core density on deformation and failure in sandwich composites subjected to underwater impulsive loads.* The International Journal of Multiphysics 2012. **Volume 6**(Number 3 ).

175. Avachat, S. and M. Zhou, *Dynamic Response of Submerged Composite Sandwich Structures to Blast Loading*, in *IMPLAST 2010 - SEM Fall Conference*, A. Shukla, Editor. 2010, Society for Experimental Mechanics, Inc.: Providence, Rhode Island, USA.

176. Triantafillou, T.C. and L.J. Gibson, *Failure Mode Maps for Foam Core Sandwich Beams.* Materials Science and Engineering, 1987. **95**: p. 37-53.

177. Triantafillou, T.C., et al., *Failure Surfaces for Cellular Materials under Multiaxial Loads .2. Comparison of Models with Experiment.* International Journal of Mechanical Sciences, 1989. **31**(9): p. 665-678.

178. Fatt, M.S.H. and L. Palla, *Analytical Modeling of Composite Sandwich Panels under Blast Loads.* Journal of Sandwich Structures & Materials, 2009. **11**(4): p. 357-380.

179. Abot, J.L. and I.M. Daniel, *Composite sandwich beams under low velocity impact.* Collection of Technical Papers – AIAA/ASME/ASCE/AHS/ASC Structures, Structural Dynamics and Materials Conference 1: 67-77, Seattle, WA (2001). 2001.

180. Arora, H., Hooper, P. and Dear, J.P., *Blast and other high rate loading composite sandwich materials.* 9th International Conf on Sandwich Structures (ICSS-9), Ravichandran, G. ed, California Institute of Technology, Pasedena, USA (June 2010), Key-note paper MA3.1., 2010.

181. Langdon, G.S., et al., *The air-blast response of sandwich panels with composite face sheets and polymer foam cores: Experiments and predictions.* International Journal of Impact Engineering, 2013. **54**: p. 64-82.

182. Langdon, G.S., et al., *The response of sandwich structures with composite face sheets and polymer foam cores to air-blast loading: Preliminary experiments.* Engineering Structures, 2012. **36**: p. 104-112.

# VITA

Siddharth Avachat was born and raised in Pune, India and obtained a Bachelor of Engineering with highest honors from the University of Pune. He worked as an undergraduate researcher at the National Chemical Laboratory in Pune, India under the direction of Dr. Ashish K. Lele in the Complex Fluids and Polymer Engineering (CFPE) research group. He entered Georgia Institute of Technology in Atlanta, GA as a graduate student in Materials Science and Engineering in the Dynamic Properties Research Laboratory (DPRL), headed by Dr. Min Zhou. He received a Master of Science degree in Materials Science and Engineering in Fall 2012 and a Doctor of Philosophy degree in Mechanical Engineering in Fall 2015. He has published papers in a number of peer-reviewed journals and international conferences. In his spare time, he enjoys digital photography, getting acquainted with innovative design and manufacturing techniques, skills-based volunteering for environmental and educational causes, and renovating vintage bicycles.